Bioinspired Iron-Carbene Models of Heme and Non-Heme Enzymes: Electronic Structure and HAA Reactivity

Dissertation

for the award of the degree

"Doctor rerum naturalium" (Dr.rer.nat.)

of the Georg-August-Universität Göttingen

within the doctoral program Chemie

of the Georg-August University School of Science (GAUSS)

submitted by

Massimiliano Morganti

from Castel del Piano

Göttingen, 2021

Thesis Committee

Prof. Dr. Franc Meyer

Institut für Anorganische Chemie, Georg-August-Universität Göttingen

Prof. Dr. Inke Siewert

Institut für Anorganische Chemie, Georg-August-Universität Göttingen

Prof. Dr. Konrad Koszinowski

Institut für Organische und Biomolekulare Chemie, Georg-August-Universität Göttingen

Members of the Examination Board

Reviewer: **Prof. Dr. Franc Meyer**

Institut für Anorganische Chemie, Georg-August-Universität Göttingen

Second Reviewer: **Prof. Dr. Inke Siewert**

Institut für Anorganische Chemie, Georg-August-Universität Göttingen

Further members of the Examination Board:

Prof. Dr. Konrad Koszinowski

Institut für Organische und Biomolekulare Chemie, Georg-August-Universität Göttingen

Prof. Dr. Ricardo Mata

Institut für Physikalische Chemie, Georg-August-Universität Göttingen

Prof. Dr. Dietmar Stalke

Institut für Anorganische Chemie, Georg-August-Universität Göttingen

Dr. Michael John

Institut für Organische und Biomolekulare Chemie, Georg-August-Universität Göttingen

Date of the oral examination: 02.09.2021

Table of Contents

1. Introduction

1.1 High-Valent Metal-Oxo Intermediates in Biology

Ever since the Industrial Revolution, which marked the beginning of the late period of the Modern Era, the scientific discoveries and technological advancements have paced the ever-growing demand of base materials, highly functionalized products and energy together with the dramatic increase of the human population.[1,2] The flourishing knowledge on the physical, biological and chemical laws governing the world allowed for a vertiginous acceleration in the development of new materials, drugs, production techniques and investigation procedures. However, while the growing demand rate have not given signs of deceleration since then, the ability of modern economy to meet its requirements has been reaching a *plateau* in the last decades, threatening the danger of slowing down growth. Therefore, modern science has focused tremendous amounts of effort on the optimization of known processes and the discovery of new paths for the production of necessary goods.

Among the most pressing issues of post-modern society, the depletion of non-renewable energy sources constitutes the most important and alarming one. In order to substitute fossil-based oil processes and find alternative (and renewable) sources to power the growth of modern society, chemists have been focusing their attention on new paths towards oxidation of hydrocarbons as a mean to exploit abundant available deposits and recycle some of the byproducts of industrial processes.[3] However, the selective functionalization of strong C–H bonds constitutes a non-trivial challenge in itself, given the high oxidizing power necessary for such reactions.

In this regard, nature constitutes a convenient source of inspiration for chemists, given the ability of natural enzymes to perform an impressive variety of challenging reactions aimed at the efficient production and utilization of energy feedstocks. A large variety of natural active centers has evolved to perform demanding oxidations of substrates by harnessing the oxidative power of an abundant and easily available molecule: dioxygen. In fact, many enzymes can perform the exergonic four-electron reduction of dioxygen to water to exploit the thermodynamically favored enthalpy change of $-80\ \mathrm{kcal \cdot mol^{-1}}$ and drive the associated catalytic cycles.[4,5] However, despite this clear thermodynamic advantage of using oxygen as oxidant, nature had to deal with the intrinsic difficulty of activating O_2 in ambient conditions. In fact, the dioxygen molecule is kinetically rather stable at 25°C, owing to its triplet ground state ($^3O_2$) which makes direct two-electron oxidations of organic substrates, usually closed-shell systems, spin-forbidden.[4,6–10] Additionally, the one-electron reduction of O_2 to superoxide is thermodynamically "uphill" by $7.8\ \mathrm{kcal \cdot mol^{-1}}$.[5,11] To overcome the obstacle of dioxygen activation and exploit spin-allowed transformations, natural enzymes

therefore activate $^3O_2$ using transition metal ions with open-shell configuration.[12–14] The availability of multiple stable spin-states with open-shell configurations and numerous oxidation states typical of transition metals allows them to behave as reductants that allow for the favorable two- or four-electron reductions of oxygen and/or promote the reduction to reactive superoxide anions.[15–18]

The most common metals found in natural enzymes that perform O_2 activation are iron, copper and manganese, and they constitute the active sites of a large assortment of enzymes capable of performing a variety of substrate transformations like hydroxylation, desaturation, halogenation, formation of heterocyclic rings, epoxidation and decarboxylation.[19–24] Usually, the catalytic cycles start with the stepwise reduction of O_2 at the metal center, with the formation of oxidized metal-O complexes.[25] In the following steps, the main active species that perform substrates oxidations are therefore complexes containing high-valent M-oxo cores that display unchallenged reactivity.[24–27] Therefore, the understanding of the nature of these intermediates is a non-trivial key requirement for the development of novel, cheap, bioinspired catalysts for industrial use, and in the last decades scientists devoted great deals of effort to characterize and model those species.

1.2 Heme and Non-Heme Enzymes

Among the transition metals cited above, iron has the highest relative abundance on earth's crust, and therefore has been integrated in numerous biological transformations in all realms of life.[28] Iron-containing enzymes that activate O_2 and H_2O_2 are key species in important metabolic processes (catabolism), chemical energy conversions (cellular respiration), the formation of blood vessels (angiogenesis), O_2 transport, cellular programmed death (apoptosis), degradation of reactive radicals and oxygenation of organic substrates.[19,26,29] Among the numerous open-shell configurations and oxidation states available for Fe, the high-spin (HS) ferrous (Fe^{II}) state is the most common in oxygen activating enzymes, and it is found in different coordination environments within enzymes structures.[27]

Three main structural motifs for oxygen-activating iron enzymes are encountered in nature (Figure 1). In heme enzymes, a mononuclear iron center is coordinated by a macrocyclic protoporphyrin IX ligand and by an axial peptide residue depending on the function of the enzyme: cysteine is bound in oxygenases, while tyrosine and histidine act as ligands in the active centers of peroxidases and catalases respectively.[5,27] The majority of such enzymes perform the activation of substrates via oxoiron(IV) reactive intermediates, the most common of which is the so called Compound-I (Cpd-I), better described as an Fe^{IV}=O center coupled with a π-radical cation lying on the porphyrin ligand (for additional information see Section 1.4).

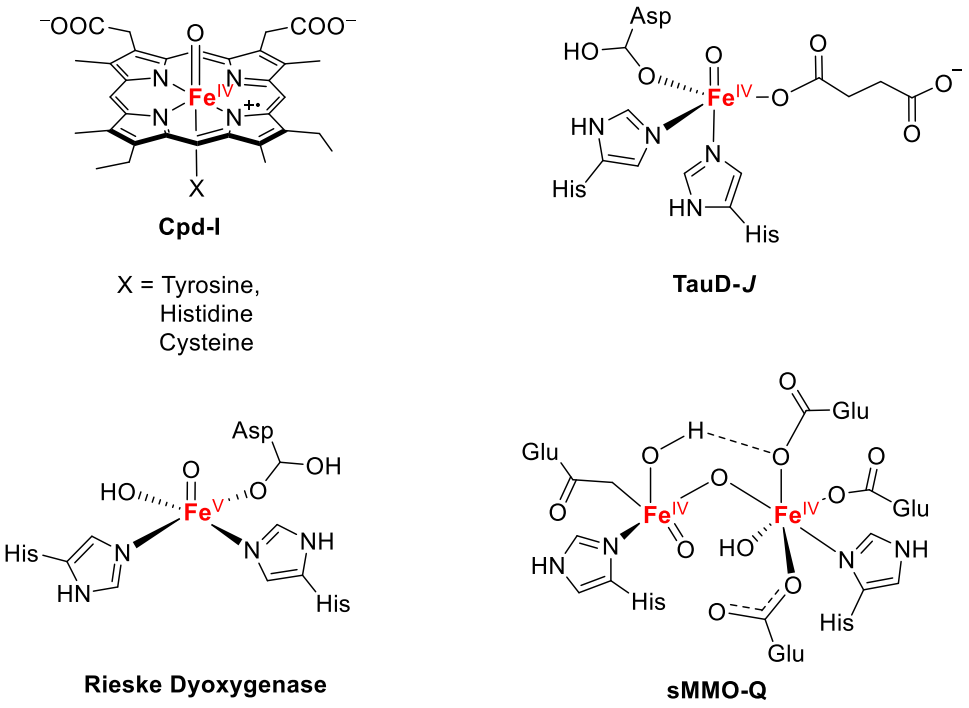

Figure 1. Representation of the three structural motifs discussed in 1.2: high-valent Fe-oxo intermediates in some heme and non-heme enzymes.

On the other hand, mononuclear non-heme active centers contain iron coordinated by a combination of peptide residues in a non-macrocyclic fashion. Most non-heme enzymes have a set of two histidine and a carboxylate (Asp or Glu) coordinating groups oriented in a facial arrangement on the metal center, forming what is commonly known as the 2-His/1-Asp (or 1-Glu) facial triad.[24,30–32] A subset of non-heme dioxygenases present instead a 3-His facial triad and perform dioxygenations of sulfur-containing residues, as in the case of cysteine dioxygenases (CDO). Prominent examples of mononuclear non-heme Fe enzymes are taurine α-ketoglutarate (α-KG) dioxygenase, which hydroxylates taurine via a non-heme Fe^{IV}-oxo active intermediate (TauD-*J*), and the family of Rieske dioxygenases, that are proposed to perform the vicinal dihydroxylation of C–C unsaturated bonds via an HO–Fe(V)O active complex.[20] The detailed mechanisms of both heme and non-heme enzymes cited above will be discussed in Section 1.4.

The last group of common structures comprises dinuclear non-heme centers that catalytically activate C–H bonds, as found in toluene monoxygenases, ribonucleotidereductases, fatty acids desaturases and the most famous and deeply investigated soluble methane monoxygenases.[23,33] These species present two non-heme iron centers coordinated by two histidine and four carboxylate residues. As an example of the involvement of high-valent Fe-oxo intermediates in this last class of enzymes, complex Q of soluble methane monooxygenase (sMMO) was characterized as a dimeric Fe^{IV} complex with a bridging oxo group and a Fe=O site, constituting the active intermediate in the

oxidation of methane to methanol.[34,35] Despite the deep interest sparked by this last class of diiron active sites, this work focuses on the investigation of mononuclear high-valent Fe^{IV}-oxo models for the first two classes of structural motifs presented; for a more detailed description of dimeric active centers, the reader is invited to explore the vast literature available on the topic.[23,36]

1.3 The Fe=O Bond

In all examples cited in Section 1.2, the active species of the catalytic cycles of either heme or non-heme enzymes are high valent Fe complexes of the oxo ligand. Therefore, the Fe=O group seems to be the key feature that nature has chosen to perform the immense variety of the reactions covered by those enzymes. In order to be able to exploit nature as inspiration for the development of new industrial processes, understanding of the nature of the iron-oxo bond in such intermediates is paramount. As shown in Figure 2, the oxoiron(IV) intermediates are mainly found in two coordination environments possessing either tetragonal (C_{4v}) or trigonal (C_{3v}) symmetry, typical of heme- and non-heme centers respectively. The nature of the Fe=O bond can be initially understood using ligand field theory.

In order to elucidate the nature of the orbitals involved in the iron-oxo bonding let us consider the tetragonal symmetry. The metal ion participates in bonding with its five d orbitals, the degeneracy of which has been lifted upon interaction with a formally octahedral ligand field, and further reduced from O_h to C_{4v} (loss of an *xy* mirror plane) by the strong interaction with the oxo ligand. The latter instead act as both σ-donor and π-donor in bonding interactions with its doubly occupied 2p orbitals.[25] Figure 2 shows the final ligand field splitting owing to the π-antibonding interactions between Fe and the oxo group, which rise the energies of orbitals $d_{xz,yz}$, and to the σ-antibonding interaction that destabilizes the d_{z^2} orbital above the $d_{x^2-y^2}$.

The six electrons that populate low energy σ- and π-bonding orbitals (not shown in Figure 2) are responsible for the triple bond nature of terminal M^{IV}-oxo complexes of early transition metals. However, in case of an Fe^{IV}=O complex the bond order is decreased to two by population of the $d_{xz,yz}$ orbitals, which are π-antibonding with respect to the Fe-O interaction. The result is a reactive iron-oxo double bond that is responsible for the catalytic activity and instability of most oxoiron(IV) complexes. Additionally, in the case of late transition metals, the instability of the terminal oxo complex can be enhanced by the valence tautomerisms of the M–O bond, which is, to some extent, relevant for Fe complexes as well.

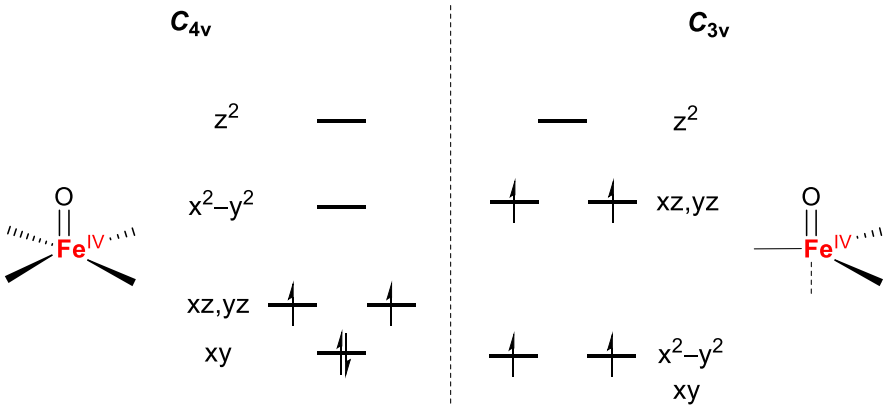

Figure 2. Orbital splitting of oxoiron(IV) intermediates in tetragonal (left) and trigonal (right) geometry.

The comparatively low energy of the d orbitals for late transition metals, close to the ones of the π-donor oxo ligand, is responsible for the high covalency of the M-oxo bond and therefore for the partial metal-oxyl radical character (with the metal reduced by one electron), which is predicted to promote reactivity towards substrates, and hence increased instability.[37,38]

The different electronic structures owing to different ligand environments, as in the heme/non-heme case, account for the fine tuning and extreme versatility of the Fe=O moiety in natural active centers, as mentioned above. In heme Fe^{IV}=oxo intermediates iron is most often found in the low spin configuration (ferromagnetically or antiferromagnetically coupled with a π-radical cation porphyrin ligand) and tetragonal symmetry due to the strong ligand field of the porphyrinato dianions, while the weak field of the facial 2-His/1-Asp(Glu, His) triad accounts for the $S = 2$ nature of iron(IV) in most non-heme trigonal complexes. However, despite the different spin states found in nature, the Fe=O double bond shows similar strengths, lengths and stretching frequencies in both $S = 1$ and $S = 2$ cases.[19,29,33,39,40] In fact, in both states the two π-orbitals that are antibonding with respect to the Fe–O bond are singly occupied regardless of the spin state, symmetry or other electronic features.

With a clearer depiction of the electronic structure of the high-valent Fe-oxo intermediates, the next section will present the different catalytic cycles of heme and non-heme natural active centers, and the typical substrate activation reactivity of such species.

1.4 Formation and Reactivity of Heme and Non-Heme High-Valent Fe=O Intermediates

Typically, catalytic cycles for oxygen activation and substrate oxidation start with the activation of dioxygen at a Fe^{II} center. Reductive binding of O_2 is accompanied by one-electron oxidation of the metal with the formation of an Fe^{III}-superoxo complex which is the first catalytic intermediate of the cycle, common to both heme and non-heme systems. From this point onward the cycles differ between different classes of enzymes, as shown in Figure 3. The cycles continue with stepwise reductions of dioxygen, in which two of the electrons necessary to complete the four-electron reduction from O_2 to oxo groups are generally provided by additional cosubstrates that behave as reductants. To this extent, many enzymes make use of tetrahydrobiopterin or 2-oxoacids (see taurine α-ketoglutarate dioxygenase below), while others exploit NADH as source of electrons (e.g. Cytochrome P450 and Rieske dioxygenases).[24,31,32] However, it has been recently discovered that a class of enzymes, isopenicillin-N synthase (IPNS), can also perform the four-electron reduction of O_2 coupled with substrates oxidation in absence of additional reductant (Figure 3 reports the mechanism for the generation of the oxoiron(IV) active intermediate of IPNS).[41]

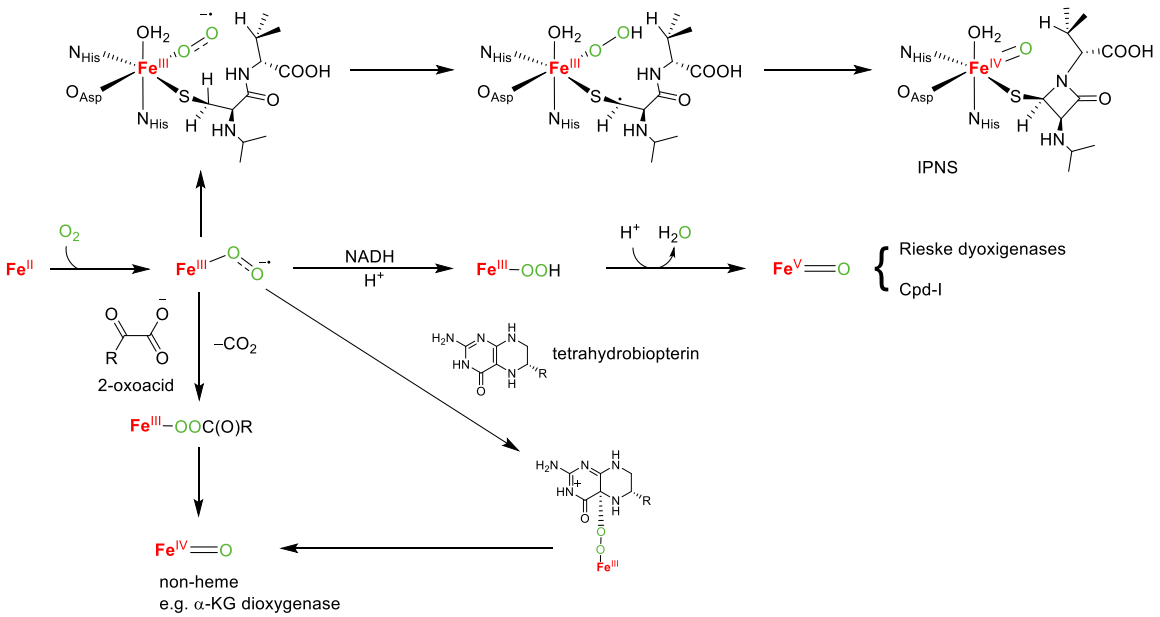

Figure 3. Biological pathways for the formation of high-valent Fe-oxo enzymatic intermediates. Adapted from reference [27].

In the catalyitc cycle of the non-heme taurine α-ketoglutarate dioxygenase enzyme the initial ferric superoxo intermediate evolves via the oxidation of the coordinated 2-oxoacid and subsequent decarboxylation, generating the high-valent TauD-*J* oxoiron(IV) active intermediate. Remarkably,

the latter species was the first non-heme oxoiron(IV) enzymatic intermediate to be fully characterized both spectroscopically and structurally.[19,42] In Rieske dioxygenases instead, the Fe^{III}–$OO^{\bullet-}$ ion is reduced with NADH and protonated to form an Fe^{III}-hydroperoxo intermediate. The subsequent proton-promoted homolytic splitting of the O–O bond releases water and generates the active oxoiron(V) species in which both redox equivalents necessary for the additional two-electron reduction of oxygen are taken from the iron center.[20,43–46] A similar path is chosen by heme-enzymes of the Cytochrome P450 family, although with an important difference: the two redox equivalents that generated the formal Fe(V) active species are stored both on the metal and on the oxidized porphyrin ligand, with the formation of an Fe^{IV}-oxo π-radical cation porphyrin system called Compound I (Cpd-I).[5,47]

Reactivity of high-valent iron-oxo heme intermediates: Cpd-I

As mentioned above, heme enzymes are responsible for an impressive variety of reactions involving oxygen in all the available oxidation states. However, most of these natural catalysts rely on Cpd-I as their common active intermediate, and Scheme 1 shows the most studied reactions that this intermediate performs in natural catalytic cycles. Among those, the involvement of this species in selective hydroxylations of very strong C–H bonds by the Cytochrome P450 family of enzymes is the main reason for the great deal of effort that scientists have devoted to its characterization and to the study of its reactivity patterns.[5,47]

Direct characterization of Cpd-I of P450 has been achieved only recently,[48] given its extreme reactivity and instability, but the results of these studies were analogous to what has been previously shown for the more stable Cpd-I of other heme enzymes such as horseradish peroxidase (HRP), chloroperoxidase (CPO) and catalase. The complex can be described as containing an $S = 1$ Fe^{IV} metal center coupled with a π-radical cation porphyrin ligand. In particular, a weak ferromagnetic coupling (imposing a total spin $S_T = 3/2$) has been observed in many peroxidases and catalases while strong ferromagnetic couplings to $S_T = 1/2$ species is typical of cysteinate-ligated CPO and P450 intermediates.[48–51]

The mechanism of hydroxylation of strong aliphatic C–H bonds was first proposed in the ‘70s by Groves and coworkers and involves an initial hydrogen atom abstraction (HAA, confirmed by large KIE values) that proceeds with the generation of the substrate radical, protonation of the oxygen moiety and the reduction of the porphyrin radical with the formation of Compound II (Cpd-II): an Fe^{IV}–OH complex.[52,53] The following step, called “oxygen rebound”, is the combination of the radical of the substrate with the hydroxyl group of Cpd-II to afford the hydroxylated product and a reduced cysteinate-Fe^{III} porphyrin center, as shown in Scheme 1.[54–57]

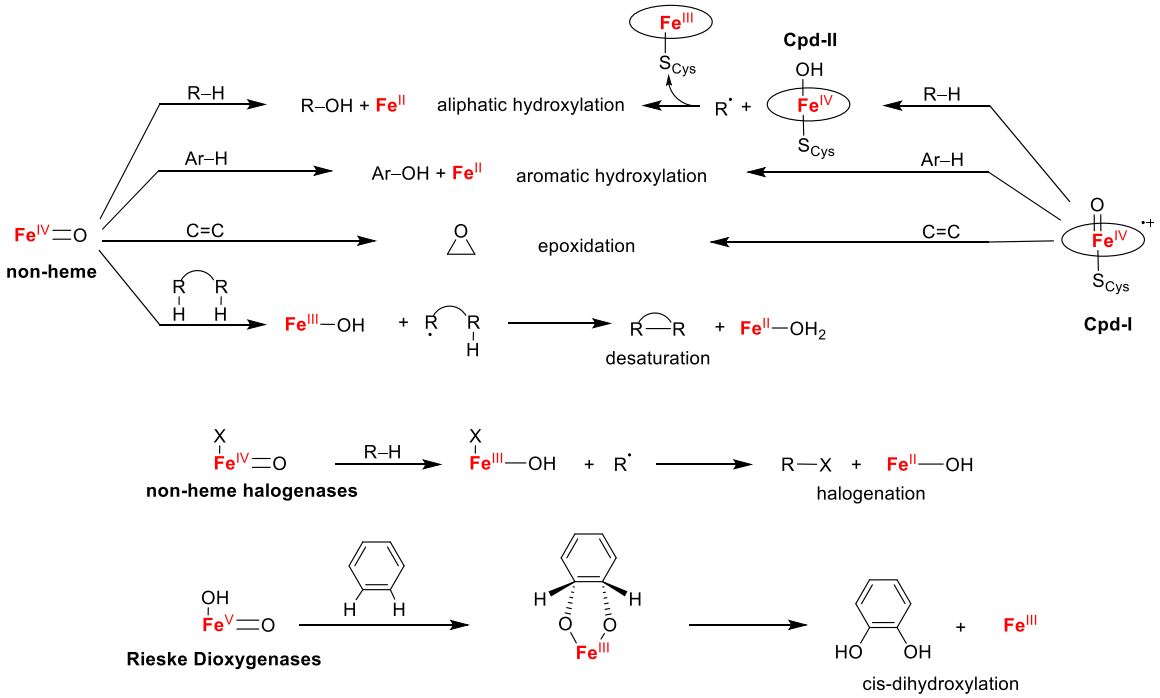

Scheme 1. Most relevant C–H or C=C activation reactions performed by mononuclear heme (Cytochrome P450) and non-heme high-valent oxoiron active intermediates. Adapted from reference [27].

Although all the enzymes cited so far form the corresponding Cpd-I as active species, a key feature that marks the difference between Cytochrome P450 and peroxidases/catalases is the fact that the latter ones are not able to activate aliphatic C–H bonds, while the Cpd-I of P450 can selectively hydroxylate bonds with BDEs well above 100 kcal·mol^{-1} with second order rate constants of 10^7 M^{-1} s^{-1} .[57] Recently, the explanation for this behavior has been found in the role of the axial cysteinate residue that is present in P450 but not in the other two classes of heme enzymes (Figure 4). In fact, a study from Green and coworkers has investigated the reason behind the fact that although Cpd-I is able to oxidize substrates that requires quite demanding thermodynamic potentials ($E^{0\prime}_{C\cdot/CH}$ ~ 1.5 V *vs.* NHE) it does so without destroying the protein framework around the active center, that contain easily oxidizable residues such as tyrosine and tryptophan. Therefore, they developed a thermodynamic model that aimed at comparing the driving force of the substrate activation with the one of the competing protein oxidation, quantified by the respective free energies of reaction. The latter depends both on the reduction potential of Cpd-I and on the pK_a of Cpd-II, as suggested by the Bordwell equation (equation 1), where $BDFE_{sol}(O-H)$ is the bond dissociation energy of the incipient O–H bond, E^0_{Cpd-I} the reduction potential of the associated Cpd-I, and $C_{G,sol}$ an experimentally determined constant.[58,59]

$$BDFE_{sol}(O-H) = 1.37pK_{a\,Cpd-II} + 23.06E^{0}_{Cpd-I} + C_{G,sol} \quad (1)$$

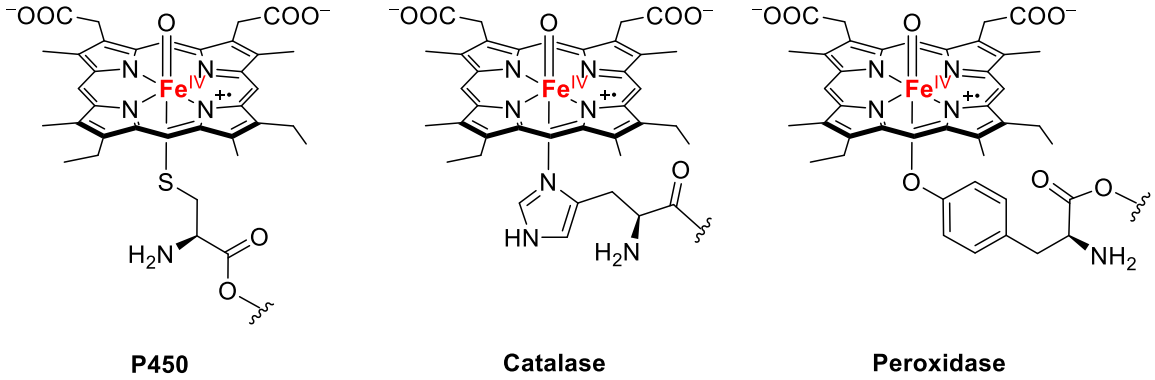

Figure 4. Schematic representation of the active centers of the three Cpd-I of Cytochrome P450, Catalase and Peroxidase with the axial cysteine, histidine, and tyrosine residues, respectively.

The model argues that the presence of the axial cysteinate promotes the activation of C–H bonds over the competing reaction by the generation of a strongly basic Cpd-II.[55,60–63] The difference between the free energy of substrate oxidation (named "productive pathway") and the free energy of protein scaffold oxidation ("non-productive pathway") was shown to be independent on the reduction potential of Cpd-I but directly affected by the pK_a of Cpd-II: a change in one unit of pK_a affects the free energy difference by 1.37 kcal·mol^{-1}, with higher pK_a corresponding to a more favorable productive pathway. At the same time, the kinetics of the non-productive pathway are decreased by the same increment in basicity of the Cpd-II intermediate. Finally, Groves and coworkers successfully measured the pK_a of Cpd-II of CYP158 obtaining a very high value of 11.9, confirming the high basicity of Cpd-II and the protonated Fe^{IV}-OH state. The work showed that the elevated basicity slows down the non-productive pathway by five orders of magnitude compared to substrate oxidation, therefore explaining the incredible proficiency in strong C–H bonds hydroxylations of the Cytochrome P450 family.[64] This successful study not only provided a solid strategy to improve the efficiency of heme model catalytic systems but also exposed the dramatic influence of the axial thiolate ligand on their reactivity.

Heme model complexes: axial ligand effect and two-state reactivity

In 1981 Groves and coworkers synthesized the first Fe^{IV}-oxo porphyrin π-cation radical model complex using the sterically hindered *meso*-tetramesitylporphyrinato ligand (TMP) by oxidation of a [(TMP)Fe^{III}(Cl)] complex with *meta*-chloroperbenzoic acid (MCPBA).[22] The Cpd-I model showed typical spectroscopic features of an Fe^{IV} metal and a radical porphyrinato ligand and exhibited a short Fe–O distance of 1.60 Å that confirmed the double bond character.[65] From that date, a large variety of [(porph$^{+\bullet}$)Fe^{IV}(O)X] complexes with different substituents on the macrocycle have been successfully studied, and their electronic structure has been determined to exhibit a total quartet ground state deriving from ferromagnetic coupling of the S = 1 Fe^{IV} center with the radical ligand.[8,21,47,66] Although this is in contrast to the total doublet ground state measured for the Cpd-I of P450 enzymes, the doublet-quartet spin state change has been shown to be rather facile for the model complexes.[5,67] The models proved to be proficient oxidants in alkane epoxidations (that proceeds through an oxygen atom transfer – OAT – mechanism) and C–H bonds hydroxylations, therefore confirming their validity as mimics of the natural active species despite the difference in magnetic ground state. To explain this similarity, Shaik, Schwarz and Schröder proposed a C–H hydroxylation mechanism in which a doublet-quartet spin crossover process would be active along the reaction coordinate, named "two-state reactivity" (TSR, shown in Figure 5).[68–70]

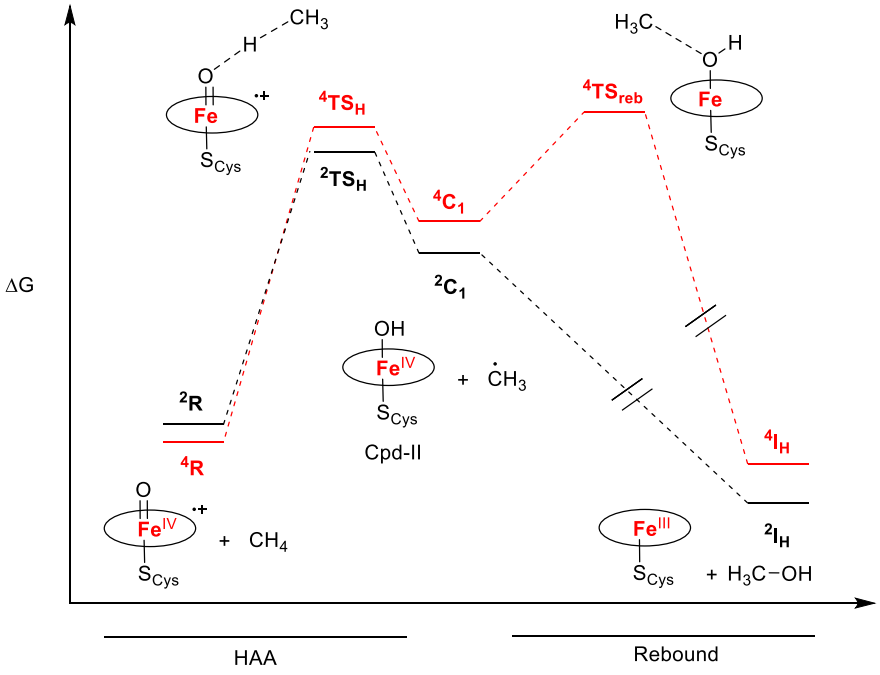

Figure 5. Energy profile of the TSR mechanism in C–H bond hydroxylation by heme models. Transition states are indicated with TS while initial states with R. The doublet path is reported in black, while the path over the quartet state is depicted in red. Adapted from references [27] and [47].

In this model, the hydroxylation process is divided into two stages: the initial C–H bond activation via hydrogen atom abstraction (HAA) and the rebound phase mentioned above. The initial doublet and quartet spin ground states (^{2}R and ^{4}R in Figure 5) are very close in energy, and they remain so during the first phase in which a transition state between the Fe=O and the C–H bond (TS_H) is formed. The small energy difference in the HS and LS transition states led to the formulation of the hypothesis according to which both spin states would significantly contribute to the reaction pathway (at least in the first phase), hence the TSR name. However, the rebound phase has been shown to possess significantly higher activation barriers on the HS path (TS_{reb}), while a rapid and essentially barrier-less collapse to the hydroxylated product is (I_H) predicted for the low-spin pathway.[26,27,47]

In 2009 Nam, Shaik and coworkers synthesized a series of axially substituted [($TMP^{+\bullet}$)Fe(O)X] complexes bearing hydroxide, acetate, chloride and triflate as axial ligand *trans* to the oxo group, allowing for the evaluation of the effect of axial ligand donor properties on the HAT and OAT reactivity of the models.[71] They have shown that both HAT and OAT rates increase with the increasing electron-donor abilities of the axial anion. Faster H-atom abstraction was supposed to be due to an increased basicity of the corresponding product Cpd-II, promoted by the higher electron density on the Fe-O group, while the weakening of the Fe=O bond in the Cpd-I intermediate would have been responsible for faster OAT rates. However, Fuji and coworkers have later reported a second series of complexes with trifluoroacetate, nitrate, acetate, chloride, fluoride, hydrocinnamate and benzoate for which the reaction rates did not correlate neither with Fe=O stretching frequencies nor with the Cpd-I model reduction potentials, but rather with the reduction potentials of the corresponding [(TMP)Fe^{III}(X)] product obtained after the rebound step.[72,73] Therefore, according to this second study the control of the axial ligand on reactivity would come from the stabilization/destabilization of the final ferric product, rather than from direct effect on the Cpd-I intermediate. However, the vast amounts of efforts dedicated to unravelling the reactivity control on Cpd-I models led to the involvement of a number of phenomena and processes that are supposed to be active during the reaction (entropic contributions to energy barriers, Brønsted-Evans-Polanyi correlations, structural effects, medium effects, etc…), that complicates the overall picture to a significant extent. Many of these phenomena are still under debate and the most relevant ones for our discussion will be described in next section.[27]

Non-heme enzymes and general reactivity

As mentioned in Section 1.2, the TauD-*J* intermediate of taurine α-KG dioxygenase (Figure 1) was the first high-valent oxoiron(IV) non-heme active intermediate to be unambiguously characterized.

The presence of a Fe=O double bond was confirmed by resonance Raman (rR) and EXAFS studies, which revealed a distance of 1.62 Å similar to the ones observed for heme analogues.[74,75] The weak ligand field exerted by the 2-His/1-Asp facial triad is reflected by the $S = 2$ spin state of the metal center, as confirmed by variable-field Mößbauer studies. To date, a large number of other non-heme active intermediates has been shown to possess similar electronic structures and to be involved in a variety of catalytic cycles of natural enzymes such as epoxidases, hydroxylases, halogenases, desaturases, epimerases and more.[27,76–78] These reactions have been shown to proceed with a mechanism similar to the one described for the P450 Cpd-I-mediated hydroxylations: an initial rate-determining HAA step (as confirmed by large KIE values)[79] is followed by the rapid oxygen-rebound (hydroxylases), a second HAA (desaturases) or a halogen-carbon bond formation (halogenases). In addition to these catalytic transformations, Section 1.2 introduced another class of non-heme iron enzymes, namely the Rieske dioxygenases, that can perform the challenging *cis*-dihdroxylation of aromatic substrates via a reactive OH–Fe(V)=O intermediate (Scheme 1).

Despite the great variety of reactions that non-heme enzymes can perform, the majority of them is found to perform hydroxylation of alkyl and aryl C–H bonds, giving us a chance to focus on two important concepts that affect the rates of this specific reaction.

As mentioned when discussing the HAA reactivity of heme systems, the high activity toward C–H bond activation of non-heme oxoiron(IV) intermediates is strongly dependent on the basicity of the one-electron reduced product of the HAA: the stronger the incipient O–H bond, the faster the HAA rates. This dependency has been shown to often overtake the effect of increased or decreased redox potential of the formal $Fe^{IV}O/Fe^{III}O$ couple, as shown by the seminal work of Mayer and coworkers.[80,81] In addition to this, the HAA reaction is also controlled by the type of orbital interaction between the substrate σ(C–H) bond and the involved frontier molecular orbitals (FMO) of the Fe=O.[27,82,83] Section 1.3 has shown that in a tetragonal symmetry the metal d_{z^2} orbital forms σ* interactions with the oxo ligand, while the d_{xz} and d_{yz} are π-antibonding towards the Fe=O interaction: these three are the FMOs with which the Fe=O group participate in C–H bond activation. In fact, the electron transferred in the HAA process can populate either the σ* d_{z^2} or one of the two π* orbitals depending on their relative energies, that in turn depend on the electronic structure of the complex enforced by the supporting ligands. However, the two different scenarios, termed σ and π reaction pathways, have different requirements for an optimal orbital overlap. If the electron is transferred from the σ(C–H) bond to the d_{z^2} orbital, maximum orbital overlap will be reached when the C–H bond approaches the Fe=O moiety in a vertical fashion (as shown in Figure 6) resulting in a linear M–O–H transition state, while a π-pathway requires donation to the π* $d_{xz,yz}$ and a side-on approach resulting in a bent M–O–H group. The second approach has intrinsically higher steric requirements due to the proximity of the substrate molecule to the supporting

equatorial ligands, and therefore it usually shows higher activation barriers for the initial HAA step, as discussed in more detail in next section.

In summary, a variety of factor can affect the hydroxylation rates in non-heme catalytic cycles, and their analysis required the development of efficient model complexes to circumvent the difficulty associated with direct study of natural intermediates.

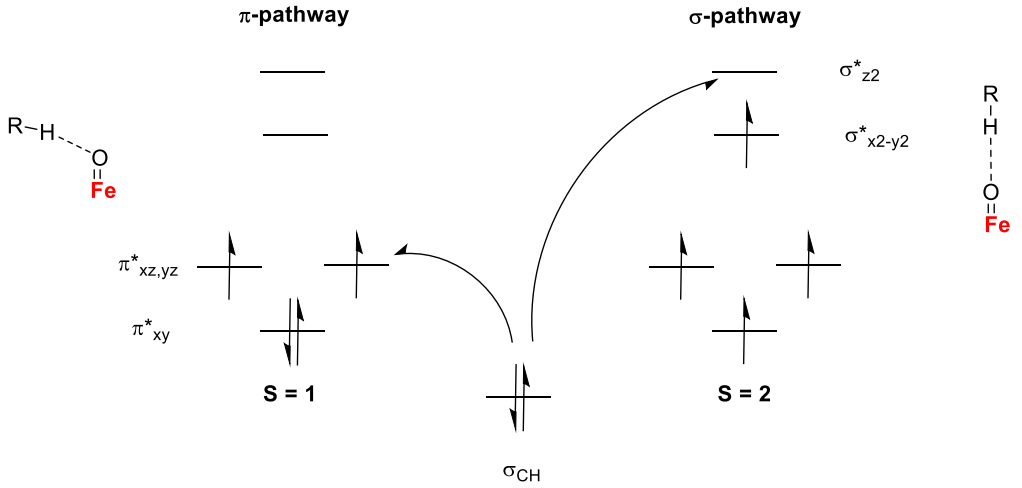

Figure 6. Representation of the σ- and π-pathway for the HAA performed by *S* = 1 and *S* =2 oxoiron(IV) centers, adapted from reference [82] .

Non-heme oxoiron(IV) model complexes: TSR and axial ligand effect

The growing interest in creating efficient model complexes for the intermediates discussed above led to the design of the first high-valent non-heme iron-oxo synthetic complex by Wieghardt and coworkers in 2000. They employed the cyclam-acetate (cyclam-ac) ligand, a modification of the cyclam scaffold, to synthesize the ferric (Fe^{III}) complex $[(cyclam\text{-}ac)Fe^{III}(OTf)]^{+}$ and performed ozonolysis at –80°C, to obtain an oxoiron(IV) *S* = 1 complex.[84] Few years later, Nam, Münck, Que and coworkers employed a methylated cyclam scaffold to obtain the first structurally characterized non-heme Fe^{IV}=O complex (Figure 7), opening a new synthetic field that led to the development of more than 80 other non-heme Fe^{IV}=O model complexes to date (Figure 7).[82,85–87]

Despite the large number of available complexes, most of them exhibit a triplet (*S* = 1) ground state, in contrast with natural non-heme intermediates. Only few examples of quintet ground states were reported when a trigonal (C_3) symmetry was enforced around iron or due to clever supporting ligand design.[87–90] One could therefore wonder why nature would have chosen to systematically employ *S* = 2 Fe^{IV}=O intermediates in HAT and OAT reactions, in place of the low-spin counterparts. An answer to this question has been extensively provided by theoretical calculations that showed the quintet-state to be more reactive in substrate oxidations compared to the triplet one.[91–95]

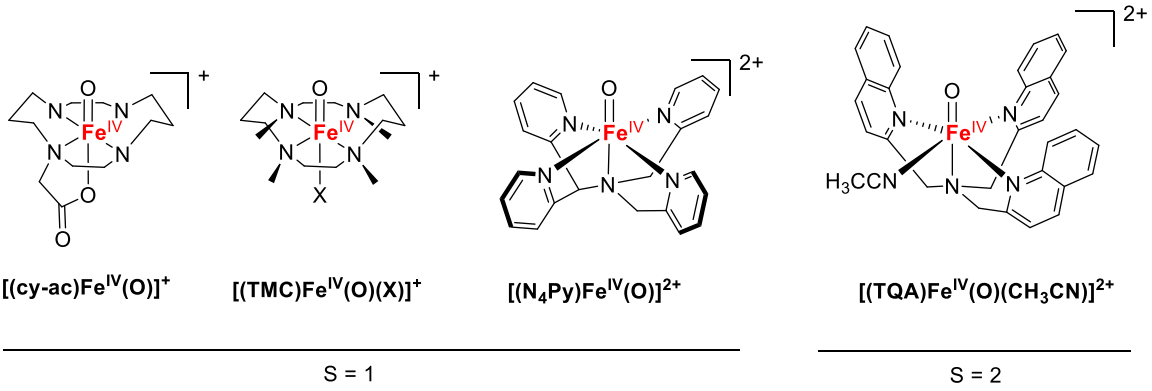

Figure 7. Notable examples of non-heme oxoiron(IV) model complexes and corresponding spin ground states. X denotes a generic axial ligand.

The reason for the enhanced reactivity of the higher spin states has to be found in the difference between the σ and π HAT pathway introduced in Section 1.4. In fact, HAT reactions that happen on the quintet surface predominantly adopt a σ pathway for the C–H activation, therefore experiencing reduced steric strain and a lower activation energy barrier. Addition of an electron in the σ* d_{z^2} orbital in a $S = 2$ configuration maximizes the number of exchange interactions, further reducing the barrier on the quintet surface. $S = 1$ complexes instead were calculated to react via a higher-barrier π pathway and therefore to show much slower reaction rates due to steric repulsion and lowered number of exchange interactions.[26,27,94] However, subsequent experimental estimation of the HAA reaction rates for $S = 1$ complexes drastically deviated from the calculated values, exhibiting unexpectedly fast reactivity. This discrepancy between experiments and theory led to the hypothesis of a two-state reactivity mechanism analogous to the one discussed above, where the $S = 1$ complexes would perform spin crossover to the more reactive quintet state during the interaction with the C–H bond of the substrate (Figure 8).

As a direct consequence of a TSR mechanism, it would seem reasonable to assess that changes that affect the energy barrier for the spin crossover phenomenon would in turn affect the rates of the HAA step. Indeed, confirmation of this hypothesis were experimentally provided by a series of axially ligated TMC-Fe^{IV}-oxo complexes bearing anions with different donor properties in the axial position *trans* to the oxo group, synthesized by Que, Shaik, Nam and coworkers in 2007.[96] When the axial CH_3CN molecule was substituted with trifluoroacetate, azide and a tethered thiolate (Figure 9), two distinct effects were observed for OAT and HAA rates: increasing axial ligand donation slowed oxygen atom transfer, according to the decreasing trend of electrophilicity of the complexes, but increased HAA rates in what has been named a “antielectrophilic trend”.

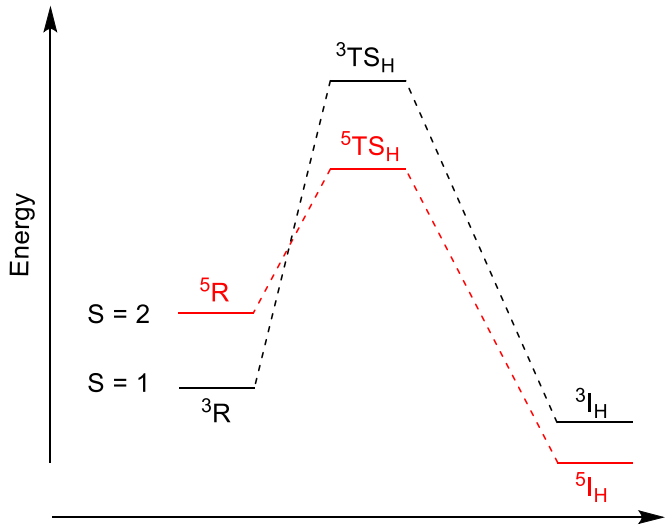

Figure 8. Depiction of the TSR phenomenon for tetragonally coordinated *S* = 1 non-heme model complexes.

This second behavior was initially explained by the fact that increased axial donation decreases the energy of the $d_{x^2-y^2}$ orbital compared to the d_{xy} (while at the same time destabilizing d_{z^2} and $d_{xz,yz}$), thereby reducing the triplet-quintet energy gap and the barrier for the spin crossover during HAA.[97]

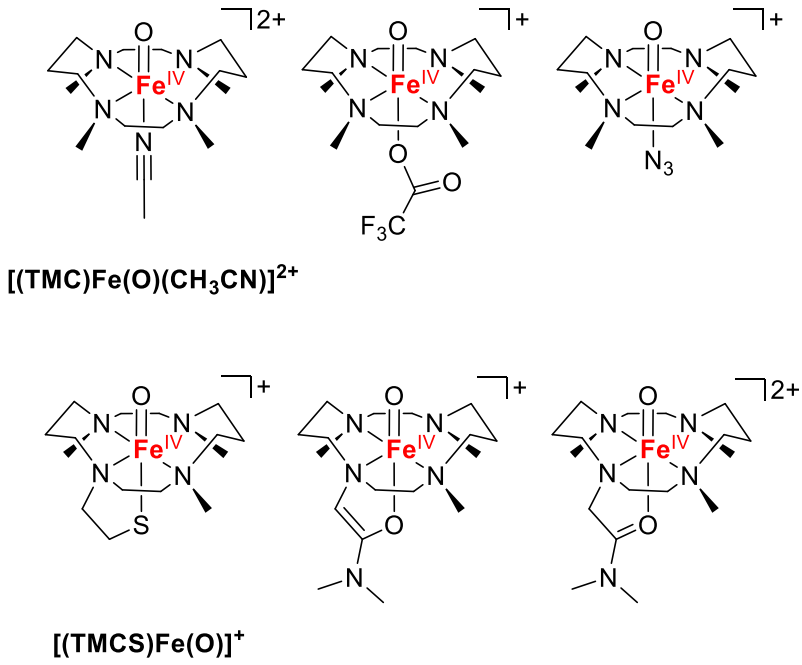

Figure 9. TMC–Fe^{IV}O complexes presented in the text. The reported names will be used in following chapters.

However, when the series was expanded to include two complexes with tethered dimethylacetamide and its conjugated base –CH=C(O) –NMe_2 (Figure 9), the reactivity trend was reversed, with the more electron donating complex showing lowest rates, following an "electrophilic" trend.[98] In depth theoretical analyses provided the explanation of this behavior and a complete depiction of the effect of axial ligands on the energy of the FMOs involved in HAT and rates. According to this improved model (Figure 10), the reduction in triplet-quintet gap is counterbalanced by the destabilization of the σ* d_{z^2} orbital, which in a σ pathway acts as the electron receiving FMO. Therefore, if the energy of the d_{z^2} orbital is raised, the activation barrier for the HAA at the *S* = 2 surface increases, slowing the overall rate. The final rate is therefore the balanced result of these two contrasting factors: the "electrophilic" trend seen for the last two complexes of Figure 9 is due to the fact that the decrease in triplet-quintet gap is not great enough to balance the increase in activation barrier, while the opposite is true in the previous series (Figure 10).

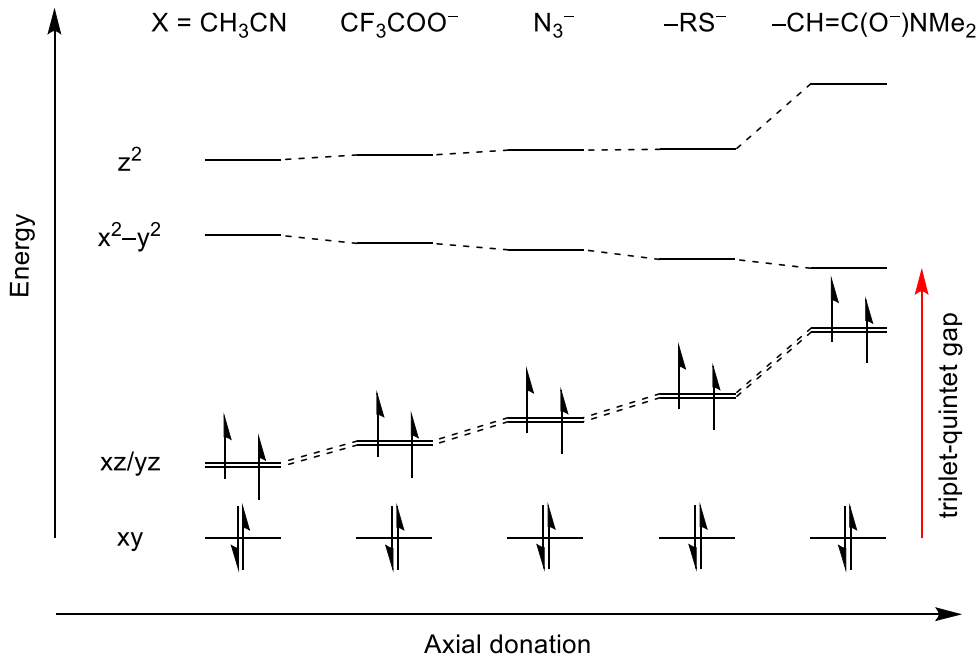

Figure 10. Effect of the donation ability of the axial ligands (X) on the series of TMC-Fe=O (*S* = 1) complexes reported by Que, Shaik and Nam (reference [96]). Adapted from reference [82] .

Although this model is still accepted as the most accurate available, Section 1.5 will discuss the challenge posed by the HAA reactivity recorded for the tetracarbene oxoiron(IV) complex reported by our group.[99] To date, the TSR model is still under debate, and further experimental efforts to refine the understanding of the axial ligand effect are needed.

Thiolate ligation in non-heme model complexes

Section 1.4 explained the fundamental role that the cysteinate residue *trans* to the oxo group of Cytochrome P450 enzymes plays in allowing for fast and efficient substrate hydroxylations without damaging the enzyme protein scaffold. Although heme-thiolate model complexes were studied as early as in 2002,[100] non-heme thiolate-bound oxoiron(IV) complexes have been much more difficult to isolate and characterize due to the instability of the thiolate moieties under oxidative conditions. The first example, already cited above, was the TMC complex **[Fe^{IV}(O)(TMCS)]$^{+}$** bearing an axial thiolate tethered to the equatorial cyclam ligand.[101] According to the authors, during the reaction with oxygen transfer reagents, oxidation of the thiolate moiety could be avoided in favor of the Fe=O bond formation due to the rigidity of the ligand scaffold. The work elucidated the effect of the thiolate ligand on the electronic structure of the oxoiron(IV) complex and showed that the strong σ- and π-donation of the RS^{-} ligand generated new signature spectroscopic features and promoted HAA reactivity over OAT. The complex showed an elongated Fe=O bond due to the competition of the thiolate ligand with the oxo group for π-donation on the metal orbitals, with an elongation much greater than the ones observed for the other axial ligands.

To date, **[Fe^{IV}(O)(TMCS)]$^{+}$** remains the only thiolate oxoiron(IV) complex that was isolated and thoroughly characterized, while the majority of non-heme thiolate bound complexes are studied in their ferrous state and used for *in situ* dioxygen activation.[102–107] Therefore, the synthesis and characterization of new non-heme thiolate bound oxoiron(IV) complexes represents a challenge that needs to be addressed using new ligand scaffolds, in order to provide a deeper understanding of the electronic structures and the reactivities to complement the work done on heme models.

1.5 The Tetracarbene Oxoiron(IV) Complex

In 2013 our group reported the synthesis of the first organometallic oxoiron(IV) complex, using a tetra-NHC macrocycle (first synthesized by Jenkins and coworkers)[108] in the equatorial position (Figure 11).[109] The strong donation in the xy plane led to the establishment of a unique electronic structure of the Fe=O group, that was explored and fully described with a variety of experimental and theoretical techniques.[110]

In particular, complex **3** was identified as a $S = 1$ oxoiron(IV) complex with a strongly anisotropic electron distribution around the metal center that reminded of the TAML system (Figure 11) with respect to the oblate electric field gradient and its effect on Mößbauer parameters.

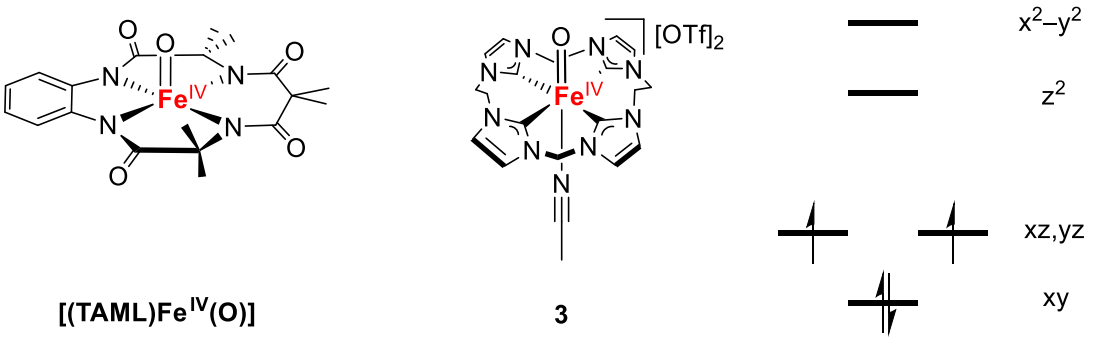

Figure 11. Structure of the TAML–Fe^{IV}=O complex (left) and of **3** together with the peculiar orbital splitting deriving from the strong tetracarbene donation.

MCD studies coupled with in depth theoretical calculations evidenced an unprecedented electronic structure of the complex, reflected in the inversion of the unoccupied d_{z^2} and $d_{x^2-y^2}$ orbitals, as shown in Figure 11. Comparison with Figure 2 in Section 1.3 demonstrates how the strong equatorial donation led to destabilization of the $d_{x^2-y^2}$ orbital while maintaining the occupied orbital largely unaffected. As a result, the triplet ground state has been calculated to lay 18.7 kcal·mol^{-1} lower than the quintet state, an energetic separation unprecedently high compared to all other S = 1 models.[99,110]

Owing to the great spin crossover barrier, the HAA reactivity of **3** with weak C–H bonds was shown to proceed completely on the triplet surface, rendering **3** the first and only model complex to not participate in a TSR mechanism and to be a unique model of a triplet state-only HAA reactivity with a π pathway.[99] Despite this, the organometallic complex exhibited reaction rates surprisingly high that were shown to be two orders of magnitude faster than the CH_3CN -coordinated TMC complex. Theoretical calculations have suggested that the complex undergoes axial CH_3CN dissociation upon interaction with the substrates, generating a pentacoordinated Fe^{IV}=O complex that is calculated to be the most reactive species in solution. Therefore, **3** evidenced that even the improved TSR mechanism for HAA reactivity of oxoiron(IV) S =1 non-heme complexes cannot fully describe the behavior of such complexes, and that new insight in this regard is required.

Interestingly, EPR measurements on the putative tetracarbene Fe^{III}–OH complex generated after the initial HAA step provided some evidence of the presence of multiple species deriving from different axial ligands *trans* to the hydroxo group, probably owing to the presence of iodoarene in solution derived from the oxidant used in the synthesis of **3**.

Given the peculiar behavior of the tetracarbene model and the invalidity of the TSR mechanism, studying the effect of axial ligands in a complex that does not perform spin crossover upon HAA would provide further insight on the strategies that can be used to tune the reaction rates of

oxoiron(IV) non-heme model complexes. Chapter 3 and 4 of this work will therefore explore these concepts and provide initial insights.

1.6 Hybrid Ligands as Heme/Non-Heme Models Precursors

Sections 1.1 to 1.4 have explained the main differences between natural or synthetic heme and non-heme systems in their electronic structures and their reactivities. Despite the massive amount of literature produced over the years, many questions remain unanswered and demand novel synthetic and spectroscopic approaches to expand our knowledge of the topic. In the field of heme models for example, studies of the effect of the axial ligands on the metal-porphyrin core (as discussed in Section 1.4) have been accompanied by modification of the porphyrin macrocycle both via variation of the backbone substituents and with the synthesis of ligands with modified donors sets or ring sizes.[111–117] In particular, exchanging one of the pyrrole groups of a porphyrin scaffold with a carbene moiety has attracted a great deal of attention, due to the peculiar features that the combined N- and C-donors are expected to provide.

The first example of porphyrin ring modified to contain a carbon donor was reported in 1994 by Ogawa and coworkers, where one of the four pyrrole rings was inverted by binding the neighboring methylene bridges at the α- and β-positions (Figure 12).[118] Thanks to this arrangement, one of the C–H groups of the inverted pyrrole group points inside of the macrocycle ring and can be deprotonated upon metalation to afford a C-donor to readily binding the metal center. This novel arrangement of the macrocycle was named "*N*-confused porphyrin" and subsequent research showed the ability of this ligands to bind high-valent metals, provide a strong equatorial donation and confer peculiar reactivity.[119,120] After these initial insight into the benefits of C-donation combined with a porphyrin-type scaffold into "non-heme heme-like structures", chemists focused on creating new systems the electronic properties of which could be easily modified by substituting the backbones of the macrocycles.

In the last two decades, the substitution of one of the pyrrole units of porphyrins with an *N*-heterocyclic carbene group has attracted considerable attention due to the possibility to synergically combine the properties of two very versatile ligands in one single macrocycle. NHCs and porphyrins in fact are both able to form strongly bound complexes with almost half of the elements of the periodic table,[121] and their electronic properties can be readily modified by substitution of their backbones with electron-donating or withdrawing groups, giving access to a variety of electronic structures and reaction pathways. NHCs have proven beneficial in stabilizing metal complexes in unusual geometries and extreme oxidation states, due to their strong σ-donation ability and the possibility to tune π-back bonding.[122–128] Moreover, the combination of NHCs and

N-donors in hybrid macrocycles has been shown to promote a wide variety of reactions and catalytic processes, together with peculiar electronic structures.[129,130]

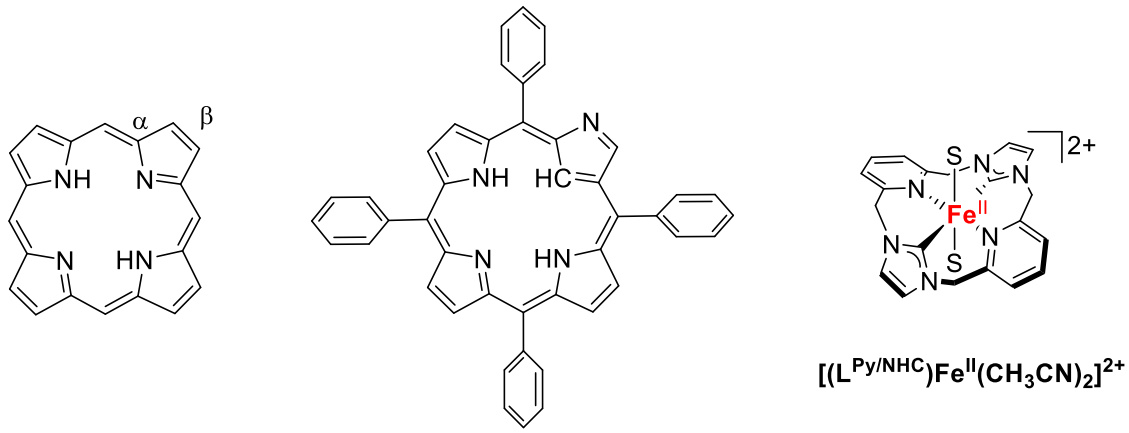

Figure 12. Left: the porphyrin scaffold and the associated α and β positions. Center: the first example of *N*-confused porphyrin. Right: cation of the NHC/pyridine Fe^{II} hybrid complex synthesized by Iris Klawitter; letter S stands for coordinated CH_3CN molecules.

For example, in 2015 our group reported the synthesis of a NHC/pyridine hybrid macrocycle Fe^{II} complex **$[(L^{Py/NHC})Fe(CH_3CN)_2]^{2+}$** (Figure 12) that showed distinctively different redox and spectroscopic properties compared to the tetracarbene complex **1**.[131] The same ligand scaffold was then used to isolate one of the very rare examples of Cu^{III} complexes, showing the ability of the macrocycle to stabilize high-valent Cu and flexibly adapt to the different requirements of the metal ion in different oxidation states from Cu^{I} to Cu^{III}.[132]

Despite these promising results, substitution of a pyrrole unit with an imidazole-2-ylidene and synthesis of metal complexes proved to be rather challenging. The main reason for this has to be found in the instability of the methylene-bridged pyrrole-imidazolium unit, that decomposes via an elimination pathway upon treatment with base.[133] To overcome this synthetic obstacle, the group of Kunz and coworkers substituted the pyrrole unit with a carbazole moiety, that can be deprotonated without elimination due to the presence of the two benzene rings fused on the "pyrrole" unit of the carbazole backbone.[134] In a recently optimized synthesis, coupling of the carbazole group with two imidazole units was easily achieved via a copper-catalyzed coupling on 1,8-diiodo-3,6-di-*tert*-butylcarbazole to obtain the bisimidazole-carbazole (bimca) ligand shown in Figure 13, left.[135] This tridentate ligand and its various modifications have been shown to form stable complexes with numerous metals and to be promising scaffolds for a variety of catalytic transformations.[136–139]

Notably, the Kunz group recently managed to synthesize the first macrocycle (CTP) containing two carbazole and two carbene (non-NHC) units that structurally mimics the tetrapyrrole arrangement of porphyrins, providing the first insights into the nature of a novel class of ligands termed

"carbenaporphyrins" (Figure 13, right). This constituted one of the most successful attempts to construct a non-heme model that mimics porphyrin systems in its structural properties.[133]

The advantage of using carbazole in modeling heme complexes does not stop at the increased stability. In 2012 the group of Niwa and Nakada reported a non-heme carbazole-bisoxazoline Fe^{III} complex that could be oxidized with iodosobenzene to afford an Fe=O intermediate capable of highly enantioselective asymmetric epoxidation of alkenes under ambient conditions (**CBX** in Figure 13).[140]

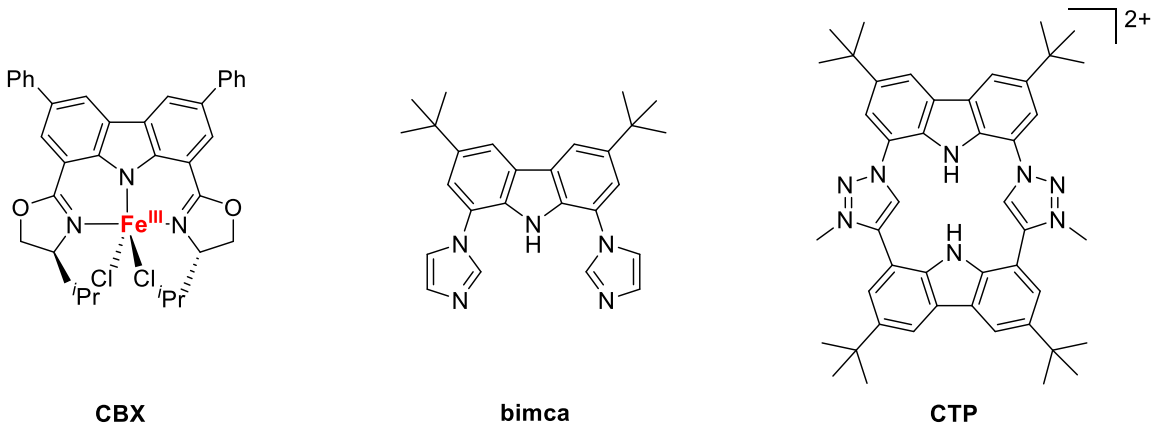

CBX **bimca** **CTP**

Figure 13. Structures of complex **CBX** from Niwa and Nakada, 1,8-bisimidazole-3,6-di-*tert*-butylcarbazole (**bimca**) and of the "carbenaporphyrin" macrocyclic precursor (**CTP**).

The oxidation of the ferric intermediate has been shown to form an oxoiron(IV) π-radical active intermediate: an non-heme species with heme-like behavior. In fact, organic carbazoles have been shown to be susceptible of oxidation to their π-radical cations under mild oxidation conditions, usually giving rise to product mixtures deriving from the coupling of the obtained radicals.[141]

Despite the results mentioned in previous paragraphs, the non-heme model complexes synthesized using carbazole and NHCs or other heterocycles constituted either structural/electronic *or* functional models of heme intermediates, leaving the bridge between the two classes of complexes incomplete. In this regard, the design of a non-heme Fe complex with a heme-like structure that also shows spectroscopic and electronic properties of Fe-porphyrins would constitute the missing link and possibly provide a new scaffold for further studies in this hybrid field. Therefore, Chapter 6 will present the results obtained in such effort and the detailed characterization of a novel carbazole-NHC non-heme Fe complex. Chapter 7 will instead provide initial results on the synthesis of {FeNO} complexes with this new hybrid system, as a starting point for studies on small molecule activations with a "non-heme heme-like" complex.

1.7 Principles of Mößbauer Spectroscopy

Ever since the discovery of the Mößbauer effect, the development of the associated spectroscopic technique allowed scientists to make fundamental discoveries not only in the field of physics but in chemistry and biology as well. Indeed, the variety of information that can be harvested by performing Mößbauer (MB) spectroscopy on natural or synthetic samples allows for a deep understanding of their electronic structure, especially when such systems contain iron as their principal and/or most relevant component, as in the biological systems discussed above and the associated synthetic models, or as in materials and catalysts for industrial and synthetic application. Given its importance, Mößbauer spectroscopy has been a fundamental tool in the studies described herein, and a brief introduction to the main information that can be derived from it is due.

The Mößbauer effect, named after the German physicist who discovered it in 1958,[142] is defined as the emission and resonant absorption of γ-radiation by atomic nuclei that occurs without loss of energy due to recoil, thanks to the embedding of the involved nuclei in solid structures or matrices. It is most used to study the electronic structure of iron compounds in solid materials (or their frozen solutions), due to particularly favored nuclear properties of the iron atom, but it can also be used to study elements such as iodine, tin, and antimony.

In particular, γ-radiation is associated with the transitions between different nuclear spins states of atoms, and MB spectroscopy studies the recoilless absorption of such radiation by atoms in an analyte (absorber). In the case of iron, a source (emitter) containing ^{57}Fe atoms in their I = 3/2 excited nuclear spin state (obtained by radioactive electron K-capture decay of ^{57}Co to I = 5/2 ^{57}Fe, which in turn decays to the wanted I = 3/2 state) emits a monochromatic γ-radiation (14.4 keV), in absence of recoil, that can be modulated exploiting the Doppler effect to irradiate the absorber with a range of singularly scanned frequencies. The nuclear spin states of the iron atoms in the analyte are energetically different from the ones of the source due to their different chemical environment, and therefore the absorption of radiation usually occurs at a frequency different from the originally emitted one. When the irradiated and modulated radiation excites a nuclear spin transition of the iron atoms of the absorber, the resonant absorption of radiation is recorded by the detector, allowing for the estimation of the energy difference between the nuclear spin ground and excited state(s) in the absorber.[143]

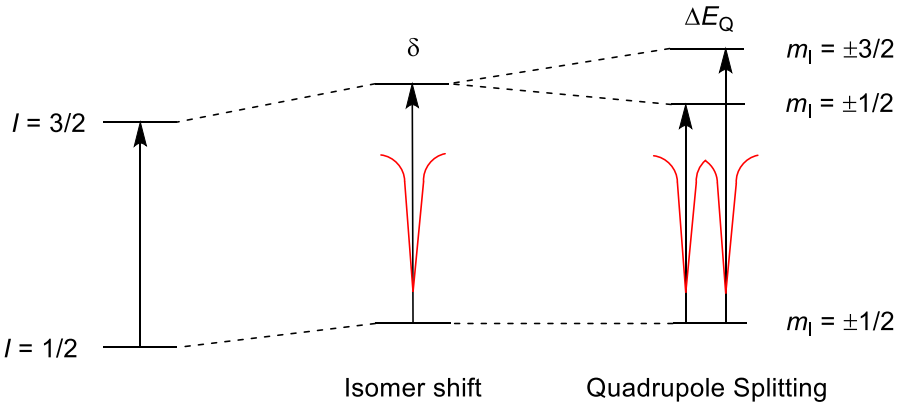

Figure 14. Schematic representation of the isomer shift and quadrupole splitting effect on the energy of ground and excited states of ^{57}Fe atoms of the absorber and associated graphical representation of the resonant absorption lines.

Two of the fundamental parameters that are can be measured with MB spectroscopy are the isomer shift (IS or δ) and the quadrupole splitting (QS or ΔE_Q), which belong to the class of hyperfine interactions that involve the nucleus and electric or magnetic (multi)polar interactions with electron density, electric fields, or magnetic fields. Isomer shift measures the energy difference between the absorbed radiation and the original monochromatic radiation emitted from the source (Figure 14). This difference originates from the electric monopole interaction between the iron nucleus and the electron density at its position, associated with orbitals of the s type, which is different for emitter and absorber. The δ parameter correlates negatively with electron density at the nucleus (ρ_0), with higher ρ_0 corresponding to lower δ values. Given this relationship, δ provides information regarding the oxidation state, the spin state and nature of the bonding of iron to other nuclei in the absorber. Regarding oxidation state, a simplified (although not formally exhaustive) trend with IS can be envisioned by comparison of structurally related iron complexes, with higher oxidation states enforcing lower IS values. In a first approximation (valid mainly for high-spin complexes) this trend can be explained introducing the concept of shielding of the nuclear charge that 3d orbitals have on the more internal s-shells (especially on the 3s and 4s orbitals). The removal one electron from a molecular orbital with major 3d component causes a decrease of the shielding, and therefore a contraction of s orbitals that increases ρ_0. The opposite is true for reduction processes, that tend to increase the IS value. However, this simple interpretation does not take in account other more important factors that better predict the behavior of the IS with addition or removal of electrons to or from the complexes.

In fact, in-depth theoretical calculations have shown that the overall IS value can be influenced more strongly by valence contributions and meal-ligand bond lengths compared to the simple shielding effect of 3d orbitals.[144] Simplifying, let's consider an oxidation process from an Fe^{II} complex to its Fe^{III} structural analogue. Removal of the electron from the 3d shell causes three main

effects: 1) the increase in effective nuclear charge from the iron nucleus would contract the 3s and 4s orbitals, increasing ρ_0; 2) it would also increase the degree of mixing between the metal 4s and σ-type combinations of ligand orbitals, causing higher covalency of the associated bonds and an expansion of the 4s orbital, thereby lowering ρ_0, 3) can cause changes of metal-ligand bond length, that in turn affect the shape of the 4s orbital: a shorter bond (often associated with increase of the oxidation number) causes its contraction towards the nucleus, thereby increasing ρ_0.The final effect on δ is therefore the careful balance of all these phenomena and can give rise to different behaviors. In a scrupulous theoretical work from Prof. Neese, the latter contribution has been shown to often be the most influential one.[144]

Although in most cases the combination of these effects leads to lower δ upon oxidation (and higher δ upon reduction), a notable work published by Neese and coworkers in 2016 theoretically explained the counterintuitive *positive* correlation between IS and oxidation state in a redox series of iron-N_2 complexes bearing a tris(phosphino)silyl ligand.[145] The stepwise reduction of the initial Fe^{II} complex to Fe^{I} and Fe^{0} analogues was associated with a decrease of the isomer shift values, caused by the stepwise *decrease* of the Fe–N_2 bond distance due to the more efficient Fe-to-N_2 backdonation upon reduction.

In conclusion, as hypothesized in the theoretical calculations discussed above and then confirmed by this last example, metal-ligand bond lengths are considered better predictors of IS compared to the oxidation state.

The quadrupole splitting (ΔE_Q) parameter instead originates from the interaction between the nuclear quadrupole moment (in the $I = 3/2$ excited state of iron) and the electric field gradient (EFG) surrounding it. The net effect is a splitting of the resonant absorption line of the Fe analyte in two bands, caused by the induced energy separation between the $m_I = \pm 1/2$ and $m_I = \pm 3/2$ states associated with the excited $I = 3/2$ nuclear spin state of iron. Thanks to this, the I = 1/2 ground state can be excited to the two different states, giving rise to the two absorption lines (Figure 14). The energy difference between the two absorption lines is ΔE_Q. This parameter is mainly influenced by two contributions: the deviation of the electronic charge distribution surrounding the iron nucleus from a cubic arrangement (“lattice contribution”) and the anisotropy of electron population of the d orbital of iron and/or of the covalent bonds to the ligands (“valence contribution”).

As illustrated above, the effect of electronic structure of iron complexes on the MB parameters can be very complicated and requires expert employment of theoretical methods to fully unravel its nature. However, within this work, the MB parameters of reported iron complexes have been interpreted on the base of comparison with similar compounds and on intuitive behaviors supported by additional spectroscopic techniques.

2. Objectives

The tetracarbene-iron system developed by our group constituted a novel approach to the bio-inspired modeling of high-valent iron-oxo enzymatic intermediates. Given the unique electronic structure of complex **3** (Figure 15), the complex was able to perform HAA reactions at rates significantly higher than the ones predicted for a triplet pathway without accessing the quintet state, therefore underlying how the TSR hypothesis cannot account for all factors governing the oxidative abilities of non-heme oxoiron(IV) model complexes.[68,69,99] On this basis, the tetracarbene scaffold can be exploited to re-evaluate the effect of axial ligands on the HAA reactivity of axially substituted analogs of **3**, gaining insight into the influence that a stronger axial donation can have on the basicity of the *ferryl* group without concomitantly affecting reactivity via a decreased triplet-quintet energy gap. To this extent, Chapters 3 and 4 will present the synthesis and characterization of a series of axially substituted tetracarbene oxoiron(IV) complexes bearing anions with different donor properties *trans* to the oxo moiety and their HAA rates with a range of substrates having weak C–H bonds.

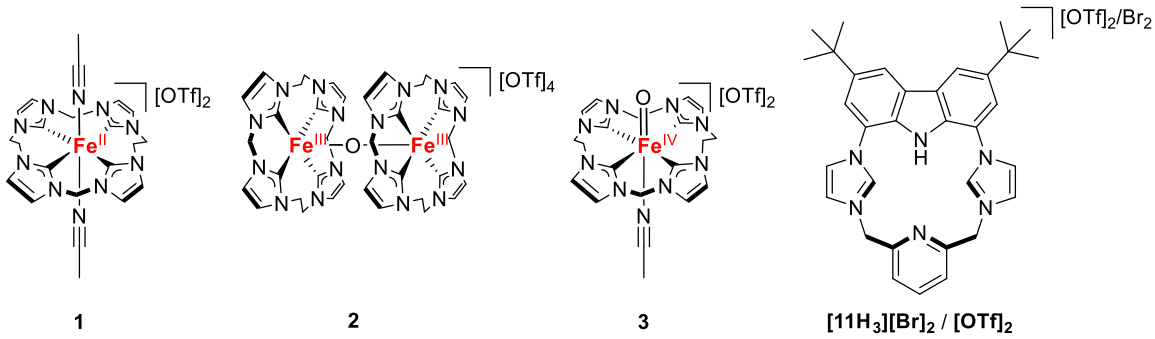

Figure 15. Structures of complexes **1**-**3** treated in Chapters 3-5 and of pro-ligands **[11H$_3$][Br]$_2$/[OTf]$_2$** discussed in Chapters 6 and 7.

Following the results obtained by Dr. Cordes and Dr. Klawitter on the HAA ability of the dimeric μ-oxo complex **2** in the activation of DHA, Chapter 5 will provide evidence of the presence of the disproportionation equilibrium of **2** into **3** and **1** in nitrile solutions, which can be putatively triggered both by coordination of a solvent molecule or by the attack of the nucleophilic **3** to the vacant axial sites of **2**. Moreover, the low electrophilicity of **3** and its poor OAT capabilities will be supported by gas-phase reactivity analyses performed during a research stay in the laboratory of Prof Fornarini, at University of Rome La Sapienza.

Together with the study of the tetracarbene-iron complexes and their peculiar features, the possibility to study the influence of NHC ligation on iron-containing systems would greatly benefit from the establishment of new hybrid NHC/N-donor systems which constitute conceptual bridges between known *N*-donor systems and the tetracarbene one. Partial substitution of the NHC moieties of complex **1** with nitrogen donor groups would therefore appear an advisable strategy. The dissertation of Dr Cordes provided initial evidence for the formation of a novel hybrid macrocycle (**[11H$_3$][Br]$_2$**) bearing two *trans* NHCs together with a carbazole and a pyridine fragments, as a suitable candidate for the creation of a new hybrid iron-containing system.[146]

Chapter 6 of this work will therefore present the optimized synthesis of the hybrid macrocycle **[11H$_3$][OTf]$_2$** and the establishment of redox and spin series of its iron complexes, with a focus on the ability of the new non-heme system to showcase heme-like features thanks to the combination of NHCs and redox non-innocent N-donors. Finally, Chapter 7 will show the initial results of the synthesis and preliminary characterization of a redox series of {FeNO}^{x} complexes of the hybrid system, which combines two redox non-innocent ligands and allows for the generation of complexes in various oxidation states.

3. Synthesis and Characterization of a Series of Axially Substituted Oxoiron(IV) Complexes

3.1 Previous Results and Motivation

The tetracarbene oxoiron(IV) complex **3** has been synthesized and characterized in our group as the first example of an organometallic *S* = 1 high-valent iron-oxo complex inspired by non-heme enzyme intermediates.[109] The novel NHC ligation at the Fe=O core was shown to confer distinctive properties to the complex regarding the electronic structure, as confirmed by IRPD and MCD studies performed in collaboration with the group of Prof Jana Roithová (at that time at Charles University of Prague) and the group of prof. Franc Neese at the Max Plank Institute for Chemical Energy Conversion in Mülheim. Indeed, the strong carbene donation on the equatorial plane was shown to profoundly affect the electronic structure of complex **3** compared to all the other known *N*- or *O*-ligated non-heme model complexes, by rising the energy of the $d_{x^2-y^2}$ orbital well above the one of d_{z^2}.[110] The increased triplet-quintet gap derived from this effect was in accordance with the *S* = 1 ground state of the complex and prevented **3** from entering the quintet state when reacting with weak C–H bonds in HAA reactivity, as explained in Chapter 1. In fact, **3** was confirmed to be the first so far model complex for a triplet-only HAA reactivity pathway, showing that C–H bond activation was possible even without entering the *S* = 2 state, still maintaining moderately high reaction rates.[99] The reactivity of **3** towards C–H bonds will be further discussed in Chapter 4.

As reported in Chapter 1, one of the most efficient strategies nature uses to tune the catalytic properties of enzymes is the modification of the chemical environment of recurring active sites, often acting on the coordination sphere of metal cofactors. In heme enzymes, for example, substitution of the axial ligand *trans* to the oxo group greatly affects the reactivity, C–H bond activation selectivity, reaction rates and oxidizing power of the active intermediates.[27] As a result, many of the known high-valent Fe^{IV}=O model systems have been synthesized with varying axial ligands, in an attempt to uncover the effect of the latter both on the electronic structure and the reactivity of the model complexes.[96,147–151] For example, the widely known $[(TMC)Fe^{IV}(O)(CH_3CN)]^{2+}$ complex has been treated with different anions in order to exchange the axial coordinated CH_3CN, and it was shown that the increased electron donation on the z-axis led to an elongation of the Fe=O bond and a decrease of the triplet-quintet gap.[97] This in turn had an effect on HAA and OAT reactivity, with the more electron-donating ligands decreasing the rates of OAT due to lower electrophilicity of the ferryl moiety and increasing the rates of HAA due to the lower *S* = 1 / *S* = 2 gap, that allowed for an easier spin state crossover during the activation of C–H bonds to the more reactive quintet state.[91,152] Given the peculiar electronic structure of **3**, the natural

evolution of the project had to deal with exploring the axial ligand effect on the tetracarbene-iron(IV)-oxo core, both on electronic structure, explored in the present Chapter, and on reactivity, discussed in Chapter 4. In particular, the unlikelihood of a two-state reactivity (TSR) scenario for HAA reactions of **3** prompted the question of whether different axial ligands could modify the electronic structure of the complex to an extent that would significantly impact the reaction rates and/or mechanism.

Thus, three anions (Figure 16) with different electron donating properties were chosen as axial ligands to be bound to the tetracarbene oxoiron(IV) scaffold: trifluoroacetate, chloride and tert-butylthiolate. This chapter reports the synthesis of the axially substituted high valent Fe-oxo complexes and their spectroscopic and magnetic characterization, together with a comparison with **3** and the corresponding TMC-ligated analogues.

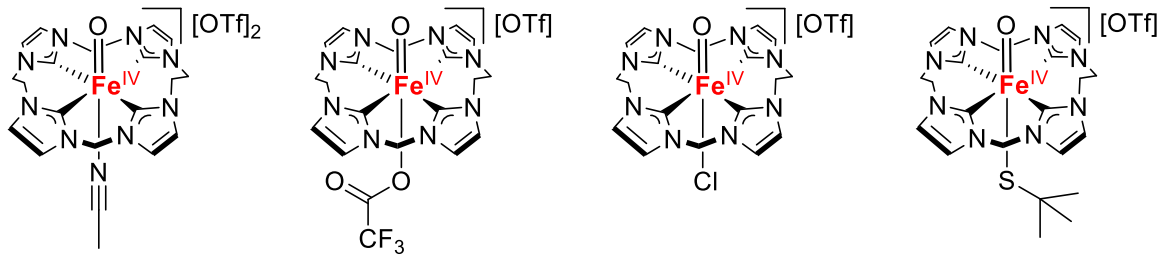

3 **4** **5** **7**

Figure 16. Parent tetracarbene oxoiron(IV) complex **3** and the axially ligated complexes **4**, **5** and **7** discussed in this chapter.

3.2 Two New Axially Ligated Tetracarbene Fe^{II} Complexes

A new *trans*-thiolate Fe^{II} model

As discussed in Chapter 1, the relevance of thiolate ligation in natural enzymes constituted a focal point for bio-inspired research and prompted for the design of new heme and non-heme model complexes with Fe^{II}-SR ligation as starting materials for the synthesis of high-valent models.[60,101,104,107,153] A convenient strategy for the introduction of anionic axial ligands on Fe^{II} non-heme complexes involves the simple treatment of the ferrous precursor with salts of the desired ligand, exploiting the presence of labile axial ligands in the starting materials.[97] This strategy was chosen to introduce an axial thiolate on complex **1**, which possesses two coordinated solvent molecules that are readily substituted by treatment with stronger ligands like CO, azide and NO.[146] When an CH_3CN solution of complex **1** was treated with sodium tert-butylthiolate (^{t}BuSNa) at room

temperature a color change from yellow to red evidenced the formation of a new thiolate-ligated Fe^{II} complex **6**.

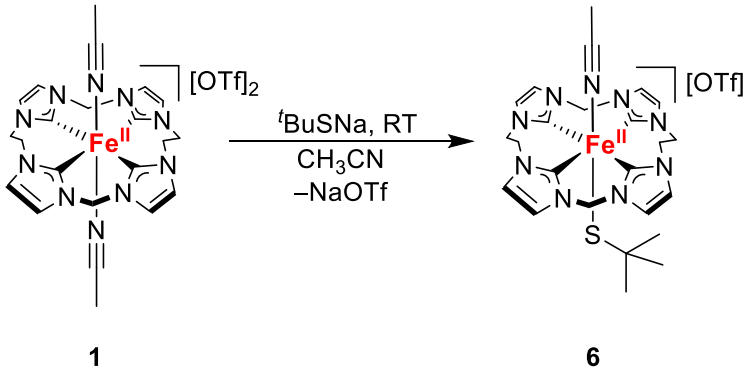

1 **6**

Scheme 2. Synthesis of the thiolate-bound Fe^{II} complex **6** starting from an CH_3CN solution of complex **1**.

Layering diethyl ether on top of the filtrated reaction mixtures led to the formation of XRD-quality crystals: Figure 17 shows the molecular structure and the Mössbauer (MB) spectrum of crystalline samples. The complex crystallizes in the space group P $2_1/n$, with an octahedral coordination geometry involving the tetracarbene macrocycle in the equatorial plane and the tert-butyl thiolate anion *trans* to one CH_3CN molecule on the axial positions. The macrocycle adopts a saddle-like shape analogous to the one of complex **1** allowing a Fe–S–$C_{t\text{-bu}}$ angle of 120°.[109] The Fe–S bond length of 2.403 Å is longer than most of the previously characterized RS–Fe^{II} complexes (2.28–2.34 Å)[104,105,107,153–156], probably due to the steric hindrance of the thiolate alkyl substituent and the presence of an electron-rich metal center, while the equatorial Fe–C and axial Fe–N_A distances are essentially unchanged compared to **1**.

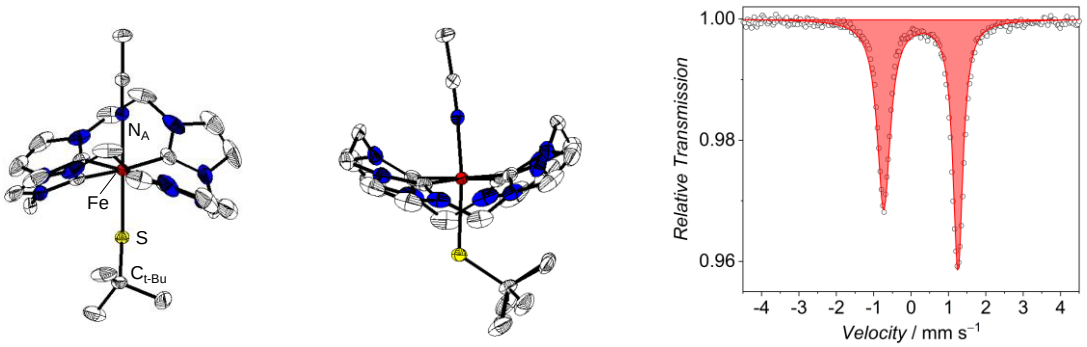

Figure 17. Left and middle: molecular structure of the cation of **6** shown as 50% thermal probability ellipsoids. Hydrogen atoms, counteranions and crystallization solvent molecules were omitted for clarity. Right: zero-field ^{57}Fe Mössbauer specrum of a solid sample of **6** recorded at 80 K (natural abundance, δ = 0.26 mm·s^{-1}, ΔE_Q = 1.99 mm·s^{-1}).

The peculiar σ- and π-electron donor abilities of the thiolate anion are nicely reflected by the MB parameters recorded for complex **6**. The isomer shift of 0.26 $mm \cdot s^{-1}$ is in accordance with the presence of a low spin Fe^{II} center bound to the tetracarbene ligand and is virtually identical to the parent complex, while the lower quadrupole splitting of 1.99 $mm \cdot s^{-1}$ evidences a lower electric field gradient around the metal atom due to the strong axial donation from the thiolate group. Indeed, similar trends were recorded in the case of the TMC complexes $[(TMC)Fe^{II}(CH_3CN)_2]^{2+}$ and $[(TMCS)Fe^{II}(CH_3CN)]^{+}$, which can be considered as structural analogues of **1** and **6**, respectively.[101]

The possibility to prepare complex **6** in high yields at room temperature and the ease of crystallization allowed for its use as precursor for further synthetic efforts. Section 3.3 will describe the successful oxidation of **6** to a thiolate-Fe^{IV}=O complex and its singular spectroscopical features.

A *quasi*-homoleptic "pentacarbene" Fe^{II} complex

One of the most remarkable features of complex **3** is the effect of the tetracarbene macrocycle on the electronic structure of the complex, and specifically on the orbital splitting arrangement of the metal-based d orbitals, as described in section 3.1. With a $d_{x^2-y^2}$ orbital lying at higher energy than the d_{z^2}, this complex constituted the first example of such electronic structure among high-valent non-heme oxoiron(IV) complexes capable of C–H bond activation. Although this property allowed for exceptional insight into the reactivity of such compound as discussed in Chapter 1, the singular electronic structure of **3** set it aside from other known model complexes, which invariably possess an inverted order of the unoccupied orbitals (Figure 18).

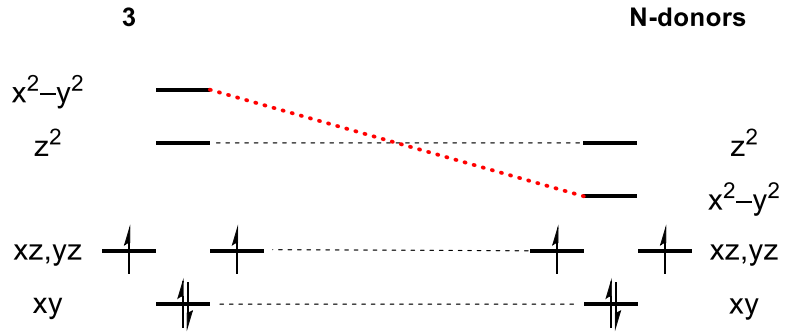

Figure 18. Ground state electronic configuration of complex **3** (left) and of typical non-organometallic Fe^{IV}=O model complexes (right). The red dashed line evidences the inversion of orbital order promoted by the strong equatorial donation of the tetracarbene macrocycle, which rises the energy of the $d_{x^2-y^2}$ orbital above the one of d_{z^2}.

This feature prompts the question of whether it is possible or not to re-establish the $(d_{x^2-y^2})(d_{z^2})$ orbital splitting pattern still maintaining the tetracarbene macrocycle ligation in the octahedral complex. In this regard, a suitable strategy would involve the substitution of the axial CH_3CN ligand of complex **3** with a very strong σ-donor, that would ideally rise the energy of the d_{z^2} orbital above the $d_{x^2-y^2}$ via a strong axial bond, further increasing the HOMO-LUMO gap. Among the numerous possibilities for such axial donors, an additional N-heterocyclic carbene appeared to be an ideal candidate, generating a unique example of a fully organometallic oxoiron(IV) complex. Indeed, NHCs have been conveniently used as axial ligands in transition metal porphyrin complexes, since the high covalency of the strong M–C bond decreases the chances of unwanted ligand dissociation in solution, a quite common inconvenience in porphyrin chemistry.[121,157–160]

In 2005, Crabtree reported a convenient route for the synthesis of a free-NHC precursor, namely *N*,*N*-dimethyl imidazolium-2-carboxylate (DMI-CO_2, Figure 19). When this zwitterion is dissolved in polar solvents such as CH_3CN, release of CO_2 generates the free *N*,*N*-dimethylimidazol-2-ylidene, which readily coordinates to metal centers.[161,162] Given this convenient synthetic route, DMI-CO_2 was chosen for the ligand substitution on complex **1**. Figure 19 summarizes the synthetic strategy for the axial ligand substitution, generating complex **8**, and the hypothetical preparation of a "*quasi*-homoleptic" penta-NHC oxoiron(IV) complex.

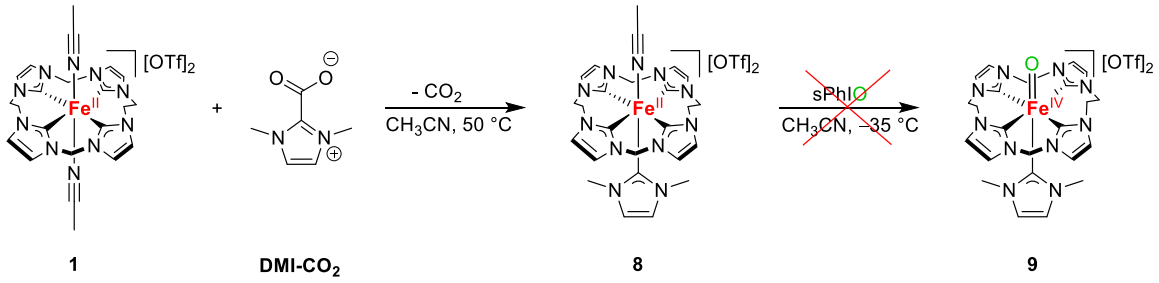

Figure 19. Synthesis of complex **8** and hypothetical stategy for the synthesis of the related oxoiron(IV) complex **9**. The acronym sPhIO stands for 2-*tert*-butylsulfonyliodobenzene, used as oxygen atom transfer reagent.

The reaction of 1 with DMI–CO_2 at 50 °C overnight resulted in the production of the bright yellow complex **8** shown in Figure 19, and slow diffusion of diethyl ether into a propionitrile solution led to the formation of crystals suitable for XRD measurements (Figure 20).

The octahedral complex crystallizes in the monoclinic P $2_1/c$ space group, with the tetracarbene macrocycle adopting the typical saddle-shaped arrangement and an axial propionitrile ligand sitting *trans* to the *N*,*N*-dimethylimidazol-2-ylidene moiety. Similar to **6**, the steric requirements of the *N*-bound methyl groups are accommodated by their orientation towards the ethylene bridges of the

tetracarbene macrocycle. All Fe–C bond lengths are similar and fall in the range between 1.94 and 1.98 Å.

A comparison of the M–C_{axial} bond with an analogue TPP-DMI-Co^{II} (where TPP = *meta*-tetraphenyl porphyrinato ligand) complex evidences a longer bond for **8**.[160] A less direct comparison can be performed considering a reported bis-DMI-dichlorophenyl-Fe^{III}-porphyrin complex axially coordinated by two DMI groups, which presents very long Fe^{III}-DMI bonds of 2.09 and 2.08 Å.[163] In that case the presence of two very strong donors *trans* to each other is the cause of long Fe–C bonds owing to the strong *trans* influence of the DMI groups. The Mößbauer spectrum of crystalline **8** shows an isomer shift value of 0.13 mm·s^{-1}, which is markedly lower than the one of **1**. This can be explained by comparing the average Fe–C bond lengths of **8** and **1** in the equatorial plane of the macrocyclic ligand (1.976 and 1.996 Å respectively): although axial bonds are longer in **8**, the shortening of the equatorial bonds intuitively causes a significant contraction of the s orbitals of Fe, thereby increasing the electron density at the nucleus and lowering the isomer shift compared to **1**. The quadrupole splitting of 1.47 mm·s^{-1} also reflects a less oblate electron density around the metal due to the additional NHC donation on the z-axis, as seen for complex **6**.

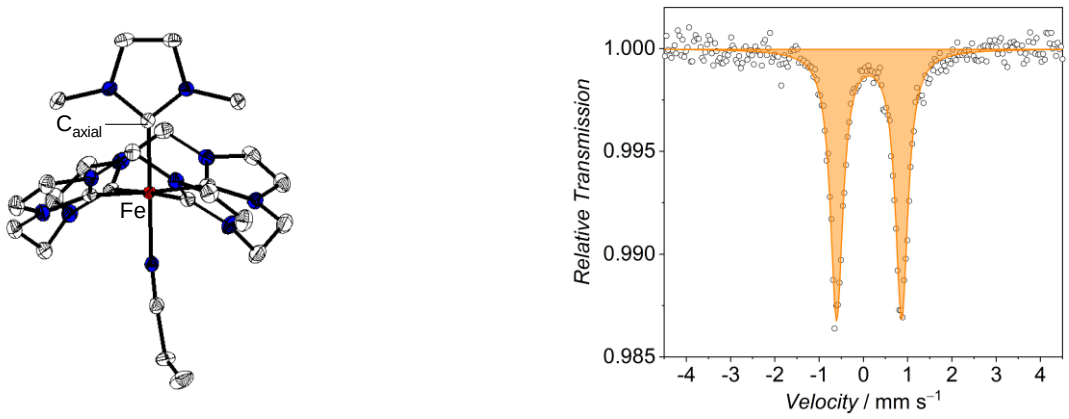

Figure 20. Left: molecular structure of the cation of **8** shown as 50% thermal probability ellipsoids. Hydrogen atoms, counteranions and crystallization solvent molecules were omitted for clarity. Right: Zero-field ^{57}Fe MB spectrum of a solid sample of **8** recorded at 80 K (natural abundance, δ = 0.13 mm·s^{-1}, ΔE_Q = 1.47 mm·s^{-1}).

This marked increase in electron density on the metal center compared to **1** was nicely reflected in the cyclic voltammograms (CV) of complex **8** in CH_3CN, shown in Figure 21 .When **8** was dissolved in an electrolyte solution in CH_3CN at RT and the potential was scanned from the open circuit potential (OCP) to the highest anodic potential and back, two redox events appeared in the voltammogram, as shown in Figure 21 (right). A first reversible oxidation assigned to the $Fe^{II/III}$ couple appeared at –0.10 V vs $Fc^{+/0}$, being 70 mV lower than the corresponding oxidation of **1** and

providing direct evidence for the higher electron density on the iron atom of complex **8**. This value falls in between the reduction potentials recorded for complex **1** and the corresponding octamethylated complex $\mathbf{1}^{\mathbf{Me}}$ (0.03 and –0.16 V vs $Fc^{+/0}$, respectively), in which the electron density was increased by methylation of the equatorial macrocycle at positions 4 and 5 of each imidazole ring.[164] In this regards, the inductive effect of alkyl substituents on the equatorial plane seems to provide a more efficient way to increase the electron density at the metal, even when compared with the effect of the strong DMI axial ligand.

Interestingly, a second oxidation wave appeared at high potentials (~ 1.39 V vs $Fc^{+/0}$), the shape of which became more reversible-like with increasing scan rate. Assuming the redox innocence of the NHC ligands, this wave could be assigned to a putative Fe^{III} to Fe^{IV} oxidation. Access to a second metal-based oxidation is in fact a remarkable feature of multi-NHC iron complexes, and it has been confirmed for a number of bis-triscarbene or cage-like hexacarbene compounds.[165–167] Despite the presence of an Fe^{IV} state at accessible potentials, all attempts to oxidize the DMI-Fe^{II} complex **8** with oxygen-atom transfer reagents failed. No reaction with 2-*tert*-butylsulfonyliodobenzene (sPhIO) or 2-iodylbenzoic acid esters (IBX)[168] was observed.

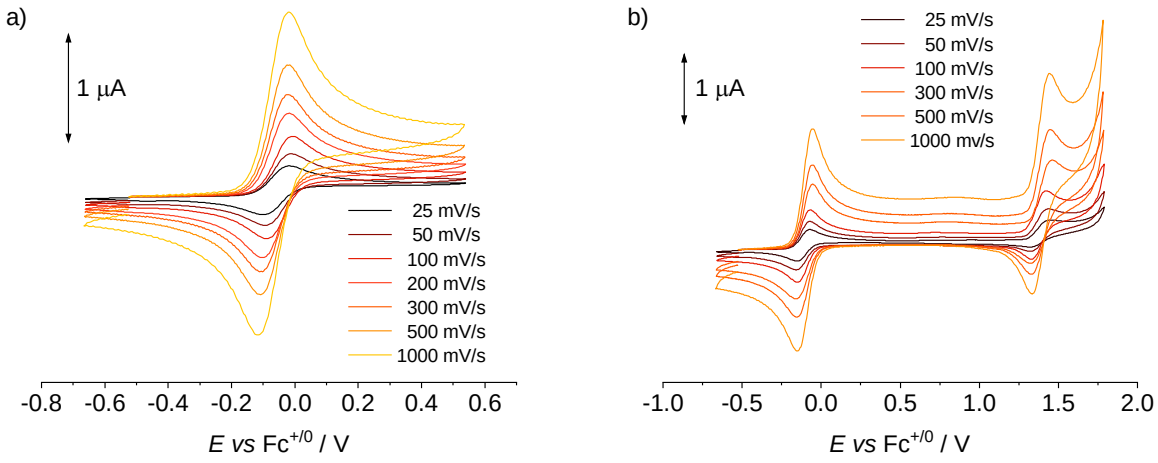

Figure 21. Cyclic voltammograms of 1 mM solutions of crystalline **8** in CH_3CN 0.1 M $^nBu_4NPF_6$ at variable scan rates at RT. Left: first oxidation only. Right: full anodic window.

Only when **8** was mixed with metachloroperbenzoic acid (MCPBA) in CH_3CN at –35 °C formation of a red species was observed over the course of 1 h. However, as shown in the Mössbauer spectrum (Figure 22), the reaction proceeded with formation of multiple products, the majority of which showed an isomer shift of 0.00 $mm \cdot s^{-1}$. This value is largely incompatible with a putative pentacarbene oxoiron(IV) complex, which should intuitively return an IS value even lower than complex **3** due to the strong DMI donation in the s orbitals of iron.

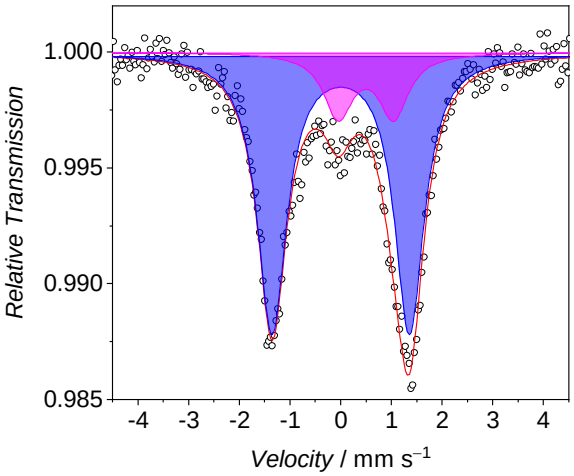

Figure 22. Zero-field ^{57}Fe MB spectrum of a solid sample of the product mixture obtained by treatment of **8** with MCPBA at −35 °C, recorded at 80 K (natural abundance. Parameters of the majoritarian product: δ = 0.00 mm·s^{-1}, ΔE_Q = 2.71 mm·s^{-1}).

Even when the oxoiron(IV) complex **3** was reacted at −35 °C with DMI-CO_2 in an attempt of substituting the CH_3CN axial ligand with the *N*,*N*-dimethylimidazol-2-ylidene moiety, the immediate formation of the dimeric μ-oxo complex **2** was observed, likely due to the formation of the urea-derivative of the DMI group upon oxygen atom transfer from **3**, and subsequent reaction of the derived Fe^{II} **1** with **3** present in solution. Indeed, imidazole-2-ylidene oxidation of the tetracarbene scaffold in **3** was already observed by Dr Steffen Meyer and Dr Claudia Cordes.[146,169]

Despite the difficulty in obtaining the DMI-oxoiron(IV) tetracarbene target complex in bulk scale, mass spectrometry and IRPD spectroscopy analysis of a mixture of **8** and sPhIO presented the possibility to isolate the corresponding ion in the gas phase, as shown in section 3.6. Hence, additional experiments for the bulk synthesis of the "*quasi*-homoleptic" pentacarbene oxoiron(IV) complex are ongoing. However, for the scope of this work only complexes **4**, **5** and **7**, for which the identity as Fe^{IV}=O complexes has been sufficiently supported, will be discussed in the following parts.

3.3 Optical Characterization of Complexes 4, 5 and 7

In situ synthesis of 4, 5 and 7

The synthesis of axially substituted oxoiron(IV) complexes **4** (axial ligand: CF_3COO^-) and **5** (Cl^-) was achieved via oxidation of the Fe^{II} complex **1** with excess 2-(tert-butylsulfonyl)iodosylbenzene (sPhIO) in presence of a salt of the desired anionic ligand (sodium trifluoroacetate and tetrabutylammonium chloride, respectively) in CH_3CN at −35 °C (Scheme 3). This synthetic

strategy have proven successful for numerous other Cpd-I and non-heme model complexes, and relies on the use of salts of inert cations that are stable under the oxidative conditions.[170] Synthesis of complex **7** instead, was achieved by oxidizing **6** with either tetrabutylammonium metaperiodate ($TBAIO_4$) or sPhIO.[171] It has to be noted that the presence of the chloride anion dramatically lowered the solubility of complex **5**, which partially precipitated from the reaction mixture and could be obtained in CH_3CN up to a maximum concentration of ~1 mM.

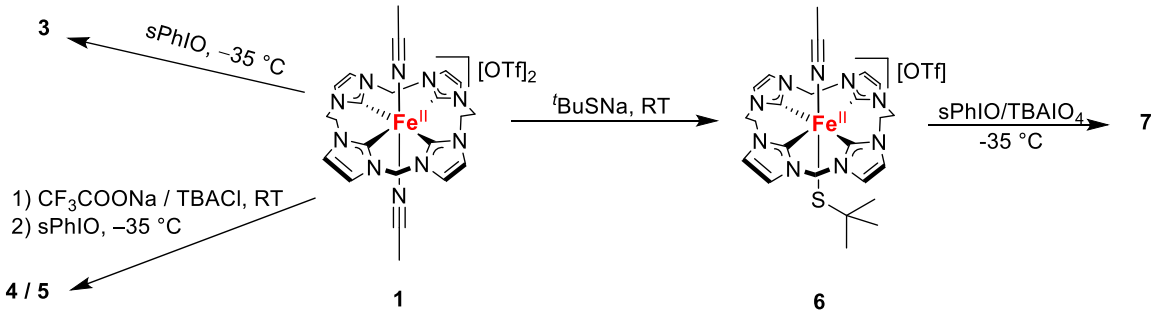

Scheme 3. Schematic representation of the synthesis of complexes **3**–**7**.

The *in situ* formation of complexes **4**, **5** and **7** was followed via UV/Vis spectroscopy at −40 °C, using a DCM solutions of sPhIO or CH_3CN solutions of $TBAIO_4$ according to the synthetic procedure reported in Scheme 3. Figure 23 shows the change in the absorption spectra during the oxidation processes. Formation of complexes **4** (axial ligand: CF_3COO^-) and **5** (Cl^-) proceeded with a decrease of intensity of the band at 339 nm (ε = 9100 $M^{-1}\cdot cm^{-1}$), typical of the starting complex **1**, and the appearance of two main bands around 410 and 600 nm over the course of approximately 1 h. Comparison of the obtained spectral patterns with the UV/Vis absorptions of complex **3** evidenced the successful synthesis of oxoiron(IV) complexes of the tetracarbene macrocycle, with slight variations due to the presence of anionic axial ligands.[109] The absence of isosbestic points support the hypothesis in which starting ferrous complexes are not directly oxidized to the target oxoiron(IV) compound in a OAT-like reaction, but rather in a multi-step synthesis.

Interestingly, the oxidation of **6** proceeded with the decrease of the band at 379 nm (ε = 4791 $M^{-1}\cdot cm^{-1}$) and the appearance of four new bands at 334, 442, 577 and 710 nm (ε_{334} = 4587, ε_{442} = 1693, ε_{577} = 662, ε_{710} = ~185 $M^{-1}\cdot cm^{-1}$ respectively). Given the strong π-interaction expected between a thiolate moiety and an Fe=O group, it is not surprising that complex **7** would show markedly distinct optical spectra, owing to its different electronic structure.[101] Due to this, the spectral features of **7** will be discussed separately from complexes **4** and **5** in the following sections.

To rationalize the effect of the axial ligands on the UV/Vis spectra of complexes **4**, **5** and **7** compared to **3** it is necessary to recall the nature of the optical features of the CH_3CN -ligated complex. Assignation of the absorption bands of **3** was performed with the help of MCD spectroscopy and in-depth DFT calculation by Dr Shengfa Ye at MPI-CEC Mülheim. Thanks to this combined approach, the weak absorption band at 600 nm was assigned to $d_{xz,yz} \rightarrow d_{z^2}$ (HOMO-LUMO) electronic transitions, while the broad more intense feature at 400 nm to $d_{xz,yz} \rightarrow d_{x^2-y^2}$ excitations, thereby confirming the unique orbital splitting pattern discussed above.[110]

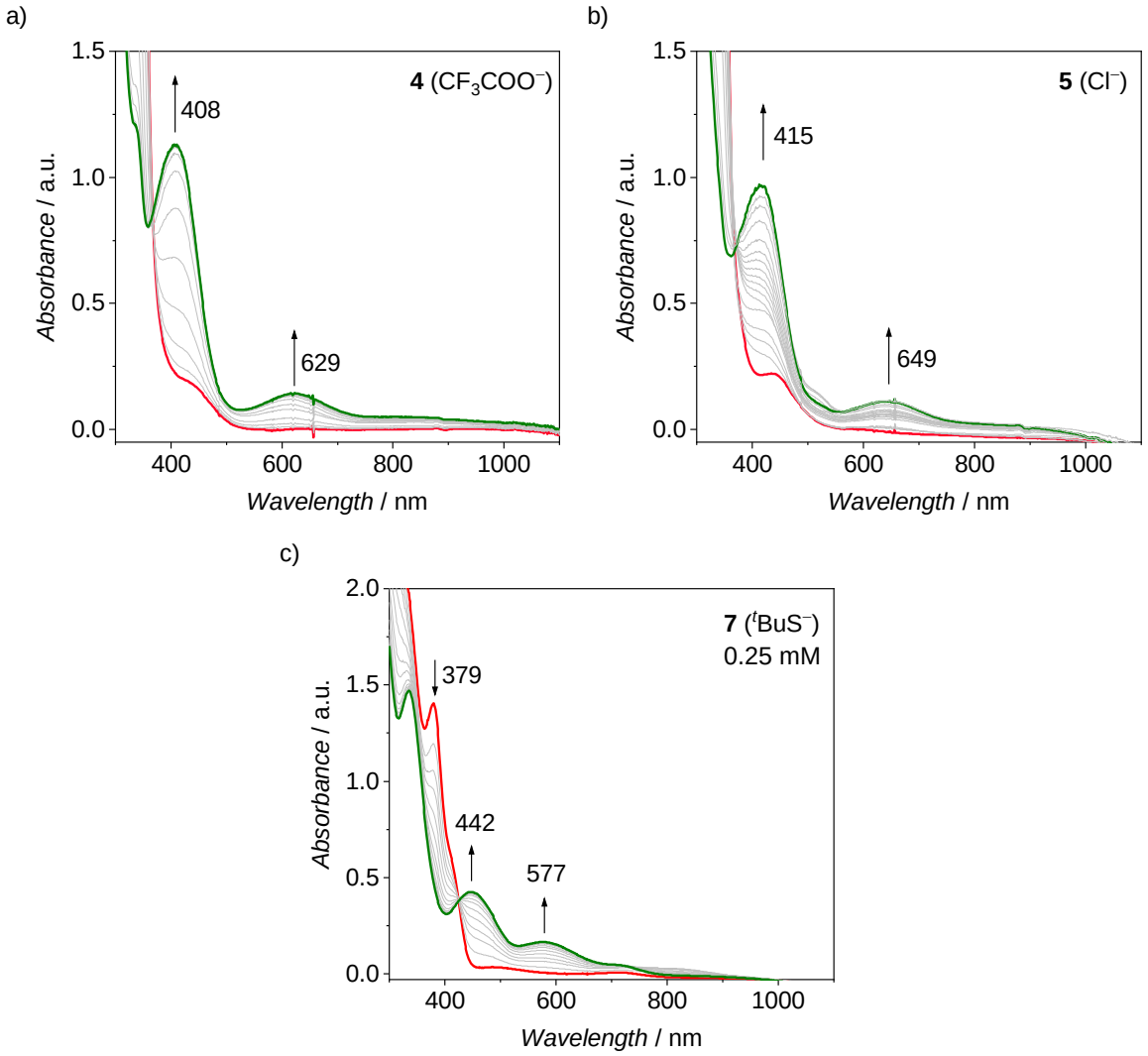

Figure 23. UV/Vis monitoring of the synthesis of axially ligated complexes **4**, **5** and **7** according to the synthetic strategy shown in Scheme 3: formation of a 1 mM solution of **4** (a) and **5** (b) and a 0.25 mM solution of **7** (d) in CH_3CN at –35 °C.

As shown in Figure 23, complexes **4** and **5** possess similar optical features, only slightly shifted compared to **3**. It is therefore reasonable to assume that the new oxoiron(IV) complexes show an ordering of the metal d orbitals qualitatively similar to the one of the parent complex **3** leading to

analogue electronic transitions. MCD studies of complexes **4**–**7** are ongoing in collaboration with the group of Prof. Neese at MPI-CEC, and first experimental results and initial theoretical calculations support this hypothesis.

Although the electronic structure seems to remain unchanged, the shift of the bands in the anion-ligated complexes provides some insight into the relative energies of the involved orbitals. First, the fact that the maxima in the 600 nm region of complexes **4** and **5** are shifted towards lower energies compared to **3** evidences that substituting the weak π-donor CH_3CN axial ligand with the corresponding anions induces a weakening of the ligand field (in case of **4**) or a modification of the relative energies (in case of the weak π-donor chloride anion in **5**) that reduce the HOMO-LUMO gap between the $d_{xz,yz}$ orbitals and the d_{z^2}.[82,170] Interestingly, since the energy of the d_{z^2} orbital is expected to rise with increasing axial donation, this implies that the destabilization of the π* orbitals $d_{xz,yz}$ involved in the Fe=O bond is much greater than the former, and therefore allows for reduction of the HOMO-LUMO gap (see Chapter 1 for comparison). In particular, the chloride anion, being a weak π-donor, expectedly provided the smallest energy gap, with the chloride complex **5** showing the maximum at 649 nm and trifluoroacetate-bound **4** at 629 nm.[172] Analogous conclusions regarding the electronic structure of **4** and **5** could be obtained analyzing the bands in the 400 nm region, which go from 400 nm for complexes **3**, to 408 nm for **4** and 415 nm for complex **5**. Indeed, stronger axial donation slightly stabilized the $d_{x^2-y^2}$ orbital in the series of TMC complexes cited above, as it is expected in the case of the tetracarbene complexes.[82]

The markedly different features of the optical spectrum of complex **7** underlined a remarkable change in electronic structure compared to the other tetracarbene oxoiron(IV) complexes. Substitution of axial CH_3CN with the 2-methyl-2-propanethiolate group caused a substantial redshift in the spectral features and the appearance of additional bands in the 550 and 700 nm regions of the spectrum. The final product in fact showed maxima at 442, 577 and 710 nm. Analogous differences were indeed reported for the TMC complexes $[(TMC)Fe^{IV}(O)(CH_3CN)_2]^{2+}$ and $[(TMCS)Fe^{IV}(O)]^{+}$, where the CH_3CN axial ligand was exchanged by a tethered thiolate moiety *trans* to the oxo ligand (see Chapter 1 for structures). This redshift of the typical TMC-Fe^{IV}=O bands and the appearance of additional features at 500 and 850 nm evidenced the formation of the first thiolate-bound model complex to be isolated and fully characterized.[101]

In summary, the optical spectroscopy analysis of complexes **4**, **5** and **7** confirmed their identity as new anion-ligated oxoiron(IV) complexes. Slight shifts in the features of **4** (axial ligand: CF_3COO^-) and **5** (Cl^-) compared to **3** provided some insight on the differences in electronic structures according to the ligand field strength and donor/acceptor character of the axial ligand, with weaker field ones causing a greater redshift of the absorption bands. Finally, the novel thiolate-Fe^{II} complex

6 could be oxidized with oxo transfer reagents to afford a species with optical features consistent with complex **7**, as supported by the comparison with the structural analogs of the TMC ligand. This constitutes a rare example of a *trans*-thiolate oxoiron(IV) complex, the formation of which would likely be possible because of the poor OAT abilities of the tetracarbene oxoiron(IV) scaffold and the strong Fe–S bond in **6**.[146]

3.4 Structural Characterization of a New Tetracarbene Oxoiron(IV) Complex

For most anion ligated complexes shown in the previous section the coordination of an axial anion increased the temperature stability of the corresponding oxoiron(IV) complex to an appreciable extent, with the exception of complex **7**. This was particularly advantageous in the case of the trifluoroacetate complex **4** which, as a result, could be stored indefinitely in CH_3CN solutions at −35 °C. This allowed for using the slow diffusion crystallization technique, that usually requires especially long times when performed at low temperatures. Single crystals of complex **4** suitable for XRD analysis were grown by slow diffusion of diethyl ether in an CH_3CN solution at −35 °C.

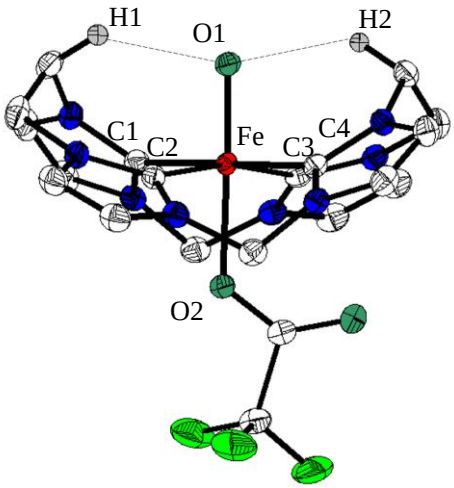

Figure 24. Molecular structure of the cation of **4** shown as 50% thermal probability ellipsoids. Most hydrogen atoms, all counteranions and crystallization solvent molecules were omitted for clarity. Hydrogen atoms participating in hydrogen bonding with the oxo group (dashed lines) are shown in grey. Selected bond lengths [Å] and angles [°]: Fe–O1 1.671(1), Fe–O2 2.069(1), Fe–C1 2.025(2), Fe–C2 1.970(2), Fe–C3 2.038(2), Fe–C4 1.980(2), O1···H1 2.244(1), O1···H2 2.251(1); O1–Fe–O2 178.849(5), C1–Fe–C3 179.40(7), C2–Fe–C4 167.90(7).

The complex crystallizes in the C 2/*c* space group, with the metal center octahedrally coordinated by the tetracarbene ligand, the oxo unit and a monodentate trifluoroacetate molecule (Figure 24).

The iron-oxygen double bond (Fe=O1) of 1.671 Å is only slightly longer then in the structure of **3-EtCN** (1.661 Å, an analogous of **3** where the axial position trans to the oxo group was occupied by EtCN), confirming that a π-donor in the axial position competes with the oxo moiety in the binding with Fe, thereby weakening the Fe=O bond.[26,152] Overall, the Fe=O bond distance falls on the upper end of the range found for oxoiron(IV) non-heme model complexes, as seen for the parent EtCN complex.[26] Expectedly, the equatorial Fe–C distances of 1.970, 1.980, 2.025 and 2.038 Å are minimally affected by the coordination of trifluoroacetate when compared to **3-EtCN**. The axial O2–Fe–O1 angle of 178.49° is closer to linearity compared to the parent complex (176.65°) but the iron atom is displaced above the C_4 plane toward the oxo ligand to a greater extent (octahedral parameter Σ = 42.78).[173–176] As per **3-EtCN**, the two ethylene bridges of the macrocycle approach the oxo moiety and form two weak hydrogen bond interactions ($d_{O1\ldots H1}$ and $d_{O1\ldots H2}$ of 2.244 and 2.251 Å), slightly shorter than in the parent oxo complex.

In conclusion, the ease of crystallization of complex **4** provided a convenient strategy for the obtainment of high purity material, which is a significant advantage when dealing with temperature unstable compounds, as many oxoiron(IV) complexes are. Moreover, although a large number of Fe^{IV}=O complexes has been synthesized in the last decade, structural characterization is often lacking due to the high reactivity and relative short life time of most of them.

3.5 Mößbauer Spectroscopy and Magnetometry

Mößbauer spectroscopy

Mößbauer spectroscopy constitutes the technique of choice when studying the electronic structure of iron complexes, given the large amount of information that can be provided and the relative ease of sample preparation. Mößbauer (MB) spectra of complexes **4**, **5** and **7** were collected on solid polycrystalline samples at 80 K and the related plots are shown in Figure 25. All the complexes showed negative isomer shift parameters and rather large quadrupole splitting values, as previously observed for complex **3**. The strong σ-donation of the equatorial tetracarbene ligand in fact produces high electron density at the iron nucleus and compresses the iron s orbitals, causing the low IS value, and generates a rather oblate electron distribution around the metal atom, thereby explaining the large electric field gradient and the large ΔE_Q.[109,143]

The measured isomer shift parameters of the trifluoroacetate complex **4** (δ = –0.14 mm·s^{-1}) and chloride complex **5** (δ = –0.12 mm·s^{-1}) were only slightly lower than the one of the parent CH_3CN oxoiron(IV) complex **3** (δ = –0.11 mm·s^{-1}), thereby confirming the Fe^{IV} oxidation state.[109] The small variations are probably due to the changes in bond distances in the coordination sphere of iron, as seen in the case of **4**, to solid state packing interactions or due to the limited accuracy of the

measurement technique itself, which often accounts for differences of 0.01–0.02 mm·s^{-1}. The quadrupole splitting parameters are virtually identical throughout the series **3**–**5** (Figure 25), underlying a very limited effect of the corresponding axial anions on the electron density distribution around the metal center, which is mainly affected by the tetracarbene macrocycle. Intuitively, the π-donor ability of trifluoroacetate and chloride would increase the electron density in the metal 3d orbitals, thereby strengthening the shielding effect on the 4s and causing an increase in the isomer shift (as evidenced for **7**, see below).[97] However, this effect seems to be minor and no significant shift of the parameters was found.

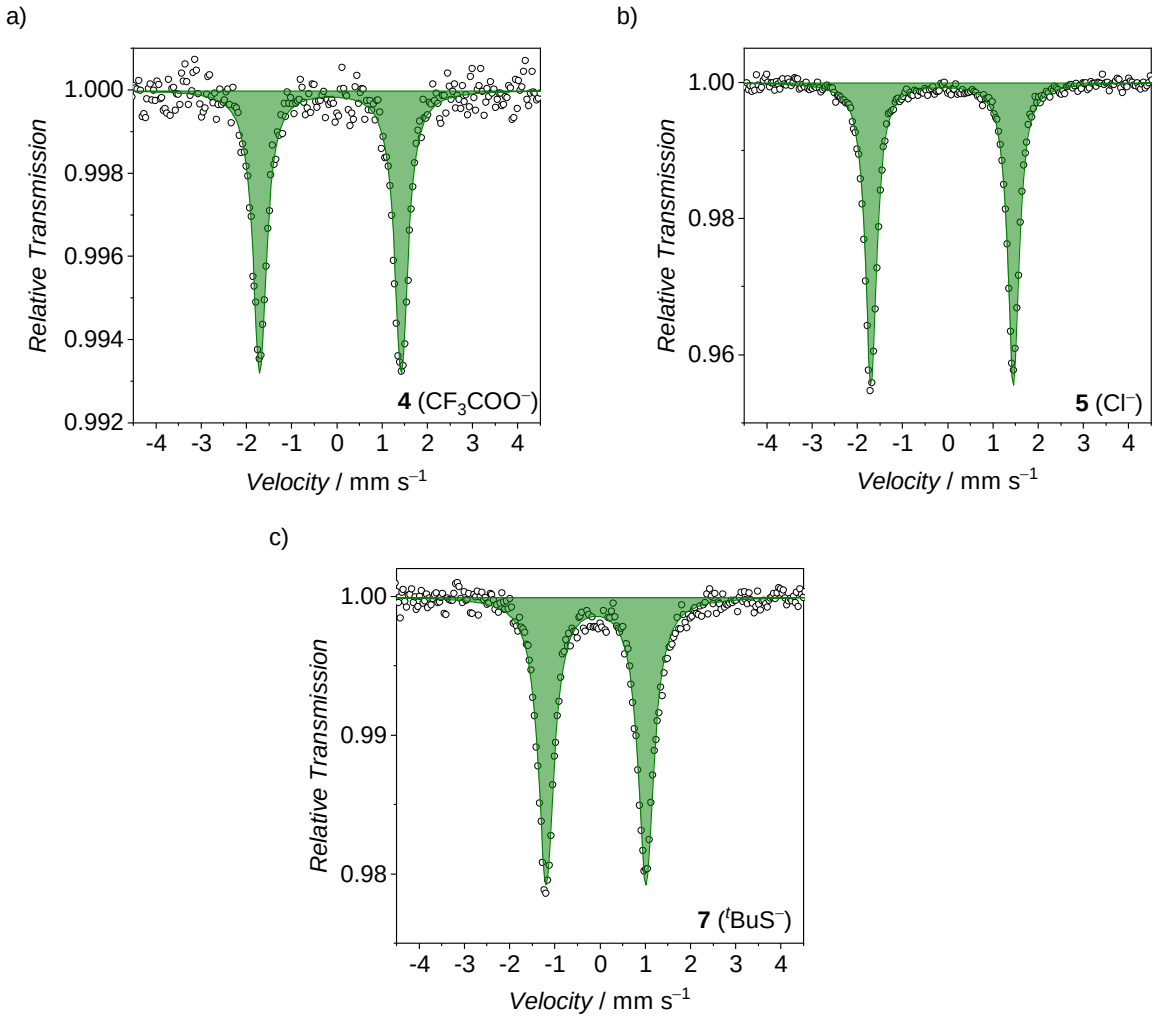

Figure 25. Zero-field ^{57}Fe Mössbauer spectra of solid **4** (a), **5** (b) and **7** (c) acquired at 80 K (natural abundance. **4**: δ = –0.14 mm·s^{-1}, ΔE_Q = 3.13 mm·s^{-1}; **5**: δ = –0.12 mm·s^{-1}, ΔE_Q = 3.15 mm·s^{-1}; **7**: δ = –0.09 mm·s^{-1}, ΔE_Q = 2.21 mm·s^{-1}).

The parameters of the thiolate complex **7** stand out from the series, with a higher isomer shift of –0.08 mm·s^{-1} and a quadrupole splitting lowered to 2.21 mm·s^{-1}. This is in accordance with the

ability of thiolate to act both as a σ-donor and a strong π-donor, thereby increasing the electron density on the 3d Fe orbitals and lowering the anisotropy of the charge distribution around the metal. Analogous trends are found in the comparison between complexes $[(TMC)Fe^{IV}(O)(CH_3CN)_2]^{2+}$ and $[(TMCS)Fe^{IV}(O)]^{+}$, with the isomer shift going from 0.17 to 0.19 $mm \cdot s^{-1}$ and the quadrupole splitting from 1.23 to 0.22 $mm \cdot s^{-1}$ upon substitution of the axial CH_3CN molecule with the tethered thiolate.[101]

Taken all together, complexes **4** and **5** present MB parameters very similar to **3**, providing experimental support of their Fe^{IV}=O nature. Although the substitution of a π-acidic CH_3CN with π-basic trifluoroacetate and chloride affected the electronic structure as evidenced by optical spectroscopy, the effect on the Mößbauer parameters seemed to be rather limited. Complex **7**, instead, provides a new example of the influence of strong σ- and π-donation of thiolates on the Fe^{IV}=O core and on the MB parameters. The comparison with the TMC analogues confirmed the trends of parameters to be due to the donor properties of the thiolate axial ligand.

Magnetometry

Magnetic susceptibility measurements on complexes **4**, **5** and **7** were performed with a SQUID magnetometer on solid polycrystalline samples in the temperature range 2–250 K; no field dependency of the $\chi_m T$ values was observed. Measurements of the temperature dependence of $\chi_m T$ are plotted in Figure 26, while variable-temperature-variable-field (VTVH) measurements are shown in the Appendix. In all cases, $\chi_m T$ is essentially constant at temperatures above 50 K, and the values recorded at 200 K were 1.01, 0.84 and 1.02 $cm^3 \cdot K \cdot mol^{-1}$ for complexes **4**, **5** and **7** respectively. These values are close to the theoretical spin-only value of 1 $cm^3 \cdot K \cdot mol^{-1}$, thereby confirming the S =1 spin state for all complexes. A decrease of $\chi_m T$ at temperatures lower than 50 K is due to zero field splitting (ZFS) effects. Fits of the magnetic curves according to the spin Hamiltonian (equation 2) return the g and D values reported in table 1 (see Materials and Methods for all equations used to fit experimental data).

$$\hat{H} = -2J\hat{S}_1\hat{S}_2 + g\mu_B\vec{B}(\vec{S}_1+\vec{S}_2) \qquad (2)$$

Table 1. Magnetic parameters of complexes **4**, **5** and **7** obtained with SQUID magnetometry.

	4	**5**	**7**
D / cm^{-1}	16.47	16.27	–20.37
$g_{average}$	2.009	1.839[a)]	2.022
TIP / 10^{-6} emu	296.4	675.0	841.4

a) The rather low g-value estimated for complex **5** was probably caused by the presence of diamagnetic impurities in the SQUID sample.

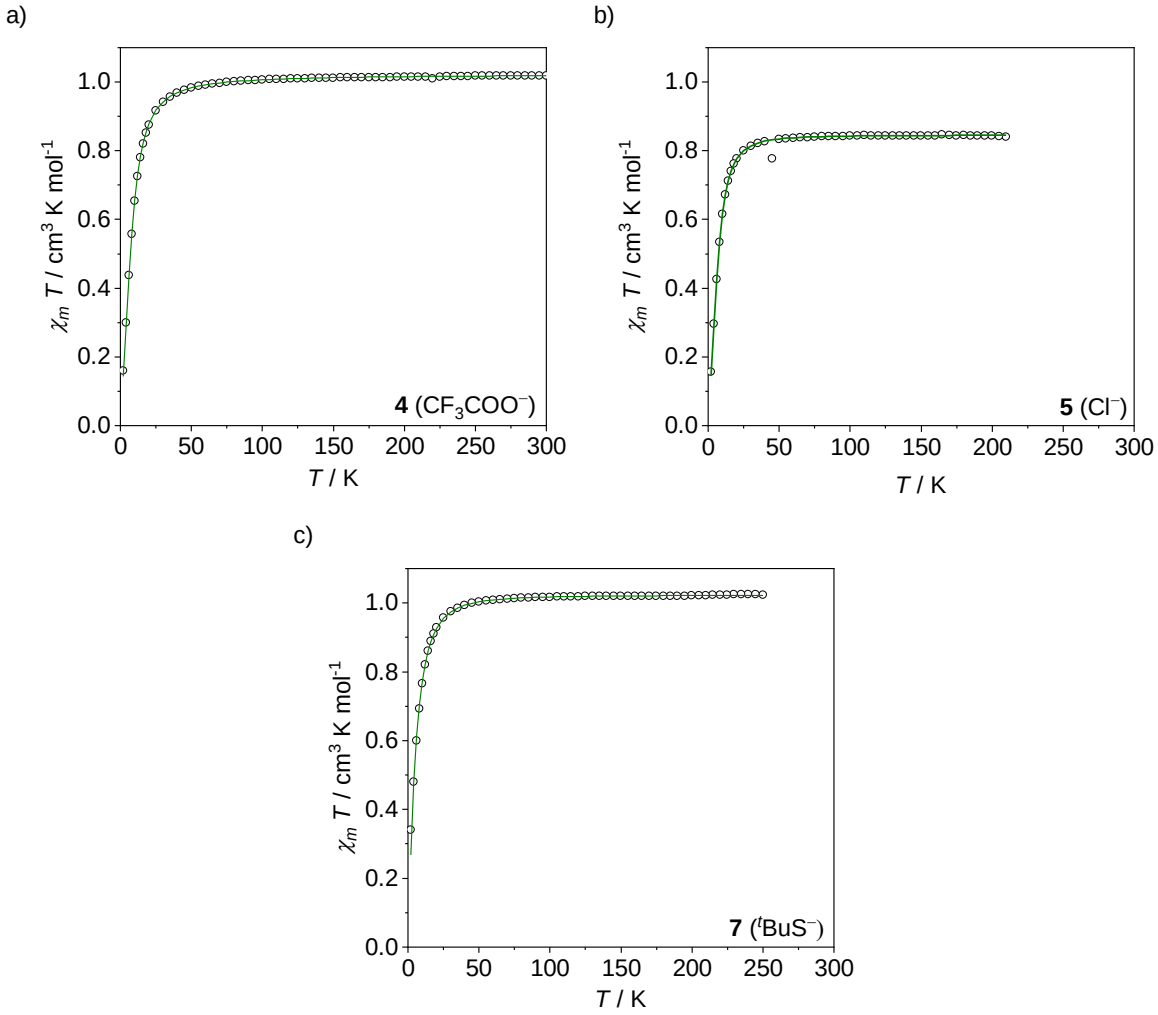

Figure 26. $\chi_m T$ *vs* T curves of solid samples of **4** (a), **5** (b) and **7** (c). The empty circlets represent experimental data, while the solid green lines are simulations using equation (2) . The lower values recorded for complex **5** were probably caused by the presence of diamagnetic impurities in the solid sample.

The obtained values are similar to the ones of **3** and in agreement with the ones obtained by the fitting of VTVH measurements. As seen for complex **3**, the relatively small ZFS parameters reflect

the large $S = 1 / S = 2$ gap and the large splitting of the t_{2g} orbitals for the whole series of complexes.[109,177] For comparison, analogous models with *N*-ligation show much larger ZFS parameters (> 27 cm^{-1}) due to spin-orbit mixing between the $S = 1$ and $S = 2$ states, allowed by the small energetic gap between the two states.[101] Accordingly, complex **7** exhibits the largest *D* value (taken as module), confirming the lower triplet-quintet gap owing to the strong thiolate donation compared to the other members of the tetracarbene series.

3.6 IRPD Spectroscopy

Given the absence of signals in resonance Raman (rR) spectra, the Fe=O stretching frequency of complex **3** was measured via IR-photodissociation (IRPD) spectroscopy with the ISORI instrument of Prof. Jana Roithová, at that time at the Department of Organic Chemistry of the Charles University in Prague (now at the Department of Spectroscopy and Catalysis of Radboud University, Netherlands).[110] The ISORI instrument allows for ESI generation and subsequent mass-isolation of selected complex ions in the gas phase, that are then injected into a cold trap kept at around 3 K. Here a helium buffer gas is injected in order to cause the collisional relaxation of the kinetic energy and to cool internal degrees of freedom of the ions. In these low internal energy conditions, the metal complexes form adducts with different numbers of helium atoms. Mass selection of adduct complexes allow their injection into a second chamber. Here the complexes are irradiated with a monochromatic infrared radiation impulse of known frequency, varied in a range of 2000-4680 cm^{-1} over the course of several irradiation cycles. If the impulse excites a stretching mode of the complex-helium adduct, the associated helium atom is detached due to the vibration of the molecule. The detector of the mass spectrometer works in ion counting mode and is set to count the number of complex-helium adducts exiting the irradiation chamber. For each frequency value, several cycles of two ion counts are performed: the first one when the IR radiation effectively irradiates the ions, and the second one on unirradiated ions. The first cycle provides the number N_i of remaining adducts after irradiation, while the second gives the total number of adducts present in the chamber N_{i0}. The spectrum is then constructed plotting the attenuation value obtained with the formula $1 - \frac{N_i}{N_{i0}}$ *versus* the frequency of the radiation.[178]

Complex **3** was found to fall in the middle of the range determined for oxoiron(IV) complexes known so far, with a Fe=O stretching frequency of 832 ± 3 cm^{-1} (for the non-labeled Fe=^{16}O).[110] Analogous measurements were performed on complexes **4** and **5** and the resulting IRPD spectra of isotopically unlabeled (black) and labeled (red) complexes are shown in Figure 27, together with the spectrum of **3**.

The spectral series provided a direct evaluation of the influence of the different axial ligands on the Fe=O bond stretching frequency in the gas phase. Substitution of CH_3CN with trifluoroacetate caused a shift of the band from 832 to 815 cm^{-1} (from 799 to 777 cm^{-1} for labeled Fe=^{18}O complexes), indicating a lengthening of the Fe-O distance. This is perfectly in accordance with the elongation of the Fe=O double bond as observed via XRD measurements. In fact, the substitution of the π-accepting CH_3CN ligand with a more π-basic carboxylate is expected to weaken the Fe–O bond due to the competition of the two axial ligands for the π-bonding with the iron d orbitals of suitable geometry, as discussed above. The downshift (Δν) of 38 ± 3 cm^{-1} associated with isotopic labeling of the oxygen atom matches the expected theoretical value of 35 cm^{-1}, thereby confirming the presence of the iron-oxo double bond.

When an even more π-basic chloride axial anion was bound to iron in complex **5**, the downshift of the bands became even more prominent, showing a reduced stretching frequency of 799 cm^{-1} (765 in case of ^{18}O labeling, $\Delta\nu$ = 34 cm^{-1}). This trend of Fe=O stretching frequency with the donor ability of axial ligands is in perfectly accordance with previously reported case. Indeed an analogous behavior was observed in the rR frequencies obtained for TMC complexes axially ligated by different anions.[97]

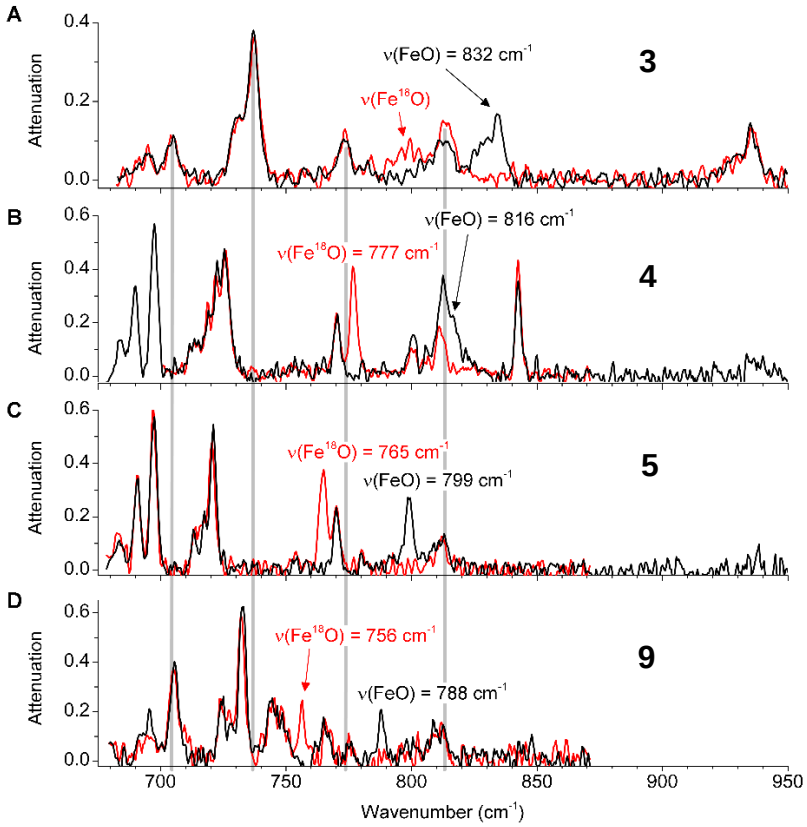

Figure 27. Helium tagging IRPD spectra of complexes **3**–**5** and of the isolated ion corresponding to the putative Fe^{IV}=O complex **9** derived from *in situ* oxidation of complex **8** with sPhIO.

Remarkably, the *in situ* reaction of the pentacarbene complex **8** with excess sPhIO allowed for the ESI-MS isolation of molecular ions corresponding to the putative DMI-Fe^{IV}=O oxo complex **9**. IRPD analysis of the isolated ions returned an extremely low Fe-O stretching frequency of 788 cm^{-1} (756 cm^{-1} for ^{18}O, $\Delta\nu$ = 32 cm^{-1}). This is the lowest value ever recorded for an Fe^{IV}-O complex, in agreement with the extreme σ-donating ability of the axial NHC moiety. The possibility to isolate the "homoleptic" pentacarbene oxoiron(IV) ion in the gas phase suggested that the species can be generated in ESI-MS conditions, and invites for further synthetic efforts to isolate the species in bulk.

3.7 Summary and Conclusions

In conclusion, this chapter presented the successful synthesis and characterization of a series of three tetracarbene oxoiron(IV) complexes coordinated by anionic axial ligands with different electron donor properties. Spectroscopic and magnetic data confirmed their Fe^{IV}-O nature and gave insight into the differences in electronic structure of the complexes. In particular, the trifluoroacetate and chloride complexes **4** and **5** showed UV/Vis features similar to parent complex **3**, with shifts compatible with the introduction of the anionic axial ligands and the associated weakening of the ligand field. Remarkably, a novel example of a thiolate-ligated oxoiron(IV) complex **7** could be synthesized, showing significant differences in the spectroscopic features owing to the strong σ- and π-donor properties of the thiolate ligand. Comparison with previously reported thiolate-bound analogues supports the axial ligation of a thiolate anion and its influence on UV/Vis features, Mössbauer parameters and magnetic properties. Notably, the trifluoroacetate-bound complex **4** could be crystallographically characterized, providing structural evidence for the elongation of the Fe=O bond owing to the competition of the π-basic carboxylate with the oxo ligand for π-donation to the corresponding orbitals on the metal center. A set of IRPD spectroscopy measurements provided final insight on the effect of the different axial ligand on the Fe=O bond nature. Indeed, progressively stronger π-donating ligands caused a downshift of the Fe=O stretching frequencies of the complexes **4** and **5**, in accordance with the expected lengthening of the Fe=O bond. Additional IRPD measurements are ongoing to derive the Fe=O stretching frequency of complex **7** and the Fe–OH one of a putative RS–Fe^{III}–OH complex described in the next chapter. With complexes **4**, **5** and **7** in hand, we moved to investigating the effect of the axial ligation on the HAA reactivity with weak C–H bonds. The results of these experiments will be the focus of Chapter 4.

4. C–H Bond Activation Reactivity of Axially Substituted Tetracarbene Oxoiron(IV) Complexes

4.1 Previous Results and Objectives

This chapter focuses on the evaluation of the axial ligand effect on the hydrogen atom abstraction (HAA) reactivity of tetracarbene oxoiron(IV) complexes coordinated by trifluoroacetate (**4**), chloride (**5**) and *tert*-butyl thiolate (**7**), based on previous results obtained in our group for the CH_3CN-ligated complex **3**.[146] As anticipated in Chapter 1, complex **3** was able to activate the weak C–H bonds of xanthene, 9,10-dihydroanthracene (DHA), 1,4-cyclohexadiene (CHD) and fluorene at –40 °C, with an initial HAA followed by decomposition to the μ-oxo complex **2** and no rebound reactivity with the substrate radical (Scheme 4). The HAA step followed pseudo-first order kinetics when performed with a large excess of substrate and a plot of the logarithm of the adjusted second order kinetic constant ($\log k_2'$, see Table 1 for the meaning of "adjusted") *versus* the bond dissociation energy (BDE, in kcal/mol) of the substrate's C–H bonds showed a linear dependency of the rate with the strength of the bond, thereby confirming the first step of the reaction to be a HAA. Table 1 shows the second order reaction rates for the oxidation of the four substrates by **3** at –40 °C.[99]

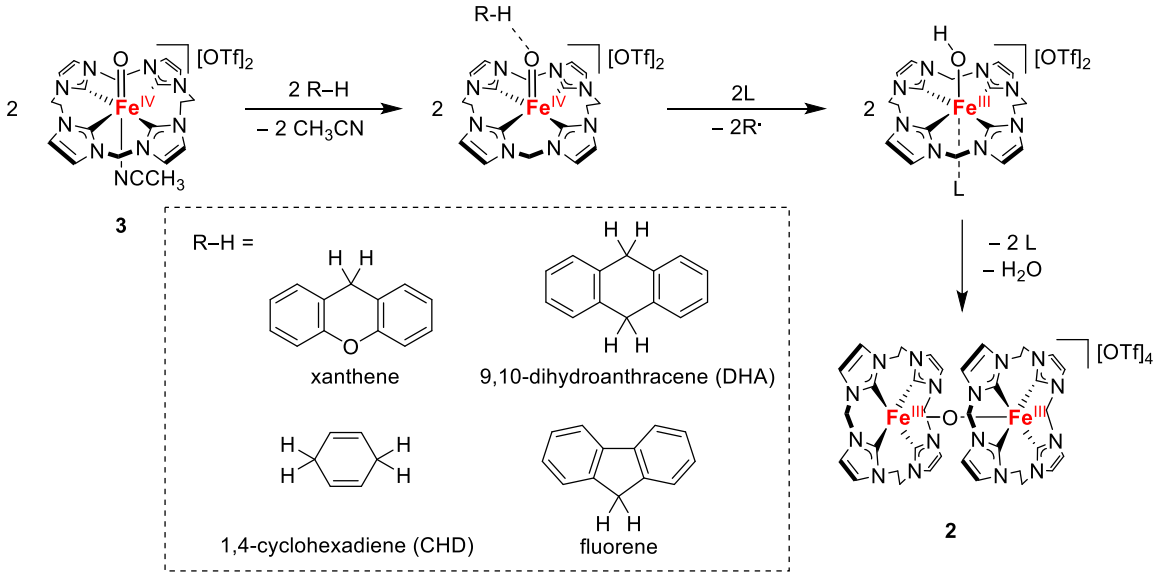

Scheme 4. Schematic representation of the HAA mechanism and subsequent decomposition of complex **3**. L represents different ligands found in solution, like solvent molecules, iodoarene derived from synthesis of **3** or others. Structures of the substrates used in the investigation of the HAA kinetics by **3** are shown within the dashed rectangle.

Table 1. BDE of substrates and associated rate constants for HAA reactions of complex **3**.

	BDE / kcal·mol^{-1}	k_2 / M^{-1}·s^{-1}	k_2' / M^{-1}·s^{-1}
Xanthene	75.5	2.2	1.1
DHA	77	0.76	0.19
CHD	78	0.47	0.12
Fluorene	80	0.0064	0.0032

k_2 represents the second order kinetic constant derived from the linear regression of the observed rate constants (k_{obs}), while k_2' is obtained dividing k_2 by the number of abstractable H atoms of the associated substrate.

Following the evolution of the optical spectra during C–H bond activation, the initial formation of an unstable intermediate with an optical feature at 448 nm was observed, before decomposition to **2**. The nature of this species was elucidated with the help of cryo-mass spectrometry, EPR spectroscopy and labelling experiments, confirming its tetracarbene–Fe^{III}–OH nature deriving directly from initial HAA. However, EPR of the *in situ* prepared hydroxo complex showed the presence of several ferric species, likely due to the binding of different axial ligands to the iron complex under the reaction conditions.[146]

In addition, extensive theoretical calculations evidenced an exciting feature of the tetracarbene oxoiron(IV) complex towards HAA reactivity: the high energy gap between the d_{xy} and the d_{z^2} orbitals, as discussed in Chapter 3, prevents the $S = 1$ complex to access the putatively more reactive quintet state during the first steps of the reaction, thereby precluding a two-state reactivity (TSR) pathway from taking place. Indeed, the $S = 1$ surface reaction pathway was shown to be energetically favored over the $S = 2$ one, rendering the complex the first and only model for a triplet-only pathway HAA reactivity. Further calculations showed that complex **3** likely reacts via an initial axial CH_3CN ligand de-coordination to generate a more reactive five-coordinate iron-oxo complex that then performs HAA.[99] Scheme 4 summarizes the mechanism of HAA by complex **3**.

Recently, a publication by Rajaraman and coworkers provided some theoretical insight on the effect of different axial ligands on the reactivity of complex **3** and four derivates bearing HS^-, trimethylamine, trimethylphosphine or no axial ligand. They investigated the HAA from methane via theoretical calculations and showed that the alternative axial ligands would have a very small effect on the HAA kinetics, due to a limited effect on the $S = 1$ / $S = 2$ energy gap, that remains too high to allow for TSR in all complexes.[179] The π-acceptor ability of the equatorial NHCs, that would counterbalance stronger axial donation, was invoked to justify the behavior of the investigated tetracarbene complexes.

Given the unique features of complex **3** in the activation of C–H bonds and the possibility to isolate the axially ligated analogues **4**, **5** and **7**, the present chapter focuses on the experimental evaluation of the axial ligand effect on the HAA reactivity of the series.

4.2 Reactivity with 1,4-Cyclohexadiene at –40 °C

The HAA reactivity of complexes **4**, **5** and **7** was studied by UV/Vis spectroscopy, monitoring the reaction with 1,4-cyclohexadiene at –40 °C in CH_3CN, using conditions analogous to the ones used for the parent complex **3**.[99] Dissolution of solid samples of **4** and **5** and *in situ* preparation of **7** (as described in Chapter 3) was followed by addition of CH_3CN solutions of CHD and acquisition of spectra of the resulting mixture at regular time intervals until completion of the reaction (~ 1.5 h). Given the limited solubility of **5** at the temperature of the experiments, a lower concentration of all the complex solutions was chosen (0.25 mM) compared to the one previously used for complex **3** (1 mM).

Effect of trifluoroacetate and chloride anions: reactivity of complexes 4 and 5

As introduced in Chapter 1, the abstraction of a hydrogen atom from CHD by the oxoiron(IV) complexes is expected to proceed with the initial reduction to reactive Fe^{III}–OH intermediates, the instability of which would cause the rapid decay to more stable compounds or follow-up reactivity with the substrate. As an example, complex **3** was shown to react with CHD via the initial formation of the corresponding (L^{NHC})–Fe^{III}–OH complex over the course of ~200 s, followed by a slow decomposition to the stable dimeric complex **2**.

Figure 28 shows the spectral changes associated with the reaction of trifluoroacetate complex **4** and chloride complex **5** with 200 equivalents of CHD. Upon substrate addition, the characteristic bands at 408 (**4**) and 416 (**5**) initially decreased with isosbestic points at 439 and 434 nm, respectively, during the first 350-400 s. No unequivocal formation of a putative Fe^{III}-OH intermediate was observed before the vanishing of the isosbestic points and the slow appearance of a sharp absorption band at 339 nm. A comparison with complex **3** evidences a different course of the reaction, which for **4** and **5** did not proceed with the formation of the μ-oxo complex **2** (Figure 28, c). Instead, in both cases, the final product showed the characteristic band of the bis-CH_3CN Fe^{II} complex **1**, as suggested by a comparison with the spectrum of the pure complex (Figure 28, c).

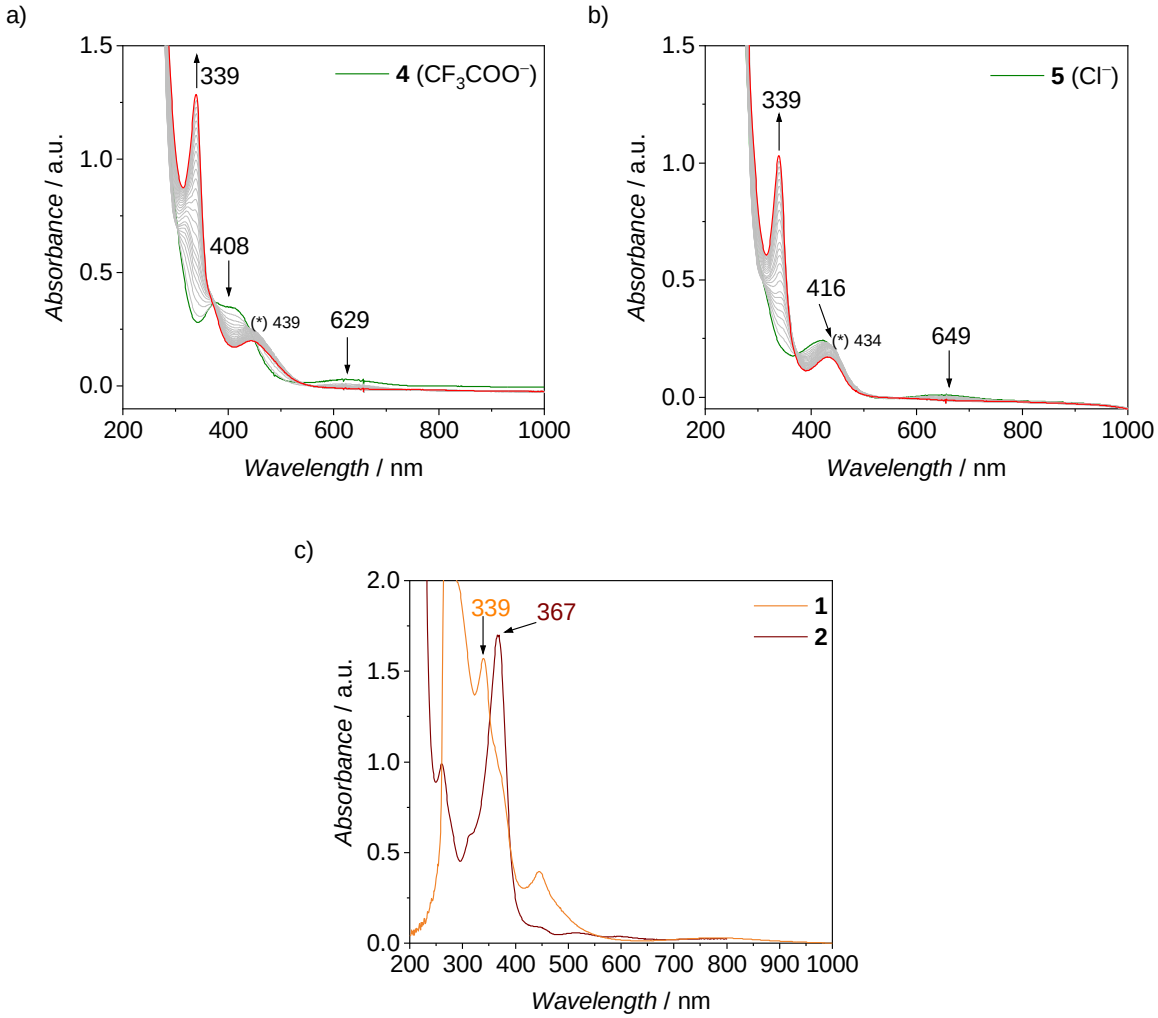

Figure 28. Spectral evolution of the optical features during the reaction of complexes **4** and **5** (a and b, respectively) with 200 equivalents of CHD in CH_3CN at –40 °C. Isosbestic points are indicated with asteriscs (vanishing ones in brakets). Spectra of pure complexes **1** and **2** are shown in c.

The vanishing of the isosbestic points suggests that the overall reaction from **4**/**5** to **1** proceeds through multiple steps. The first process is likely the HAA to form the corresponding ferric-hydroxo complexes, as confirmed by the kinetic analysis described in Section 4.4. The different follow-up reactivity compared to **3** implies that the presence of the axial trifluoroacetate (**4**) and chloride (**5**) anions prevents the decomposition of the intermediates via dimerization (Scheme 4). Indeed, as discussed in more detail in Chapter 5, the iron(III) centers in the μ-oxo complex **2** possess a 5-coordinated square pyramidal geometry, and coordination of an additional axial ligand triggers the breaking of one of the Fe–O bonds. As a result, the formation of a dimeric complex like **2** is only possible if the axial ligands of the hydroxo intermediates are weakly bound and can be easily released during the dimerization process. Therefore, it appears reasonable to hypothesize that the presence of strongly bound axial ligands in **4** and **5** and their corresponding Fe^{III}–OH derivates would stabilize the complexes with respect to dimerization. The formation of Fe^{II} complexes after

the initial HAA can be associated with two possible follow-up reactions, as introduced in Chapter 1: in case of an oxygen-rebound, transfer of the hydroxyl radical from the Fe^{III}–OH intermediate to the organic substrate radical would generate the ferrous complex and the an organic alcohol, while in a desaturation scenario a second HAA abstraction would generate an Fe^{II}-aquo complex, where the H_2O ligand would be readily displaced by CH_3CN. Given that the abstraction of a second hydrogen atom from the cyclohexadienyl radical is even more favorable than the first one due to the formation of an aromatic product (benzene), desaturation appears to be the most probable evolution pathway of the reactions of **4** and **5** with CHD (Scheme 5). ^{1}H-NMR and GC-FID experiments aimed at the characterization of the product mixtures are ongoing, in order to confirm the formation of benzene and complex **1**.

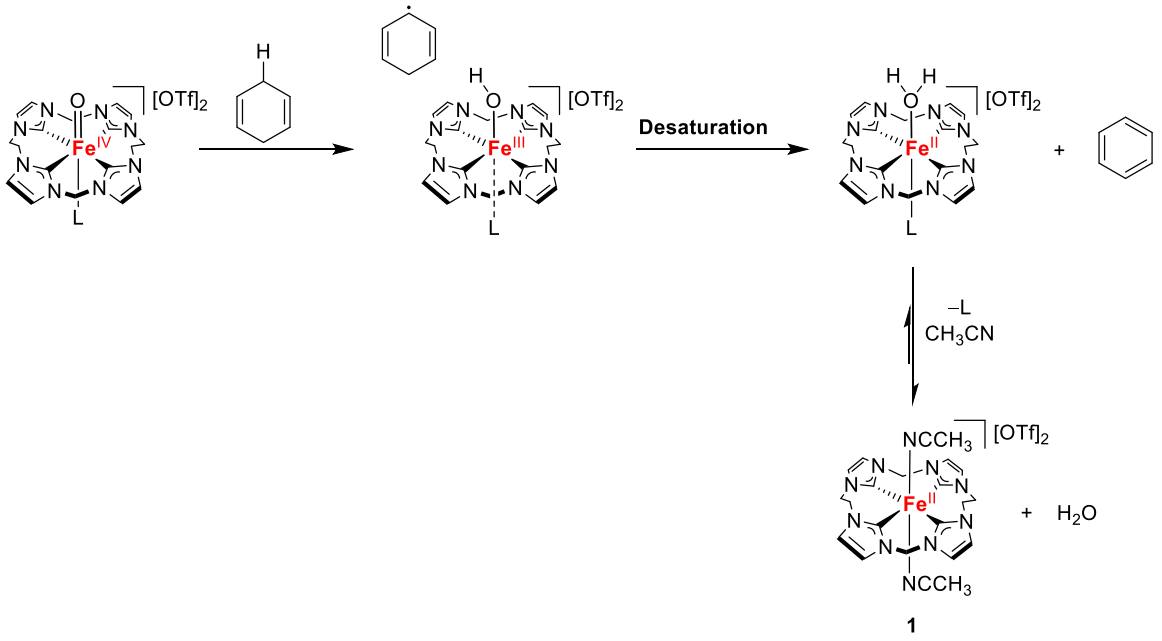

Scheme 5. Schematic representation of the desaturation pathway for the reaction of complexes **4** and **5** with CHD in CH_3CN.

Reactivity of the thiolate-bound complex 7

Evaluation of the reactivity of complex **7** with 200 equivalents of CHD proved to be more straightforward. Figure 29 shows that the reaction proceeded with the disappearance of the bands at 334 and 442 nm typical of **7**, and the appearance of an intense feature at 609 nm over the course of 1.5 hours. The spectral changes were accompanied by the presence of five isosbestic points at 327, 360, 398, 548 and 683 nm, clearly indicating a single-step transformation. The product of the reaction is expected to be a thiolate-bound Fe^{III} hydroxo complex ($[(L^{NHC})Fe^{III}(OH)(^tBuS)]^+$), as a

result of the initial HAA step. Remarkably, this product appeared to be stable for more than four hours at –40 °C.

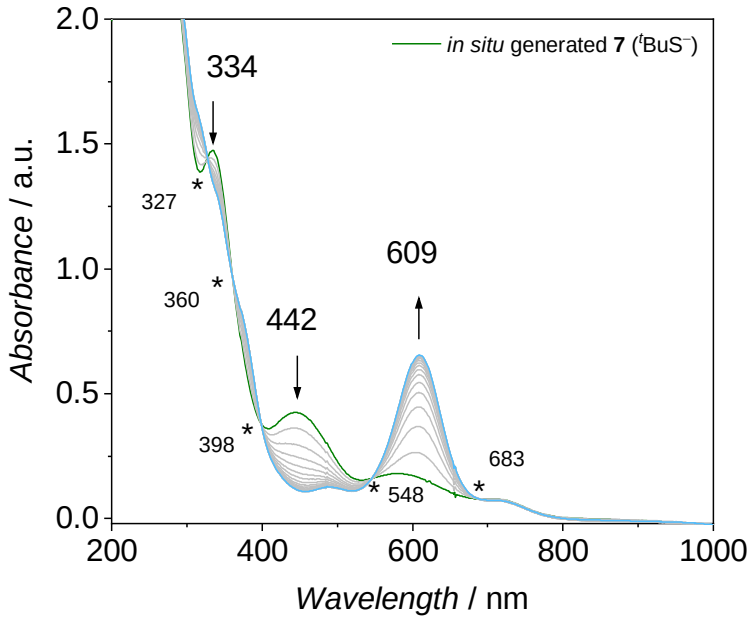

Figure 29. Spectral evolution of the optical features during the reaction of complex 7 with 200 equivalents of CHD in CH_3CN at –40 °C. Isosbestic points are indicated with asteriscs. Reaction time: 1.5 h.

Typically, ferric-hydroxo intermediates of heme- and non-heme models are extremely reactive species, but the unusual stability of the putative $[(L^{NHC})Fe^{III}(OH)(^tBuS)]^+$ complex introduces the possibility of isolation and characterization of the product. Indeed, current efforts are aimed at the purification of such intermediate in bulk, to allow for the determination of its electronic and molecular structures.

With this spectral information and hypothesis in hand, the reactions were repeated using different concentrations of CHD and kinetic data was derived.

Kinetic measurements of HAA reactions with 4, 5 and 7

The usual approach to obtain kinetic data from HAA reactivity of Fe^{IV}-oxo complexes involves following the decrease over time of the characteristic optical band of the oxo-complex upon reaction. However, given the complicated spectral changes recorded in the case of parent **3** (which possesses CH_3CN as axial ligand), a different approach was chosen, following the initial formation

of the Fe^{III}–OH complex with its characteristic band at 448 nm, that was proposed to be proportional to the consumption of **3** upon HAA.[99] As shown in Figure 28, the time decay of complexes **4** and **5** was not accompanied by the clear rising of bands attributable to the ferric intermediates, and at this concentration the spectral changes associated to the decrease of the bands around 600 nm were too limited to provide unequivocal data. Hence, the best choice to get preliminary kinetic information appeared to be following the initial decay of the bands in the 400 nm region of **4** and **5** as long as the initial isosbestic points were present. In fact, a similar approach was used by Sen Gupta and coworkers to obtain kinetic parameters for the HAA reactivity of a unique oxoiron(V) TAML complex. In that case the initial HAA was followed by several decomposition steps, and kinetic data relative to the Fe(V)-oxo complex were derived by following the changes in optical features until the initial isosbestic points were broken, and discarding following data points.[180]

Due to the limited timeframe (350-400 s) and the limited spectral changes in absorbance associated with the HAA processes for the trifluoroacetate (**4**) and chloride complex (**5**), only kinetic data of limited quality were obtained. Higher quality data were collected using different conditions as discussed in the next section. In the straightforward case of complex **7**, however, both the decay of the oxo complex and the formation of the ferric product were followed until completion of the reaction. The substantial changes in absorption of the bands during the reaction allowed to obtain kinetic data of adequate quality.

The plots of the observed reaction rates *versus* concentration of CHD for **4**, **5** and **7** are shown in Figure 30 together with the linear fits of the observed rate constants. The obtained second order rate constants k_2 had to be corrected for the number of abstractable hydrogen atoms of the substrate, four in the case of 1,4-cyclohexadiene, to obtain k_2' constants. Table 2 shows the approximated k_2 and k_2' values for complexes **4** and **5**, the value obtained for **7** and a comparison with parent complex **3**.

Table 2. Estimated second order reaction rates for the reaction of complexes **4**, **5** and **7** with CHD in CH_3CN at –40 °C and comparison with parent complex **3**.[99]

	3 (CH_3CN)	**4** (CF_3COO^-)	**5** (Cl^-)	**7** ($^tBuS^-$)
k_2 / $M^{-1}\cdot s^{-1}$	0.470	~0.093	~0.128	0.128
k_2' / $M^{-1}\cdot s^{-1}$	0.120	~0.023	~0.032	0.032

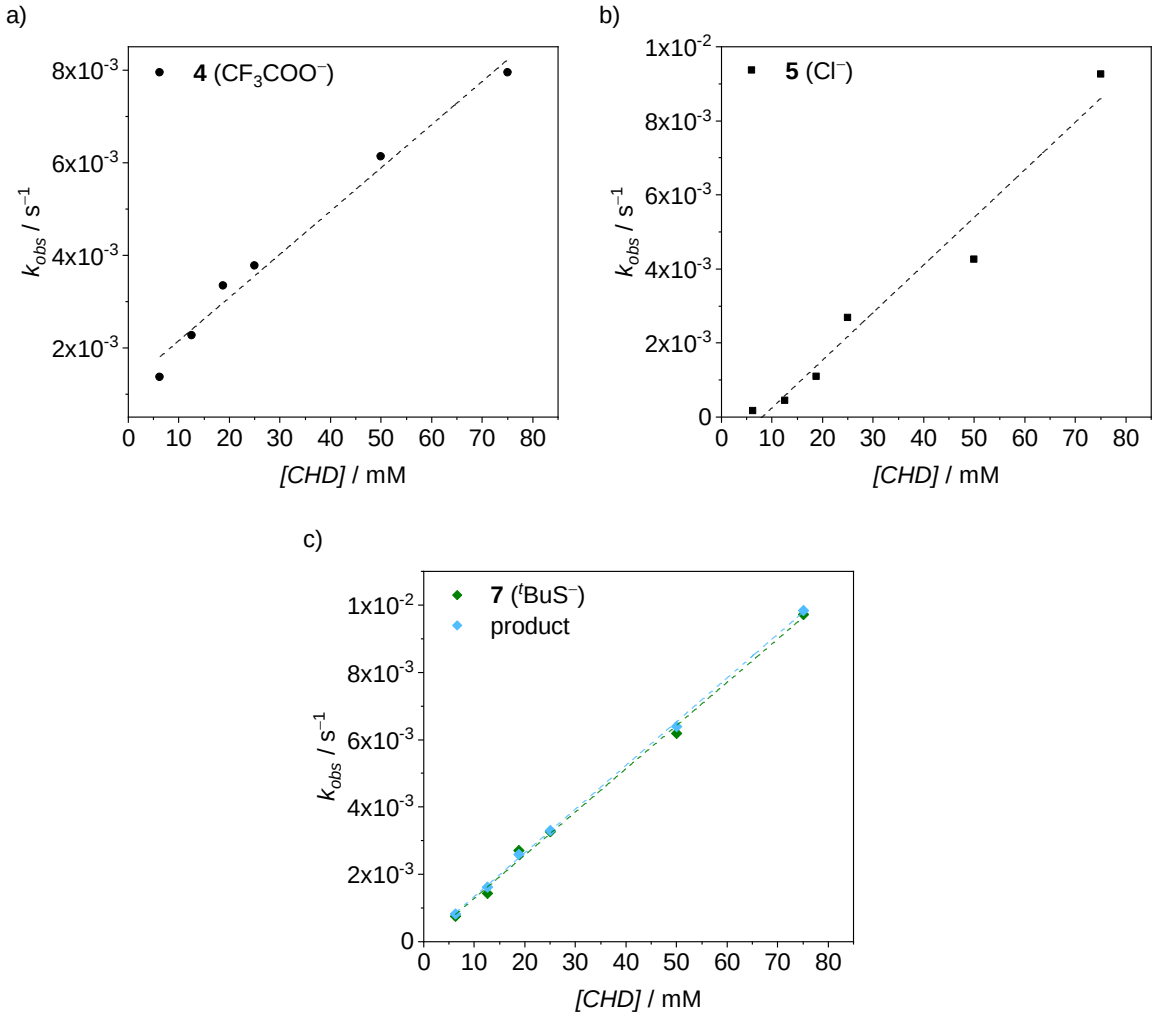

Figure 30. Plots of the observed reaction rates (k_{obs}) of complexes **4**, **5** and **7** (0.25 mM, a, b, c, and d respectively) *vs*. concentration of CHD at –40 °C in CH_3CN. The green and blue dots and linear plots related to complex **7** correspond to the data obtained by following the disappearance of the band at 442 nm (green) or the appearance of the product band at 609 nm (blue).

As predicted by Rajaraman, the parent complex **3** and the axially substituted derivatives showed similar second order rates for the HAA step, providing experimental support for the theoretical hypothesis according to which the stronger axial donation could be counterbalanced by the π-acceptor ability of the NHC ligands.

With these preliminary findings in hand, we moved to investigate the kinetic parameters at higher temperatures. However, in order to obtain kinetic traces of higher quality, an increase of the concentration of the complexes was needed. Given the very low solubility of complexes **5** in CH_3CN, the subsequent measurements were performed only on complexes **3**, **4** and **7** using a concentration of 1 mM in the reaction cell. This also allowed to obtain the kinetic trace of complex **4** following the disappearing of the band at 629 nm, which decreases continuously throughout the HAA reaction (Figure 28), thereby allowing for more accurate estimations of the rate constants.

4.3 Reactivity with 1,4-Cyclohexadiene at Higher Temperatures

The kinetic measurements of the HAA reactivity of the axially bound complexes **4** (CF_3COO^-), **5** (Cl^-) and **7** ($^tBuS^-$) with excesses of CHD were repeated at 25 °C, a temperature at which the reactions were expected to be completed in few seconds. However, given the thermal instability of all the iron-oxo compounds at that temperature, complex stock solutions were prepared at −40 °C and the experiments were performed using a stopped-flow UV/Vis spectrometer capable of recording extra-fast spectral acquisitions (up to 500 spectra recorded in 85 ms) and equipped to quickly warm-up the complexes sample solutions from −40 to 25 °C right before mixing with the substrates, avoiding significant self-decomposition. Figure 31 shows the k_{obs} plots obtained and their linear fit, while Table 3 reports the second order rate constant values.

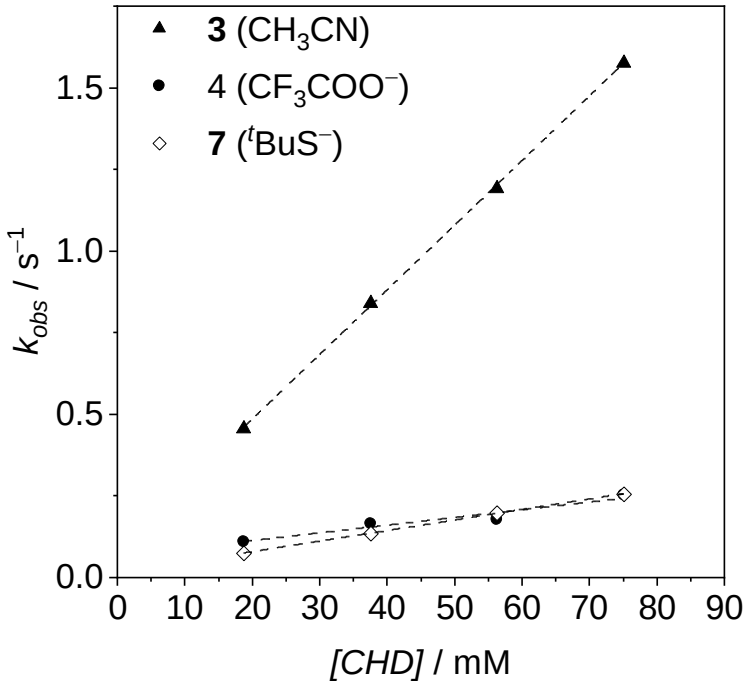

Figure 31. Plots of the observed reaction rates (k_{obs}) of complexes **3** (triangles), **4** (dots) and **7** (empty diamonds), (1 mM) *vs.* concentration of CHD at 25 °C in CH_3CN.

Table 3. Second order reaction rates for the reaction of complexes **3**, **4** and **7** with CHD in CH_3CN at 25 °C.

	3	**4**	**7**
k_2 / $M^{-1}\cdot s^{-1}$	20.03	2.35	3.26
k_2' / $M^{-1}\cdot s^{-1}$	5.01	0.59	0.82

In agreement with the results obtained at −40 °C, all complexes showed similar second order rate constants, with complex **3** reacting approximately one order of magnitude faster than **4** and six times faster than **7**. According to the k_2' values, coordination of trifluoroacetate (**4**), chloride (**5**) or thiolate (**7**) to the tetracarbene oxoiron(IV) core seems to cause a slight decrease of the experimental second order rate constant of the HAA process compared to the parent CH_3CN complex **3**. This constitutes a distinctive behavior of the anion-ligated tetracarbene complexes when compared to the studies performed on other oxoiron(IV) model complexes, e.g., the tetramethylcyclam [(TMC)Fe^{IV}(O)(X)] series (structures in Chapter 1). For the latter, axial coordination of trifluoroacetate, azide or tethered thiolate was able to substantially increase the reaction rate.[96] In particular, coordination of trifluoroacetate caused an increase of one order of magnitude in the value of k_2 for the activation of CHD when compared to the CH_3CN -ligated TMC complex, and tethering a thiolate allowed for the oxidation of 9,10-dihydroanthracene to proceed 38 times faster. According to the authors, this "antielectrophylic" trend of HAA kinetics could be ascribed to three main reasons, already introduced in Chapter 1. First, more electron-donating axial ligands increase H-atom tunneling contributions, as shown by higher KIE values.[96,181] Additionally, the increased electron density on the z-axis induces a decrease in the triplet-quintet gap (S = 1 / S = 2), making the quintet reaction pathway more accessible. During the HAA reaction, which for the TMC complexes is proposed to proceed via a two-state reactivity (TSR) mechanism, the quintet pathway has a lower energy barrier compared to the triplet owing to the preferred σ-pathway for the formation of the first transition state and to the exchange enhanced reactivity phenomenon.[82,94,182] Finally, in the case of thiolate axial ligands, the enhanced reactivity owes to the strong "push-pull" effect of the sulfur donor, which increases the basicity of the ferryl group as well as the BDE_{OH} of the generated Fe^{III}-OH, thereby increasing the driving force of the HAA reaction.[57,64,149,183,184]

As shown previously, a TSR scenario is not likely for complex **3**, given the large triplet-quintet energy gap of 18.6 kcal·mol^{-1}, and Rajaraman's study predicted a single state reactivity mechanism for axially ligated analogues as well.[99,179] However, even when taking into account the unlikelihood of the TSR mechanism for **4**, **5** and **7**, the increased H-atom tunneling and the "push-pull" effect should enhance their rates compared to **3**. The explanation of the higher rates of complex **3** lays in the mechanism of the HAA step, which was calculated to proceed through an initial axial CH_3CN

dissociation to generate a pentacoordinated tetracarbene oxoiron(IV) complex. This species was calculated to show higher HAA rates compared to the 6-coordinated (6C) **3** in the case of CHD, and to all 6C axially substituted analogues in the case of methane.[99,179] This was explained by taking in consideration that the HAA reaction of **3** proceeds via a σ-pathway, where the addition of the electron to the Fe-oxo complex happens on the d_{z^2} frontier orbital. Dissociation of the axial ligand therefore lowers the energy of the target orbital and allows for faster reactivity. As introduced in the previous sections, the strongly bound axial anions in **4** (CF_3COO^-), **5** (Cl^-) and **7** ($^tBuS^-$) would likely prevent (or at least slow down) the axial ligand dissociation for these complexes, therefore justifying the slightly lower rates of **4**, **5** and **7** compared to **3**. In fact, the different follow up reactivity of **4** and **5**, and the clean one-step conversion of **7** to the putative hydroxo intermediate upon HAA (see Section 4.2) could suggest that the axial anions remain bound in the hydroxo intermediate, preventing ligand dissociation to the more reactive 5C intermediate.

Although activation parameters for complex **3** were already derived for temperatures between −40 °C and 0 °C, the possibility to follow the very fast reactions at room temperature allowed for the acquisition of additional data for **3** up to room temperature, together with the estimation of the activation parameters of complexes **4** and **7**. To this extent, the HAA experiments were performed with 75 mM solutions of CHD at three additional temperatures, 15 °C, 5 °C and −5 °C, and the Eyring plots shown in Figure 32 were produced by dividing the observed rate constant (k_{obs}) by the CHD molar concentration and the number of abstractable H-atoms of CHD (four) to obtain the corresponding k_2' values. Activation enthalpy, entropy and free energy of all reactions were calculated using Equation (3).

$$\ln\frac{k}{T} = \frac{-\Delta H^{\ddagger}}{R}\cdot\frac{1}{T} + \ln\frac{k_B}{h} + \frac{\Delta S^{\ddagger}}{R} \qquad (3)$$

As expected, reaction rates decreased by lowering the temperature for all complexes, and Table 4 reports the obtained activation parameter values. Overall, all the complexes show similar activation parameters, reflecting the minor differences in their HAA rate constants.

Table 4. Activation parameters for the reaction of **3**, **4** and **7** with CHD, as derived from the Eyring plots.

	3	**4**	**7**
$\Delta \boldsymbol{H}^{\ddagger}$ / kcal·mol^{-1}	6.0	5.0	9.7
$\Delta \boldsymbol{S}^{\ddagger}$ / cal·K^{-1}·mol^{-1}	–36.4	–42.8	–25.8
$\Delta \boldsymbol{G}^{\ddagger}_{\mathbf{20}^{\circ}\mathrm{C}}$ / kcal·mol^{-1}	16.7	17.6	17.3

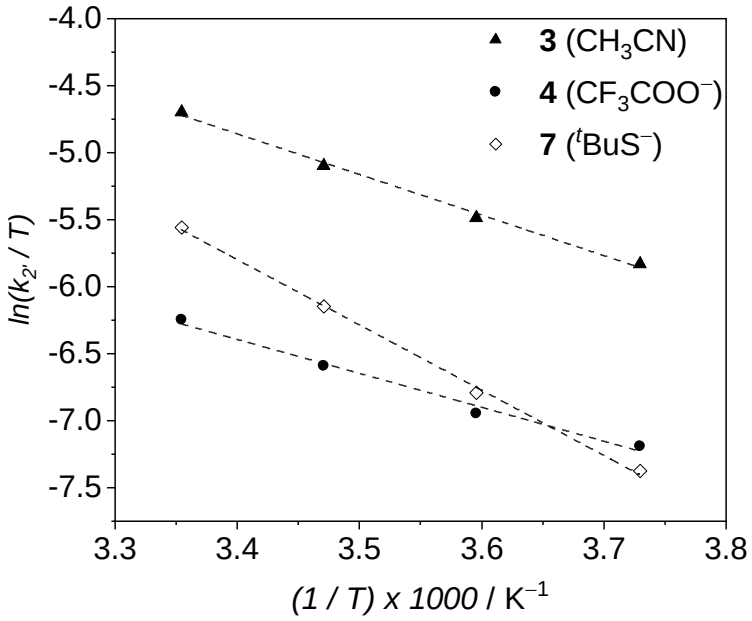

Figure 32. Eyring plots for the reactions of **3** (triangles), **4** (dots) and **7** (diamonds) with CHD (75 mM) at 25 °C, 15 °C, 5 °C and –5 °C in CH_3CN.

4.4 Reactions with Other Substrates

The kinetic measurements at 25 °C were performed with two additional substrates with lower C–H bond dissociation energy (BDE) compared to CHD: 9,10-dihydroanthracene (DHA, 77 kcal·mol^{-1}) and xanthene (75.5 kcal·mol^{-1}). Given their low solubility in CH_3CN, substrate stock solutions were prepared in mixtures of DCM and CH_3CN, therefore providing slightly different reaction environments compared to CHD. Nevertheless, the k_{obs} plots gave linear trends and the derived second order rates were in accordance with the lower BDE of these two substrates, which reacted faster compared to CHD (Figure 33 and Table 5).

Table 5. Calculated adjusted second order rate constants (k_2', in $M^{-1}\cdot s^{-1}$) for the reactions of **3**, **4** and **7** with xanthene, DHA and CHD in CH_3CN at 25 °C.

	3	**4**	**7**
Xanthene	13.17	2.02	3.30
DHA	6.80	1.04	3.12
CHD	5.01	0.59	0.82

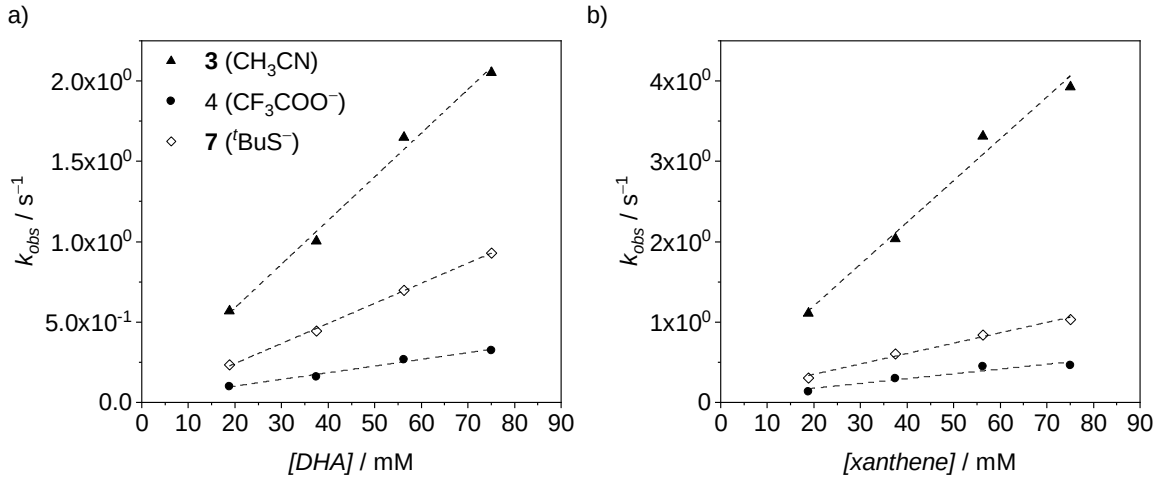

Figure 33. Plots of the observed reaction rates (k_{obs}) of complexes **3** (triangles), **4** (dots) and **7** (empty diamonds), (1 mM) *vs.* concentration of a) DHA and b) xanthene at 25 °C in CH_3CN.

Moreover, plots of the $\log k_2'$ versus the BDE (in kcal·mol^{-1}) of the three substrates (Figure 34) gave a linear trend with a slope of –0.17 and –0.21 for **3** and **4**, respectively, thereby supporting the hypothesis of a C–H bond activation that proceeds via an initial HAA step, as previously shown in the case of complex **3** at – 40°C.[99,185–188] Interestingly, the behavior of complex **7** deviates from the ideal linearity experimentally observed for direct HAA mechanisms. Usually, deviations from linearity have been interpreted introducing the possibility of an asynchronous PCET mechanism, in which the electron and the proton of the formal H-atom are abstracted from the substrate in two different steps.[82,189] Alternatively, the activation of weak C–H bonds has been shown to be independent from the substrate's BDE_{CH} in cases in which the entropic contribution to the free-energy barriers exceeded the enthalpic one (which is directly influenced by the BDE), as seen both for some enzyme Fe^{IV}-oxo active intermediates and thiolate-bound heme model complexes.[5,190] Given the peculiar nature of the thiolate ligation and the singular electronic structure of complex **7**, it would be reasonable to hypothesize a different behavior in the activation of weak C–H bonds, and current efforts are focused on a rigorous investigation of the deviation.

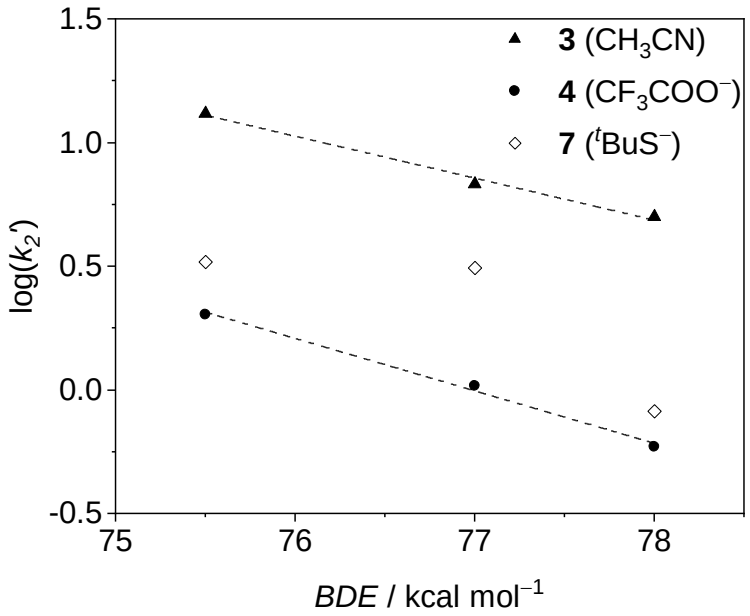

Figure 34. Plots of log k_2' versus the C–H BDE of xanthene, DHA and CHD for complexes **3** (black triangles), **4** (black dots) and **7** (empty diamonds).

Taken together, the kinetic measurements on complexes **4**, **5** and **7** provided insight into the effect of the axial coordination of different anions and supported the initial findings about **3** and theoretical calculations performed by Rajaraman. Reaction rates at −40 °C and 25 °C were shown to be similar for all complexes, regardless of the presence of activating axial ligands. The slight differences in reaction rates and product mixtures between **3** and the anion-coordinated complexes evidenced possible differences in the reaction mechanism. The decrease of reaction rates with coordination of activating axial ligands could in fact be envisioned by taking into account the effect of strong axial coordination on the mechanism of the reaction, which is supposed to proceed via ligand dissociation only for **3**, generating a more reactive 5C intermediate, while a direct HAA on the less reactive 6C Fe^{IV}=O complexes is more likely for **4**, **5** and **7**.

4.5 Electrochemical Investigations of the Tetracarbene Oxoiron(IV) Complexes

In order to gain additional insight into the HAA step of the reactions performed by the tetracarbene complexes, it is advisable to investigate the one-electron reduction of the complex series, with the aim of estimating the reduction potential of the $Fe^{IV}O/Fe^{III}O$ couple. However, cyclic voltammetry measurements on temperature unstable and reactive species require suitable experimental set-ups to avoid decomposition of the analytes during the experiments. Therefore, cyclic voltammetry measurements of complexes **3**, **4** and **5** were performed during a research stay in the lab of

Dr. Nicolas Le Poul, at the Laboratoire de Chimie, Electrochimie Moléculaires et Chimie Analytique of the Université de Bretaigne Occidentale, Brest. There, measurements at low temperature and fast scan rates were performed using an in-house built cryo-cyclic voltammetry set-up, in order to investigate the behavior of the complexes upon reduction.

In a typical experiment, a 0.75 mM EtCN solution of the chosen iron-oxo complex containing 0.1 M tetrabutylammonium hexafluorophosphate ($TBAPF_6$) was kept at temperatures between –35 °C and –70 °C and cyclic voltammograms (CV) were recorded using a glassy carbon working electrode. Figure 35 shows the full voltammograms of complexes **3**–**5** at –35 °C when the CVs were started at the open circuit potential (OCP) and scanned cathodically first, at a scan rate of 0.1 V/s. All three complexes showed two irreversible reductive waves in the region between –1.25 and –1.60 V and irreversible oxidative events around 0.75-1.0 V.

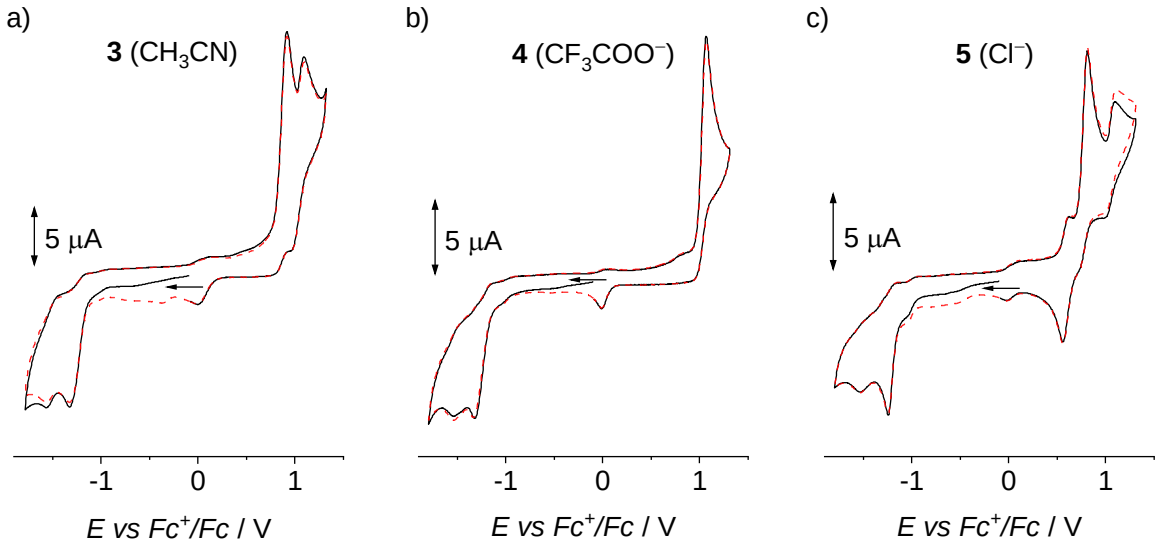

Figure 35. Cyclic voltammograms of complexes **3** (a), **4** (b) and **5** (c) (0.75 mM) in EtCN 0.1 M $TBAPF_6$ at –35 °C using a glassy carbon working electrode and referencing vs $Fc^{+/0}$. All the measurements were scanned cathodically first starting from OCP at 0.1 V/s; two cycles were completed (first cycle: black solid line, second cycle: red dashed line).

Reversibility of a redox event is a key requirement to accurately obtain the associated reduction potentials.[191] Hence, the reductive region of the CVs were recorded at increasingly higher scan rates and progressively lower temperatures in an attempt to reach reversibility conditions for the reductions of the complexes. However, even at rates of 100 V/s and temperatures of –70 °C none of the complexes showed signs of a reversible reduction. This rendered an accurate quantification of the potential associated with a formal $Fe^{IV}O$ to $Fe^{III}O$ reduction impossible. According to literature, the irreversibility of the one-electron reduction would be ascribed to a very fast chemical

process following the electron transfer, in which the generated formal Fe^{III}-oxo complex would abstract a proton from the nitrile solvent or traces of water in the electrolyte due to its extreme basicity, as suggested by the seminal work of T. J. Meyer and the gas-phase experimental evidences from Roithová and co-workers.[192,193] The latter showed that the formal Fe^{III}-O complexes derived from a variety of oxoiron(IV) complexes with different supporting ligands and geometries react as extremely strong bases rather than as hydrogen atom abstractors.

Interestingly, a dependence of the two reductive waves on scan rate was observed for all tetracarbene complexes. For the sake of brevity, only the findings related to complex **4** will be discussed here, given the totally analogous behaviors of complexes **3** and **5** in these initial investigations.

Figure 36 shows the cyclic voltammograms of the reductive region of trifluoroacetate complex **4** at scan rates between 0.05 and 2 V/s at −35 °C in CH_3CN. At lower scan rates, two clear reduction events are observable, with peak potentials of −1.292 V and −1.574 V at 0.05 V/s. A progressive increase of the scan rate caused both a cathodic shift in the peak potential of the first reductive event and its decrease in intensity compared to the second wave. At 5 V/s and up to 20 V/s, the first redox event appeared almost completely suppressed, with only the reduction at lower potential showing prominently. A similar behavior can be seen in the second scan of each CV (red dashed line), although to a lower extent.

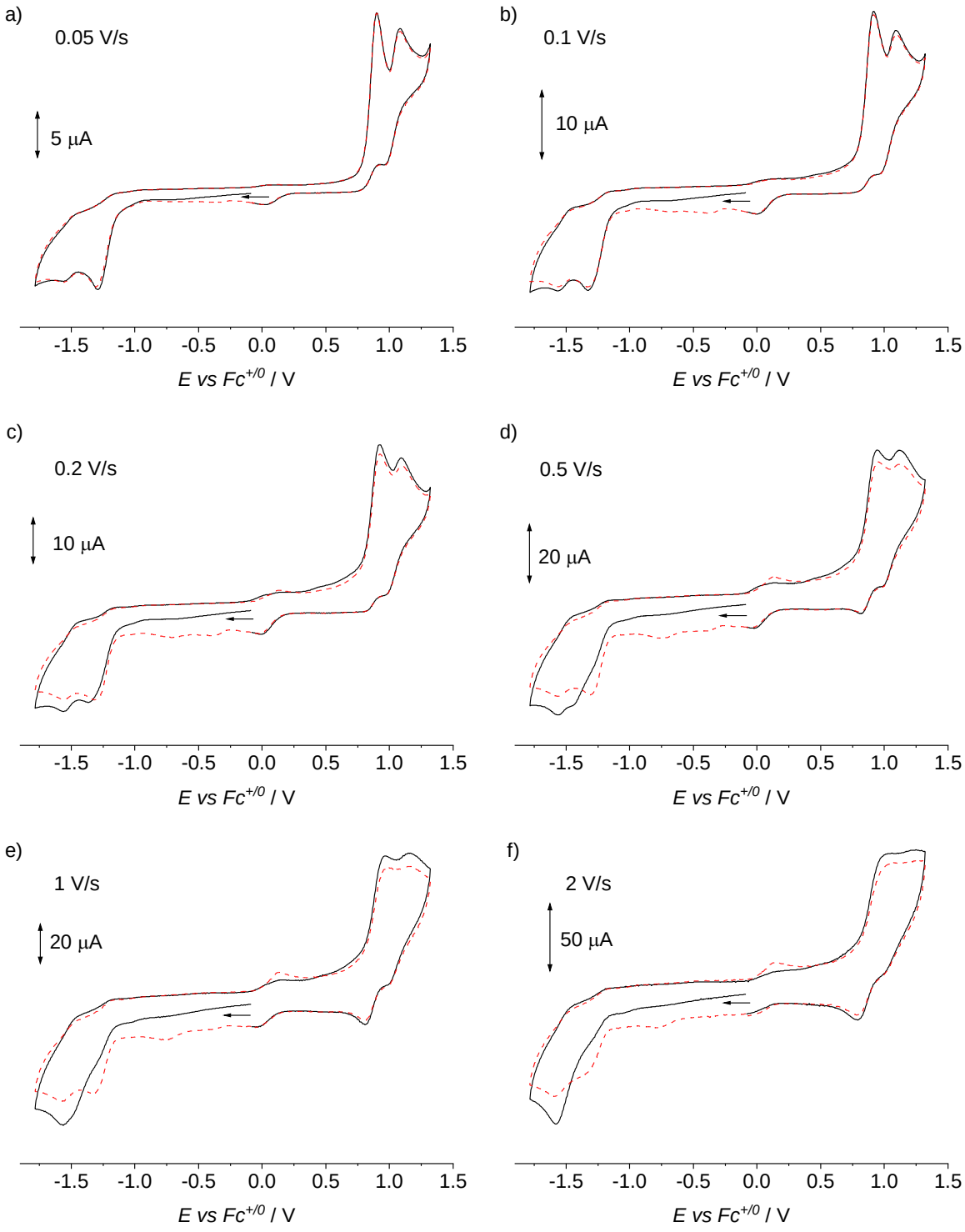

Figure 36. Cyclic voltammograms of complex **4** (1 mM) performed at differen scan rates (0.05, 0.1, 0.2, 0.5, 1 and 2 V/s for a-f, respectively) in CH_3CN 0.1 M $TBAPF_6$ at –35 °C using a glassy carbon working. All the measurements were scanned cathodically first starting from OCP; two cycles were completed (first cycle: black solid line, second cycle: red dashed line).

In a second experiment, the temperature was kept constant at −56 °C and the scans were performed at different rates. When the intensity of current of each scan was normalized by the square root of the corresponding scan rate, an interdependency of the two reductive waves was found (Figure 37). At 0.005 V/s the first reduction event was the only one recorded (red line) but increasing the scan rate caused a gradual disappearance of this first event in favor of the second wave, until only the reduction at lower potential was present at 0.1 V/s (blue line).

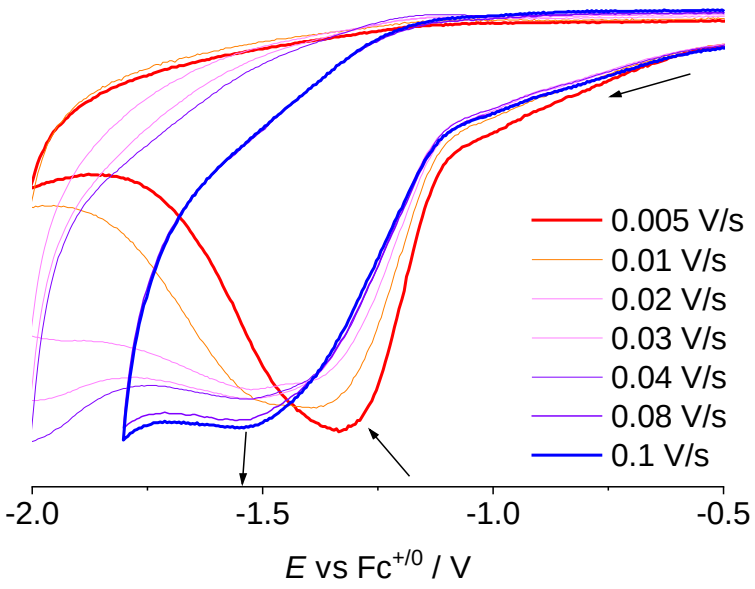

Figure 37. Excerpts of the cyclic voltammograms of complex **4** (1 mM) performed at scan rates increasing from 0.005 (red curve) to 0.1 V/s (blue curve) in EtCN 0.1 M $TBAPF_6$ at −56 °C using a glassy carbon working electrode. The intensity of current of each scan was normalized by the square root of the corresponding scan rate. All the measurements were scanned cathodically first, from 0.0 V.

When taken together, these experiments allow for the formulation of preliminary hypotheses to explain the experimental results. The fact that at fast scan rates, *e.g.*, 5 V/s at −35 °C, the second reduction at −1.57 V is the only one observed in the CV and that it shows no potential shift with higher scan rates suggests that the two reductions are not sequential but would rather belong to two different species in solution. The two compounds would therefore differ for the relative reduction potentials (*e.g.*, for the electron density on the Fe=O group). The interdependence shown in Figure 37 would imply that the two species are in equilibrium in solution, the position of which can be shifted by scan rate. Finally, the fact that higher scan rates only the lower potential reduction is present also implies that the equilibrium in solution lays predominantly on the side of the species responsible for this second reductive event.

Considering that the same behavior was observed for all three complexes **3**, **4** and **5**, both *in situ* prepared and from isolated and purified solid samples, a preliminary hypothesis regarding the nature of the equilibrium could involve a slow ligand dissociation process in nitrile solutions (Scheme 6). In the case of complex **4**, the two different species observed in solution would be the trifluoroacetate six-coordinated complex **4** itself, giving rise to the reduction at lower potentials, and a penta-coordinated tetracarbene oxoiron(IV) complex formed upon dissociation of the axial anion. The lower electron density on the Fe=O group of the latter complex would be responsible for its higher reduction potential. As expected, the position of the equilibrium would strongly lay on the side of the six-coordinated complex, but when lower scan rates are used, the consumption of traces penta-coordinated complex would drag the equilibrium toward the product of ligand dissociation, therefore provoking and increase of the intensity of the first reduction process, as observed experimentally.

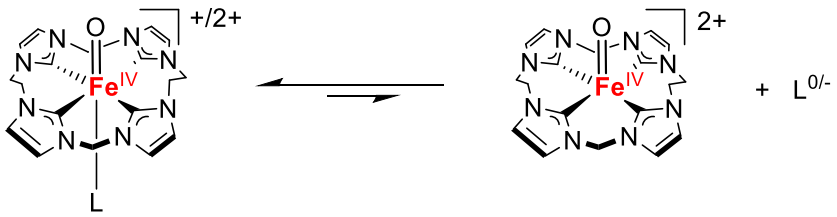

Scheme 6. Depiction of the proposed axial ligand dissociation equilibrium taking place in solutions of complexes **3**-**5**.

Testing the validity of this hypothesis will be of fundamental importance to fully explain the electrochemical behavior of the tetracarbene oxoiron(IV) complexes investigated herein. Moreover, it would be interesting to understand the reason behind the different behaviors observed in the case of the HAA reactivity, where the axial ligands seem to remain bound (or where the equilibrium seems to be slow enough to avoid formation of the more reactive penta-coordinated complex) and the electrochemical measurements reported in this section. To this regard, it would be advisable to design future titration experiments to explore the effect of addition of free axial ligand both on the peak potential of the first reductive wave and on the kinetics of HAA of complexes **4** and **5**.

4.6 Outlook

This chapter presented the investigation of the HAA reactivity performed by the anion-ligated complexes **4**–**6** toward different substrates at variable temperatures, and comparison to parent **3**. As predicted by theory, exchanging the axial CH_3CN ligand of complex **3** with trifluoroacetate (**4**),

chloride (**5**), and tert-butyl thiolate (**7**) caused contained differences in HAA reaction rates both at −40 °C and at 25 °C, although more significant than the theoretically predicted ones. However, follow-up reactivity of **4** and **5**, with generation of the tetracarbene-Fe^{II} complex **1** as final product, evidenced how coordination of an anionic axial ligand prevents the decomposition of the ferric hydroxo intermediates to the dimer μ-oxo complex **2**, as previously reported for **3**, and allows further reactivity with the organic substrate radical. Remarkably, the thiolate-bound complex **7** reacts with weak C–H bonds in a clean one-step HAA, generating a putative thiolate–Fe^{III}–OH intermediate that shows outstanding stability at −40 °C. This stability will allow for attempts of isolating this exciting intermediate, hopefully returning structural and electronic information about this unique example of a RS–Fe^{III}–OH complex.

Comparison of the second order reaction rates at 25 °C showed that coordination of activating anions *trans* to the oxo moiety in the tetracarbene system caused a decrease of the k_2' values of approximately one order of magnitude compared to the CH_3CN -coordinated parent **3**, contrary to what has been show for other oxoiron(IV) model complexes. This behavior suggests that while the HAA reaction proceeds through an axial ligand dissociation mechanism in the case of **3**, generating a penta-coordinated complex with increased reactivity, the axial anions remain bound during activation of C–H bonds in the case of **4**, **5** and **7**, justifying slower reaction rates.

Finally, cryo-electrochemical analysis of solutions of **3**, **4** and **5** evidenced the presence of an equilibrium in nitrile solutions of the oxo-complexes. Initial hypothesis on the nature of the equilibrium could involve an axial ligand dissociation process. However, the position of the slow equilibrium is shown to lay predominantly on the exa-coordinated complex side, compatible with the results of the HAA rates investigations.

Overall, this complex series provides a basis to get additional insight on the nature of the tetracarbene complexes, for which the equatorial macrocycle seems to affect the electronic structure granting additional peculiarities depending on the axial ligation. A comprehensive understanding of these new phenomena would help expanding the horizon of processes involved in the HAA reactivity of non-heme oxoiron(IV) model complexes.

5. Insight into the Disproportionation Equilibrium of 2 and Gas-Phase OAT Reactivity of 3: a Nucleophilic Fe=O Group

This chapter has been partially adapted from: Cordes, C.; Morganti, M.; Klawitter, I.; Schremmer, C.; Dechert, S.; Meyer, F. Disproportionation Equilibrium of a μ-Oxodiiron(III) Complex Giving Rise to C−H Activation Reactivity: Structural Snapshot of a Unique Oxoiron(IV) Adduct. *Angew. Chem. Int. Ed.*, **2019**, *58* (32), 10855–10858. DOI: 10.1002/anie.201900683.

5.1 Introduction and Previous Results

The previous chapter provided insight into the HAA reactivity of the oxoiron(IV) complexes **4**, **5** and **7** of the tetracarbene macrocycle under the effect of different axial ligands. Likely, coordination of an anionic group promoted the follow-up rebound/desaturation mechanism by avoiding the accumulation of the stable μ-oxo dimer **2**, which is the end-product of the C–H bond activation by complex **3**. Decomposition to stable oxo-bridged dimers is in fact the common final stage of the catalytic processes involving highly reactive heme- and non-heme iron complexes as found both in natural enzymes, in synthetic models and catalysts.[194–199] These dimeric complexes, often inert under aerobic conditions, have been widely investigated as starting points for oxygenation of substrates in presence of external oxidants, or as catalysts for acylation reactions.[200–212] More recently, photoexcitation proved to be a convenient strategy to activate the ferric oxo-bridged dimers towards oxidation reactivity.[213,214] Previously, our group has shown that complex **2** was able to activate the weak C–H bonds of DHA without addition of external oxidants and demonstrated that it is able to do so thanks to a disproportionation equilibrium that generates complexes **3** (the active species that performs HAA) and **1** in CH_3CN at room temperature. This hypothesis was verified by ^{1}H-NMR monitoring of the reaction of **2** with DHA, that proceeded to the quantitative formation of anthracene and complex **1** over the course of several weeks, according to the mechanism shown in Figure 38.[146,215]

Although the reaction rates were shown to be rather sluggish, the finding provided insight into the possibility of avoiding the HAA reactivity dead-end by the use of the unique tetracarbene ligand. However, some questions remained unanswered. Additional experiments were needed to understand the nature of the disproportionation equilibrium, to further support its presence and to shine light onto its mechanism. To this extent, parts of the experiments reported below were performed in collaboration with Dr. Cordes and Claudia Schremmer, both former members of our group.

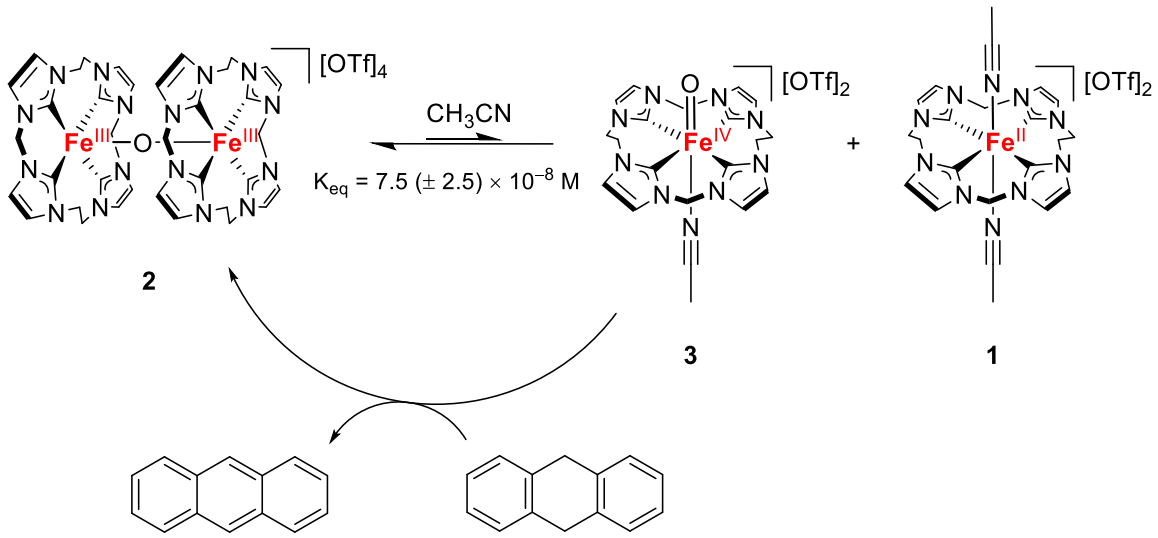

Figure 38. Scheme of the disproportionation equilibrium of complex **2** in CH_3CN that gives rise to HAA reactivity on DHA via the formation of the reactive oxoiron(IV) complex **3** and the ferrous complex **1**.

Studies of OAT reactivity in solution evidenced the inertness of **3** towards typical substrates, suggesting a strong nucleophilic nature of the Fe=O moiety.[146] Numerous reports on the OAT reactivity of N-ligated non-heme analogues of complex **3** demonstrate in fact that the rates of the two-electron reaction with oxo-accepting substrates directly correlated with the electrophilicity of the Fe=O moiety in what has been named "electrophilic trend".[82,96,101] Moreover, the oxyl radical character of the oxo group has been directly linked to OAT reactivity, showing that its absence is responsible for the kinetic inertness of some metal-oxo complexes.[216,217] Despite a significant degree of oxyl character calculated for **3**, the complex was able to activate only the very oxophilic trimethylphosphine with appreciable rates, while it was inert towards thioanisole or styrene in CH_3CN at –40 °C.[110,146,179] Therefore, the apparent nucleophilicity of the tetracarbene oxoiron(IV) complex had to be attributed to the unique electronic structure deriving from the effect of the strong equatorial donation.

In order to confirm this assumption, gas phase reactivity analyses could provide a suitable mean to remove any matrix interactions and to explore the intrinsic reactivity of complex **3** towards OAT substrates, as will be presented in section 5.5.

In addition to the mechanistic evidence for the disproportionation equilibrium of **2**, this chapter discusses the results of said gas-phase OAT studies on complex **3** and the structural characterization of an unprecedented adduct that constitutes a snapshot of the disproportionation mechanism and experimental support for the nucleophilicity of **3**.

5.2 Further Insights Into the HAA Reactivity of 2

In order to determine whether the disproportionation of **2** into **3** and **1** at room temperature is caused by light excitation, the HAA reaction with DHA at room temperature was monitored both under ambient light conditions and in complete darkness, acquiring ^{1}H-NMR spectra at regular time intervals over the course of more than two weeks and recording the integral values (normalized by an internal standard of 1,3,5-trimethoxybenzene) of signals corresponding to **2**, **1** and anthracene. To this extent, CD_3CN solutions of complex **2** were treated with 7 equivalents of DHA and left reacting in two different NMR tubes, one of which was kept under ambient light and the other one under complete darkness for the full course of the reaction.

As shown in Figure 39, no significant difference in the integrals time traces of the decay of **2**, the formation of **1** or anthracene was found between the two sets of experiments. This confirmed the presence of a rare thermal disproportionation equilibrium, rather than a light driven one, that generates reactive **3** and **1**.

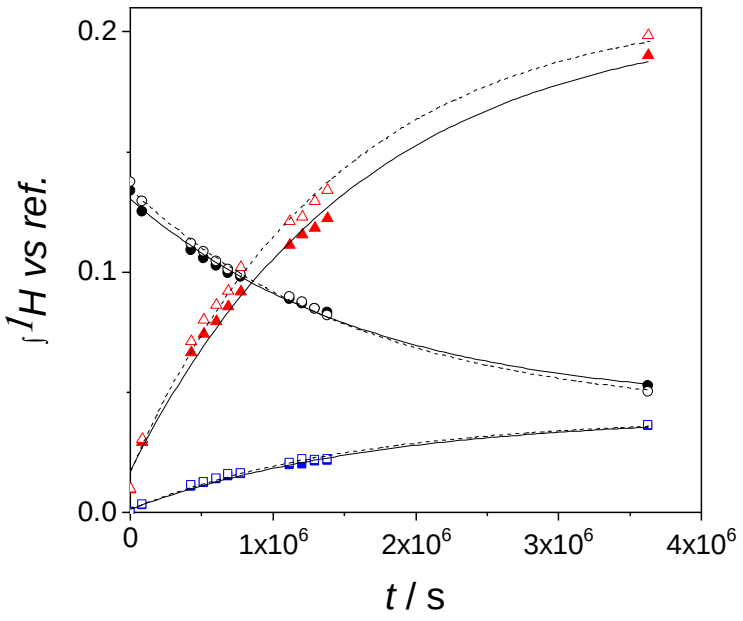

Figure 39. Time traces of ^{1}H-NMR integrals showing the consumption of complex **2** (black circles), the formation of anthracene (blue squares) and complex **1** (red triangles) during the reaction of **2** with 7 equivalents of DHA in deuterated CH_3CN at room temperature. The reaction was performed in complete darkness (full symbols and solid lines) and under ambient light conditions (empty symbols and dashed lines) and integrals were referred to an internal standard of 1,3,5-trimethoxybenzene,

A possible explanation for the presence of such disproportionation in nitrile solvents was proposed in the dissertation of Dr. Cordes, after theoretical calculations that were performed to elucidate the

electronic structure of complex **2**. The pentacoordinated ferric ions were calculated as having an intermediate $S = 3/2$ spin state, allowed by the square pyramidal geometry.[218] The calculated molecular orbital scheme of the ferric centers showed the presence of a singly occupied slightly antibonding d_{z^2} orbital, that provided a justification for the absence of a second axial ligand on the iron centers (Figure 40).[146]

In light of these results, it was proposed that coordination of a nitrile molecule on the axial position *trans* to the μ-oxo moiety would populate an antibonding orbital and significantly decrease the Fe–O bond order, thereby triggering the disproportionation of **2** to **3** and **1** that would allow for subsequent HAA reactivity.

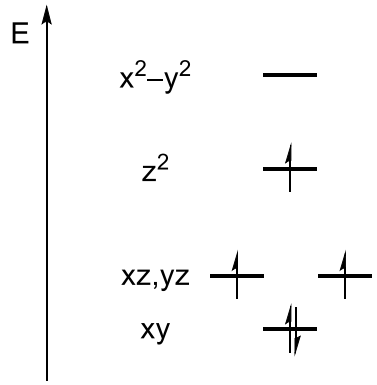

Figure 40. Energy splitting of the d orbitals of the iron ions in complex **2**, as calculated in reference [146].

5.3 Scrambling Experiments in Different Nitrile Solvents

To support the hypothesis of a disproportionation equilibrium triggered by solvent coordination on complex **2**, we designed a suitable experiment exploiting the possibility of detection of the complex via mass-spectrometry. In a related project, our group previously reported an analogous Fe^{III}–O–Fe^{III} tetracarbene complex $\mathbf{2^{Me}}$ where the backbone of the imidazole-2-ylidene moieties is methylated in positions 4 and 5.[164] The work of Claudia Schremmer showed that $\mathbf{2^{Me}}$ could also be characterized by mass spectrometry and disproportionated into the corresponding Fe^{II} and oxoiron(IV) monomers upon ES ionization.

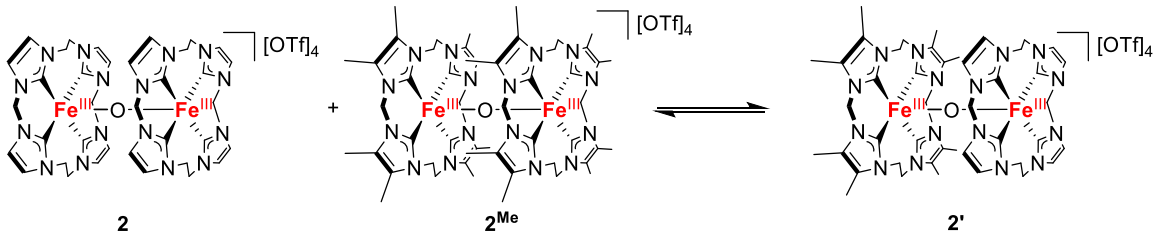

Figure 41. Scrambling equilibrium between complex **2** and the methylated analogue complex **2^{Me}** as hypothesized in nitrile solutions.

Assuming the presence of a disproportionation equilibrium similar to the one of **2** for the methylated analogue, a mass-spec analysis of an CH_3CN solution containing equimolar mixtures of **2** and **2^{Me}** was carried out at regular time intervals after the initial mixing of the two complexes.

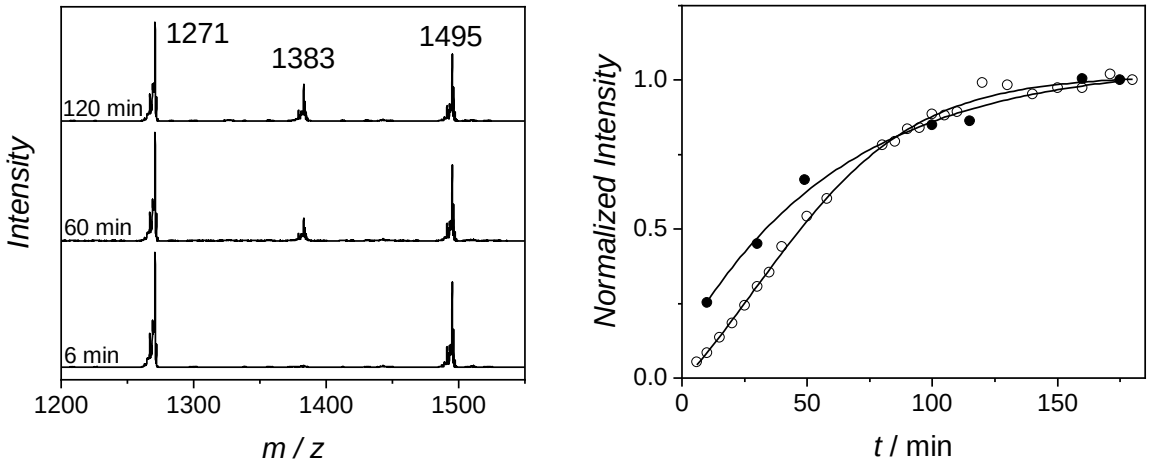

Figure 42. Left: time evolution of the ESI(+)-MS spectra of an equimolar mixture ($4.3 \cdot 10^{-2}$ mM) of complexes **2** and **2^{Me}** in butyronitrile at room temperature. Right: timetraces of the intensity of the peak at *m/z* 1383 (corresponding to the scrambled complex) normalized by the final value at 180 minutes from mixing in butyronitrile (empty circles) and CH_3CN (full circles).

The initial spectrum (Figure 42, left, lower spectrum) showed the exclusive presence of both **2** and **2^{Me}**, as evidenced by the presence of ions at *m/z* 1271 and 1495, respectively. However, the appearance of a third intermediate signal over approximately 240 minutes suggested the presence of an ongoing process. Indeed, the *m/z* ratio of 1383 corresponded to the formation of a scrambled Fe^{III}–O–Fe^{III} complex **2'** in which only one of the tetracarbene ligands is methylated on the backbone, supporting the establishment of the disproportionation equilibria in solution for both μ-oxo complexes as prerequisite for the scrambling.[215]

Recalling the hypothesis according to which the breaking of the Fe–O bond would be triggered by coordination of a nitrile molecule,[146] it is reasonable to expect that the exposure to ligands with

stronger donation abilities would shift the disproportionation equilibrium towards the monomers, thereby allowing for a faster scrambling of complexes **2** and **2^{Me}**. In order to test this hypothesis, the MS experiment was repeated using butyronitrile (PrCN) as solvent, comparing the time traces of the formation of the scrambled complex with the previous experiment in CH_3CN, as shown in Figure 42 (right). In fact, the longer aliphatic chain of PrCN increases the σ-donation properties due to the increased inductive effect of the additional $-CH_2-$ fragment. Unfortunately, only limited differences compared to CH_3CN were recorded in the scrambling process, and both reactions were completed after approximately three hours. A possible explanation could be found in the contained variation in σ-donor strength of the two nitriles, possibly not large enough to cause a detectable difference. Moreover, the very low solubility of complexes **2** and **2^{Me}** in stronger nitrile donors (isopropylnitrile or tert-butylnitrile) prevented any additional experiment in this regard. Hence, an evidence for the hypothesized scrambling mechanism had to be found elsewhere, as shown in next section.

5.4 Structural Analysis of a Unique Fe^{IV}=O-Fe^{III}-O-Fe^{III} Adduct

In an additional scrambling experiment performed by Dr. Cordes, complex **3** and **2^{Me}** were mixed in CH_3CN at −30 °C and mass-spectrometry analyses revealed the formation of the scrambled dimer **2'**.[215] In this case, the cleavage of the Fe−O bond of **2^{Me}** was attributed to the attack from the oxygen atom of **3** to an Fe^{III} center of the dimer, with formation of the scrambled product and a putative oxoiron(IV) complex of the methylated tetracarbene ligand. This hypothesis was in fact coherent with the nucleophilicity of complex **3**, that would explain the interaction of the oxo atom with a ferric center of the μ-oxo dimer. Nevertheless, spectroscopic analyses performed on mixtures of oxoiron(IV) complexes and μ-oxo dimers could not provide any additional evidence to support the validity of the mechanistic hypothesis.

However, when Et_2O was allowed to diffuse into an CH_3CN mixture of **3** and **2** at −35 °C, crystallization of a unique adduct (**10**) of the two complexes allowed for the structural characterization of an adduct that represents a snapshot of the scrambling process (Figure 43).

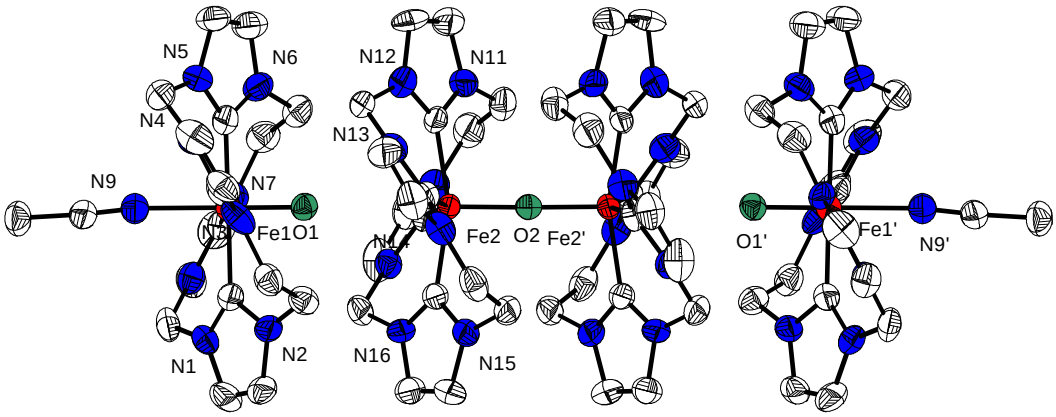

Figure 43. Molecular structure of the cation of **10** shown as 50% thermal probability ellipsoids. Hydrogen atoms, counteranions and crystallization solvent molecules were omitted for clarity. Selected bon lengths [Å] and angles [°]: Fe1–N9 2.069(6), Fe1–O1 1.673(4), O1–Fe2 3.193(5), Fe2–O2 1.7685(9), O2–Fe2' 1.7685(9), Fe2'–O1' 3.193(5), Fe1'–N9' 2.069(6); N9–Fe1–O1 179.4(4), Fe1–O1···Fe2 178.2(3), Fe2–O2–Fe2' 179.7(8), Fe2'···O1'–Fe1' 178.2(3), O1'–Fe1'–N9' 179.4(4).

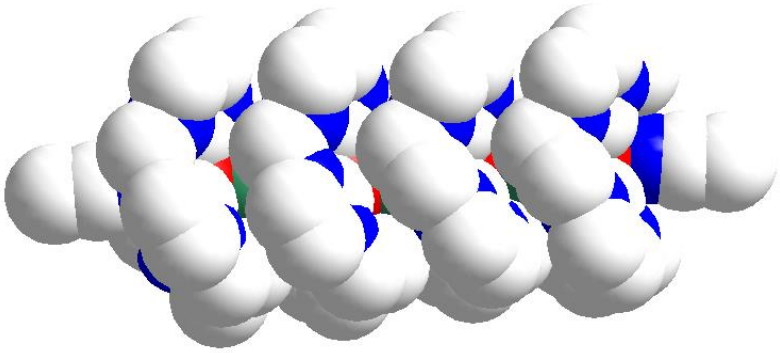

Figure 44. Space filling model of the molecular structure of **10** that evidences the close packing of the four subunits.

Adduct **10** is constructed by the lateral interaction of two Fe=O units of **3** with the iron centers of a central molecule of complex **2**, as shown in Figure 43. The four ligand subunits are closely packed by dispersive interaction in a cylindrical arrangement around the Fe–O bonds, that are arranged in a quasi-linear fashion. The two lateral Fe^{IV}=O units orient the macrocyclic ligand to match the alternate pattern of the central dimer, where the ethylene bridges of one tetracarbene macrocycle are stacked upon the methylene bridges of the other. The interaction between the lateral oxo moieties and the iron(III) centers (O1···Fe2 and O1'···Fe2'), with a distance of 3.19 Å, are weak enough to allow for the unambiguous assignment of the identity and oxidation states of the various subunits. Indeed, the integrity of the three different subunits is confirmed by analysis of the respective Fe–O distances: the Fe^{IV}=O bonds (Fe1–O1 and Fe1'–O1') show a distance of 1.673(4) Å, just slightly longer than in the parent **3**, while the central Fe–O–Fe bonds of 1.769(2) Å are

elongated by only 1.7 Å compared to **2**.[109] The elongation of the Fe^{IV}=O bond upon interaction with a cationic metal center has been shown by several examples in literature, although the majority of them reported cases of interactions between oxoiron(IV) complexes and inert metals used as Lewis acids.[147,219] In conclusion, the structural characterization of the adduct provided an evidence for the high nucleophilicity of complex **3**, that allows for direct attack on a ferric ion of **2** as a trigger of the disproportionation reaction.

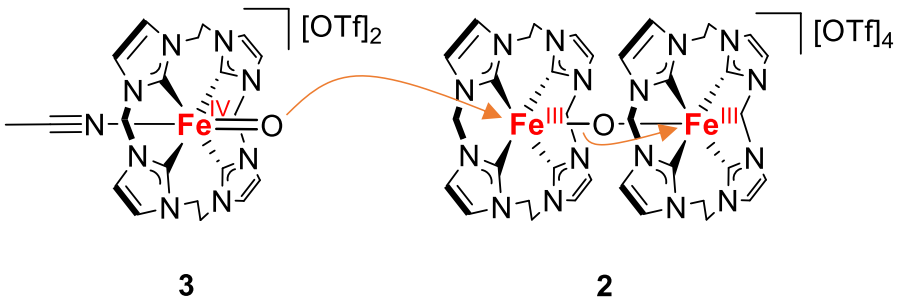

Figure 45. Schematic representation of the scrambling process upon attack of complex **3** on the dimeric μ-oxo complex **2**, as supported by the structural characterization of adduct **10**.

5.5 OAT Reactivity Studies of 3 via FT-ICR Mass Spectrometry Measurements

The FT-ICR technique

In order to evaluate the reactivity of **3** towards OAT substrates in absence of solvents or other matrix interactions, and to confirm its intrinsic nucleophilicity, our group has established a collaboration with the research group of Professor Fornarini of the University La Sapienza in Rome (Italy), where FT-ICR mass spectrometry measurements were performed.

The FT-ICR is a mass spectrometry detector set-up that allows for the simultaneous determination of the mass-to-charge ratio of a mixture of ions generated with an ionization apparatus, based on the cyclotron frequency that the different ions show when immersed in a fixed magnetic field under extremely high vacuum conditions. After ionization, the ions are selected via several concatenated multipoles, before being injected into a collision cell where they can be reacted with substrates in the gas phase, and hence in absence of any solvent or matrix. The mixture of product ions is then transferred under extreme vacuum into a Penning trap. Here, the ions are immersed in a strong magnetic field and kept in circular motion with orbits of a given cyclotron radius and a constant cyclotron frequency that depend on their *m/z* ratio. When a radiofrequency of appropriate energy

and orthogonal to the applied magnetic field is irradiated, the ions with a corresponding *m/z* ratio are excited to a higher cyclotron radius. By scanning the irradiated frequency, the detector causes all ions to reach their maximum cyclotron orbit, where they coalesce into "packets", each containing all ions of a given *m/z* ratio. The maximum cyclotron orbit allows the ions to pass close to electric plates that detect the charge induced by the passage of ion "packets" in front of them, and when the radio frequency is switched off, the ions start to decay back to the initial cyclotron orbits in spiraling motions. Since the cyclotron frequency depends on the *m/z* ratio of each ion type, the plates will record oscillating electric currents deriving from the superposition of the motions of each packet of ion, each with a different cyclotron frequency. The detector plates record the decay through the cyclotron orbits and a Fourier-Transform allows the determination of the *m/z* ratio of each "packet" of ions.[220]

FT-ICR has been successfully employed by the group of Prof. Fornarini to study the reactivity of a naked Cpd-I model constructed by ozonolysis with a protoporphyrin-IX iron complex, the reactivity of a Cpd-I model (tetrakis(pentafluorophenyl)porphyrin-$Fe^{IV}O$) and the axial ligand effect on a manganese(V)-oxo porphyrin complex, among other applications.[221–226]

FT-ICR reactivity analyses of complex 3

The set-up was used to study the gas-phase reactivity of complex **3** with NO, allyl acetate and thioanisole, all substrates capable of accepting an oxygen atom. Given the instability of **3** in the conditions of the injection (room temperature and under atmospheric conditions), the corresponding ions were generated by ESI of a sample of complex **2**, which disproportionates to ions corresponding to **3** and **1** in the ionization process.[215] The ions with a *m/z* ratio of 210.058^{2+} (**3**') corresponding to the molecular ion of **3** upon loss of the triflate counterions and the coordinated CH_3CN were mass-selected via the multipoles and then injected in the collision chamber, where the reaction with the substrate was allowed to proceed with different times ("pumping delay") between 5 and 100 seconds. In case of OAT reactivity, the transfer of the oxygen atom to the substrate was expected to generate a molecular ion at *m/z* 202.06^{2+} corresponding to a tetracarbene-Fe^{II} square planar ion (**1**'). Figure 46 shows the mass-spectra of the three different reaction mixtures with NO, allylacetate and thioanisole (in the latter case the reaction was not performed on the mass-selected *m/z* 210.058^{2+} ion, but on the mixture of ions obtained by ESI of **2**, due to experimental constraints. Hence no direct evidence of OAT reactions could be confirmed/excluded in this case).

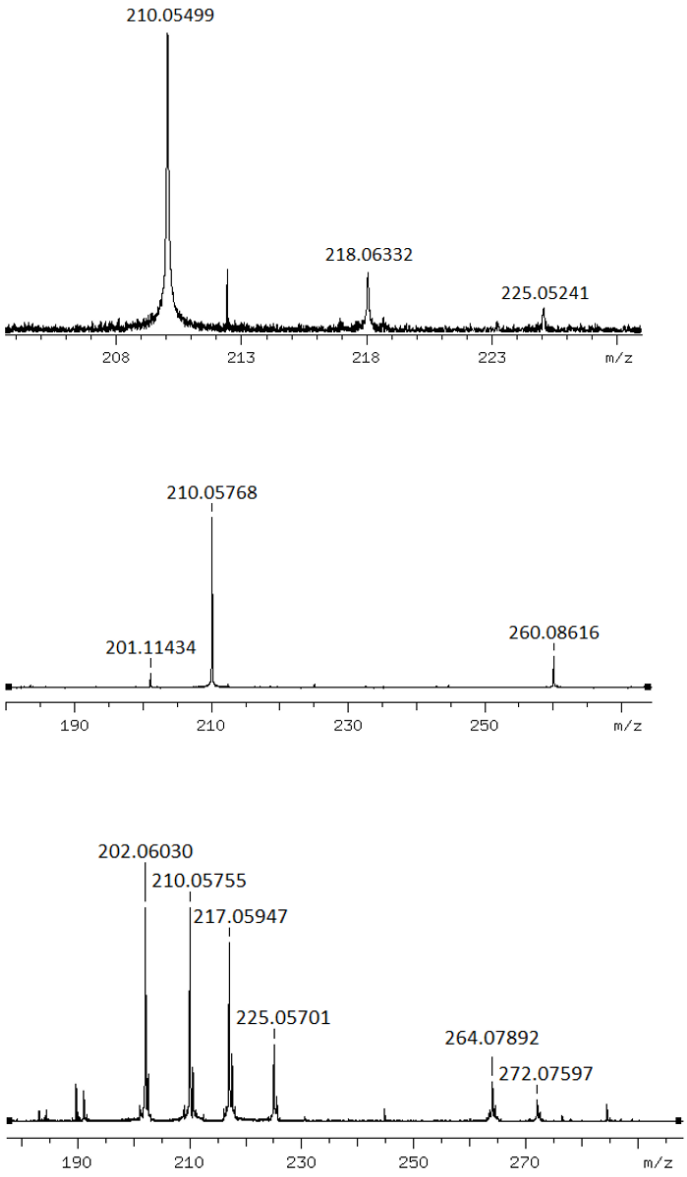

Figure 46. Top: MS spectrum of the product mixture resulting from treatment of the isolated molecular ion at *m/z* 210.05 with NO using a pumping delay of 50 s. Middle: MS spectrum of the product mixture resulting from treatment of the isolated molecular ion at *m/z* 210.05 with allylacetate using a pumping delay of 30 s. Bottom: MS spectrum of the reaction mixture (plasma) of the ionization products of **2** treated with thioanisole with a pumping delay of 30 s.

Evidently, neither the reaction mixture with NO nor the one with allylacetate showed the molecular ion associated with loss of the oxygen atom from the complex, underlying once again the extremely poor oxygen atom transfer abilities of complex **3** and the stability of the Fe=O bond even in absence of matrix interactions. Interestingly though, all the reaction mixtures showed molecular ion peaks of adducts between **3'** and the corresponding substrate: the peak at *m/z* 225^{2+} corresponds to a **3'**-NO adduct, the one at 260^{2+} to a **3'**-allylacetate adduct and the one at 272^{2+} to a **3'**-thioanisole adduct.

Mass-selecting the adduct ions after their formation allowed for an attempt to force OAT reactivity exploiting collision induced dissociation (CID) experiments for the adducts with allylacetate and thioanisole. However, even when forcefully dissociated, the adduct ions returned the intact **3'** dication, with no sign of **1'** (Figure 47).

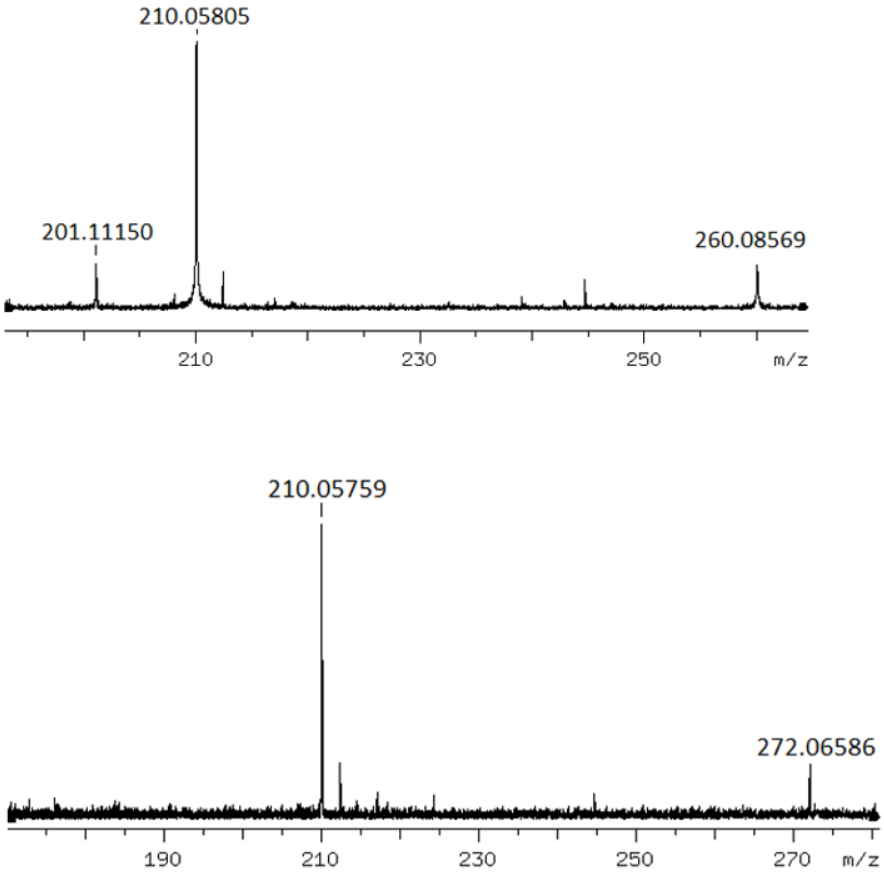

Figure 47. Mass spectra deriving from CID experiments on the mass-selected **3'**-allylacetate (top) and **3'**-thioanisole (bottom) adduct ions.

In conclusion, the lack of OAT reactivity in the gas phase confirmed that complex **3** possesses a distinctive nucleophilic character imparted by the peculiar tetracarbene ligation and ruled out a possible influence of solvent or matrix interaction on this behavior.

5.6 Conclusions and Outlook

This chapter provided insight into the disproportionation mechanism of the μ-oxo dimer complex **2** into **3** and **1** with a variety of tailored experiments. Oxidation of DHA to anthracene performed in CH_3CN at RT both under ambient light conditions and in the dark confirmed the thermal nature of the disproportionation equilibrium, that is unaffected by light irradiation, in contrast to previously reported examples. A series of scrambling experiments with the methylated analogous of **2** (**2^{Me}**) allowed for the formulation of an hypothesis regarding the mechanism of the disproportionation, that can be triggered both by axial coordination of nitrile molecules and by attack of complex **3** on the ferric dimer. The latter was supported by the structural characterization of a unique and unprecedented $Fe^{IV}O–Fe^{III}–O–Fe^{III}–OFe^{IV}$ adduct (complex **10**), that constitutes the structural snapshot of the disproportionation-scrambling reaction. The postulated nucleophilicity of **3**, responsible for the formation of the adduct and for the lack of OAT reactivity in solution, was confirmed by FT-ICR experiments in the gas phase: isolated ions corresponding to **3** showed no reactivity with typical OAT substrates even under exclusion of matrix interactions, therefore owing to an intrinsic low electrophilicity of the tetracarbene oxoiron(IV) complex.

6. Redox and Spin States Series of a New Organometallic Heme Analogue

6.1 Introduction and Aim of the Project

Previous chapters and related works clearly evidenced the special features the tetracarbene ligation provides when bound to a central iron atom. The equatorial NHC donation, the strong ligand field and the electronic properties of the derived complexes provided the basis for unique electronic structures and reactivity models, as exemplified by the oxoiron(IV) complexes **3**–**5** and **7** and the $\{FeNO\}^x$ series investigated by Dr. Cordes.[146] Combining the electronic effects with the ability of NHCs to stabilize metal complexes in unusual oxidation states is indeed one of the most fruitful strategies that has been exploited to synthesize new catalysts for synthetic and industrial applications.[135,227,228] Therefore, in the last decades scientists devoted great amounts of effort to synthesize a variety of multidentate hybrid ligands and complexes containing both NHC and heteroatoms as donors, in an attempt to obtain intermediate properties and fine tune the reactivities of the related complexes.[123,130,131] As introduced in Chapter 1 these new hybrid systems were successfully employed both as catalysts and as enzymatic models, quickly establishing the popularity of the hybrid approach.

Given the successful chemistry of the tetracarbene-iron complexes, the design of a hybrid macrocycle bearing both NHC and nitrogen-donors appears to be an attractive way to bridge the differences between heme models and complexes **1**-**7**. Therefore, the design efforts were focused on integrating all the typical features of porphyrin ligands into a novel non-heme hybrid structure: the anionic character of the coordinating ligand, an extended degree of electron delocalization, an intermediate ligand field strength that would allow for spin state variations of the complexes and a redox-non innocent moiety. Inspired by the work of the Kunz research group, our group opted for the "**bimca**" scaffold as initial building block that provides two NHC moieties *trans* to each other and a carbazole backbone that acts as anionic *N*-donor and as potential redox non-innocent fragment.[133,134] Successful macrocyclization of the tridentate precursor with 2,6-dibromomethylpyridine to obtain proligand **[11H$_3$][Br]$_2$** was evidenced by mass spectrometry and ^{1}H-NMR analyses (Scheme 7).[146]

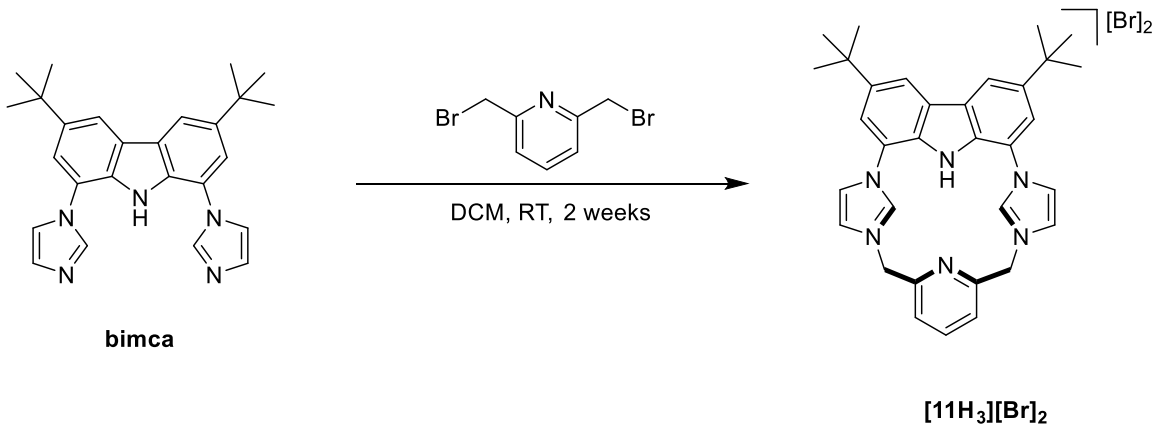

Scheme 7. Synthesis of pro-ligand **[11H$_3$][Br]$_2$** as proposed in the dissertation of Dr. Kupper (Ref. [146]).

However, low yields and reaction times longer than two weeks constituted drawbacks that needed to be addressed. This chapter reports the optimized synthesis of the hybrid macrocycle [**11H$_3$**]$^{2+}$, the synthesis of its low-spin and intermediate-spin ferrous complexes and the products of their one- and two-electron oxidations, together with the thorough electronic structure determination of all products, aimed at demonstrating the ability of the new non-heme hybrid system to efficiently mimic heme analogues in electronic structure as well as redox and magnetic properties.

6.2 Ligand Design and Characterization

As mentioned in Section 6.1, preliminary results on the synthesis of the target macrocycle were reported in the dissertation of Dr. Kupper. In the initial attempts, a mixture of **bimca** and 1,2-dibromomethylpyridine in DCM was stirred at room temperature for 10 days. NMR and mass spectrometry provided evidence for the formation of **[11H$_3$][Br]$_2$**. Therefore this approach served as starting point for the optimization of reaction conditions performed herein.

Initial variations of the concentration of the reagents in DCM led to an increasing of side reactions products when higher concentrations were used, as expected for a macrocyclization reaction. In order to shorten the reaction times and to obtain the products via a more selective macrocyclization, CH_3CN was chosen as a solvent and the reaction was performed at high temperatures. Equimolar amounts of **bimca** and 1,2-dibromomethylpyridine were mixed in dry and degassed CH_3CN under inert atmosphere, and the mixture was heated to reflux for several days, regularly monitoring the reaction via NMR spectroscopy. After 48-72 hours the reaction reached completion and a scarcely soluble white precipitate appeared in the reaction mixture. Isolation of the solid via filtration and washings with DCM afforded a sparingly soluble off-white solid, the ^{1}H-NMR and MS spectra of which matched with the ones obtained previously, confirming the identity of **[11H$_3$][Br]$_2$**.

The product showed very little solubility in most organic solvents, rendering further characterization and purification challenging and therefore requiring a counteranion exchange from bromide to triflate to improve solubility. Two equivalents of silver triflate were added to a white suspension of **[11H$_3$][Br]$_2$** in methanol. Formed solid AgBr was removed by filtration and the solvent was evaporated from the filtrate. **[11H$_3$][OTf]$_2$** was obtained as an off-white solid (Scheme 8). The product, now well soluble in polar organic solvents, was then purified by recrystallization with diethyl ether from CH_3CN solutions.

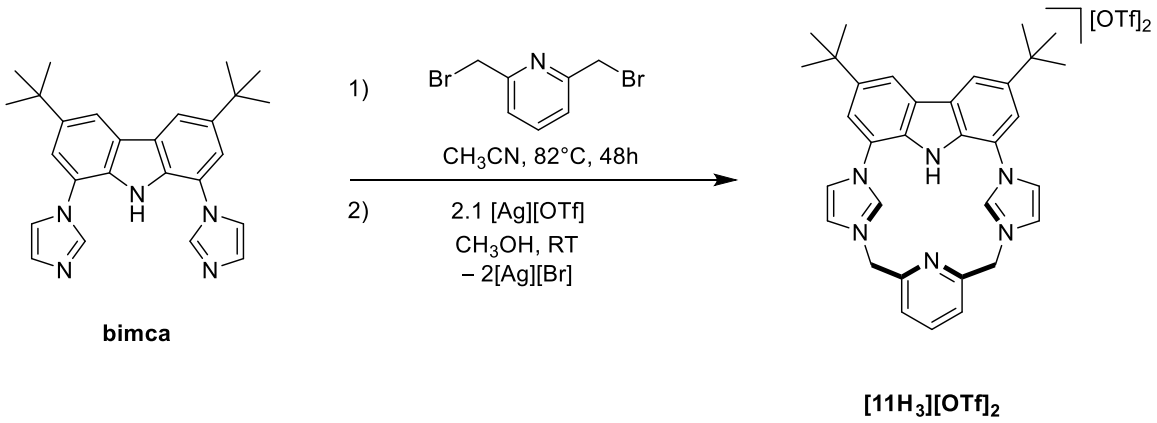

Scheme 8. Optimized procedure for the synthesis of pro-ligand **[11H$_3$][OTf]$_2$** from **bimca** and 2,6-dibromomethylpyridine.

Analysis of a CH_3CN solution of **[11H$_3$][OTf]$_2$** by ESI mass spectrometry revealed three main signals in the positive ion mode spectrum at *m/z* 667, 517 and 259, corresponding to [{**[11H$_3$][OTf]**}$^+$+2H], [**[11H$_3$]**$^+$+H] and [**[11H$_3$]**$^{2+}$+2H] (Figure 48, simulations in the Appendix). A CID analysis on the isolated peak at *m/z* 667 led to the formation of the ion at *m/z* 517, proving the identity of the analyte.

Slow diffusion of diethyl ether in a concentrated CH_3CN solution of **[11H$_3$][OTf]$_2$** afforded colorless single crystals suitable for X-ray diffraction measurements (the corresponding dication is shown in Figure 49). The cation **[11H$_3$]$^{2+}$** shows C_S symmetry in the solid state and crystallizes in the monoclinic space group $P2_1/n$. In accordance with previously reported di-*N*-substituted **bimca** molecules, the macrocycle arranges in an overall concave shape, with the plane of the carbazole slightly distorted by the steric strain of the macrocyclic ring. The two imidazolium groups and the pyridine point out from the plane of the carbazole, with angles of 56.7, 49.7 and 38.1° respectively, and the two six-membered rings of the carbazole form an angle of 6.2° with respect to each other. The hydrogen atom bound to N_{carb} shows a short contact with a triflate molecule, which sits in the cavity of the macrocycle (Figure 49 right).

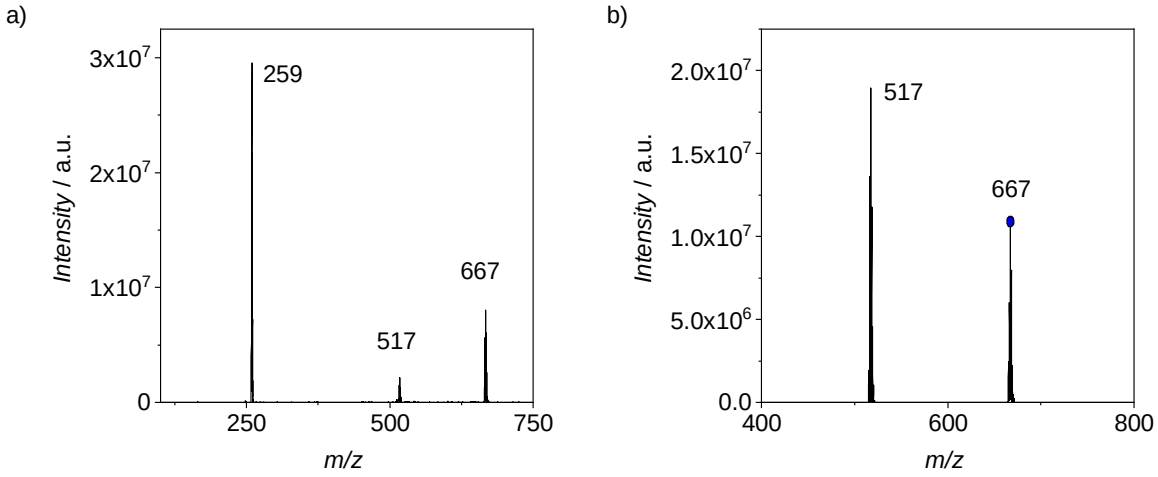

Figure 48. ESI(+)-MS spectra of an CH_3CN solution of pro-ligand **[11H$_3$][OTf]$_2$**. Left: full spectrum; right: CID experiment on isolated molecular ion at *m/z* 667.

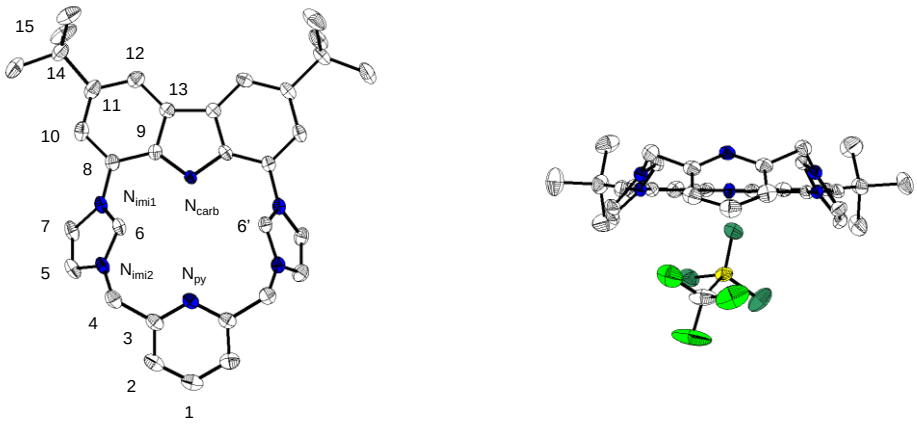

Figure 49. Molecular structures of the dication of pro-ligand **[11H$_3$][OTf]$_2$** drawn as 50% probability thermal ellipsoids. Left: viewed perpendicularly to the carbazole plane. Counterions, hydrogen atoms and crystal lattice solvent molecules are omitted for clarity. Right: view parallel to the carbazole plane. One of the triflate molecules, which shows short contact with the N_{carb}–H group, is reported. Other counterions, solvent molecules and hydrogen atoms are omitted.

NMR analyses of **[11H$_3$][OTf]$_2$** were performed in DMSO-d6. Room temperature ^{1}H-NMR spectra (Figure 50) showed apparent C_{2v} symmetry, as evidenced by the singlet at 5.59 ppm integrating for four protons, assigned to the $-CH_2-$ linkers in position 4 and 4'. This suggested a fast dynamic process in solution, in which the pyridine and the imidazolium groups flip rapidly, bringing N_{py} and C6/6' from above and below the plane of the carbazole, and resulting in an average planar structure. The protons in position 10 and 12 resonate at 8.57 and 7.81 ppm, being slightly shifted compared to the **bimca** precursor, while the ones in position 6 and 6' expectedly resonate at low fields (10.01 ppm).[135] Even more low field shifted is the N_{carb}–H proton, which appears at 11.30 ppm.

Surprisingly, a signal integrating for 2 protons is missing in the spectrum: only one doublet integrating for 2 protons is present at 8.30 ppm, that could be assigned at either couple of protons in 5/5' or 7/7' (see Appendix for the full list of 2D NMR experiments), while the other putative doublet does not appear. A look at the ^{13}C-NMR spectrum (see Appendix) reveals a triplet at 122.9 ppm, slightly distorted by the overlap with other signals. Protons of the backbone of imidazolium groups usually appear in this region, and the presence of a triplet suggests a rather unusual H/D exchange taking place in solution, involving the deuterated solvent.

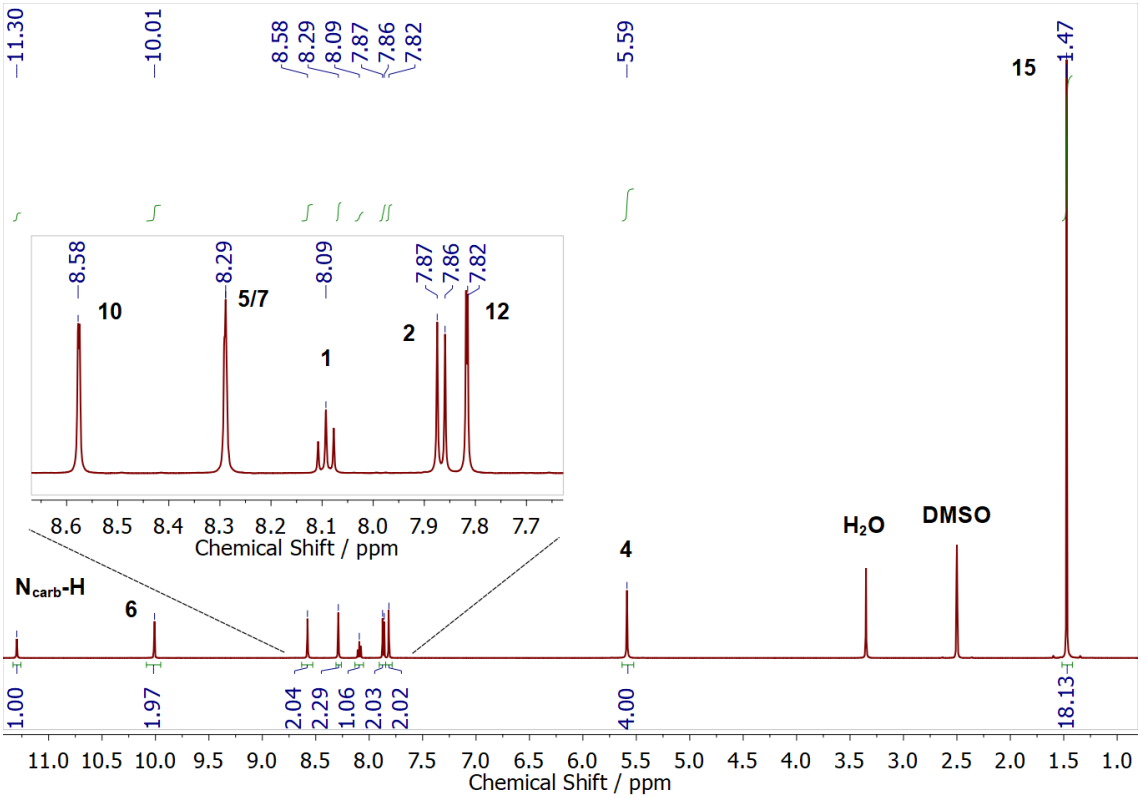

Figure 50. ^{1}H-NMR spectrum of a solution of **[11H$_3$][OTf]$_2$** in DMSO-d6 at RT. Bold black numbers refer to the position of the proton in the structure as shown in Figure 49 left. Each peak is assigned to the couple of protons in corresponding positions denoted with X and X', except for the ones in position 1 and N_{carb}-H.

Figure 51 shows the UV/Vis spectrum of **[11H$_3$][OTf]$_2$** at various concentrations. As expected, all the features of the macrocycle appear in the high energy region below 400 nm. The two bands at 280-300 nm can be assigned to electronic transitions within the carbazole moiety by comparison with reported carbazole-containing ligands and complexes.[229–232] Interestingly, a pattern of four bands as seen in the 250-400 nm region of the spectrum of **[11H$_3$][OTf]$_2$** is reported for a macrocyclic ligand bearing two carbazole moieties and two pyridines in a trans fashion.[231] As shown in the following paragraphs, these four distinctive bands will be retained in all the iron complexes of the hybrid ligand.

Thanks to this optimized synthesis, the possibility to obtain clean pro-ligand **[11H$_3$][OTf]$_2$** in bulk amounts allowed for the formation of the target iron(II) complexes as presented in the next section.

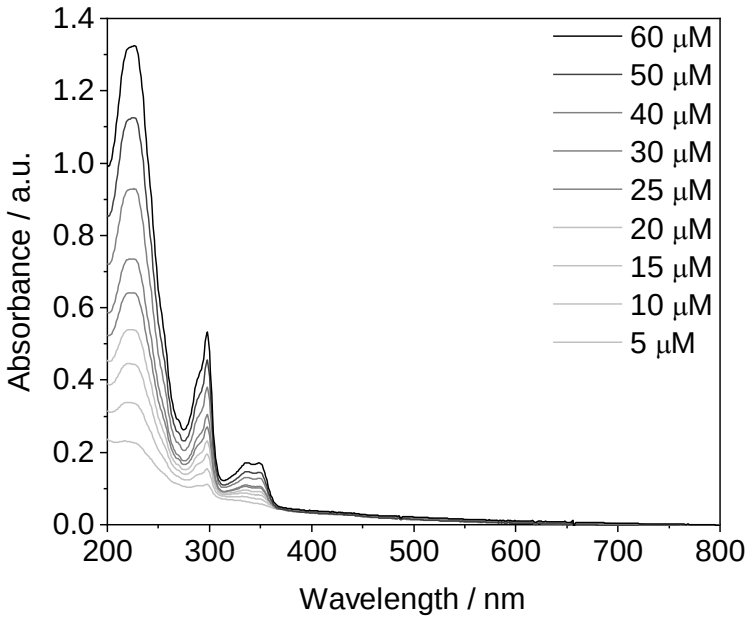

Figure 51. UV/Vis spectra of CH_3CN solutions of pro-ligand **[11H$_3$][OTf]$_2$** at different concentrations and room temperature.

6.3 Synthesis of Iron(II) Complexes of Pro-Ligand [11H$_3$][OTf]$_2$

Typical approaches to synthesize iron(II) complexes of carbene ligands involve three main strategies: a) deprotonation of the pro-lingand with a base followed by metalation with ferrous halides, b) transmetallation with ferrous halides from the corresponding silver complexes, commonly obtained by treatment of the pro-ligand with silver oxide (which acts both as a base and as a metal source), c) use of an iron precursor which acts both as base and as a metal precursor.

Inspired by the successful results with the iron tetracarbene complexes synthesized by our group, the latter approach was chosen to synthesize the ferrous complex of pro-ligand **[11H$_3$][OTf]$_2$**, taking advantage of the one-step procedure. To this ent, iron(II) bis-(trimethylsilyl)amide (FeHMDS), a commonly used basic iron salt, was employed.[233]

When equimolar amounts of **[11H$_3$][OTf]$_2$** and FeHMDS were mixed in CH_3CN at room temperature inside a glovebox, an initial yellow precipitate was quickly formed. A similar behavior is reported for the tridentate **bimca** precursor and its various modifications, suggesting the yellow solid to be partially deprotonated ligand.[135] Hence, the mixture was left stirring for 48 hours during which the yellow intermediate slowly dissolved to give a dark orange/brown solution. Filtration,

removal of the solvent and subsequent dissolution/filtration/drying cycles in less polar solvents (THF, DCM, 1,2-difluorobenzene), followed by a final dissolution in a small amount of CH_3CN and precipitation with diethyl ether, afforded **12a** as a well soluble red/orange crystalline powder (Scheme 9).

Slow diffusion of diethyl ether in a concentrated CH_3CN solution of **12a** led to the formation of single crystals suitable for X-ray diffraction measurements. Figure 52 shows the molecular structure of the monocation while selected structural parameters are reported in Table 1.

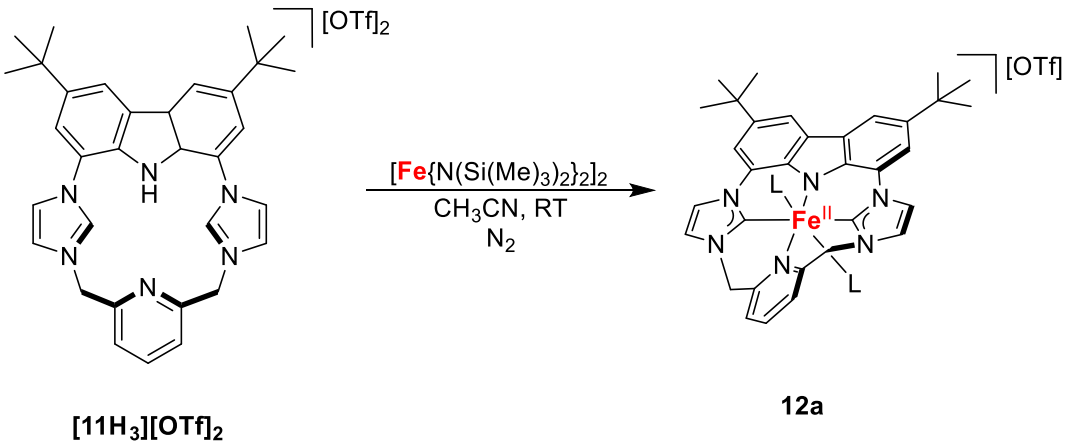

Scheme 9. Synthesis of the low-spin complex **12a** from the reaction of proligand **[11H$_3$][OTf]$_2$** with one equivalent of FeHMDS in CH_3CN at room temperature.

The complex crystallizes in the monoclinic space group P21/*c*, and the corresponding cation shows C_1 symmetry. As expected, the macrocyclic ligand coordinates in an equatorial square-planar geometry via the *trans*-{N_2C_2} 16-membered ring, while two CH_3CN molecules axially coordinate the metal ion, providing an overall octahedral geometry. The macrocycle twists around an axis passing through N_{carb}, N_{py} and C1 to accommodate the metal center. This causes the carbazole aromatic rings to be distorted from full planarity by an angle of 3.9°, and the imidazole-2-ylidene rings and pyridine fragment to form angles of 21.1, 25.1 and 35.8° with the ideal plane of the carbazole backbone. The twisting of the structure is likely caused by the higher C3–N_{py}–C3' angle (116.1°) compared to the C9–N_{carb}–C9' (105.2°) and $N_{imi1/imi1'}$–C6/6'–$N_{imi2/imi2'}$ ones (104.2 and 104.3° respectively) combined with the intrinsic rigidity of the carbazole backbone, which prevents the expansion of the ring restricting the motion of the imidazole-2-ylidene groups. Nevertheless, the iron center sits roughly within the {N_2C_2} plane (deviation 0.0054 Å), and the corresponding octahedral geometry is close to ideal, with a deviation parameter Σ of 18.1.[173–176,234]

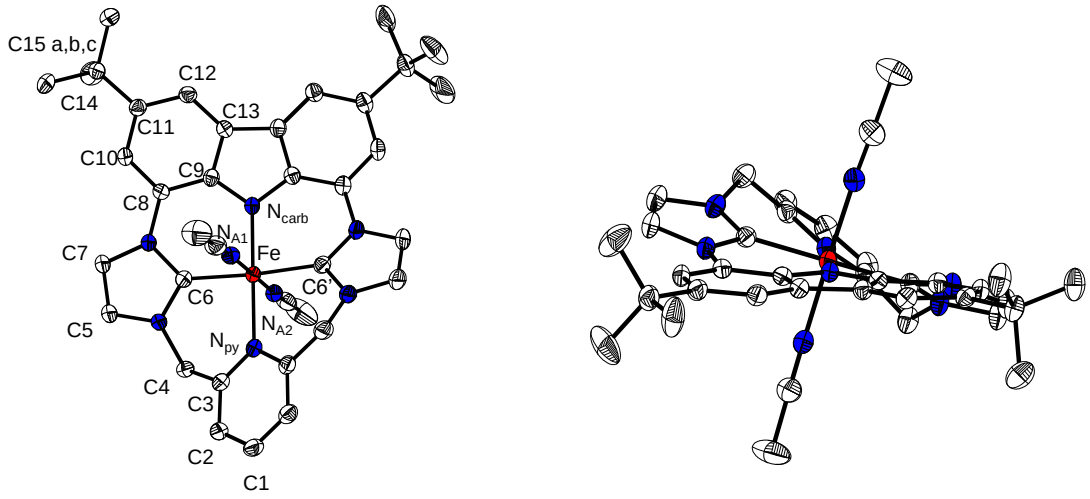

Figure 52. Molecular structure of the cation of **12a** reported as 50% thermal ellipsoids. Counteranions, lattice solvent molecules and hydrogen atoms omitted for clarity. Left: view perperndicular to the carbazole plane; right: view parallel to the carbazole plane. Selected bond lengths [Å] and angles [°]: Fe–N_{carb} 1.9380(16), Fe–C6 1.942(2), Fe–C6' 1.941(2), Fe–N_{py} 2.0713(17), Fe–N_{A1} 1.9338(18), Fe–N_{A2} 1.9377(18); N_{A1}–Fe–N_{A2} 178.83(7), C6–Fe–C6' 175.86(8), N_{carb}–Fe–N_{py} 179.88(7).

The Fe–C and Fe–N_{py} bond lengths of 1.94 Å and 2.07 Å fall in the typical ranges for ferrous NHC/pyridine hybrid complexes (1.80 – 2.16 Å and 1.89- 2.28 Å respectively),[126,128,131,235–241] while the Fe–N_{carb} bond (1.9380(16) Å) is the shortest among the Fe^{II}-carbazole complexes reported so far.[242–245] Given the π-donating ability of the carbazolide fragment, a short bond with iron can be explained by the presence of a π-acceptor pyridine moiety *trans* to the carbazole, which synergically removes electron density from the metal and allows for the formation of short bonds.[246] The influence of π-acceptors on the length of the carbazolide–M bond can be envisioned if we take in account that similar Fe–N bond lengths were found for a ferrous low-spin octahedral pyrrole-Fe pincer complex and some of its carbonyl derivatives, reported by Tonzetich *et al.* Similar carbazole–M distances are also described for a Co^{II} complex with a carbazole-bisimine ligand scaffold published by Williams *et al*.[247,248]

^{1}H-NMR analysis of **12a** in CD_3CN at room temperature (Figure 53, top) showed signal patterns compatible with a C_{2v} symmetry, suggesting that a fast dynamic process is present in solution. The singlet at 5.63 ppm, assigned to the methylene linkers, and the two signals for the protons in *ortho* and *para* of the pyridine imply an average structure in which the macrocycle is completely co-planar to the carbazole group, obtained by the rotation of the pyridine ring on a non-crystallographic axis that passes through C1, N_{py}, N_{carb} and bisecting the C13–C13' bond. As expected, a signal at 202.2 ppm in the ^{13}C-NMR spectrum confirms the presence of the two imidazole-2-ylidene moieties.[127] VT-NMR spectra in CH_3CN from 25 to –35 °C showed no sign of de-coalescence of

the signals, implying a high rate of the dynamic process. However, when **12a** was dissolved in solvents that would allow for the use of lower temperatures, a change in the signal pattern was observed: the use of THF-d_8, DMF-d_7 and CD_3OD caused the appearance of a clearly paramagnetic complex in solution, as depicted in Figure 53 (bottom).

Even more interestingly, when the new NMR samples were dried under vacuum and the orange residue dissolved in CD_3CN, the NMR spectrum changed back to the one of **12a**. This behavior suggested an effect of the nature of the solvent on the spin state of the ferrous complex, underlying the labile coordination of the axial nitrile molecules. In order to confirm the latter hypothesis, the possible loss of coordinated solvent was tested with Mößbauer (MB) spectroscopy. The analysis of the Mößbauer parameters will be discussed in the following paragraphs, while at this stage only the change of the shape of the MB signals is relevant for this preliminary investigation (Figure 54). A crystalline sample of **12a** was initially measured and then exposed to high vacuum for several hours. A second MB measurement of the solid residue was performed, evidencing a profound spectral change due to the formation of a complex with higher isomer shift and very large splitting of the MB doublet (purple species in Figure 54-b). When the obtained solid was redissolved in CH_3CN, recrystallized by slow diffusion of Et_2O and measured a third time, almost full restoration of the MB features of **12a** was achieved.

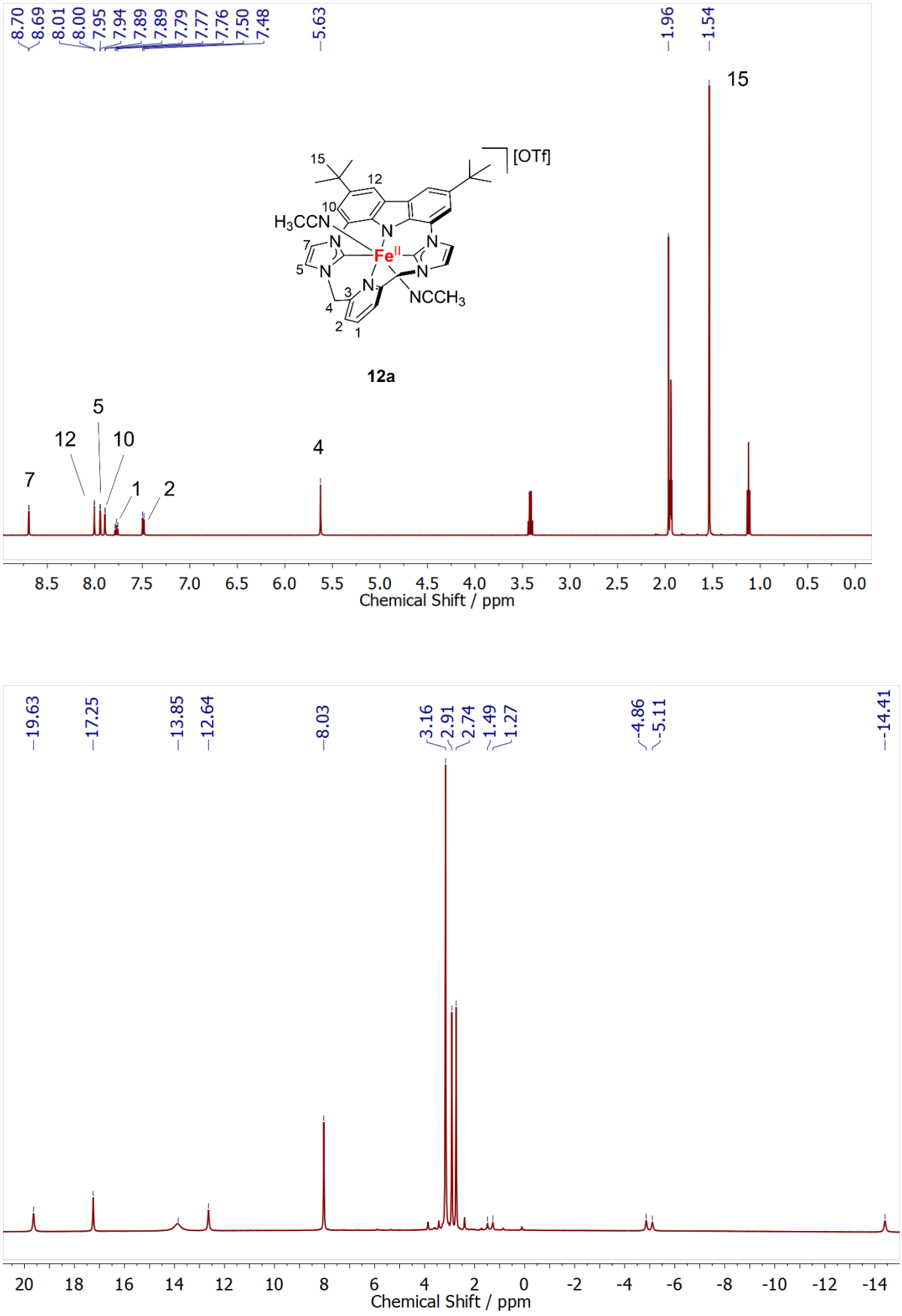

Figure 53. Top: ^{1}H-NMR spectrum of a solution of **12a** in CD_3CN at RT. Bottom: ^{1}H-NMR spectrum of a solution of **12a** dissolved in THF-d8 at RT.

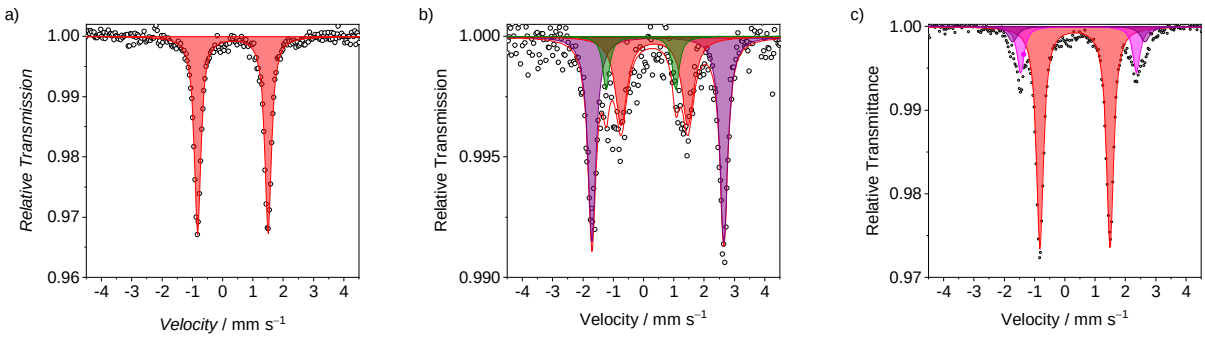

Figure 54. a) Zero-field ^{57}Fe MB spectrum of a solid sample of complex**12a**, recorded at 80K (natural abundance). b) MB spectrum acquired on the same sample after vacuum was applied to the solid sample for 3 hours, recorded at 80 K. c) MB spectrum of the solid obtained by redissolving the sample b) in CH_3CN and re-precipitating with diethylether, recorded at 80 K.

These experimental findings hinted towards the possibility to modify the spin state of the ferrous complex **12a** simply by acting on the axial ligation (e.g., by using solvents with different coordinating abilities). Indeed, when bulk amounts of **12a** were repeatedly dissolved and recrystallized from 1,2-difluorobenzene (DFB) (or THF) and a final saturated solution of the orange solid in DFB was concentrated under vacuum, orange crystals of a new ferrous complex (**12b**) suitable for XRD measurements grew at RT in the course of several days. Complex **12b** formed upon loss of the two axial nitrile molecules and coordination of a triflate anion, resulting in a square pyramidal complex.

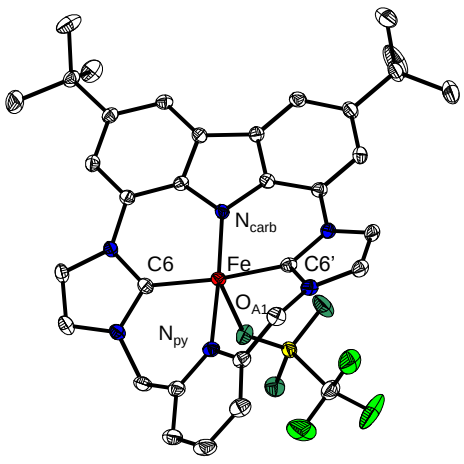

Figure 55. Molecular structure of complex **12b** reported as 50% thermal ellipsoids. Lattice solvent molecules and hydrogen atoms omitted for clarity. Selected bond lengths [Å] and angles [°]: Fe–N_{carb} 1.8994(12), Fe–C6 1.9431(15), Fe–C6' 1.9443(15), Fe–N_{py} 2.1003(13), Fe1–O_{A1} 2.3221(11); C6–Fe1–C6' 173.82(6), N_{carb}–Fe–N_{py} 173.64(5).

Table 1. Selected bond lengths (Å), angles (°) and parameters of BP86 optimized geometries (italics) of complexes **12a** and **12b**. A1 and A2 refer to the axial ligands.

Bond	**12a**	**12b**
Fe–N_{carb}	1.938(2) / *1.937*	1.899(1) / *1.888*
Fe–N_{py}	2.071(2) / *2.051*	2.100(1) / *2.079*
Fe–C6	1.941(2) / *1.939*	1.944(2) / *1.927*
Fe–C6’	1.942(2) / *1.938*	1.943(2) / *1.917*
Fe–A_1	1.934(2) / *1.875*	2.322(1) / *2.194*
Fe–A_2	1.938(2) / *1.876*	-
Angle	**12a**	**12b**
N_{carb}–Fe–C6	87.90(7) / *87.91*	88.40(6) / *88.03*
N_{carb}–Fe–C6’	88.01(8) / *87.97*	88.25(6) / *88.7*
N_{py}–Fe–C6	92.04(7) / *92.03*	91.12(6) / *91.08*
N_{py}–Fe–C6’	92.06(8) / *92.09*	91.62(6) / *91.82*
N_{carb}–Fe–N_{py}	179.9(7) / *179.94*	173.64(5) / *174.78*
C6–Fe–C6’	175.9(1) / *175.88*	173.82(6) / *174.53*
N_{A1}–Fe–N_{A2}	178.8 (1) / *174.17*	-

12b crystallizes in the monoclinic space group $P2_1/c$. The conformation of the macrocyclic ligand around the metal center is very similar to the one in **12a**, but the Fe–N_{py} and Fe–C bond lengths are significantly elongated, compatible with a complex with higher spin state. The Fe–O axial bond is especially long, while the Fe–N_{carb} distance is shorter than in the low spin complex **12a**.

With the two ferrous complexes in hand, the next sections will describe the result of electrochemical, spectroscopic, and magnetic analyses aimed at exploring the nature of the newly established system and its ability to showcase properties typical of the porphyrin-Fe analogues.

6.4 Optical Spectroscopy, Cyclic Voltammetry and Spectroelectrochemistry of 12a and 12b

Optical spectroscopy in solution was used to characterize UV/Vis absorption properties of complexes **12a** and **12b** and assignation of the bands was performed with the aid of TDDFT calculations (B3LYP) based on BP86-optimized molecular structures. The latter were obtained using initial coordinates derived from XRD analyses and Table 1 in Section 6.3 shows a good agreement of the optimized and experimental structures. Further information regarding DFT determination of the electronic structures of the complexes will be discussed in Section 6.6.

UV/Vis spectroscopy analysis of an CH_3CN solution of complex **12a** and a THF solution of **12b** confirmed that the difference in electronic structure of the complexes is maintained in solution. Figure 56 shows the spectra of 25 μM solution of the complexes at room temperature.

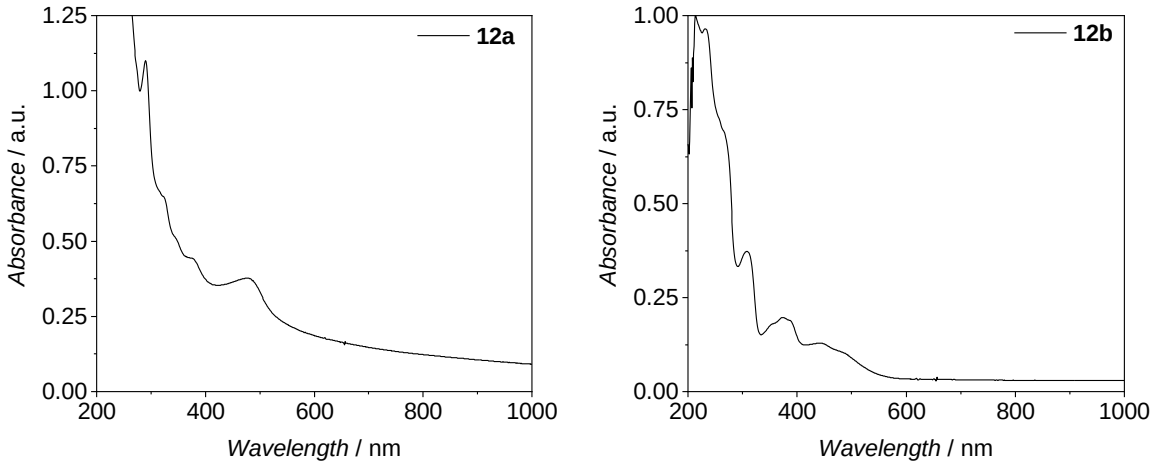

Figure 56. UV/Vis spectra of 25 μM solutions of **12a** (in CH_3CN, left) and **12b** (in THF, right).

12a shows absorptions at 321 and 377 together with a more pronounced feature at 480 nm with an extinction coefficient (ε) of approximately 5319 $L \cdot mol^{-1} \cdot cm^{-1}$ (plots for the determination of ε in Appendix). While the first two likely belong to electronic transitions on the ligand scaffold, the latter could be assigned to a MLCT-like transition from an orbital localized on Fe and on the anionic nitrogen atom of carbazole to the carbazole backbone (see Figure 85 in Chapter 10). The bands in the 400–500 nm region of the spectrum of **12b** instead were assigned to two MLCT transitions involving the carbazole and the pyridine units, and to a d-d transition on Fe (see Figure 88 in Chapter 10).

In order to elucidate the redox properties of complexes **12a**/**b**, providing evidence for the redox non-innocence of the ligand scaffold, cyclic voltammetry experiments were conducted in CH_3CN (**12a**) and THF (**12b**) solutions at room temperature.

Four different redox processes appeared in the voltammogram of **12a**: two rather facile oxidations at $E_{1/2}$ = −0.37 and +0.62 V, and two irreversible reductions at $E_{p,f}$ = −1.58 and −1.86 V, respectively. As shown in Figure 57 the two oxidations presented peak-to-peak separation values (74.4 and 81.0 mV for first and second oxidation respectively) that are close to the ideal reversible one electron process (57 mV at 25°C), and their peak potentials were largely independent from the scan rate. When scanning anodically first, a plot of the peak intensity of the forward scan versus the square root of the scan rate according to the Randles-Sevcik equation showed linear behavior for both oxidative processes, as expected for reversible redox events of a freely diffusing species (see Appendix for additional plots).

The first oxidation process could be assigned to the Fe^{III}/Fe^{II} redox couple, as confirmed by MB analysis (see corresponding section). The presence of three strongly donating groups in the macrocycle likely increases the electron density at the metal center compared to other NHC/pyridine complexes like $[(L^{Py/NHC})Fe^{II}(CH_3CN)_2][OTf]_2$ (E_{pf} $[Fe^{III}/Fe^{II}]$ = 0.7 V *vs.* $Fc^{+/0}$, see structure in Chapter 1), as readily shown by the lower potential for the one-electron oxidation of **12a**.[131,164,235] The anionic nature of the macrocyclic ligand further facilitates electron removal by lowering the overall positive charge of the complex. The latter effect can be easily visualized by a comparison with the Fe^{III}/Fe^{II} redox potentials of most dicationic tetracarbene complexes reported so far, usually appearing in the range between −0.16 and 0.15 V.[164,235,249–252]

The second reversible anodic event can be formally assigned to an Fe^{III} to Fe^{IV} oxidation, which appears to be rather facile. Indeed, when comparing this redox potential to other non-heme octahedral iron complexes coordinated by anionic variations of the cyclam scaffold, it becomes evident how a potential of just 0.62 V *vs.* $Fc^{+/0}$ would be rather unusual for the generation of a Fe^{IV} species of a hybrid macrocycle like **[11H$_3$][OTf]$_2$**.[84,253,254] Indeed, a series of three iron complexes coordinated with the cyclam-acetate (cy-ac) ligand and halide or azide anions show a redox event associated with the Fe^{IV}/Fe^{III} redox couple at potentials between $E_{1/2}$ = 1.15 and 1.38 V *vs.* $Fc^{+/0}$.[253] Instead, the second oxidation of complex **12a** would be compatible with the possibility of the redox event taking place on a different site of the complex, e.g. the carbazole backbone, rather than the metal center. Indeed, Lapkowski and Robert have previously shown that 3,6-disubstituted carbazoles can be oxidized to their corresponding radical cations in similar potential ranges ($E_{½}$ = 0.40 – 1.00 V *vs.* $Fc^{+/0}$).[141,255]

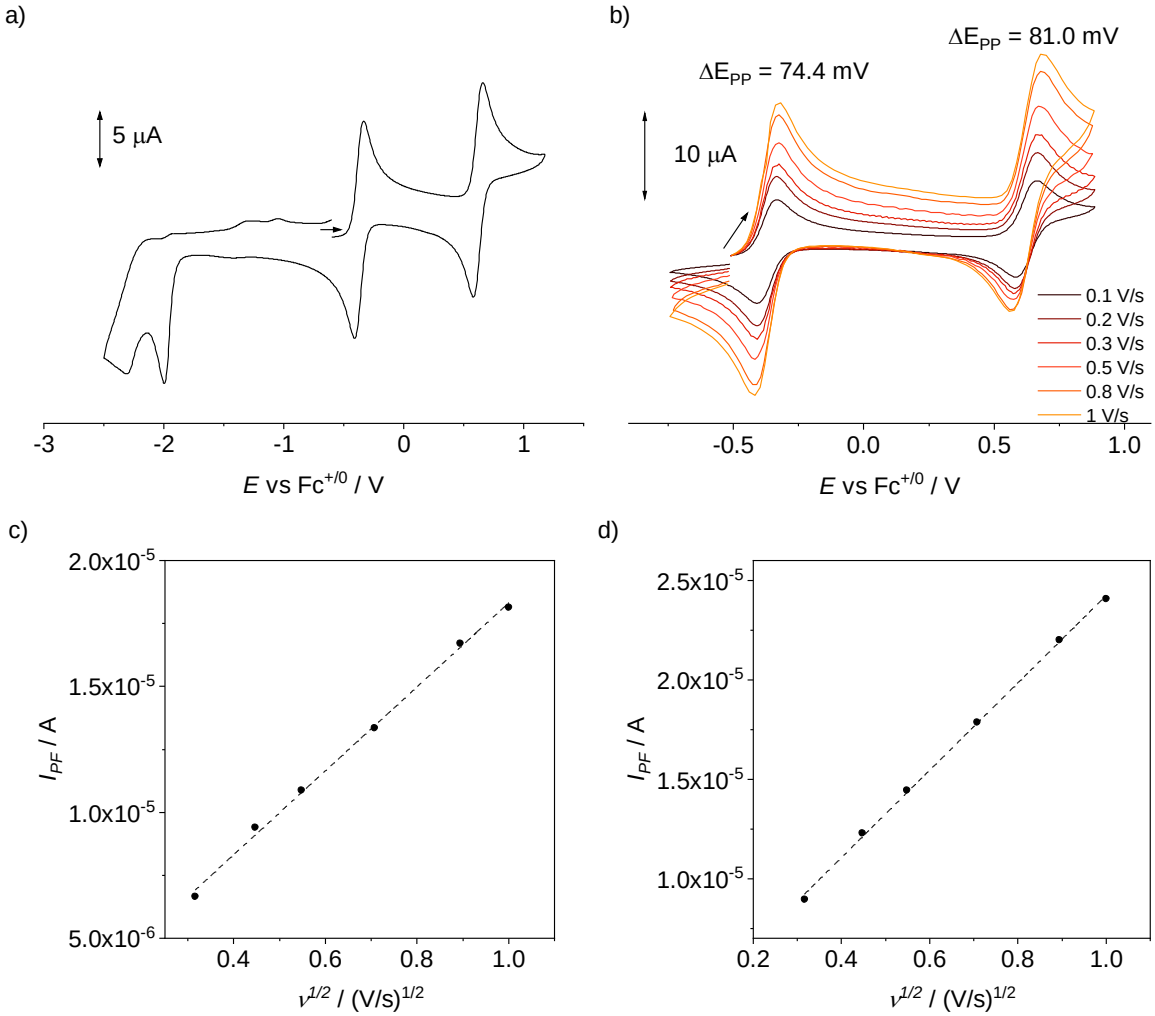

Figure 57. a) Cyclic voltammogram of a 1 mM solution of crystalline **12a** in CH_3CN with 0.1 M $^nBu_4NPF_6$ at a scan rate of 0.1 V/s. b) Scan rate dependency of the first two oxidative events. c,d) Plots of the peak intensity in the forward scan (I_{Pf}) of the first (c) and second (d) oxidation *versus* square root of scan rate and corresponding linear fits (dashed lines).

Support for the ligand-based nature of this second oxidation was provided by UV/Vis spectro-electrochemistry (UV-SEC) experiments. When a potential of –0.14 V vs $Fc^{+/0}$ was applied to a solution of **12a**, a clean one-step conversion to a new species took place in the course of 300 seconds, as evidenced by the presence of multiple isosbestic points (Figure 58). The one-electron oxidized species showed five new bands in the 300–600 nm region and a broad band at λ_{max} = 1005 nm (full spectrum in the following section). When the potential was switched to –0.9 V, re-establishment of the initial spectrum of **12a** was observed, providing evidence for full chemical reversibility of the redox process. The optical features of the two-electron oxidized species were recorded during the application of a potential of 0.76 V after the initial formation of the one-electron oxidized species. This second one-electron oxidation generated a complex with three main features at 511, 728 and 804 nm, the last one of rather high intensity. Comparison with literature shows that

carbazole dimers and poly-*N*-vinylcarbazole radical cations possess intense features in the same region as a signature of their radical nature.[256,257] Moreover, similar bands were recorded in the case of the carbazole-bisoxazoline catalyst of Nakada and coworkers (see Chapter 1) after oxidation with iodosobenzene, a ferric porphyrin π-radical cation complex, iron complexes of biquinazoline macrocycles, and some free corroles.[140,258–260] Application of a potential of –0.14 V only partially restored the spectrum of the parent complex, thereby indicating the instability of the generated radical complex. Taken together, these findings introduced the possibility of the carbazole unit of the ligand scaffold to be the site for the second electron removal from complex **12a**.

Complex **12b** in THF shows similar redox behavior (Figure 59), with two oxidation waves at $E_{½}$ = –0.36 and E_{pf} = 0.66 V vs $Fc^{+/0}$ and an irreversible reduction at higher potential (–1.88 V) compared to the first one of **12a**. Interestingly, the two oxidations show potentials virtually identical to the ones of **12a**, despite the profound differences in the solid structure and charge of the complexes, perhaps suggesting that the triflate anion in **12b** could dissociate in solution. Spectroelectrochemical one-electron oxidation of **12b** reveals the chemically reversible formation of a new complex with a broad feature at λ_{max} = 713 nm, reminiscent of the one at 1005 nm in **12a** but significantly higher in energy. No spectral changes were recorded when applying a potential high enough to perform the second oxidation, suggesting a rather high instability of the doubly oxidized product, which could decompose in solution after diffusing away from the anode (thermal decomposition of the doubly oxidized species returns the corresponding Fe^{III} complex, as discussed below).

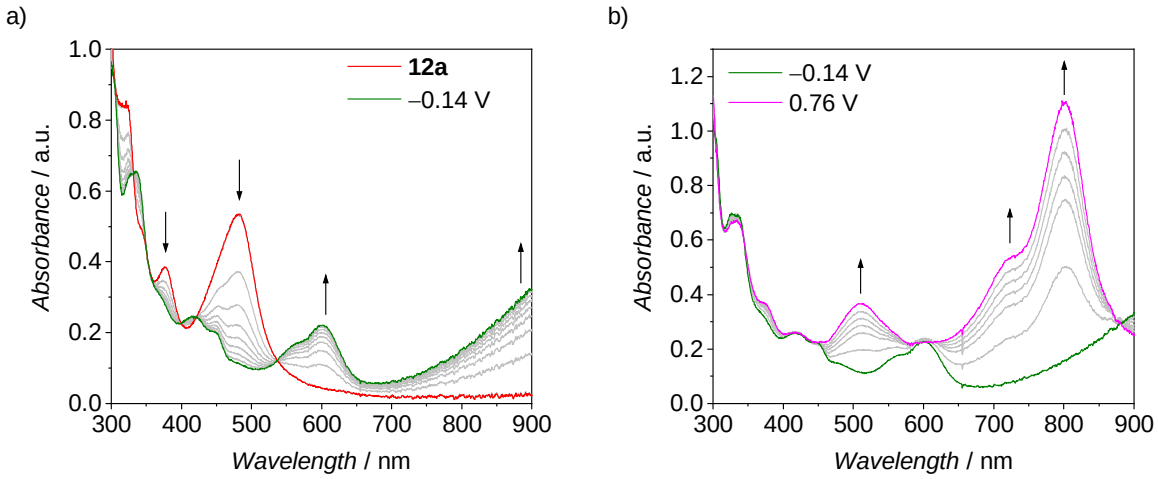

Figure 58. UV/Vis spectroelectrochemistry of a 1 mM solution of complex **12a** in CH_3CN 0.1 M $^nBu_4NPF_6$. a) first oxidation of **12a** (red spectrum) at an applied potential of –0.14 V vs $Fc^{+/0}$; b) second oxidation of the mono-oxidized complex (green spectrum) at an applied potential of 0.76 V vs $Fc^{+/0}$.

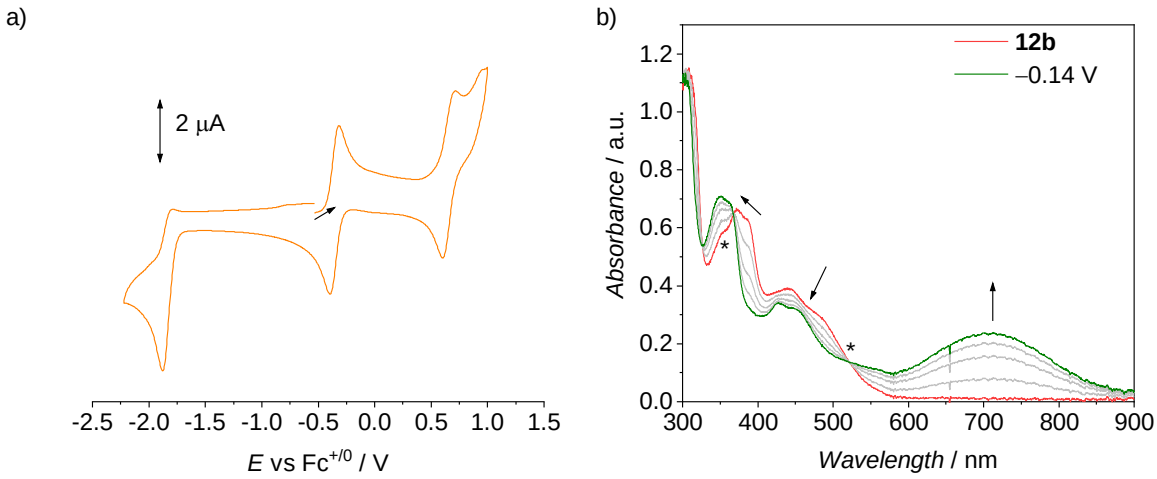

Figure 59. a) Cyclic voltammogram of a 1 mM solution of crystalline **12b** in THF 0.1 M $^{n}Bu_4NPF_6$ at a scan rate of 0.1 V/s. b) UV/Vis spectroelectrochemistry of a 1 mM solution of complex **12b** in THF 0.1 M $^{n}Bu_4NPF_6$: first oxidation of **12b** (red spectrum) at an applied potential of –0.14 V vs $Fc^{+/0}$.

Given the comparable redox behavior of the two ferrous complexes and the possibility to access both metal- and ligand-based oxidations, the prospect of isolating two redox series differing in spin state of the complexes prompted for the synthesis of the oxidated products in bulk.

6.5 One- and Two-Electron Oxidations of 12a and 12b

Scheme 4 reports the synthetic strategies employed for the oxidations of the Fe^{II} complexes. The first oxidation of **12a**/**b** to **13a** and **13b** was performed using silver triflate as oxidant (formal potential of 0.04 V vs $Fc^{+/0}$ in CH_3CN)[261] in CH_3CN and acetone, respectively. Slow diffusion of diethyl ether in a propionitrile solution of **13b** afforded single crystals suitable for XRD analysis, while crystals of **13b** were obtained by layering of diethyl ether on a concentrated acetone solution. Figure 60 shows the molecular structure of the ferric complexes.

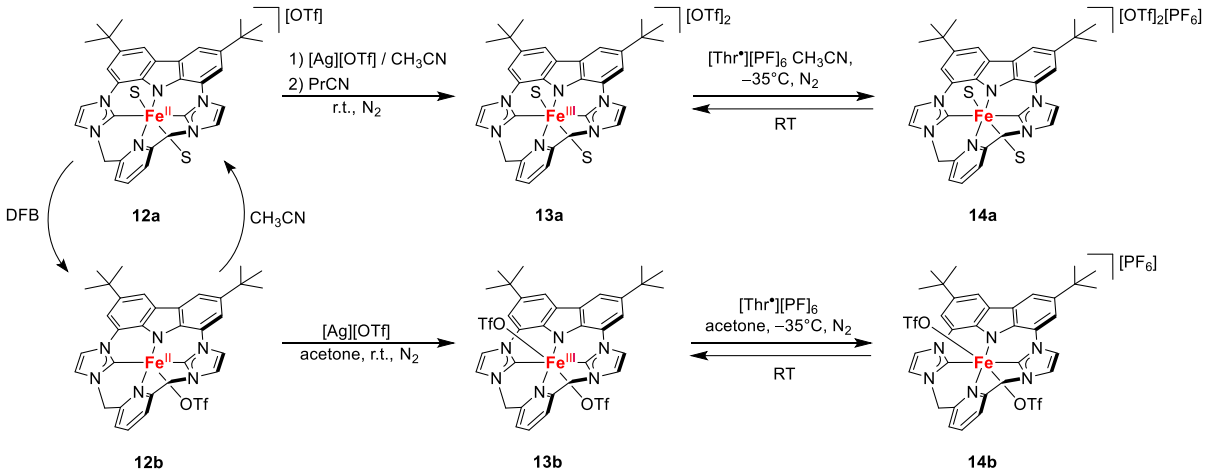

Scheme 10. Synthesis of the oxidized complexes **13a/b** and **14a/b** starting from **12a/b**. "S" represents coordinated solvent molecules.

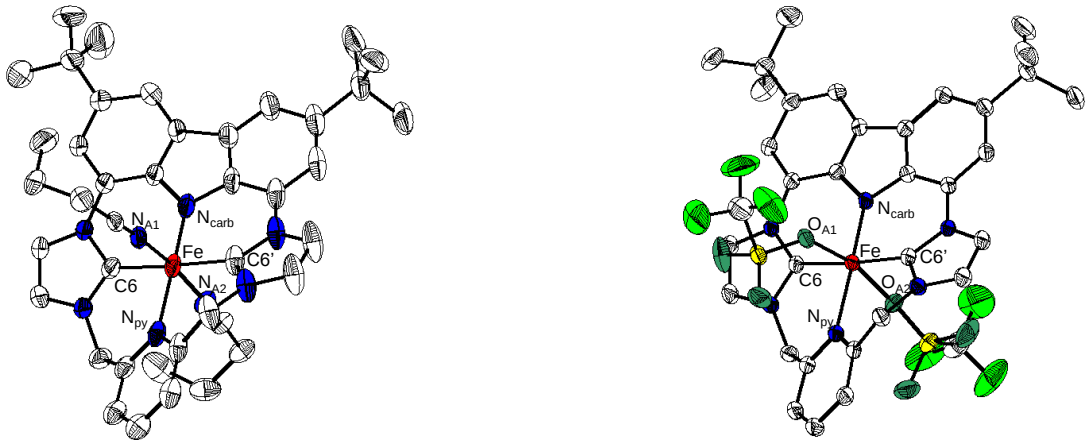

Figure 60. Molecular structures of the cation of complex **13a** (left) and of complex **13b** reported as 50% thermal ellipsoids. Lattice solvent molecules, hydrogen atoms and counteranions (for **13a**) omitted for clarity. Selected bond lengths [Å] and angles [°]: **13a**) Fe–N_{carb} 1.859(3), Fe–C6 1.956(3), Fe–C6' 1.958(3), Fe–N_{py} 2.104(3), Fe–N_{A1} 1.937(2), Fe–N_{A2} 1.950(6); N_{A1}–Fe–N_{A2} 172.5(4), C6–Fe–C6' 177.39(15), N_{carb}–Fe–N_{py} 179.19(10). **13b**) Fe–N_{carb} 1.884(3), Fe–C6 1.976(2), Fe–N_{py} 2.133(3), Fe–$O_{A1/A2}$ 2.2261(17); C6–Fe–C6' 176.45(14), N_{carb}–Fe–N_{py} 180.0, O_{A1}–Fe1–O_{A2} 167.62(9).

13a crystallizes in the triclinic space group $P\bar{1}$. The octahedral geometry with two axial nitrile ligands found in **12a** is maintained and all the coordinative bond lengths are elongated compared to **12a**, apart from the Fe–N_{carb} bond, which is the shortest among all ferric-carbazolide complexes characterized so far (1.959 – 1.967).[140,246] This suggests that the removal of one electron from the metal center decreases the backdonation to the pyridine and imidazolylylidene groups, while the coulombic attraction between the Fe^{III} center and the anionic carbazolide moiety pulls the Fe and N_{carb} atoms closer together.[164,262] On the contrary, **13b** appears octahedrally coordinated with two triflate anions in the axial positions, and crystallizes in the monoclinic space group C2/*c*. Its

intermediate spin nature, confirmed by magnetometry (see following section) is in accordance with the elongation of all coordinative bonds compared to **13a**.[263,264] This second ferric complex presents higher symmetry in the solid structure compared to **13a** and possesses a C_2 axes passing through N_{carb}, N_{py} and C1.

Table 2. Selected bond lengths, angles and parameters of BP86 optimized geometries (italics) of complexes **13a** and **13b**. A1 and A2 refer to the axial ligands.

Bond	**13a**	**13b**
Fe–N_{carb}	1.859(3) / *1.881*	1.884(3) / *1.883*
Fe–N_{py}	2.104(3) / *2.088*	2.133 (3) / *2.130*
Fe–C6	1.956(3) / *1.940*	1.976(2) / *1.956*
Fe–C6’	1.958(3) / *1.939*	1.976(2) / *1.956*
Fe–A_1	1.950(6) / *1.893*	2.226(2) / *2.201*
Fe–A_2	1.937(2) / *1.896*	2.226(2) / *2.199*
Angle	**13a**	**13b**
N_{carb}–Fe–C6	89.1(1) / *88.77*	88.22(7) / *88.48*
N_{carb}–Fe–C6’	88.5(1) / *88.79*	88.22(7) / *88.53*
N_{py}–Fe–C6	90.9(1) / *91.27*	91.78(7) / *91.47*
N_{py}–Fe–C6’	91.5(1) / *91.17*	91.78(7) / *91.52*
N_{carb}–Fe–N_{py}	179.2(1) / *179.73*	180.00 / *179.80*
C6–Fe–C6’	177.4 (2) / *177.55*	176.5(1) / *177.01*
N_{A1}–Fe–N_{A2}	172.5 (4) / *177.65*	167.62(9) / *170.83*

The axial coordination of weak triflate anions in **13b** allows for the stabilization of the intermediate spin thanks to a marked axial elongation (Fe–OTf distance of 2.226 Å) and the weaker ligand field. It is interesting to compare this behavior with the spin state variations of ferric octaethyltetraphenyl porphyrins obtained with a series of axial ligands of progressively stronger donor properties. In those complexes, the use of a stronger chloride donor in the axial position led to the elongation of the equatorial Fe–$N_{pyrrole}$ bonds, an overall weakening of the ligand field and therefore the

stabilization of the high-spin state. Substituting chloride with weaker triflate, chlorate or I_3^- ions instead formed intermediate spin complexes via the contraction of the equatorial bonds, and spin-admixed states were obtained when using ligands of intermediate strength such as iodide anions.[172] In the case of complexes **12a**/**b** and **13a**/**b**, the presence of the carbazole backbone does not allow for an expansion/contraction of the equatorial ring at the imidazole-2-ylidene groups, and the effect of different axial ligand donor strength follows a more intuitive behavior.

The second one-electron oxidation was performed on **13a** and **13b** using thianthrenium hexafluorophosphate (0.86 V vs $Fc^{+/0}$)[261] in CH_3CN and in acetone at −35 °C, to avoid decomposition of the radical complexes to the ferric precursors. A gradual color change to purple accompanied both reactions, indicative of the formation of carbazole-based radicals. Isolation of the low-spin complex **14a**, dissolution in cold CH_3CN and slow diffusion of Et_2O into the solution at −35 °C afforded single crystals suitable for XRD analysis (Figure 61).

14a maintains the octahedral geometry with two nitrile ligands and crystallizes in the monoclinic space group $P2_1/c$. All Fe–L distances are shorter than in the ferric precursor, but no significant changes in bond lengths were observed otherwise. The extended π-conjugation on the carbazole backbone probably allows the unpaired electron to be partially delocalized on orbitals of the phenyl rings, thereby decreasing the effect of the ligand-based oxidation on the bond lengths of the carbazolide fragment.

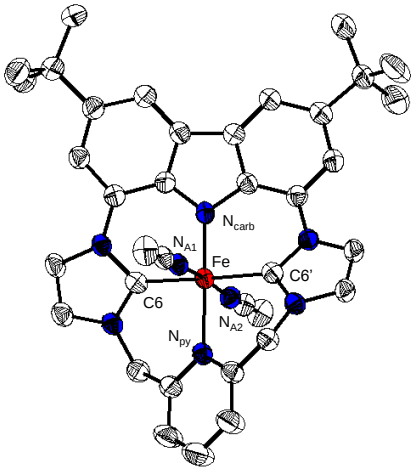

Figure 61. Molecular structures of the cation of complex **14a** reported as 50% thermal ellipsoids. Lattice solvent molecules, hydrogen atoms and counteranions omitted for clarity. Selected bond lengths [Å] and angles [°]: Fe–N_{carb} 1.837(3), Fe–C6 1.942(3), Fe–C6' 1.944(3), Fe1–N_{py} 2.087(3), Fe–N_{A1} 1.917(3), Fe–N_{A2} 1.921(3); N_{A1}–Fe–N_{A2} 175.76(12), C6–Fe–C6' 178.70(14), N_{carb}–Fe–N_{py} 178.90(11).

Table 3. Selected bond lengths, angles and parameters of BP86-optimized geometries (italics) of complexes **14a** and **14b**. A1 and A2 refer to the axial ligands.

Bond	**14a**
Fe–N_{carb}	1.837(3) / *1.863*
Fe–N_{py}	2.087(3) / *2.117*
Fe–C6	1.944(3) / *1.947*
Fe–C6’	1.942(3) / *1.945*
Fe–A_1	1.917(3) / *1.901*
Fe–A_2	1.921(3) / *1.901*
Angle	**14a**
N_{carb}–Fe–C6	89.10(12) / *89.39*
N_{carb}–Fe–C6’	89.60(12) / *89.45*
N_{py}–Fe–C6	90.52(12) / *90.59*
N_{py}–Fe–C6’	90.77(12) / *90.56*
N_{carb}–Fe–N_{py}	178.9(1) / *179.96*
C6–Fe–C6’	178.7(1) / *178.85*
N_{A1}–Fe–N_{A2}	175.8(1) / *175.81*

6.6 Electronic Structure Determination of the Series of complexes 12a/b – 14a/b

Spin modulation via axial ligand substitution

In order to provide support to the idea of a spin state change upon modification of the axial ligation in complexes **12a**/**b** and **13a**/**b**, all ferrous and ferric species were characterized with a combination of techniques aimed at determining their electronic structure, specifically Mößbauer and EPR spectroscopy and SQUID magnetometry. The experimental results were compared with (TD)DFT calculations that were performed starting from the atomic coordinates obtained from XRD analyses. Tables 2 and 3 in the previous section show the good agreement between the experimental and DFT-optimized molecular structures.[265,266]

The low-spin state of complex **12a** was well reflected by the complex’s MB spectrum shown in Figure 62: the isomer shift of 0.33 $mm \cdot s^{-1}$ is very similar to the one of the hybrid complex

$[(L^{Py/NHC})Fe^{II}(CH_3CN)_2][OTf]_2$ (0.32 mm·s^{-1}), and slightly higher than for Fe-tetracarbene complexes (0.21 – 0.24 mm·s^{-1}) due to the weaker donor properties of carbazolide and pyridine compared to imidazolyl-2-ylidenes and to larger Fe–L bond lengths with some of the donor atoms in **12a**.[109,131,164] For a diamagnetic Fe^{II} complex the quadrupole splitting is expected to be rather low, if present, but **12a** shows a splitting of 2.33 mm·s^{-1} due to the rather oblate electron density around the metal center, owing to the presence of strong donors in the equatorial plane. Indeed, similar considerations were proposed for other low-spin tetracarbene-Fe^{II} complexes that presented a rather similar electron distribution.[109,267,268] The S = 1 complex **12b** instead has a much higher isomer shift (0.48 mm·s^{-1}) and quadrupole splitting (4.26 mm·s^{-1}), in agreement with an intermediate-spin nature, longer coordinative bonds and the asymmetric distribution of electron density around Fe.[143]

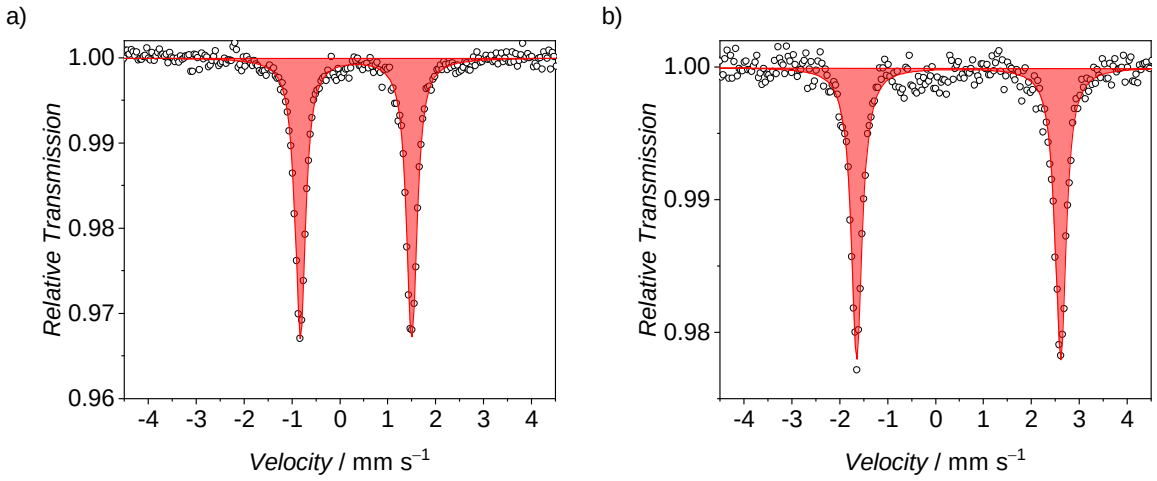

Figure 62. Zero-field ^{57}Fe Mössbauer spectra of solid **12a** (a) and **12b** acquired at 80 K (natural abundance. **12a**: δ = 0.33 mm·s^{-1}, ΔE_Q = 2.33 mm·s^{-1}; **12b**: δ = 0.48 mm·s^{-1}, ΔE_Q = 4.26 mm·s^{-1}).

SQUID magnetometry measurements on a solid sample of **12b** conducted at 0.5 T between 2 and 298 K finally confirmed the S = 1 state of the complex. $\chi_m T$ values were temperature-independent above 50 K, while below that temperature their decrease was probably due to zero-field splitting. The $\chi_m T$ value of 1.24 recorded at 210 K is close to the spin-only value of 1 cm^3·K·mol^{-1} expected for an S = 1 complex and the calculated g_{avg} values (2.242) significantly deviate from the free electron value owing to spin-orbit coupling phenomena involving the metal-based unpaired electrons.

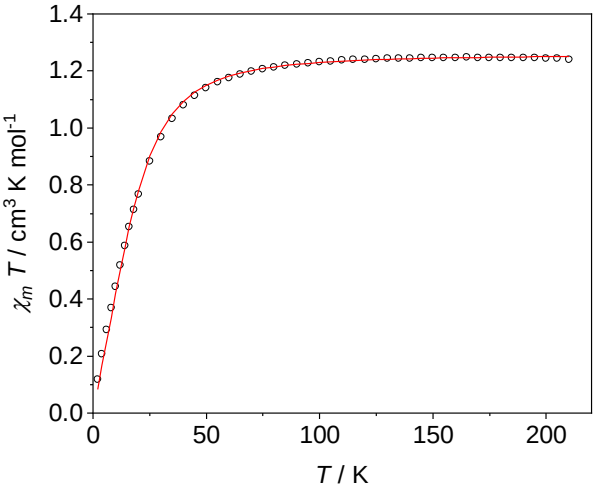

Figure 63. $\chi_m T$ *vs* T curves of a solid samples of **12b**. The empty circles represent experimental data, while the solid red line is a simulations using equation 2 described in Chapter 3.

The experimental MB parameters were well reproduced by DFT calculations, as shown in Table 4, supporting the validity of the electronic structure interpretation. Moreover, plot of the spin density and singly occupied magnetic orbitals of complex **12b** support the $S = 1$ nature found in SQUID, as show in Figure 64.

Table 4. Experimental and DFT-calculated (italics) Mößbauer parameters of complexes **12a** and **12b**.

Complex	δ	$\lvert\Delta E_Q\rvert$	Γ
12a	0.34 / *0.21*	2.33 / *2.23*	0.26
12b	0.48 / *0.31*	4.26 / *4.02*	0.28

Γ represent the linewidth in the experimentally recorded spectra.

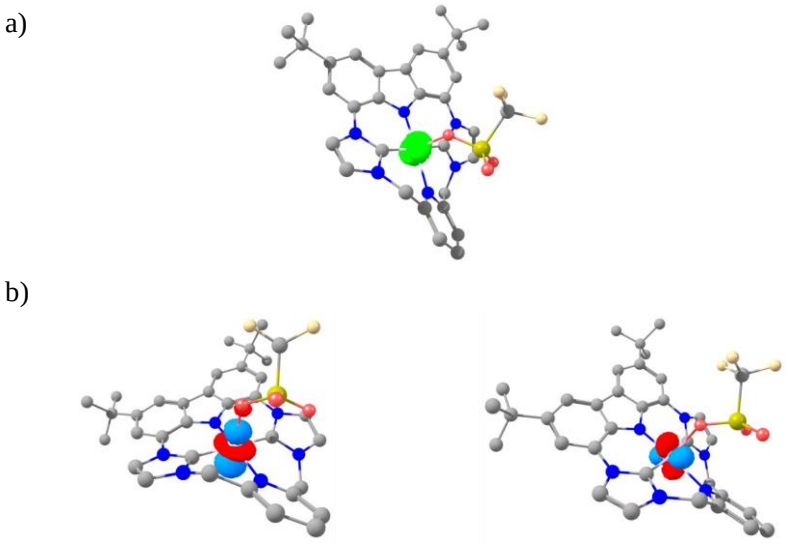

Figure 64. a) Spin density plot for complex **12b**. b) Magnetic "spin up" orbitals plots for complex **12b**.

The one-electron oxidation of **12a** generated the low-spin complex **13a**, as confirmed by MB analysis. The IS value decreased to 0.18 mm·s^{-1} (Figure 66) upon electron removal and the large quadrupole splitting parameter (3.84 mm·s^{-1}) was attributed to the asymmetric population of the metal d orbitals and to the covalent nature of the Fe–N_{carb} bond. The asymmetry of the doublet probably derives from fast paramagnetic relaxation, as seen in many other low-spin ferric complexes.[268] Further proof for the S = 1/2 nature of **13a** was provided by an EPR spectroscopy measurement in frozen ^{n}PrCN solution, shown in Figure 65. **13a** presents a typical rhombic spectrum with g-anisotropy attributable to a metal-based spin (g-values of 2.13, 2.05 and 1.96). Finally, SQUID measurements on a solid sample recorded at 0.5 T in the range between 2 and 298 K confirmed the S = 1/2 ground state, with a $\chi_m T$ of 0.534 cm^3·K·mol^{-1} at 295 K. Antiferromagnetic intermolecular interactions likely caused the slight decrease of the $\chi_m T$ curve below 30 K (Figure 66).

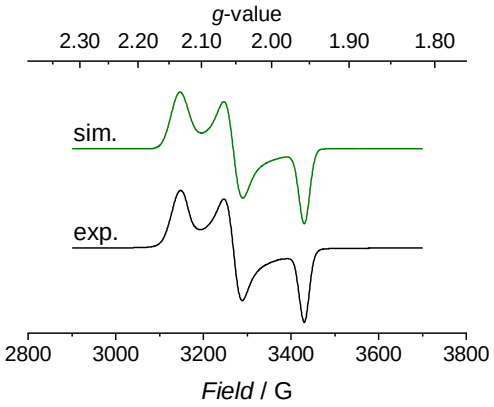

Figure 65. X-band EPR spectrum of complex **13a** in frozen PrCN solution at 146 K. The green line represents a simulation with g-values 2.13, 2.05 and 1.96.

When oxidizing complex **12b** to **13b**, the changes in the MB spectrum evidenced the formation of the intermediate spin Fe^{III} complex, with a IS of 0.29 mm·s^{-1} similar to other known intermediate spin ferric complexes of strong field ligands.[269–272] The weak axial coordination of a triflate anion leads to an energetically low-lying d_{z^2} orbital and stabilizes the S = 3/2 ground state, and the long Fe–O bonds contribute to the increase in IS, as well as to a higher quadrupole splitting due to increased anisotropy of the electron distribution around Fe. Indeed, SQUID measurements gave a $\chi_m T$ value of 2.122 cm^3·K·mol^{-1} at 205 K, which is in proximity of the theoretical value (1.87 cm^3·K·mol^{-1}). Zero field splitting is responsible for the decrease of χ_mT at temperatures lower than 30 K, as shown in Figure 66.

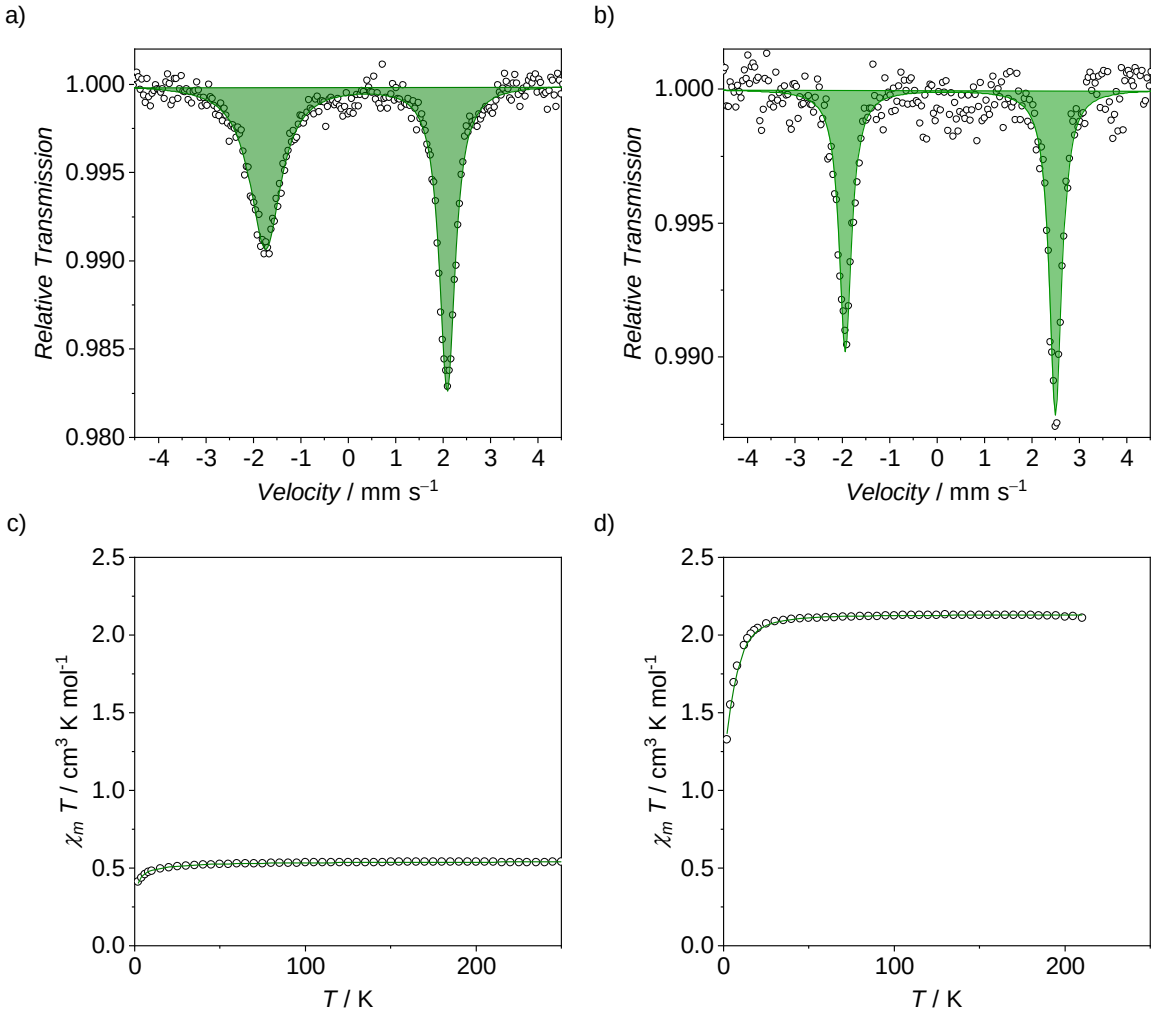

Figure 66. a)-b) Zero-field ^{57}Fe Mössbauer spectra of solid **13a** (a) and **13b** acquired at 80 K (natural abundance. **13a**: $\delta = 0.18$ mm·s^{-1}, $\Delta E_Q = 3.84$ mm·s^{-1}; **13b**: $\delta = 0.29$ mm·s^{-1}, $\Delta E_Q = 4.43$ mm·s^{-1}). c)-d) $\chi_m T$ *vs* T curves of solid samples of **13a** and **13b**, respectively. The empty circlets represent experimental data, while the solid green lines are simulations using equation 2 described in Chapter 3.

Comparison of the experimental results with DFT calculations provided a good depiction of the differences of MB parameters between the two compounds, as shown in Table 5. Plots of spin density and magnetic orbitals of complex **13a** confirmed the presence of an unpaired electron, which appears to be localized both on iron and on the coordinating nitrogen atom of the carbazole fragment (Figure 67), suggesting a strong covalency of the bond. In case of complex **13b** instead, the spin density is completely localized on iron, where all three unpaired electrons are located (Figure 68), providing support for the $S = 3/2$ ground state found experimentally.

Table 5. Experimental and DFT-calculated (italics) Mößbauer parameters of complexes **13a** and **13b**.

Complex	δ	$\lvert\Delta E_Q\rvert$	Γ
13a	0.18 / *0.15*	3.84 / *3.05*	0.41
13b	0.29 / *0.18*	4.43 / *3.88*	0.32

Γ represent the linewidth in the experimentally recorded spectra.

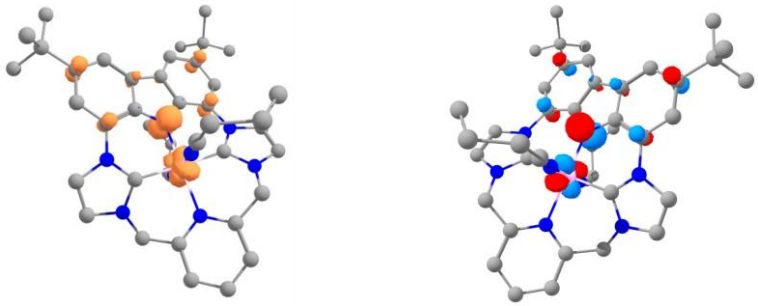

Figure 67. Left: Spin density plot of complex **13a** calculated at the B3LYP level. Spin distribution according to Mulliken population analysis: 37% on iron, 30% on nitrogen. Right: plot of the magnetic orbital of complex **13a**.

a)

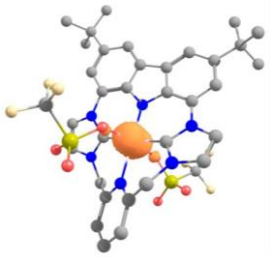

b)

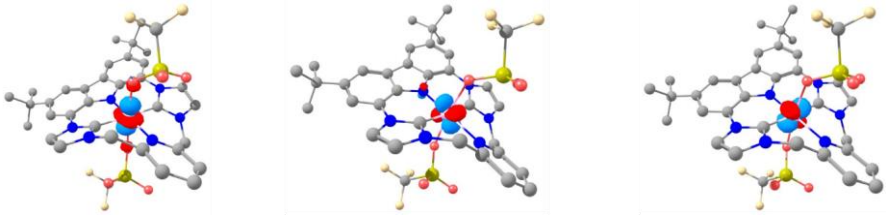

Figure 68. a) Spin density plot of complex **13b** calculated at the B3LYP level. B) Plot of the magnetic orbitals of complex **13b**.

Finally, the broad bands in the optical spectra of **13a** and **13b** first obtained in the UV-SEC experiments and then confirmed with UV/Vis analyses on solution of crystalline materials (Figure 69), were assigned with the help of TDDFT calculations. The broad band at 1005 nm in the absorption spectrum of **13a** belongs to a π to π* transition between orbitals of the Fe–N_{carb} bond (with N_{carb} being the coordinating nitrogen atom of the carbazole fragment, see Figure 94 in Chapter

10), while the feature at 703 nm in the spectrum of **13b** is assigned to two LMCT transitions involving iron and the carbazole fragment of the macrocycle (Figure 98, Chapter 10).

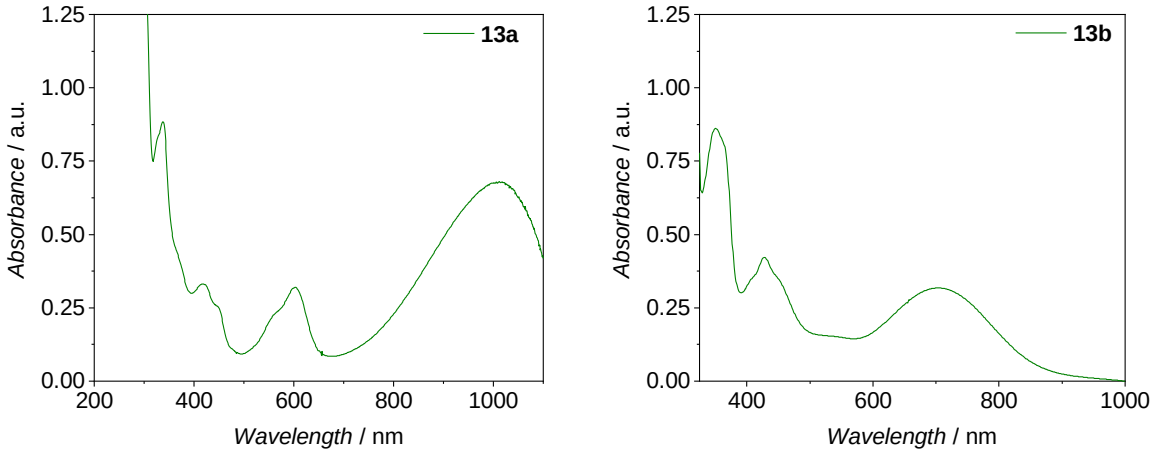

Figure 69. UV/Vis spectra of 0.1 mM solutions of **13a** (in CH_3CN, left) and **13b** (in acetone, right)

Overall, experimental and theoretical analyses on complexes **12a**/**b** and **13a**/**b** confirmed the initial hypothesis according to which the hybrid ligand is able to stabilize iron in different spin states depending on the axial donors. These findings resemble the behavior of typical heme-complexes, although it is more intuitive compared to the one of porphyrin model systems, with the weaker field ligand triflate allowing for the stabilization of the higher spin state.

Ligand-based oxidations

The successful one-electron oxidation of complex **13a** to**14a** was evidenced by the substantial decrease of the isomer shift parameter from 0.18 to 0.09 $mm \cdot s^{-1}$ (Figure 70). Taking into consideration the entire **12a**–**13a**–**14a** redox series we can get initial insight into the nature of the second oxidation by considering the trend in isomer shift upon sequential electron removal. In a redox series of quasi-octahedral low-spin Fe^{II}-Fe^{IV} complexes, the isomer shift trend would return a linear correlation if the valence electron of all complexes are restricted to non-bonding t_{2g} orbitals.[273] In this case **14a** would be the product of a second metal-based oxidation and would possess a Fe^{IV} core. However, experimental isomer shift measurements showed **14a** to possess a lower IS value compared to the expected one (Figure 70 b). If combined with the results of UV-SEC and UV/Vis spectroscopy (Figure 73, see below), this supported the hypothesis that the oxidation from **13a** to **14a** is not metal-based, but rather happening on the carbazolide backbone,

thereby justifying a more contained effect on the metal s orbital and the electron density at the nucleus.

SQUID magnetometry measurements on a powdered sample of complex **14a** revealed a diamagnetic ground state in the whole temperature range between 2-220 K with trace amounts of paramagnetic impurities (see Appendix). Although magnetic susceptibility alone does not rule out the possible formation of a diamagnetic Fe^{IV} complex, assuming the more likely option of the presence of a low-spin Fe^{III} center antiferromagnetically coupled with an unpaired electron on the oxidized carbazolide backbone would return a J value higher than 1000 cm^{-1} according to the temperature dependence of the magnetic susceptibility.[274] Confirmation of the diamagnetic ground state of complex **14a** was provided by ^{1}H-NMR spectroscopy in CH_3CN at −35°C, which shows signal patterns similar to the ones of **12a** (see Appendix). The broadening of all the signals would be in accordance with the presence of some residual paramagnetism in solution.

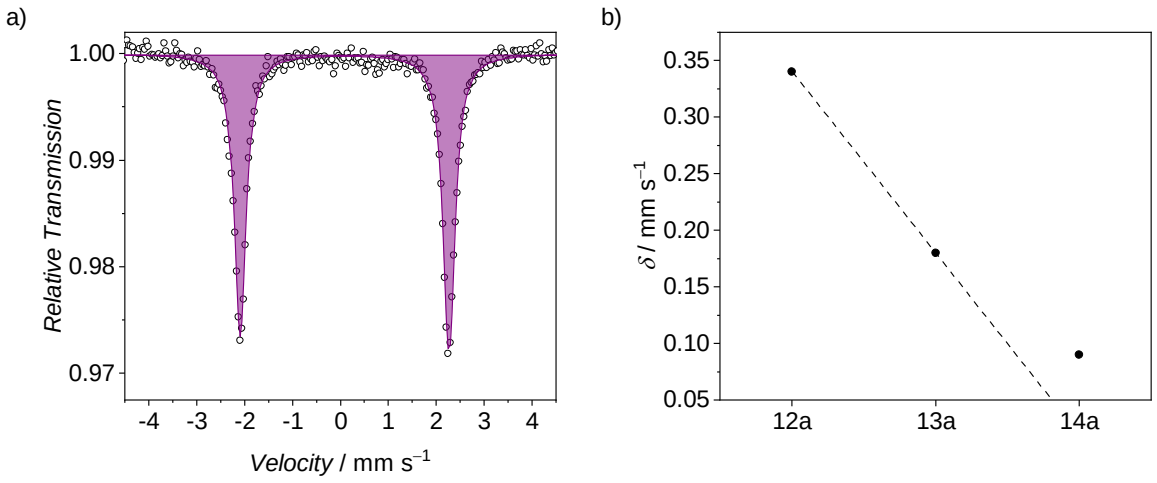

Figure 70. a) Zero-field ^{57}Fe Mössbauer spectrum of solid **14a** acquired at 80 K (natural abundance. **14a**: δ = 0.09 mm·s^{-1}, ΔE_Q = 4.36 mm·s^{-1}). b) plot of isomer shift parameters for complexes **12a**, **13a** and **14a** and linear projection of the theoretical trend explained in the text.

An analogous situation, albeit more straightforward, arose in the case of intermediate-spin complexes **12b**, **13b** and **14b**. For this second redox series, the isomer shift trend with increasing formal oxidation state also deviated from linearity, with a smaller effect of the second oxidation. SQUID magnetometry measurements of complex **14b** provided support for the presence of an S = 3/2 Fe^{III} center coupled with a radical cation on the ligand: fitting of the dependency of the susceptibility with temperature above 30 K returned a coupling constant J of –61 cm^{-1}.

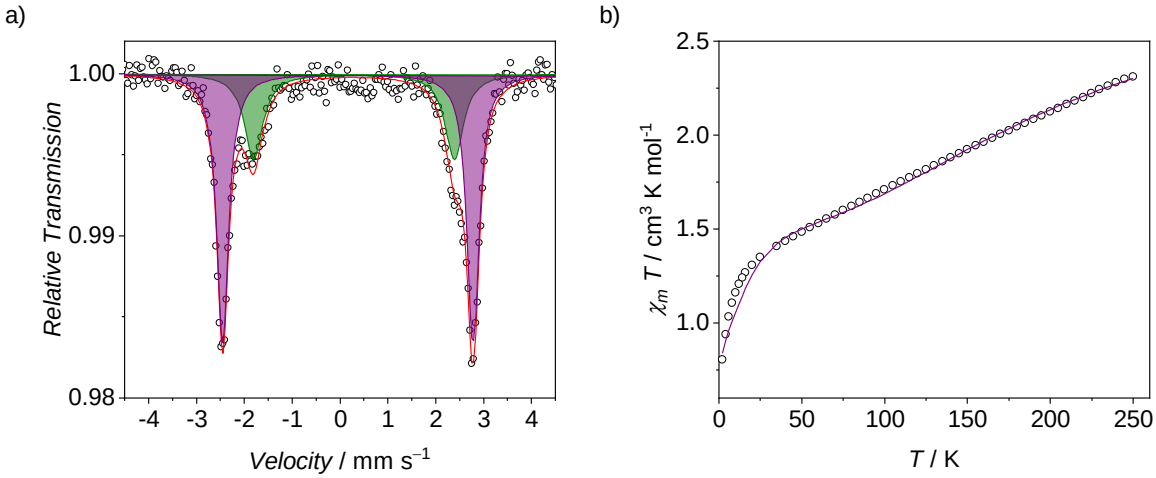

Figure 71. a) Zero-field ^{57}Fe Mössbauer spectra of solid **14b** acquired at 80 K (natural abundance. **14b**: δ = 0.16 mm·s^{-1}, ΔE_Q = 5.23 mm·s^{-1}); The green subspectrum evidences the presence of starting material **13b** in the solid mixture. b) $\chi_m T$ *vs* T curves of a solid sample of **14b**. Best fit parameters for **14b** are: g_{Fe} = 2.42, g_R = 2.00 (fixed), D_{Fe} = –29 cm^{-1}, $J_{Fe\text{-}R}$ = –62 cm^{-1}, *TIP* = 122.4·10^{-6} cm^3·mol^{-1} (see section 9.1 Materials and Methods for details). The empty circlets represent experimental data, while the solid purple line is a simulations using equation 2 described in Chapter 3.

DFT calculations for **14a** and **14b** were performed on different possible electronic configuration, in order to assess the nature of the respective ground states in comparison with the experimental spectroscopic results. The lowest energy configurations for both complexes describe them as containing Fe^{III} centers antiferromagnetically coupled with radicals on the carbazole scaffold, thereby supporting the hypothesis formulated from the experimental findings. Indeed, the broken symmetry state of **14a** lays 2.43 kcal·mol^{-1} lower than a Fe^{IV} singlet state and the one of **14b** lays 3.64 kcal·mol^{-1} lower than the corresponding S = 2 Fe^{IV} state.

Further support for the presence of a radical cation ligand in the complexes was provided by the plots of the magnetic orbitals for the energetically more stable broken symmetry states showed in Figure 72. Complex **14a** expectedly possesses two magnetic orbitals, one localized on the iron atom and the other on the ligand scaffold, albeit with major contributions from the metal center due to the covalent bonding, as explained above. **14b** instead shows four distinct magnetic orbitals, three of which spin up and located on iron and the spin down one on the carbazole ligand.

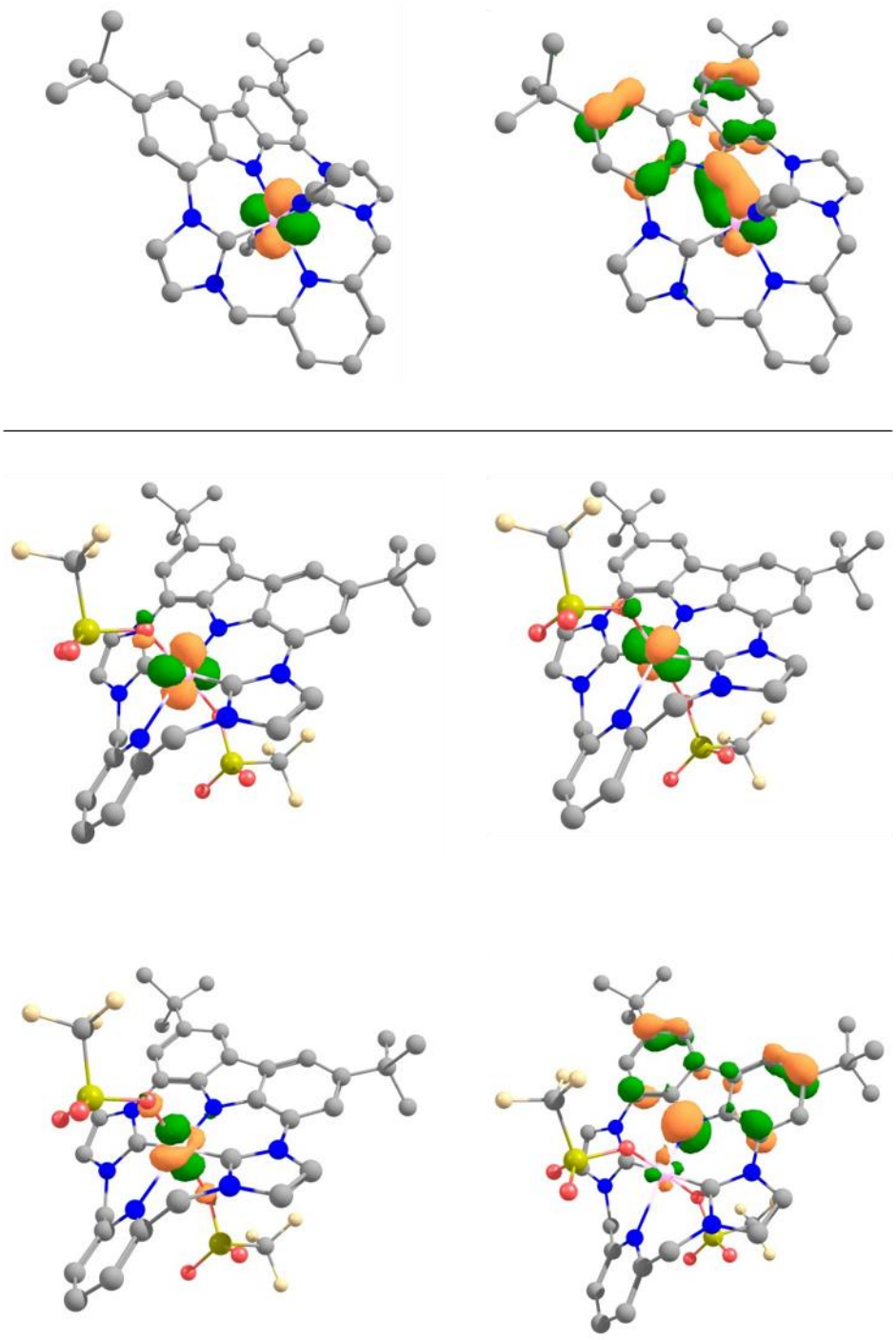

Figure 72. Plots of magnetic orbitals obtained at the B3LYP level of theory for complex **14a** (top two) and **14b** (bottom). **14a** left: spin up orbital; right: spin down orbital. **14b**: metal-based spin up orbitals: top two and bottom left; ligand-based spin down orbital: bottom right.

TDDFT calculations allowed the interpretation of the optical spectra of **14a**/**b** (Figure 73) confirming that the low energy bands belong to intervalence charge transfer transitions between π-orbitals of the ligand scaffold for both complexes, as signature of the radical character, as shown

by the plots the natural transition orbitals that contribute to the states involved in the low energy transitions (see Chapter 10 Figure 103 and Figure 107).

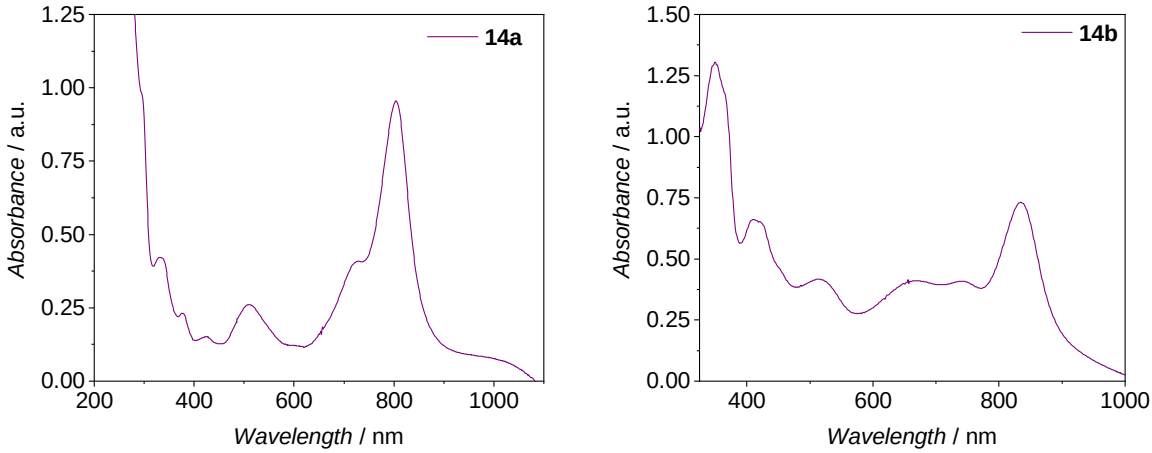

Figure 73. UV/Vis spectra of a 37.5 μM solution of **14a** in CH_3CN (left) and of a 75 μM solution of **14b** in acetone (right) at –40 °C.

Overall, density functional theory calculations provided strong support for the redox-non innocent nature of the hybrid macrocycle and the possibility to access ferric-π-radical cation complexes in two different spin states, although the covalency of the Fe–N_{carb} bond in the low-spin complex **14a** renders the assignment of formal oxidation states more challenging.

The combination of theoretical results with the experimental electronic structure determination of the complexes provided solid evidence for the ability of this new non-heme hybrid system to efficiently showcase typical features of heme analogues.

6.7 Conclusions

This chapter presented the synthesis of a new NHC/N-donor hybrid macrocycle containing two trans imidazolium moieties, a redox-non innocent carbazole and a pyridine unit. Upon metalation with FeHMDS in CH_3CN, the formation of the octahedral low-spin complex **12a** was confirmed by structural and spectroscopic analysis. Dissolution of the complex in non-coordinating solvents allowed for the isolation of the square pyramidal, S = 1 complex **12b** formed upon loss of axial CH_3CN molecules and coordination of the weaker field triflate counterion. Electrochemical and optical studies on both complexes suggested the possibility to isolate one- and two-electrons oxidized complexes, the latter of which showed optical signatures of the presence of carbazolide-based radicals. The successful synthesis and structural characterization, combined with

spectroscopic and DFT analyses that provided electronic structure insights, confirmed the ability of the new ligand scaffold to stabilize iron complexes with different spin states by variation of the axial coordination, and the redox-non innocent nature of the macrocycle upon second oxidation to complexes **14a**/**b**. Overall, this new non-heme system shows spectroscopic and structural properties similar to analogous heme systems, where anionic macrocycles can stabilize iron in different spin states depending on axial ligation, and where the porphyrin macrocycle can be oxidized to form ferric-π-radical cation complexes. Therefore, these new complexes constitute a promising base to study the effect of spin states and non-innocent ligands on the activation of small molecules by a non-heme system that contains NHC donors and mimics some features of porphyrin complexes found in natural enzymes. The next chapter will present the initial results on the synthesis of a series of $\{FeNO\}^{x}$ complexes using **12a** as starting scaffold.

7. A Hybrid {FeNO}^{7} Complex and Initial Characterization of a New {FeNO}$^{"5"–8}$ Complexes Series

7.1 Introduction and Previous Results

The design of model heme and non-heme iron-nitrosyl complexes has attracted a growing deal of attention in the last decade, although the involvement of such Fe–NO species in the biology of both mammals and bacteria has been known for long time.[275] Low concentrations of otherwise toxic NO radical are produced in the body of mammals by nitric oxide synthase (NOS) enzymes to perform a variety of functions that range from activating immune responses, modulating vasodilation, transduction of nervous signals and carcinogenesis.[276,277] Bacteria instead, are capable to mitigate the toxicity of NO by reduction to N_2O exploiting nitric oxide reductases (NORs) and NO-reducing flavodiiron enzymes (FNORs), as part of the denitrification cycle that transforms nitrate into dinitrogen.[278–284] Indeed, both heme and non-heme iron-nitrosyl compounds and their corresponding redox products have been characterized as key intermediates in the catalytic cycles of such enzymes and prompted for the synthesis of model compounds to overcome their high instability and the challenges posed by their direct characterization.

In Fe–NO complexes nitric oxide acts as a redox non-innocent ligand that can be found in a variety of redox and spin states and that forms strongly covalent bonds with the metal center. Since iron is also capable of accessing multiple oxidation and spin states, assignation of formal oxidation states to the metal and the NO moiety in such complex is often extremely challenging. Therefore, iron-NO compounds are best described using the Enemark-Feltham notation {FeNO}^{x}, in which the Fe-NO group is treated as a single unit and where x is the sum of the valence electrons in the d orbitals of iron and in π* orbitals of NO.[285]

Natural heme and non-heme iron-nitric oxide complexes show differences in electronic structures, with heme-{FeNO}^{7} complexes most often found in low-spin states, while non-heme intermediates have predominantly high-spin S_T = 3/2 ground states coming from the antiferromagnetic coupling between a high-spin Fe^{III} center with a triplet NO^- ligand.[286–288] However, many low-spin (S = 1/2) non-heme model complexes have been synthesized after the first report from Wieghardt and coworkers in 2000, who presented an {FeNO}^{6,7,8} series of low-spin cyclam-Fe-NO octahedral complexes followed by in-dept spectroscopic and structural characterization of a series with a modified macrocycle (although the latter was limited to the {FeNO}$^{6-7}$ couple).[289,290] In 2016 our group reported a complete series of low-spin {FeNO}$^{6-8}$ complexes stabilized by the tetracarbene macrocycle and provided the first XRD analysis of a non-heme {FeNO}^{8} complex.[291] The {FeNO}^{7} complex of the series presented an unusual linear arrangement of the Fe-NO moiety deriving

directly from the electronic structure, in contrast to the steric strain that forced linearity in other model complexes.[292] More recently, the strong donor properties of NHCs have been exploited by the group of Prof. K. Meyer to isolate and fully characterize an outstanding {FeNO}$^{6\text{-}10}$ series of non-heme complexes that constituted an invaluable system to understand the effect of the electronic structure of the complexes on their spectroscopic and magnetic properties.[293]

Given the beneficial use of NHCs in the isolation of unstable {FeNO}^{x} models and the interest in evaluating the effect of the electronic structure of the complexes on the properties of the Fe-NO moiety, the design of new supporting ligands for the generation of iron-nitrosyl systems is a lively field of organometallic chemistry.

The novel combination of a macrocycle bearing NHCs and a redox active carbazole group and the ability of such system to stabilize iron in different redox and spin states provided an exciting framework to build a new {FeNO}^{x} series with electronic properties at the boundary between heme and non-heme model systems. This chapter reports the synthesis of a novel {FeNO}^{7} complex starting from complex **12a**, and the isolation and initial characterization of a {FeNO}$^{\text{"5"}\text{-}8}$ series of complexes of the hybrid macrocycle.

7.2 A {FeNO}^{7} Complex of the Hybrid Ligand 11

In Chapter 6 it has been shown how the axial CH_3CN molecules of complex **12a** can be readily displaced by the triflate counteranion via simple dissolution in non-coordinating solvents, and how exposing **12a** to vacuum for some time caused the removal of the coordinated solvent. Hence the substitution of coordinated CH_3CN with stronger donor ligands is expected to be easy, especially with π-acceptors which can reduce electron density on the electron-rich Fe center of **12a**. Convenient strategies for the synthesis of {FeNO}^{7} complexes usually involve treatment of the Fe^{II} species with either NO gas or a NO radical releasing agent to displace a labile axial ligand. One of the most common NO releasing agents soluble in organic media is trityl *S*-nitrosothiol, which can readily release NO radicals and form a stable disulfide as driving force of the reaction (Scheme 11).[294–296]

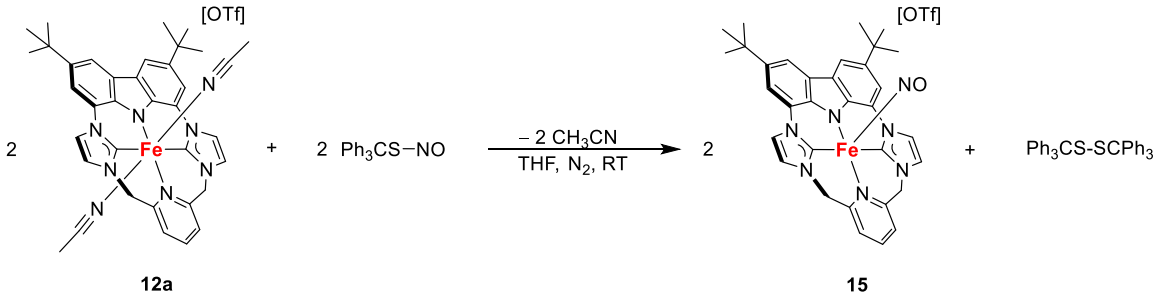

Scheme 11. Reaction equation for the synthesis of the {FeNO}^{7} complex **15**.

When **12a** was dissolved in THF and treated with equimolar amounts of trityl *S*-nitrosothiol, a fast color change from orange to deep green/brown was observed together with the precipitation of a solid product. Full precipitation with diethyl ether afforded a dark green powder that could be dissolved in CH_3CN and analyzed by mass spectrometry. The ESI-MS analysis of the solution showed a single peak at *m/z* 599.1 matching with the molecular weight and isotopic pattern of the cation [(**11**)Fe(NO)]$^+$ of complex **15** (Figure 74 and Appendix). When the ion was dissociated in CID experiments, formation of the molecular ion at *m/z* 569.1, corresponding to **12a** upon loss of coordinated CH_3CN and the triflate counterion, was the only process recorded, and the difference of 30 units in the *m/z* ratio between parent and dissociated ion confirmed the loss of coordinated NO.

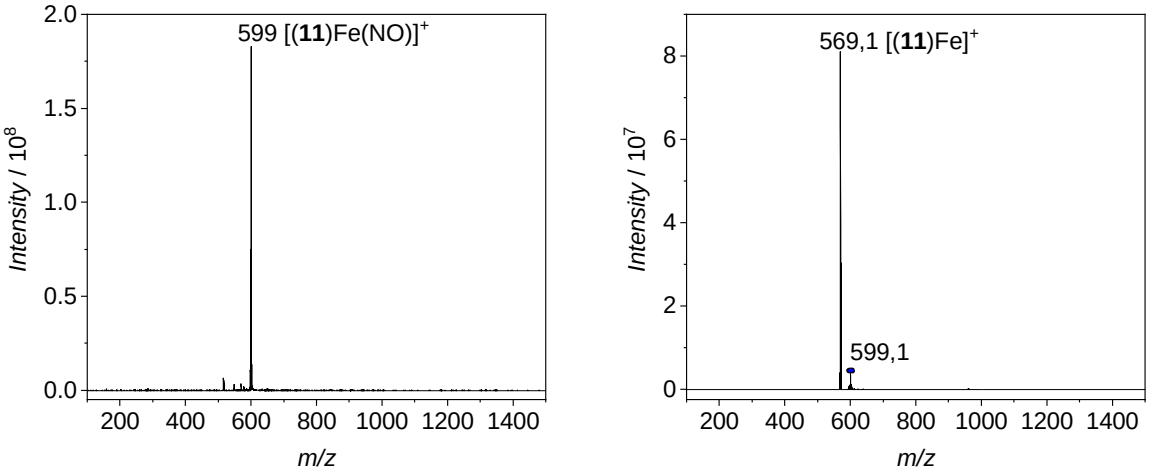

Figure 74. ESI-MS spectra of an CH_3CN solution of **15** at room temperature. Left: total spectrum. Right: CID experiment on the isolated ion at *m/z* 599.

Slow diffusion of diethyl ether into a concentrated solution in CH_3CN afforded single crystals suitable for XRD measurements. Complex **15** crystallizes in the orthorhombic space group *Pbca*, with a five-coordinated metal center. The complex adopts a square pyramidal geometry with NO

coordinating in the axial position and the hybrid ligand in the equatorial plane adopting the ruffled/twisted arrangement seen in all complexes **12**–**14 a**/**b**. The C–Fe–C and N–Fe–N angles of 163.0 and 166.1° respectively give a geometric parameter τ of 0.05 close to the perfect tetragonal geometry.[297] Although a triflate anion is located on the opposite side of the macrocycle with respect to NO, the distance between Fe and one of the oxygen atoms is about 3.01 Å, suggesting the absence of any significant bonding interaction (Figure 75).

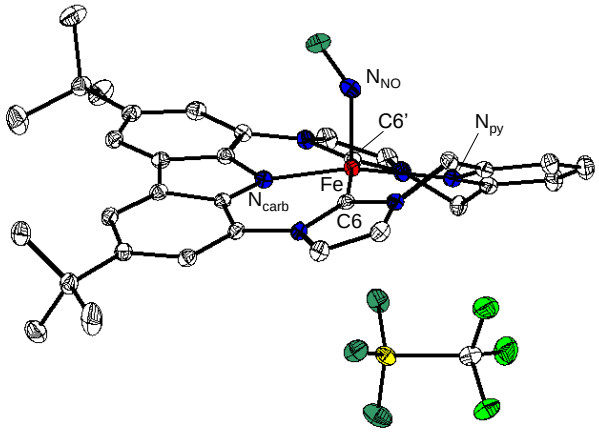

Figure 75. Molecular structure of complex **15** reported as 50% thermal ellipsoids. Lattice solvent molecules and hydrogen atoms omitted for clarity.

The iron center of **15** is located 0.26 Å above the {N_2C_2} plane in the direction of the NO ligand, as expected due to the typically strong covalent Fe–NO interaction. The Fe–NO distance of 1.714 Å is slightly longer compared to the analogous tetracarbene {FeNO}^{7} complex but still falls among the shortest ones compared to reported non-heme {FeNO}^{7} complexes.[298] The bent Fe–N–O angle of 143.7° reminds of the range reported for heme-based {FeNO}^{7} models (140–145°) and falls among the lower values for synthetic non-heme ranges, which show a large variability of angles due to different electronic structures or to steric requirements of the supporting ligands.[298–300] The N–O distance of 1.177 Å is instead within the expected range for {FeNO}^{7} complexes.[301] As seen for complexes **12a**–**14a**, the Fe-N_{carb} bond is the shortest among the ones of the equatorial plane, probably due to the covalent interaction present in the low-spin complexes.

In order to investigate the redox properties of the complex and the role of the non-innocent hybrid ligand, crystals of **15** were dissolved in a 0.1 M $TBAPF_6$ CH_3CN solution and cyclic voltammetry

measurements were conducted. When the applied potentials were scanned, anodically first, in a window between −2.0 and +1.2 V *vs.* $Fc^{+/0}$ three reversible redox events were recorded: two oxidations at −0.09 and 0.54 V and a reduction at −1.42 V (Figure 76).

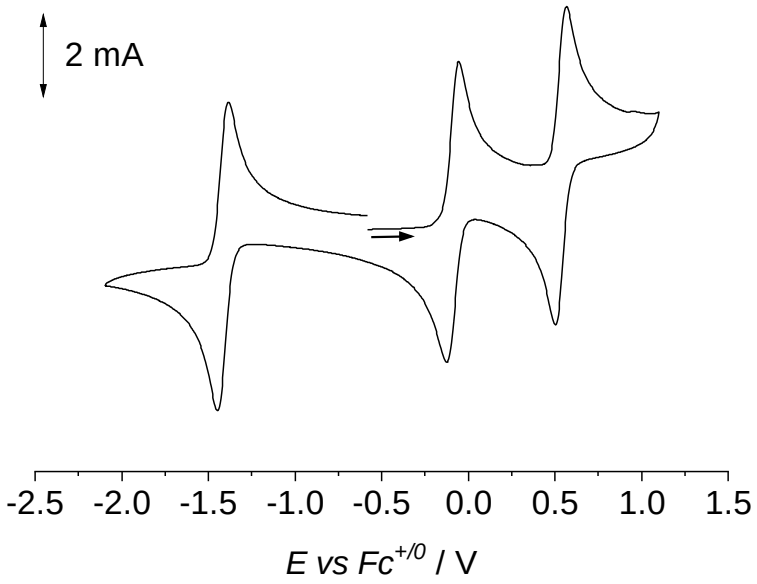

Figure 76. Cyclic voltammogram of a 1 mM solution of crystalline **15** in CH_3CN 0.1 M $^nBu_4NPF_6$ at a scan rate of 0.1 V/s.

All three events showed Δ*E* parameters close to the ideal 57 mV (74, 64 and 70 mV for first, second oxidation and reduction respectively) expected for a reversible one-electron process.

The rich electrochemistry of complex **15** in solution opened the interesting possibility to isolate a series of {FeNO}^{X} complexes spanning from a formal {FeNO}^{5} to a {FeNO}^{8} complex, the synthesis and characterization of which will be explored in the next section. Moreover, when a cathodic scan down to −3 V was performed, a second irreversible reduction at −2.51 V appeared, suggesting the possibility to form an {FeNO}^{9} complex. However, the synthetic challenge posed by such a low reduction potential did not allow for the isolation of such species so far.

The two reversible oxidations of complex **15** deserve special consideration. In the case of a redox-innocent supporting ligand, the appearance of two oxidation events in the cyclic voltammograms would indicate two processes that would yeld the corresponding {FeNO}^{6} and {FeNO}^{5} complexes. However, in Chapter 6 the hybrid ligand was shown to be redox active towards oxidation, with the electrochemically reversible formation of the corresponding π-radical cation at potentials around 0.6 V *vs.* $Fc^{+/0}$ in CH_3CN. Therefore, it is reasonable to assume that one of the oxidations may occur on the macrocyclic ligand scaffold, rather than on the Fe-NO unit, leading to the formation of either a (**11**$^{\bullet+}$){FeNO}^{7} or a (**11**$^{\bullet+}$){FeNO}^{6} complex. As shown in the case of complexes **14a**/**b** the

presence of a radical macrocycle can be easily confirmed by optical spectroscopy, given the signature of the typical carbazole-based radical in the 700-900 nm region.

In order to elucidate the nature of the redox events seen for complex **15**, UV-SEC experiments were performed for all three electrochemically reversible events, the results of which are shown in Figure 77 and in the Appendix.

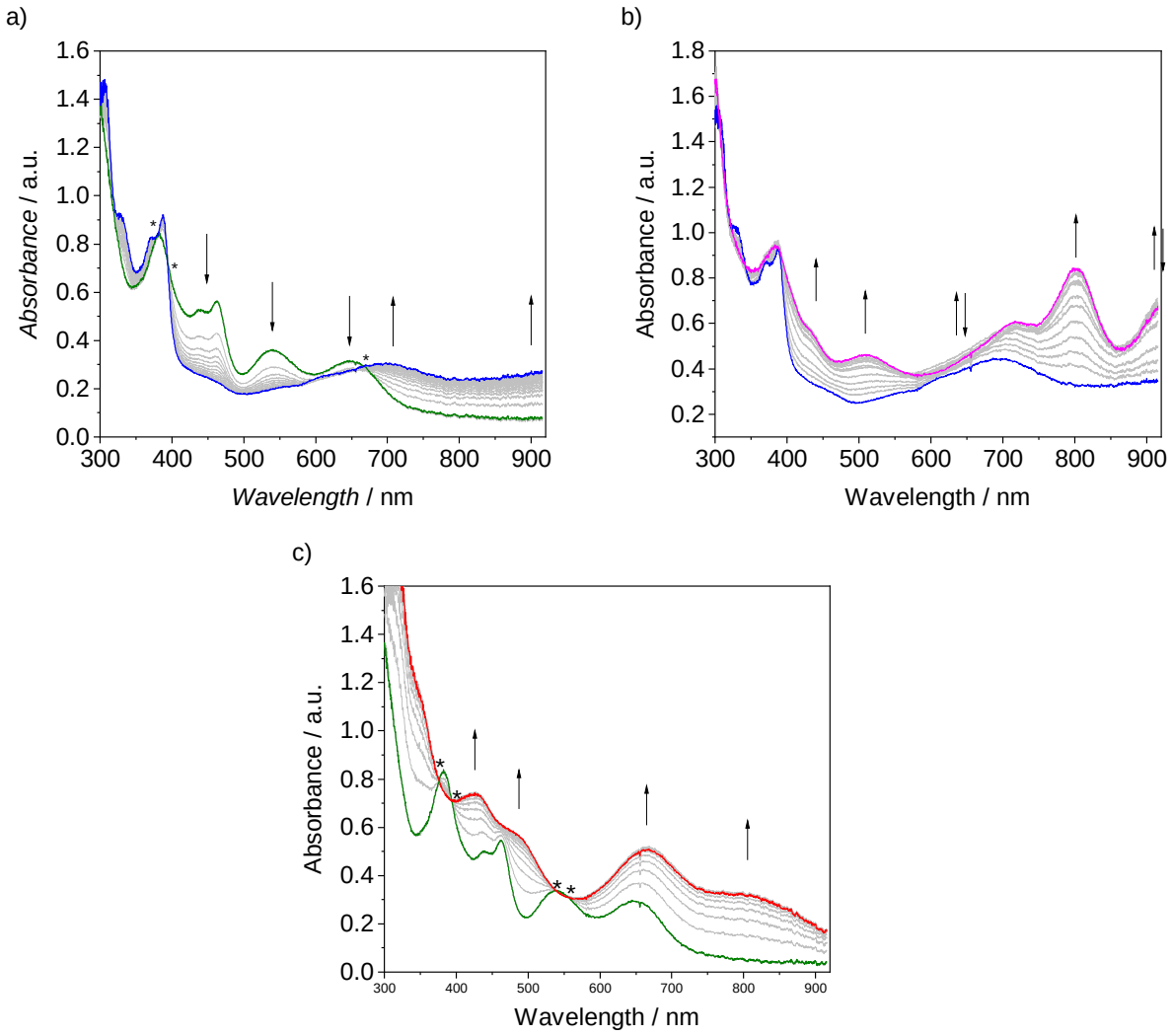

Figure 77. UV/Vis spectroelectrochemistry of a 1 mM solution of complex **15** in CH_3CN 0.1 M $^n Bu_4NPF_6$. a) first oxidation of **15** (green spectrum) at an applied potential of 0.4 V vs $Fc^{+/0}$; b) second oxidation of the mono-oxidized complex (blue spectrum) at an applied potential of 1.1 V vs $Fc^{+/0}$; c) reduction of complex 15 at an applied potential of –1.9 V vs $Fc^{+/0}$.

The application of a potential of 0.4 V *vs* $Fc^{+/0}$ for 600 seconds caused the disappearance of the optical features of complex **15** (plotted in green) and the rising of bands at 388 and 698 nm with two isosbestic points at 380 and 393 nm, accompanying the formation of a blue compound. Re-reduction at –0.6 V afforded complex **15** (as shown in Appendix) thereby confirming the chemical

reversibility of this first oxidation. No intense features in the 700-900 nm region were observed, thereby suggesting a metal- or NO-based oxidation to a {FeNO}^{6} complex. Indeed, the rise of a broad band in the NIR portion of the spectrum reminds of the broad NIR band of the ferric complex **13a** (a full UV/Vis spectrum of the {FeNO}^{6} complex is shown in the Appendix). Applying a potential of 1.1 V for 600 seconds to this blue oxidized species led to the chemically irreversible formation of a temperature sensitive purple complex showing two absorptions at 700 and 800 nm similar to the ones of the radical complex **14a** and an intense NIR band. The first spectroscopic signature suggested the carbazolide-based nature of this second oxidation, that would give a complex better described as (**11**$^{\bullet+}$){FeNO}^{6}.

When a cathodic potential of −1.9 V was applied to a fresh solution of complex **15** for 10 minutes, the appearance of a red-fuchsia species was accompanied by the rising of optical features at 427, 668 and 797 nm with isosbestic points at 376, 393, 539 and 555 nm thereby evidencing a clean "A to B" one-step reduction. However, re-oxidation only partially recovered the initial spectrum of **15**, indicating chemical irreversibility of the process. Indeed, as mentioned below, the putative {FeNO}^{8} complex appeared to be unstable in solution at room temperature when synthesized in bulk.

These promising initial findings prompted for the isolation of the three putative {FeNO}^{8,6} and (**11**$^{\bullet+}$){FeNO}^{6} complexes, as described in the following section.

7.3 Synthesis of the Series and Structure of the {FeNO}^{6} Complex

Comparison of the redox properties of **15** and **12a** evidenced similar potentials for both oxidation events and allowed for the use of silver triflate and tianthrenium hexafluorophosphate as oxidants of suitable strength, cf. Chapter 6. Bulk reduction to the putative {FeNO}^{8} complex proved to be more challenging. In fact, only few reducing agents of suitable strength (potential lower than −1.4 V *vs.* $Fc^{+/0}$) are available for use in nitrile solvents. Treatment of **15** with decamethylcobaltocene afforded mixtures of products the purification of which proved particularly challenging. Therefore, the incompatibility of CH_3CN with stronger reductants prompted for the use of THF as a more reduction-inert solvent. However, the use of potassium graphite led to decomposition of the complexes, possibly due to the challenging control of stoichiometry, while stoichiometric amounts of sodium naphtalenide also led to the formation of mixtures. The recent work from K. Meyer and co-workers reported a convenient strategy for reduction of their novel {FeNO}^{X} series of complexes by use of electropositive metals as reductant in organic solvents.[302] In particular, the use of zinc turnings in CH_3CN allowed for the reduction of their {FeNO}^{6} complex to the corresponding {FeNO}^{7} analogue ($E_{1/2}$ = 0.32 V vs $Fc^{+/0}$), while treating the latter with magnesium in CH_3CN

allowed for the synthesis of the reduced {FeNO}^{8} complex ($E_{1/2}$ = –0.75 V vs $Fc^{+/0}$).[293] Taking this work as inspiration, treatment of an CH_3CN solution of **15** with magnesium turnings for several hours at RT caused a color change of the solution from orange to red-fuchsia, as seen in the UV-SEC experiments. After filtration of excess Mg metal, the reddish product proved to be unstable at room temperature but indefinitely stable at –40°C, thereby allowing for precipitation of the product.

Scheme 12 summarizes the synthetic strategies used for the isolation of complexes **15**–**18**, while their initial spectroscopic characterization will be treated in the next section.

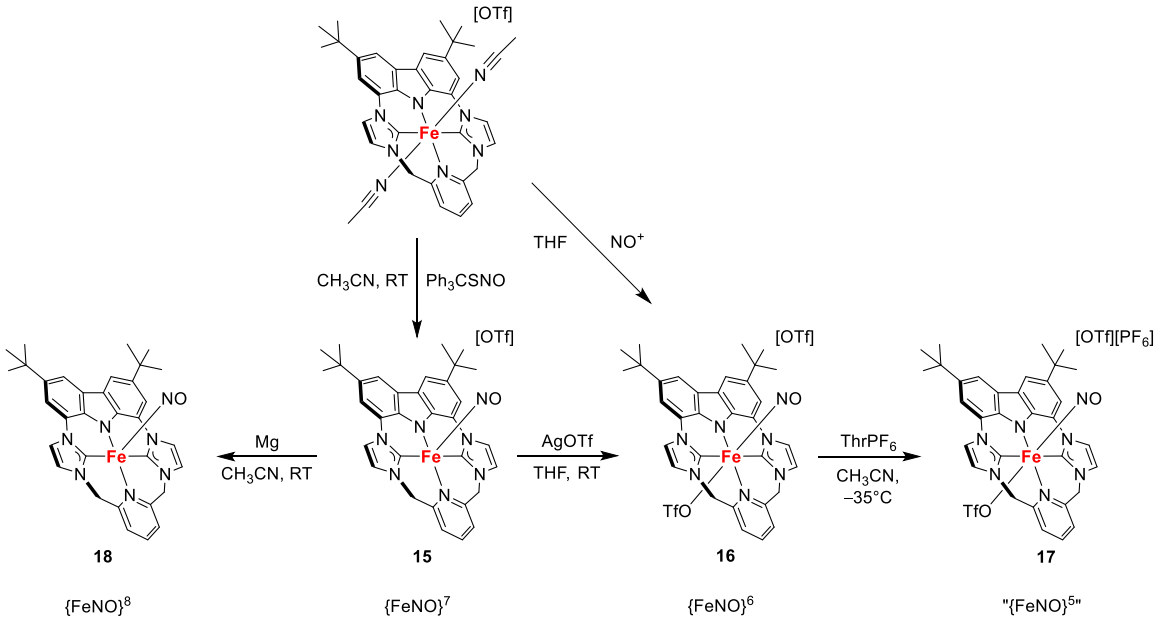

Scheme 12. Synthesis of complexes **15**–**18** starting from **12a**.

When a THF solution of **15** was treated with 1 eq. of [Ag][OTf] at room temperature, a fast color change from deep green/brown to blue and the precipitation of the product together with Ag particles provided evidence for the successful oxidation. Dissolution of the blue product in CH_3CN, filtration, and slow diffusion of diethyl ether afforded single crystals suitable for XRD measurements. Figure 78 shows the molecular structure of the cation of complex **16**.

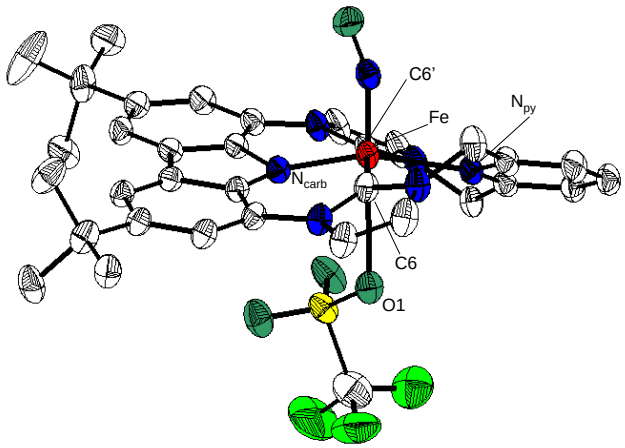

Figure 78. Molecular structure of the cation of complex **16** reported as 50% thermal ellipsoids. Counteranions, lattice solvent molecules and hydrogen atoms omitted for clarity.

Table 1. Selected bond lengths (Å), angles (°) of complexes **15** and **16**.

Bond	**15**	**16**
Fe–N$_{carb}$	1.895	1.868
Fe–N$_{py}$	2.140	2.142
Fe–C6	1.964	1.964
Fe–C6’	1.967	1.952
Fe–NO	1.714	1.659
N–O	1.177	1.152
Angle		
N$_{carb}$–Fe–C6	87.46	88.11
N$_{carb}$–Fe–C6’	87.43	88.04
N$_{py}$–Fe–C6	90.15	88.30
N$_{py}$–Fe–C6’	90.96	90.40
N$_{carb}$–Fe–N$_{py}$	166.11	161.50
C6–Fe–C6’	163.01	163.87
Fe–N–O	143.67	158.10

The complex crystallizes in the triclinic space group $P\bar{1}$ and octahedral geometry with a triflate anion as axial ligand occupying the position *trans* to NO. Despite the coordination of triflate (Fe–O_{OTf} distance = 2.823 Å) the iron center sits now 0.30 above the $\{N_2C_2\}$ plane, significantly closer to NO compared to **15**. All coordinative bonds apart from the Fe–N_{py} are shorter than in the parent {FeNO}^{7} complex, as one would expect from the metal-based oxidation suggested by UV-SEC experiments. In particular the Fe–NO bond of 1.659 Å is 0.027 Å shorter than in **15**, and the Fe-N-O angle of 158.1° is broader than in the parent compound, as expected for an oxidized {FeNO}^{6} complex.[303–305] The N-O distance is also slightly shorter (1.152 Å), compatible with lower back donation derived from the oxidation of the metal center.

Therefore, the oxidation of **15** in THF proceeds via the coordination of the additional triflate anion on the axial position. This behavior is in agreement with the one seen for complex **12b** and **13b**, where the use of non-coordinating solvents forced the pentacoordinated ferrous precursor to accept an additional triflate ligand upon oxidation, although with a very weak bond. The Fe–O_{Otf} distance of 2.823 Å in **16** is much longer than the corresponding iron-triflate interaction seen in complexes **12b** and **13b**, underlying the strong trans influence of the NO ligand and a very weak bonding interaction. However, complex **16** constitute an example of an octahedrally coordinated non-heme {FeNO}^{6} complex, a class of model compounds that is still not common in presence of a weakly bound axial triflate, more often found bearing nitrito, nitro or other oxidation products of NO bound *trans* to the NO ligand.[306]

7.4 Infrared and Mößbauer Spectroscopy of the {FeNO}^{x} Series

Infrared spectroscopy

IR spectroscopy is a convenient technique to study the electronic structure of Fe-NO complexes, given the typically intense stretching vibrations of the NO moiety. In fact, the position of the band in the spectrum provides a convenient probe for the nature of the bond with the iron center, giving insight into the degree of σ-donation and π-backdonation of the coordinative bond. Figure 79 shows the IR spectra of solid samples of complexes **15**–**18**.

Complex **15** shows an intense peak assigned to the N-O stretching at 1661 cm^{-1}, falling in the expected range of the non-heme low-spin {FeNO}^{7} complexes characterized so far, and similar to low-spin heme models.[290,298,307–310] Comparison with the tetracarbene {FeNO}^{7} complex cited in 7.1, the NO stretching frequency of which was found to be much higher (1748 cm^{-1}), confirms that bent Fe–NO moieties show lower NO stretching frequencies compared to *quasi*-linear ones due to

the more efficient backdonation promoted by increased orbital overlap.[292] One-electron oxidation to complex **16** causes a shift of the NO stretching frequency to 1804 cm^{-1}.

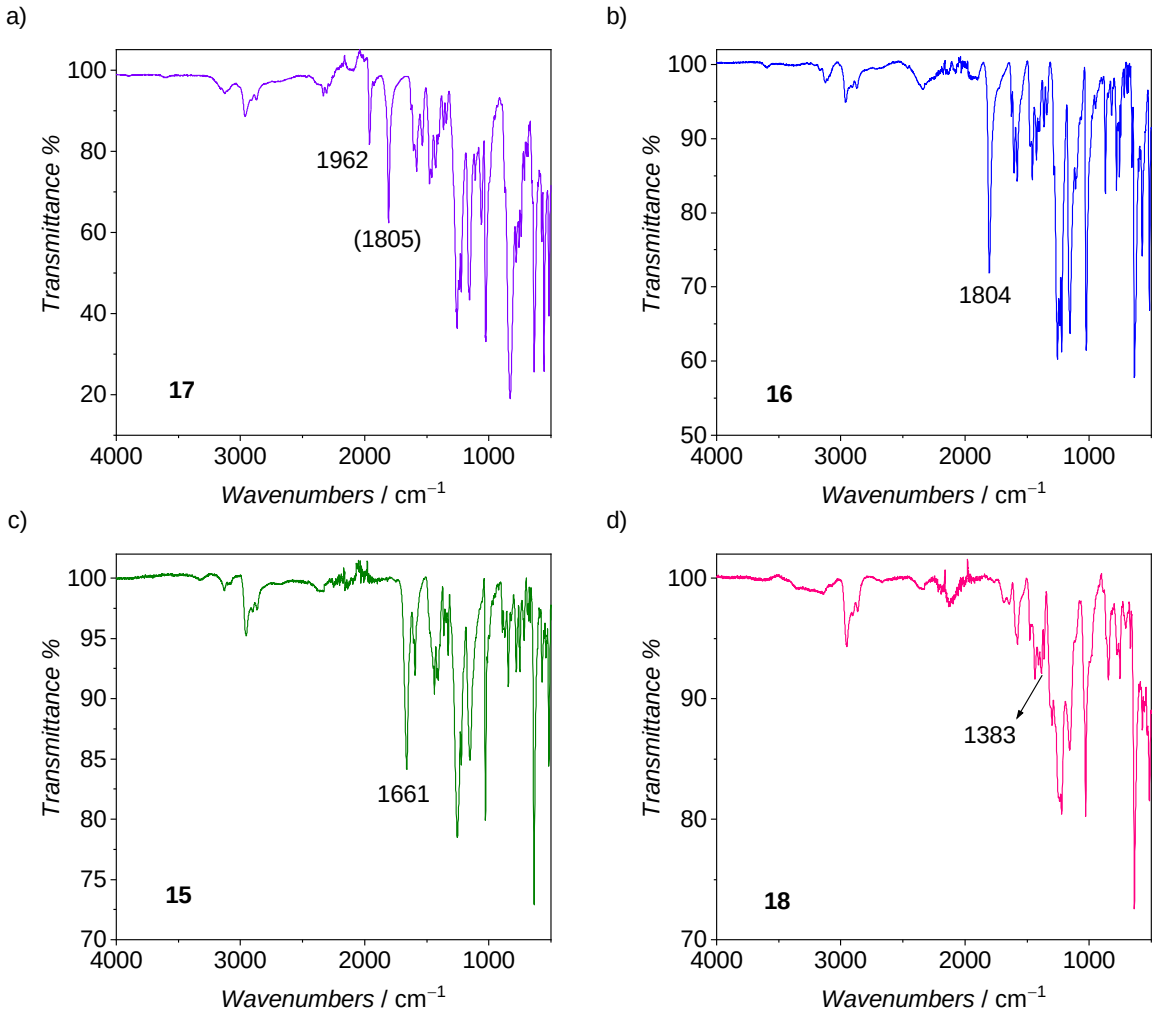

Figure 79. FT-ATR spectra of solid samples of complexes **15**–**18** (c, b, a, d respectively). The instability of complex **17** at room temperature did not allow for recording of clean spectra: the additional band at 1805 cm^{-1} is attributed to the precursor complex **16**.

The higher stretching frequency is in accordance with the removal of one electron from the Fe-NO group, that causes a decrease of backdonation from Fe to a π-antibonding orbital of NO, thereby increasing the bond order of the NO fragment. The shift of 143 cm^{-1} can be considered moderate, in comparison to the ones found in the cyclam-ac complex of Wieghardt and co-workers.[290] The strong changes in the stretching frequency upon oxidation/reduction recorded for the modified-cyclam series were associated with purely NO-based oxidations, while in the case of **15** and **16** the moderate shift could be due to a metal-based electron removal, as suggested by the presence of the NIR band in the optical spectrum of **16** and from structural analysis. The second oxidation to

complex **17** causes a shift of 158 cm^{-1} to 1962 cm^{-1}, confirming the removal of a second electron. It is interesting to note that despite the spectroscopic evidence for a ligand-based oxidation involving the carbazolide moiety of the hybrid macrocycle, the effect on the NO stretching frequency is quite marked and similar to the one obtainable via a metal-based oxidation. A possible explanation of this behavior is the high covalency of the Fe–N_{carb} bond, discussed in chapter 6, that would allow for a substantial decrease of electron density on the metal center even after electron removal from the carbazolide side. Reduction of **15** to the putative {FeNO}^{8} complex **18** causes the disappearance of the band at 1661 cm^{-1} and the slight increase of a feature at 1383 cm^{-1}. The assignment of a proper band associated with the NO stretching is challenging due to the fact that the new feature appeared within the fingerprint region of the spectrum, with massive band overlapping. Moreover, the rather low intensity of the band does not allow for the unambiguous confirmation of the presence of an Fe-NO moiety. {FeNO}^{8} complexes are well known for their instability compared to the stable {FeNO}^{7} analogues, and the UV-SEC experiment already showed the reduction of **15** to be chemically irreversible.[311–313] Therefore, additional measurements will be necessary to confirm the nature of the reduced complex and rule out possible degradation paths.

Mößbauer spectroscopy

Figure 80 shows the MB spectra of complexes **15**–**18**. Complex **15** has an isomer shift parameter of 0.l4 mm·s^{-1} and a quadrupole splitting of 2.61 mm·s^{-1} that suggest its low-spin nature when compared to **12a** (LS, ΔE_Q = 2.33 mm·s^{-1}) and **12b** (IntS, ΔE_Q = 4.26 mm·s^{-1}). Although the iron center is displaced towards the NO ligand to a significant extent, the Fe–C distances similar to the ones in **12a** suggest the interaction with the NHC groups to be strong, and hence to significantly contribute to the anisotropy of the electron density around Fe. The lower isomer shift compared to **12a** can be envisioned as the effect of the σ-donation from and π-backdonation to the NO ligand, which shorten the Fe–NO bond and cause the compression of the metal s orbitals. In fact, donation to the metal via a strong σ-bond directly increases the electron density in metal orbitals with non-zero electron charge at the nucleus, while the backdonation from Fe 3d orbitals to the NO-π* decreases the shielding effect on the s orbitals of the metal. Therefore, both bonding interactions can cause the decrease of isomer shift parameter compared to **12a**.

As introduced previously, redox events on {FeNO}^{x} complexes can take place both on the metal center or on the non-innocent NO ligand. Although the nature of the Fe–NO bond often accounts for major deviations of MB parameters from expected values, the trends of IS and ΔE_Q upon oxidation and reduction can sometimes provide some insight on the nature of the redox process, or at least serve as base for an initial guess. In other cases the non-trivial superimposition of multiple

effects and peculiar electronic structures can cause counterintuitive trends in MB parameters,[293] or can balance out and limit the effect of redox events on isomer shifts, as seen for the tetracarbene series.[291] However, even if the electronic structure of complexes **15**–**18** is not fully elucidated at this stage, the changes of MB parameters upon oxidation and reduction could be interpreted in a straightforward way to provide some initial hypothesis.

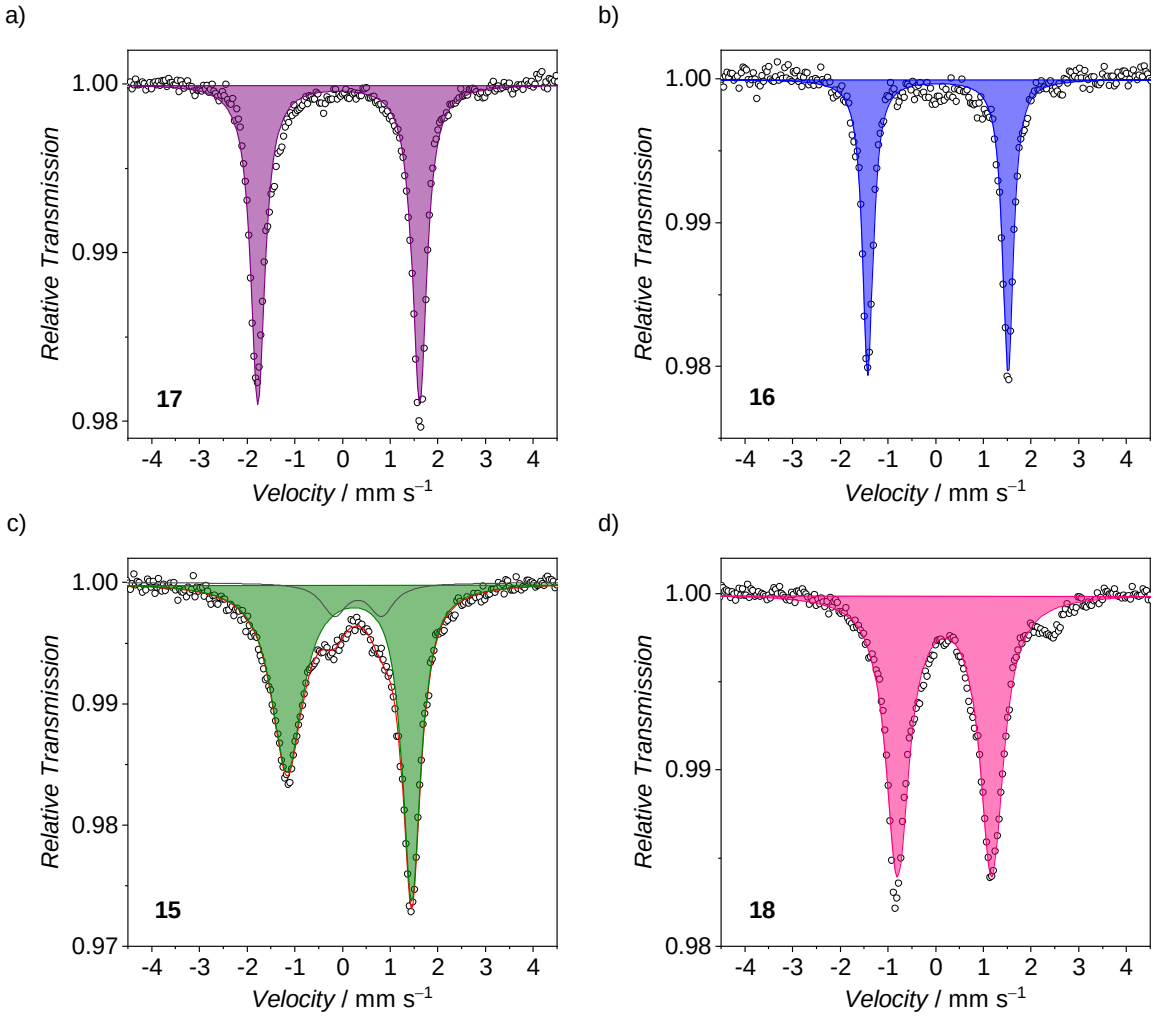

Figure 80. Zero-field ^{57}Fe Mössbauer spectra of solid **17** (a), **16** (b), **15** (c) and **18** (d) acquired at 80 K (natural abundance. **17**: δ = –0.08 mm·s^{-1}, ΔE_Q = 3.42 mm·s^{-1}; **16**: δ = 0.05 mm·s^{-1}, ΔE_Q = 2.94 mm·s^{-1}; **15**: δ = 0.14 mm·s^{-1}, ΔE_Q = 2.61 mm·s^{-1}; **18**: δ = 0.19 mm·s^{-1}, ΔE_Q = 1.98 mm·s^{-1}).

Oxidation from **15** to complex **16** caused a considerable decrease of the IS (from 0.14 to 0.05 mm·s^{-1}) and an increase of the quadrupole splitting to 2.94 mm·s^{-1}. Such a major decrease of IS is typically ascribed to a metal-based oxidation, which directly impacts the population of the metal 3d orbitals and their shielding ability. Indeed, complexes in which the {FeNO}^{7} to {FeNO}^{6} oxidation was assigned to the NO moiety showed a limited indirect effect on the IS.[290] It must be also noted

that the coordination of an additional triflate molecule on the axial position would also contribute to the decrease of the isomer shift. Together with the insight provided by UV-SEC experiments, IR spectroscopy and XRD measurements, it is reasonable to hypothesize the oxidation as being metal-centered.

The second oxidation from **16** to the putative (**11**$^{\bullet+}$){FeNO}^{6} complex **17** caused an even more substantial decrease of the IS to –0.08 mm·s^{-1} and an additional increase of the quadrupole splitting. Keeping in mind the evidence for a macrocycle-based oxidation provided by optical spectroscopy and the proposed covalency of the Fe–N bond as seen for **12a**, we can imagine the impact of the electron removal to substantially influence the metal center, possibly via decreasing the π-donor abilities of the carbazole moiety. The resulting decrease of the shielding effect of the 3d orbitals would then explain the lower IS of **17**. The increase of the electron density anisotropy, seen also for **14a**, can be justified invoking similar considerations on the donor abilities of an oxidized carbazolide group.

Reduction of complex **15** to the putative {FeNO}^{8} analogue increased the IS parameter to the highest value of the series (0.19 mm·s^{-1}), although with only a slight variation compared to **15**. Unfortunately, the absence of structural information for **18** prevents any deeper interpretation of the nature of the reduction. In literature, a small increase of IS upon reduction has often been interpreted with NO-based processes, while addition of an electron to the metal valence shell often caused major shifts. Additional spectroscopic analysis and theoretical calculations will be needed to elucidate the nature of this reduction process, given the possibility of decomposition paths typical of {FeNO}^{8} complexes.

Overall, initial synthetic efforts and spectroscopic characterization provided a strong basis for the establishment of the new series of {FeNO}^{x} complexes, combining the properties of the hybrid complexes with the electronic and redox properties of the NO ligand.

7.5 Conclusions and Outlook

This chapter introduced the synthesis and basic characterization of a new {FeNO}^{7} complex (**15**) derived from the low-spin ferrous complex **12a** upon reaction with an NO releasing agent in THF solution. The successful synthesis of the target compound was confirmed by ESI-MS analysis and single crystal XRD measurements. The complex possesses a square pyramidal geometry, as often observed for {FeNO}^{7} models due to the strong trans influence of the NO ligand. As commonly observed in both heme and non-heme iron-nitrosyl models, the Fe–N–O angle is significantly smaller than 180°, and the N–O bond is longer compared to the ones observed in the linear

arrangement of some sterically constrained complexes or the tetracarbene {FeNO}^{7} complex isolated by Dr. Cordes. Cyclic voltammetry measurements for **15** showed two reversible oxidations at moderate potentials, and a reversible reduction at −1.42 V *vs* $Fc^{+/0}$. UV-SEC experiments suggested the first oxidation to generate a ferric complex with a NIR feature similar to the one of **13a/b**, while the second electron removal to occur on the carbazole backbone and generate a π-radical cation complex (**17**) analogous to **14a/b**. The one-electron oxidized complex **16** could be structurally characterized as a novel example of octahedrally coordinated {FeNO}^{6} complex, deriving from a metal-based electron removal.

IR and MB spectroscopy on complexes **15**–**18** provided initial support to the hypothesis of prevalently metal-based redox processes, although the instability of the putative {FeNO}^{8} complex **18** did not allow for the exclusion of decomposition pathways that would explain the low intensity of the associated IR NO stretching signal.

Overall, the hybrid ligand scaffold provides an interesting new system to exploit the heme-like properties discussed in Chapter 6 in influencing the electronic structure of the {FeNO} unit. In particular, the possibility to access both metal- and macrocycle-based oxidations within the same system provides an exciting possibility to study the effects of electron removal from a site adjacent to the Fe-NO group, compared to direct oxidations on the iron-nitrosyl core.

8. Summary

This work presented the investigation of the electronic structure and reactivity patterns of a range of non-heme iron-carbene complexes that are inspired by enzymatic intermediates. Two main systems were studied: the family of iron-tetracarbene complexes **1**-**10** and the series of complexes **12**-**18** of a newly synthesized NHC/N-donor hybrid ligand framework **11**.

Chapter 3 described the synthesis and characterization of three new tetracarbene oxoiron(IV) complexes where the axial position *trans* to the oxo atom was substituted with a series of coordinating anions: trifluoroacetate (giving rise to complex **4**), chloride (**5**), and *tert*-butyl thiolate (**7**) (Figure 81). The latter represents a rare example of an iron(IV)-oxo complex bearing axial thiolate ligation, which was isolated despite the usual instability of the thiolate ligand toward oxidation in presence of high-valent M-oxo species.

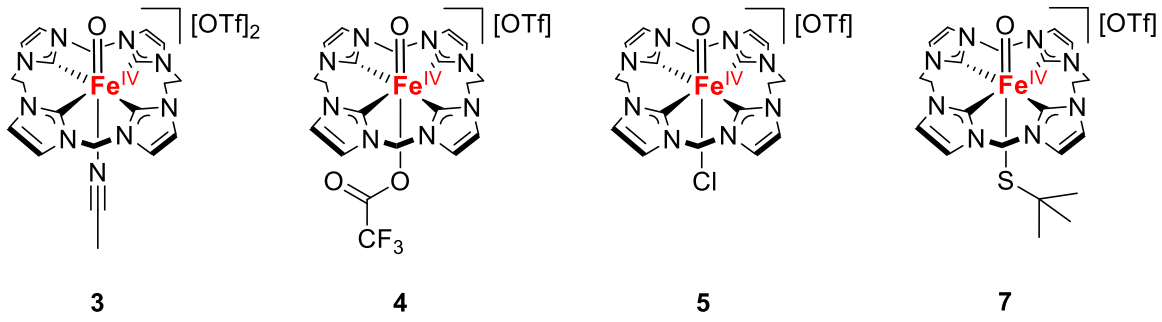

3 **4** **5** **7**

Figure 81. Molecular structure representation of complex **3** and the axially substituted analogues **4**, **5** and **7**.

The series was designed to evaluate the effect of the axial ligand donation ability on the electronic structure of the tetracarbene oxoiron(IV) core. Complexes **4** and **5** showed optical features comparable to the CH_3CN-ligated precursor **3**, with the band corresponding to d-d transitions shifted to lower energies. Indeed, substituting the axial CH_3CN with weaker field anions causes the decrease of the electronic transition energies within the orbital ordering typical of the oxoiron(IV) core, as evidenced by reported cases with the TMC ligand scaffold. Thiolate complex **7** presented a unique absorption pattern due to the modification of the electronic structure owing to the coordination of a σ- and strong π-donor thiolate. Similar changes in electronic absorptions were in fact reported for the tetramethylcyclam (TMC) complexes $[(TMC)Fe(O)(CH_3CN)]^{2+}$ and $[(TMCS)Fe(O)]^{+}$. Complexes **4** and **5** showed Mössbauer parameters comparable to **3**, with negative isomer shifts ($\delta \sim -0.10$ mm·s^{-1}) and large quadrupole splitting ($\Delta E_Q \sim 3.10$ mm·s^{-1}) while the strong thiolate donation in **7** caused the increase of δ to -0.09 mm·s^{-1} and a lower $\Delta E_Q = 2.21$ mm·s^{-1}. SQUID magnetometry confirmed the $S = 1$ ground state for all the new axially substituted

complexes, while IRPD spectroscopy revealed that Fe=O stretching frequency correlated with the increase of axial donation going from **3** (ν_{FeO} = 832 cm^{-1}) to **4** (ν_{FeO} = 816 cm^{-1}) to **5** (ν_{FeO} = 799 cm^{-1}). Finally, the structure of the trifluoroacetate tetracarbene oxoiron(IV) complex **4** was elucidated by XRD measurements on single crystals, revealing a typical Fe=O distance of 1.6 Å.

Chapter 4 investigated the HAA reactivity of the axially substituted tetracarbene oxoiron(IV) complexes towards a variety of substrates (1,4-cyclohexadiene – CHD –, 9,10-dihydroanthracene – DHA –, and xanthene) and their comparison with the reactivity of the parent CH_3CN complex **3**. As predicted by theory, substitution of the axial position *trans* to the oxo ligand affected the HAA second order rate constants only to a very limited extent. Remarkably, coordination with activating axial anions that weaken the Fe=O bond caused a slight decrease of the reaction rates for complexes **4** (CF_3COO^-), **5** (Cl^-) and **7** ($^tBuS^-$) compared to **3**, contrary to what has been reported for other non-heme oxoiron(IV) models. Indeed, the reaction of **3** with substrates was previously calculated to proceed through an initial de-coordination of the axial CH_3CN, leading to a very reactive penta-coordinated complex, while the different product mixtures obtained for the anion-ligated complexes suggested that the axial ligands remain bound during HAA. The presence of the strongly bound axial ligand seems to force the reaction to happen on the 6-coordinated complexes, which show intrinsically slower rates compared to the reactive 5-coordinated analogue. Remarkably, the thiolate-bound complex **7** reacts with CHD in a clean one-step conversion, as evidenced by the presence of multiple isosbestic points in the time-resolved UV/Vis spectra. The putative $^tBuS–Fe^{III}–OH$ product shows outstanding stability at –40 °C in CH_3CN, that will allow for future attempts of isolation, purification and full electronic and molecular structure investigations on a unique intermediate. This complex would constitute the first example of a thiolate-bound Fe^{III}-hydroxo species as analogue of cysteine-bound enzymatic intermediates.

The work presented in Chapter 5 provided mechanistic support for the presence of a disproportionation equilibrium of the diferric complex **2** to complexes **1** and **3** in CH_3CN. As previously reported, this allows for observation of HAA reactivity of **2** with substrates such as 9,10-dihydroanthraene in absence of additional oxidants. ^{1}H-NMR monitoring of the reaction mixture both under ambient light and darkness confirmed the thermodynamic nature of the disproportionation, that was hypothesized to proceed after axial coordination of a solvent molecule to **2**. When complex **2** was mixed with the fully methylated analogue $\mathbf{2^{Me}}$ the disproportionation in solution was confirmed by scrambling of the complexes to a partially methylated species, as observed in time-resolved ESI-MS experiments. Additional experiments performed prior to this work showed that the disproportionation/scrambling process can be triggered by attack of the oxo ligand of complex **3** to $\mathbf{2^{Me}}$, suggesting a nucleophilic character of the ferryl group (Figure 82).

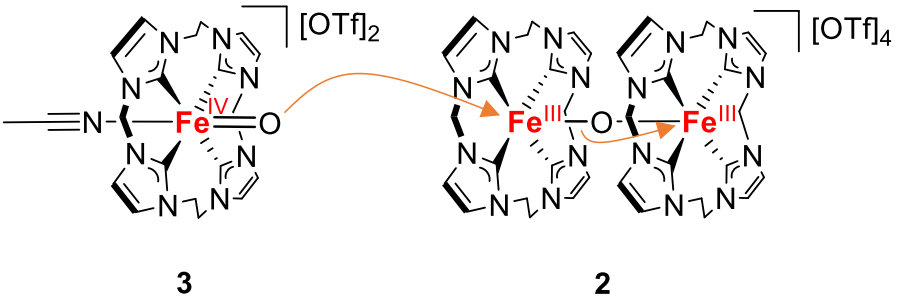

Figure 82. Schematic representation of the scrambling process upon attack of complex **3** on the dimeric μ-oxo complex **2**, as confirmed by the structural characterization of adduct **10**.

Crystallization and XRD analysis of a unique $Fe^{IV}O–Fe^{III}–O–Fe^{III}–OFe^{IV}$ adduct where the Fe=O groups of two subunits of **3** interact with the ferric ions of **2** provided a structural snapshot of the scrambling process and confirmed the low electrophilicity of **3**. Finally, gas-phase FT-ICR OAT reactivity studies on the tetracarbene oxoiron(IV) complex with NO, allylacetate and thioanisole showed only the formation of adducts between the reagents but no transfer of the oxygen atom, even in absence of solvent and matrix interactions, thereby providing further evidence for the very low electrophilicity of the tetracarbene oxoiron(IV) complex **3**.

Complementing the studies on the tetracarbene series, Chapter 6 introduced the synthesis of a novel hybrid NHC/N-donor macrocycle (**[11H$_3$][OTf]$_2$**) bearing two *trans* imidazole groups, a pyridine and a redox-active carbazole fragment. Treatment of the pro-ligand with FeHMDS in CH_3CN allowed for the formation of the low-spin octahedral ferrous complex **12a**, that was fully characterized. Dissolution of **12a** in non-coordinating solvents allowed for the isolation of the intermediate-spin square pyramidal complex **12b**, introducing the possibility of tuning the spin state of the complex by acting on the axial ligation. One- and two-electron oxidations of the complexes allowed for the isolation of two formal Fe^{II}-Fe^{IV} redox series (Scheme 13).

A bouquet of spectroscopic and magnetometric techniques demonstrated that the first oxidation generates the low-spin and intermediate-spin complexes **13a** and **13b**, respectively, while the second electron removal happens on the carbazole fragment of the macrocycle, with the formation of two Fe^{III}-π-radical cation complexes**14a** and **14b**. Five of the six complexes of the series were structurally characterized, and their spectroscopic and computational investigation suggested a significant degree of covalency of the iron-carbazole bond in the low-spin series. Taken together, the possibility of both metal- and ligand-based oxidations and the ability of the hybrid scaffold to stabilize the redox series in two different spin states reminds of some of the main characteristics of iron-porphyrin complexes, rendering the hybrid system a non-heme model with some heme-like features.

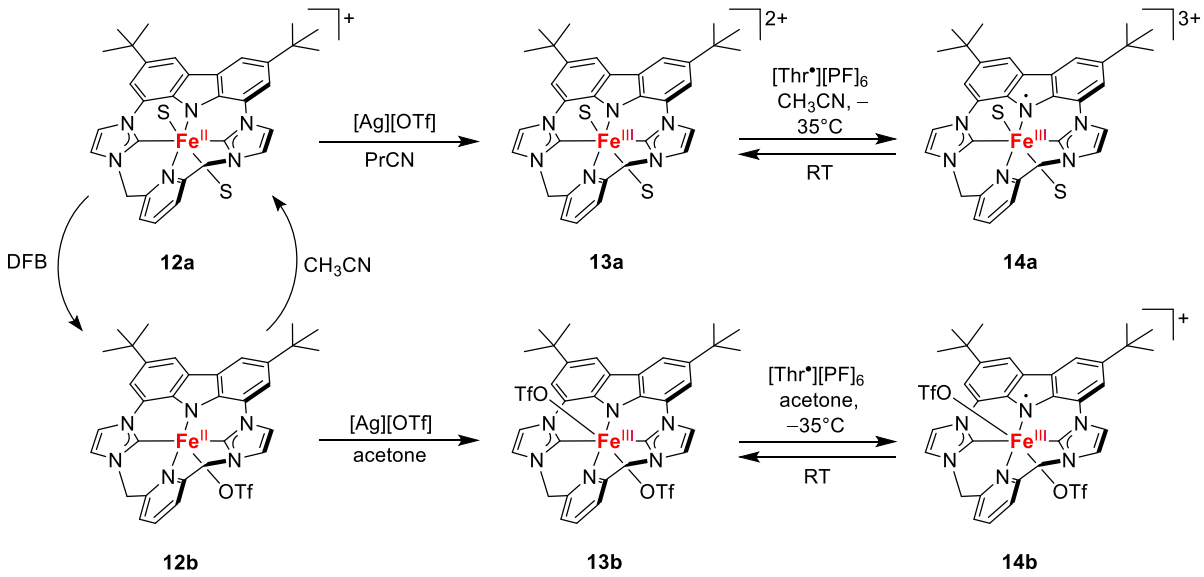

Scheme 13. Schematic representation of the redox series of low-spin complexes **12a**–**14a** and intermediate complexes **12b**–**14b** of the novel hybrid macrocycle presented herein. S stands for coordinated solvent molecules.

Finally, treatment of **12a** with a NO transfer reagent allowed for the isolation and crystallization of a new {FeNO}^{7} complex of the hybrid scaffold (**15**). Cyclic voltammetry indicated the possibility of isolating a novel {FeNO}$^{\text{"5"}\text{-}8}$ complex series, obtained via sequential one- and two-electron oxidation and through the one-electron reduction of **15**. UV/Vis spectroelectrochemical measurements suggested both {Fe–NO} based and equatorial ligand-based oxidations, leading to a {FeNO}^{6} and a [(**11**$^{\bullet+}$){FeNO}^{6}(OTf)]$^{2+}$ complex. Preliminary isolation of the full series, structural analysis of the corresponding {FeNO}^{6} complex and spectroscopic analyses on all solid products showed encouraging results and set a solid starting point for the full electronic structure determination of the novel {FeNO}^{x} redox series.

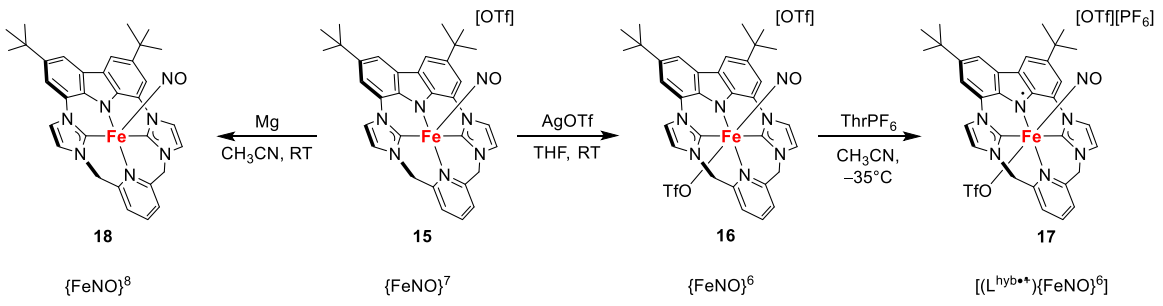

Scheme 14. Schematic representation of the redox series of {FeNO} complexes derived from **12a**.

9. Experimental Section

9.1 Materials and Methods

General Synthetic Procedures and Chemicals

The synthesis of air or moisture-sensitive substances was carried out under an inert atmosphere of dry dinitrogen or argon gas using standard Schlenk techniques or a glovebox (MBraun Unilab sp Plus ECO, O_2 and H_2O concentration lower than 0.1 ppm). All the synthetic procedures here reported were carried out in those conditions unless otherwise stated. Solvents (including deuterated ones) were dried by standard distillation procedures and/or using activated molecular sieves of appropriate pore size.

Starting materials, unless otherwise stated in the following, were purchased from commercial sources, and used as received. The tetracarbene ligand,[108] 2-*tert*-butylsulfonyliodosobenzene, complexes **1**–**3**,[109] DMI-CO_2,[161,162] trityl S-nitrosothiol,[295] **bimca**,[135] iron bis(trimethylsilyl)amide[233] and thianthrene radical cation hexafluorophosphate[314] were prepared according to reported procedures. High-purity tetrakis(n-butyl)ammonium hexafluorophosphate for electrochemical analysis was purchased and dried by warming up to 125°C and applying vacuum for several days prior to use.

UV/Vis Spectroscopy

Optical spectroscopy analyses were performed in solution using quartz cuvettes with 1 cm pathlength and a Cary 8454 spectrometer from Agilent Technologies equipped with an Unisoku Cryostat (CoolSpek, Unisoku Scientific Instruments) to allow for temperature control and magnetic stirring.

IR Spectroscopy

Solid state ATR measurements were performed on solid samples using a Cary 630 FTIR instrument from Agilent Technologies kept inside an argon-filled glovebox (O_2 and H_20 concentration lower than 0.1 ppm).

ESI-MS Measurements

ESI-MS analyses were performed using a Bruker HCT Ultra spectrometer. Air-sensitive compounds were analyzed by injecting solutions into a capillary from inside an argon-filled glovebox.

Helium Tagging IRPD Spectroscopy

IRPD spectroscopy measurements were performed in the lab of Prof Jana Roithová at Charles University, Prague. The ions were generated with a room-temperature ESI source capable of soft ionization. Then a first quadrupole allowed for the isolation of the $[(L^{NHC})]Fe(O)(X)]^{2+}$ ions, that were subsequently injected (in 200 ms) in a cryo-cooled wire quadrupole trap operating at a temperature of 3 K and a frequency of 1 Hz. Ions were trapped with a helium buffer gas for 130 ms and partially transformed into Helium adducts $[(L^{NHC})]Fe(O)(X)(He)]^{2+}$. After a delay of 400 ms an optical parametric oscillator/amplifier (OPO/OPA) operating at 10 Hz was used to irradiate the ions with 8 photon pulses on alternate cycles. After an additional delay, the ions were mass analyzed by a second quadrupole and a Daly type detector operating in ion-counting mode determined their number N when analyzing the irradiated ions, and the total number of unirradiated ions N_0 when the irradiation was blocked with a mechanical shutter. The spectra were plotted reporting values of $(1 - N/N_0)$ *vs.* the wavenumber of the irradiation. The accuracy of the measurement is ± 3 cm^{-1}.

NMR Spectroscopy

NMR spectra were recorded on Bruker Avance III HD 300, 400 or 500 instruments. ^{1}H- and ^{13}C{^{1}H}-NMR chemical shifts given in ppm were reported against a standard of tetramethylsilane and referenced using the residual proton signal or the resonance of natural abundant ^{13}C atoms of deuterated solvents, respectively.[315] Signal multiplicity is expressed with the following abbreviations: s = singlet, d = doublet, t = triplet, m = multiplet, b = broad signal.

Cyclic Voltammetry and UV/Vis Spectroelectrochemistry

Cyclic voltammetry (CV) and UV/Vis spectroelectrochemical (UV-SEC) measurements were performed inside a nitrogen-filled glovebox (O_2 and H_2O concentration lower than 0.1 ppm) using a Gamry Interface 1000B potentiostat and the associated Gamry Framework program. Electrolyte solutions were prepared dissolving dry $[^{n}Bu_4N][PF_6]$ in dry solvent to obtain a 0.1 M concentration.

A tree-electrode set-up was used with an ALS Glassy Carbon disc electrode (1.6 mm diameter) as working electrode, a 1 mm platinum wire used as counter electrode and a silver wire enclosed in a glass sample holder (equipped with a Vycor glass frit) containing electrolyte solution as pseudo-reference electrode.[316] All potentials were then referenced against the ferrocenium/ferrocene couple ($Fc^{+/0}$) by addition of the standard into the analyte solution and subsequent measurement. All experimental data were analyzed and worked up using the EchemAnalyst software from Gamry. UV-SEC analyses were performed using the mentioned potentiostat in combination with a BWTek deuterium/tungsten light source, a BWTek Exemplar LS spectrometer, BWTek UV/Vis grade optic fibers and a thin-layer quartz cuvette (light path length 1 mm). Electrolyte solutions were prepared as mentioned and a platinum mesh was used as working electrode. Optical spectra were recorded and analyzed using the BWSpec software.

Elemental Analysis

CHN analyses were conducted by the analytical laboratory of the Institute of Inorganic Chemistry of the Georg-August University of Göttingen using an Elementar Vario EL III instrument.

Mößbauer Spectroscopy

MB spectra of solid samples or frozen solutions were recorded using a ^{57}Co source embedded in a Rh matrix as part of an alternating constant-acceleration *WissEl* Mößbauer spectrometer operating in transmission mode and equipped with a *Janis* closed-cycle helium cryostat. Fitting of the experimental data was performed with the MFit software package using Lorentzian doublets.[268] All isomer shifts (IS or δ) and quadrupole splitting (QS or ΔE_Q) parameters measured in $mm \cdot s^{-1}$ are referred to a standard of iron metal at ambient temperature.

EPR Spectroscopy

X-band EPR spectra were recorded using a Bruker E500 ELEXSYS spectrometer equipped with a standard cavity (ER4102ST, 9.45 GHz). Temperature control was achieved by the use of an Oxford Instruments Helium flow cryostat (ESP910) and an ITC-4 Oxford temperature controller. Simulations of experimental data were performed using the EasySpin program.[317]

SQUID Magnetometry

Magnetic susceptibility measurements were recorded using a Quantum-Design MPMS-XL-5 SQUID magnetometer equipped with a 5 Tesla magnet, at a magnetic field of 0.5 T and temperatures between 2 and 298 K. Powdered samples were contained in a Teflon bucket and fixed in a non-magnetic sample holder. Data filed were corrected for diamagnetic contributions of the bucket according to

$$M^{\mathrm{dia}}(bucket) = \chi_g \cdot m \cdot H$$

Were *H* is the magnetic field, χ_g the experimental gram susceptibility of the Teflon gelatin capsule and *m* its mass. Fitting of the experimental data were done according to the appropriate Heisemberg-Dirak-van-Vlek (HDvV) spin Hamiltonian for Zeeman splitting, zero-field splitting (ZFS) and isotropic exchange coupling:

$$\widehat{H} = -2J\hat{S}_1\hat{S}_2 + g\mu_B\vec{B}\left(\vec{S}_1+\vec{S}_2\right) + D_{Fe}\left[\hat{S}_z^2 - \frac{1}{3}S(S+1)\right]$$

Curie-behaved paramagnetic impurities (PI) with S = 5/2 spin and temperature-independent paramagnetism were included in the fitting according to

$$\chi_{\mathrm{calc}} = (1 - PI) \cdot \chi + PI \cdot \chi_{\mathrm{mono}} + TIP$$

And experimental data were modeled using the *julX* program.[318]

9.2 Synthetic Procedures

General Procedure for the HAA Kinetics Measurement for the Reaction of Complexes 4, 5 and 7 with CHD at –40 °C

The appropriate amount of solid oxoiron(IV) complex (**4**, **5** or **7**) was dissolved in cold (–35 °C) dry and degassed CH_3CN inside a glovebox to give 6 mL of a 0.25 mM solution. A defined volume of the solution, obtained by subtracting the substrate addition volume from 3 mL, was transferred into a precooled cuvette sealed with a septum, taken out of the glovebox, and inserted into the UV/Vis spectrometer, the sample holder of which was thermostated at −40 °C. The corresponding amount of CHD (30 to 300 equivalents) to reach 3 ml of total volume was then injected in the cuvette using a gas-tight syringe. UV/Vis spectra were acquired every second until completion of the reaction. For the *in situ* preparation of complex **7**, 1.5 mL of a 0.5 mM stock solution of complex $[(L^{NHC})Fe(^{t}BuS)(CH_3CN)][OTf]$ (**8**) were transferred into a cuvette, diluted with CH_3CN to a volume equal to 2.850 mL minus the substrate addition volume, than placed into the spectrometer and allowed to equilibrate to −40 °C. A 5 mM solution of $TBAIO_4$ in CH_3CN was prepared in a glovebox and 150 μL of it were then injected into the cuvette containing **6** to start the oxidation. Complete formation of complex $[(L^{NHC})Fe(O)(^{t}BuS)][OTf]$ (**7**) was attained after 1h. Then the appropriate amount of CHD was injected into the cuvette and spectra were acquired (60 spectra/min) until completion of the reaction.

General Procedure for the HAA Kinetics Measurement for the Reaction of Complexes 3, 4 and 7 (1 mM) with CHD, DHA and Xanthene at 25 °C

Three 2 mM stock solutions were prepared dissolving in 30 mL of dry and degassed CH_3CN respectively: a) 47.1 mg ($6.0\cdot10^{-5}$ mol) of complex $[(L^{NHC})Fe(CH_3CN)_2][OTf]_2$ (**1**); b) 47.1 mg ($6.0\cdot10^{-5}$ mol) of complex **1** and 8.2 mg ($6.0\cdot10^{-5}$ mol) of dry sodium trifluoroacetate; c) 41 mg ($6.0\cdot10^{-5}$ mol) of complex $[(L^{NHC})Fe(^{t}BuS)(CH_3CN)][OTf]$ (**6**). The three stock solutions were allowed to cool down to −35°C into the freezer of the glovebox and 3 mL of each were retrieved and treated with 5.7 mg ($1.7\cdot10^{-5}$ mol) of sPhIO at low temperature. The reaction mixtures were left reacting for 1.5 h. In the meantime, substrates stock solutions were prepared dissolving the appropriate amount of substrate in CH_3CN (CHD) or into a 7:3 CH_3CN /DCM mixture (DHA and xanthene). Then, 3 mL of substrate solution and 3 mL of oxoiron(IV) complex were quickly charged into the syringes of the stopped-flow instrument, the reaction cell of which was thermostated at 25°C. The reactions took place after mixing of equal amounts of oxoiron(IV) and substrate solutions

into the instrument reaction cell, obtaining reaction mixtures with 1 mM concentration of oxoiron(IV) complex.

General procedure for the preparation of Helium Tagging IRPD Spectroscopy Samples of complexes 3, 4, 5 and the product of oxidation of 8 with sPhIO.

A 1 mM solution of complex [(L^{NHC})Fe(O)(CF_3COO)][OTf] (**4**) in dry, degassed, and cold CH_3CN was prepared in the freezer of a glovebox by dissolving 2.0 mg ($3.0\cdot10^{-6}$ mol) of crystalline material in 3 mL of solvent. The cold solution contained in a vial was quickly transferred out of the glovebox and inserted into a thermostat operating at −20 °C. The solution was injected into the mass spectrometer via a short capillary. A 1 mM solution of complex [(L^{NHC})Fe(O)(Cl)][OTf] (**5**) was prepared and analyzed in an analogous way, dissolving 1.8 mg ($3.0\cdot10^{-6}$ mol) of solid material in 3 mL of cold solvent. Complex [(L^{NHC})Fe(O)(CH_3CN)][OTf] (**3**) was instead prepared *in situ*, by dissolving 2.4 mg ($3.0\cdot10^{-6}$ mol) of crystalline [(L^{NHC})Fe($CH_3CN)_2$][OTf]$_2$ (**1**) in 3 mL of solvent, cooling down the solution to −40 °C, treating it with 2.9 mg ($8.4\cdot10^{-6}$ mol, 2.8 eq) of 2-(^{t}BuSO_2)-CH_6H_4–IO (**sPhIO**) and letting the mixture react for 1.5 h. An analogous procedure was used to in situ oxidize complex **8** with sPhIO: 2.7 mg ($3.0\cdot10^{-6}$ mol) of crystalline [(L^{NHC})Fe(DMI)(CH_3CN)][OTf]$_2$ (**8**) in 3 mL of solvent, cooling down the solution to −40 °C, treating it with 2.9 mg ($8.4\cdot10^{-6}$ mol, 2.8 eq) of 2-(^{t}BuSO_2)-CH_6H_4–IO (**sPhIO**) and let the mixture react for 1.5 h.

^{18}O labeled complexes were prepared by addition of 8 μL of $H_2{}^{18}O$ into the cold CH_3CN solutions of complexes.

General procedure for the ^{1}H-NMR monitoring of the reaction of complex 2 with 7 eq. of DHA at RT under ambient light and under complete darkness.

Complex [{(L^{NHC})Fe}$_2$O][OTf]$_4$ (**2**) (9.0 mg, $6.0\cdot10^{-6}$ mol) was dissolved in 1 mL of CD_3CN and transferred into two Young NMR tubes in portions of 500 μL. DHA (7.6 mg, $4.2\cdot10^{-5}$ mol, 7.0 eq) and 1,3,5-trimetoxybenzene (1.5 mg, $9\cdot10^{-6}$ mol) were dissolved in 200 μL of CD_3CN and added to each tube in in 100 μL portions. One of the tubes was immediately covered with aluminum foil to avoid exposure to ambient light. ^{1}H-NMR spectra were recorded once a day for approximately 15 days, monitoring the consumption of complex **2**, the formation of anthracene and the appearance of complex **1** by comparison of the integrals of characteristic proton shifts to the internal standard of 1,3,5-trimetoxybenzene.

Synthesis of complex [(L^{NHC})Fe(O)(CF_3COO)][OTf] (4)

Complex [(L^{NHC})Fe($CH_3CN)_2$][OTf]$_2$ (**1**) (30.0 mg, $3.8\cdot10^{-5}$ mol) and CF_3COONa (5.5 mg, $4.0\cdot10^{-5}$ mol, 1.0 eq) were dissolved in 3 mL of dry and degassed CH_3CN and cooled down to −35 °C. Solid 2-(^{t}BuSO_2)-CH_6H_4–IO (**sPhIO**) (36.4 mg $10.7\cdot10^{-5}$ mol, 2.8 eq) was added to the yellow solution and the reaction mixture was left reacting at −35 °C for 3 h. During the reaction, the color of the mixture changed to deep green. The mixture was separated from unreacted solid sPhIO by filtration.Slow diffusion of diethyl ether into the green CH_3CN solution at −35 °C allowed for the isolation of crystalline material of complex [(L^{NHC})Fe(O)(CF_3COO)][OTf] (**4**) suitable for XRD analysis.

Yield 19.9 mg, $2.9\cdot10^{-5}$ mol, 76%.

UV/Vis (CH_3CN): λ_{max} / nm (ε / L·mol^{-1}·cm^{-1}) = 408 (1135), 629 (143).

MB (solid, 80K): δ = −0.14 mm·s^{-1}; ΔE_Q = 3.13 mm·s^{-1}.

SQUID (solid): S = 1, $g_{1,2}$ = 1.844, g_3 = 2.339, D = 16.5 cm^{-1}, TIP = $296.4\cdot10^{-6}$ emu, $\chi_m T_{200\ K}$ = 1.01 cm^3·K·mol^{-1}.

IRPD (CH_3CN): $\nu_{Fe=O}$ = 816 cm^{-1}, $\nu_{Fe=18O}$ = 777 cm^{-1}

Synthesis of complex [(L^{NHC})Fe(O)(Cl)][OTf] (5)

Complex [(L^{NHC})Fe($CH_3CN)_2$][OTf]$_2$ (**1**) (20.0 mg, $2.6\cdot10^{-5}$ mol) and ^{t}Bu$_4$NCl (7.1 mg, $2.6\cdot10^{-5}$ mol, 1.0 eq) were dissolved in 3 mL of dry and degassed CH_3CN and cooled down to −35 °C. Solid 2-(^{t}BuSO_2)-CH_6H_4–IO (**sPhIO**) (24.3 mg, $7.1\cdot10^{-5}$ mol, 2.8 eq) was added to the yellow solution and the reaction mixture was left reacting at −35 °C for 3 h. During the reaction, the color of the mixture changed to deep green and a bright green precipitate appeared. The green product was fully precipitated by addition of cold diethyl ether. The product was then separated from unreacted solid sPhIO by extractions with 5 mL fractions of cold CH_3CN, followed by filtration of the green solutions and precipitation of the green solid product with cold diethyl ether. Complex [(L^{NHC})Fe(O)(Cl)][OTf] (**5**) was collected as a bright green powder.

Yield 10.0 mg, $1.7\cdot10^{-5}$ mol, 65%.

UV/Vis (CH_3CN): λ_{max} / nm (ε / L·mol^{-1}·cm^{-1}) = 415 (924), 629 (115).

MB (solid, 80K): δ = −0.12 mm·s^{-1}; ΔE_Q = 3.15 mm·s^{-1}.

SQUID (solid): S = 1, g_{avg} = 1.839, D = 16.3 cm^{-1}, TIP = $675.0\cdot10^{-6}$ emu, $\chi_m T_{200\ K}$ = 0.84 cm^3·K·mol^{-1}.

IRPD (CH_3CN): $\nu_{Fe=O}$ = 799 cm^{-1}, $\nu_{Fe=18O}$ = 765 cm^{-1}

Synthesis of complex [(L^{NHC})Fe(^{t}BuS)(CH_3CN)][OTf] (6)

Complex [(L^{NHC})Fe(CH_3CN)$_2$][OTf]$_2$ (**1**) (50 mg, 6.4·10^{-5} mol) was dissolved in 4 mL of dry and degassed CH_3CN and treated with solid ^{t}BuSNa (7.2 mg, 6.4·10^{-5} mol, 1.0 eq). The reaction mixture was left stirring at RT for 6 hours, during which the color changed from yellow to reddish. The solution was filtered, and then underlayered under diethyl ether, letting the two layers slowly mix over time. After 48 hours the red product was isolated in pure crystalline form (suitable for XRD analysis) by decantation and removal of the mother liquor.

Yield 41.6 mg, 6.1·10^{-5} mol, 95%.

UV/Vis (CH_3CN): λ_{max} / nm (ε / L·mol^{-1}·cm^{-1}) = 379 (5623).

MB (solid, 80K): δ = 0.26 mm·s^{-1}; ΔE_Q = 1.99 mm·s^{-1}.

Synthesis of complex [(L^{NHC})Fe(O)(^{t}BuS)][OTf] (7)

Complex [(L^{NHC})Fe(^{t}BuS)(CH_3CN)][OTf] (**8**) (25.0 mg, 3.7·10^{-5} mol) was dissolved in 3 mL of dry and degassed CH_3CN and cooled down to −35 °C. Solid 2-(^{t}BuSO$_2$)-CH_6H_4–IO (**sPhIO**) (35.2 mg, 10.4·10^{-5} mol, 2.8 eq) were added to the reddish solution and the reaction mixture was left reacting at −35 °C for 3 h. During the reaction, the color of the mixture changed to deep green/brown. Unreacted sPhIO was filtered away, and the green/brown product was fully precipitated by addition of cold diethyl ether. [(L^{NHC})Fe(O)(^{t}BuS)][OTf] (**7**) was collected as a green/brown powder.

Yield 18.0 mg, 2.7·10^{-5} mol, 74%.

UV/Vis (CH_3CN): λ_{max} / nm (ε / L·mol^{-1}·cm^{-1}) = 335 (5878), 447 (1702), 577 (662).

MB (solid, 80K): δ = –0.09 mm·s^{-1}; ΔE_Q = 2.18 mm·s^{-1}.

SQUID (solid): S = 1, g_{avg} = 2.022, D = –20.4 cm^{-1}, TIP = 841.4·10^{-6} emu, $\chi_m T_{200\ K}$ = 1.02 cm^3·K·mol^{-1}.

Synthesis of complex [(L^{NHC})Fe(DMI)(CH_3CN)][OTf]$_2$ (8)

Complex [(L^{NHC})Fe(CH_3CN)$_2$][OTf]$_2$ (**1**) (50 mg, 6.4·10^{-5} mol) was dissolved in 4 mL of dry and degassed CH_3CN and treated with solid DMI-CO_2 (10.7 mg, 7.7·10^{-5} mol, 1.2 eq). The reaction mixture was transferred into a Schlenk tube, taken out of the glovebox, warmed up to 50 °C and

left stirring at that temperature overnight, during which the color changed to bright yellow. The solution was then transferred back into the glovebox, filtered, the solvent removed, and the yellow residue dissolved in 2 mL of EtCN. The product was then crystallized via slow diffusion of diethyl ether into the EtCN solution at RT, obtaining orange crystals suitable for XRD measurements.

Yield 32.2 mg, $3.8 \cdot 10^{-5}$ mol, 60%.

UV/Vis (CH_3CN): λ_{max} / nm (ε / $L \cdot mol^{-1} \cdot cm^{-1}$) = 300 (17333), 344 (10780).

^{1}H-NMR (500 MHz, CD_3CN) δ (ppm) = [1 and 2 refer to the two isomers in solution: 1 = red coded isomer, 2 = green coded isomer, see Appendix] 7.47 ($H_{imi\text{-}NHC}$1, d, 4H, *J* = 2.0 Hz), 7.25 ($H_{imi\text{-}NHC}$2, d, 4H, *J* = 2.0 Hz), 7.21 ($H_{imi\text{-}NHC}$2, d, 4H, *J* = 2.0 Hz), 7.12 ($H_{imi\text{-}NHC}$1, d, 4H, *J* = 2.0 Hz), 6.75 ($H_{imi\text{-}DMIf}$1+2, d, 4H, *J* = 5.0 Hz), 6.24 (–C*H*$_2$– 1, d, 2H, *J* = 13.3 Hz),6.11 (–C*H*$_2$– 1, d, 2H, *J* = 13.3 Hz), 5.69 (–C*H*$_2$– 2, d, 2H, *J* = 13.2 Hz), 5.01 (–C*H*$_2$–CH_2– 2, m, 4H), 4.47 (–C*H*$_2$–CH_2– 2, m, 4H), 4.03 (–CH_2–C*H*$_2$– 1, m, 4H), 3.61 (–C*H*$_2$– 2, d, 2H, *J* = 13.2 Hz), 3.48 (–CH_2–C*H*$_2$– 1, m, 4H), 2.33 (–C*H*$_{3DMI}$ 2, s, 6H), 1.96 (–C*H*$_{3DMI}$ 1, s, ~6H).

MB (solid, 80K): δ = 0.13 $mm \cdot s^{-1}$; ΔE_Q = 1.47 $mm \cdot s^{-1}$.

MS (ESI(+), CH_3CN): *m/z* = 202 [M–DMI –2OTf –CH_3CN]$^{2+}$, 649 [M–CH_3CN –OTf]

Synthesis of adduct [{(L^{NHC})Fe(O)(CH_3CN)}$_2$[(L^{NHC})Fe]$_2$O}][OTf]$_8$ (9)

Adduct [{(L^{NHC})Fe(O)(CH_3CN)}$_2$[(L^{NHC})Fe]$_2$O}][OTf]$_8$ (**9**) was obtained as single crystals suitable for XRD analysis by dissolving complex [(L^{NHC})Fe(O)(CH_3CN)][OTf]$_2$ (**3**) (10.0 mg, $1.3 \cdot 10^{-5}$ mol, 2 eq) and complex [{(L^{NHC})Fe}$_2$O][OTf]$_4$ (**2**) (10.0 mg, $6.6 \cdot 10^{-6}$ mol, 1 eq) in CH_3CN at (–35 °C) and allowing diethyl ether to slowly diffuse into the solution at –35 °C. Only XRD analysis was performed on **9**.

Synthesis of pro-ligand [11H$_3$][OTf]$_2$

3,6-di-tert-butyl-1,8-bis(imidazole-1-yl)carbazole (**bimca**) (2.0 g, 4.86 mmol, 1 eq.) and 1,6-bis(bromomethyl)pyridine (1.3 g, 4.86 mmol, 1 eq.) were mixed in a Schlenk flask equipped with reflux condenser, oil bubbler and magnetic stirring bar. The apparatus was degassed and 250 mL of dry and degassed CH_3CN were added, obtaining a milky white suspension. The mixture was heated to reflux and stirred for 48 hours, during which a white precipitate appeared. The mixture was then let to cool down to RT, open to air and the solvent was removed with a rotary evaporator. The yellowish residue of **[11H$_3$][Br]$_2$** was washed multiple times with DCM and dried under vacuum to obtain 1.65 g of yellowish solid (50% yield). Due to the low solubility of the product in

most organic media, a subsequent counteranion exchange was performed without further purification. The solid was then suspended in methanol and treated with [Ag][OTf] (1.32 g, 2.1 eq.), stirring the mixture for 2 hours. After removal of [Ag][Br] by filtration, the solvent was evaporated, the off-white residue dissolved in CH_3CN, filtered, and recrystallized with diethyl ether multiples times (1.55 g, 78%). Single crystals suitable for X-ray diffraction were obtained by slow diffusion of diethyl ether into a CH_3CN solution of **11** at RT.

Yield 1.55 g, $1.9 \cdot 10^{-3}$ mol, 39%.

IR (ATR): $\tilde{\nu}$ / cm^{-1} = 3117 (w), 3049 (w), 2958 (w), 2908 (w), 2867 (w), 1597 (w), 1576 (w), 1553 (w), 1527 (w), 1494 (w), 1477 (w), 1455 (w), 1433 (w), 1363 (w), 1253 (s), 1223 (s), 1157 (s), 1137 (s), 1026 (s), 996 (m), 937 (w), 870 (m), 842 (w), 793 (w), 770 (w), 758 (m), 746 (w), 738 (w), 713 (w), 691 (w), 669 (m), 636 (s), 571 (s), 540 (m), 514 (s).

^{1}H-NMR (500 MHz, DMSO-d6) δ(ppm) = 11.29 (N_{carb}–H, s, 1H), 10.01 (H6, d, 2H, J = 1.5 Hz), 8.57 (H10, d, 2H, J = 1.4 Hz), 8.29 (H7/H5, d, 2H, J = 1.3 Hz), 8.09 (H1, t, 1H, J = 7.7 Hz), 7.86 (H2, d, 2H, J = 7.7 Hz), 7.81 (H12, d, 2H, J = 1.6 Hz), 5.58 (H4, s, 4H), 1.47 (H15, s, 18H).

^{13}C-NMR (126 MHz, DMSO-d6) δ(ppm) = 153.7, 144.0, 139.2, 137.0, 133.3, 125.4, 125.0, 119.6, 119.5, 119.3, 67.0, 54.5, 35.0, 31.8, 25.1 ppm.

MS (ESI(+), CH_3CN): m/z = 665 $[M–OTf]^+$, 516 $[M–2OTf]^+$, 258 $[M–2OTf]^{2+}$.

UV/Vis (CH_3CN): λ_{max} / nm (ε / $L \cdot mol^{-1} \cdot cm^{-1}$) = 226 (19775), 298 (7578), 337 (1868), 349 (1954).

Synthesis of complex [(11)Fe(CH_3CN)$_2$][OTf] (12a)

[11H$_3$][OTf]$_2$ (300.0 mg, $0.368 \cdot 10^{-3}$ mol, 1eq.) was dissolved in dry and degassed CH_3CN in a nitrogen-filled glovebox. Solid $[Fe\{N(Si(Me)_3)_2\}_2]_2$ (FeHMDS) (0.277 g, $0.368 \cdot 10^{-3}$ mol, 1 eq.) was added, and the mixture was stirred at RT for 48 hours. An initial yellow precipitate formed, which dissolved overtime to give an orange-brown solution. The mixture was filtered, and the solvent removed under reduced pressure. The residue was dissolved in DCM, filtered, then the solvent was removed under vacuum. The orange residue was finally dissolved in 1,2-difluorobenzene (DFB), the solution filtered, the solvent was removed under vacuum and the orange powder dried. Dissolution in CH_3CN and reprecipitation with Et_2O afforded the orange-red crystalline product (214.0 mg, 73%). Single crystals suitable for X-ray diffraction were grown by slow diffusion of Et_2O in a concentrated solution in CH_3CN inside a glovebox.

Yield 214.0 mg, $2.7 \cdot 10^{-4}$ mol, 73%.

IR (ATR): $\tilde{\nu}$ / cm^{-1} = 3162 (w), 3135 (w), 3102 (w), 2953 (w), 2902 (w), 2865 (w), 1583 (w), 1480 (w), 1448 (m), 1419 (m), 1363 (w), 1321 (w), 1304 (m), 1258 (s), 1223 (s), 1158 (m), 1148 (m), 1106.2 (m), 1072 (w), 1026 (s), 993 (w), 888 (w), 861 (w), 842 (m), 817 (w), 774 (w), 752 (m), 740 (w), 719 (w), 709 (w), 687 (w), 674 (w), 665 (w), 636 (s), 614 (m), 572 (m), 541 (w), 516 (m).

^{1}H-NMR (500 MHz, CD_3CN) δ (ppm) = 8.68 (d, H7, 2H, J = 2.1 Hz), 8.00 (d, H12, 2H, J = 1.6 Hz), 7.93 (d, H5, 2H, J = 2.1 Hz), 7.88 (d, H10 ,2H, J = 1.5 Hz), 7.76 (t, H1, 1H, J = 7.7 Hz), 7.48 (d, H2, 2H, J = 7.7 Hz), 5.62 (s, H4, 4H), 1.53 (s, H15, 18H).

^{13}C-NMR (126 MHz, CD_3CN) δ (ppm) = 202.2, 162.8, 138.8, 138.4, 137.5, 129.4, 126.0, 125.0, 124.5, 119.6, 114.6, 108.9, 54.6, 35.4, 32.6.

UV/Vis (CH_3CN): λ_{max} / nm (ε / $L{\cdot}mol^{-1}{\cdot}cm^{-1}$) = 290 (~28560), 321 (10095), 377 (4422), 480 (5319).

MB (solid, 80K): δ = 0.33 $mm{\cdot}s^{-1}$, ΔE_Q = 2.33 $mm{\cdot}s^{-1}$.

Synthesis of complex [(11)Fe(OTf)] (12b)

Synthesis of complex [(**11**)Fe(OTf)] (**12b**) followed the same procedure as for complex [(**11**)Fe(CH_3CN)$_2$][OTf] (**12a**), except for the last reprecipitation, which was performed dissolving the orange powder in THF and precipitating the product with diethyl ether. Alternatively, the product could be obtained by dissolving complex [(**11**)Fe(CH_3CN)$_2$][OTf] (**12a**) in THF, acetone, DFB, DMF or MeOH and re-precipitating with Et_2O, obtaining a bright orange powder. Drying under vacuum afforded the pure product in yields similar to **12a**. Single crystals suitable for X-ray diffraction were grown by concentration of a saturated DFB solution at RT inside a glovebox.

IR (ATR): $\tilde{\nu}$ / cm^{-1} = 2953 (w), 2902 (w), 2867 (w), 1593 (w), 1478 (w), 1438 (w), 1414 (w), 1406 (w), 1394 (w), 1363 (w), 1256 (m), 1233 (m), 1220 (s), 1155 (m), 1028 (s), 88 (w), 866 (w), 844 (w), 774 (w), 751 (w), 716 (w), 691 (w), 667 (w), 635 (s).

UV/Vis (THF): λ_{max} / nm (ε / $L{\cdot}mol^{-1}{\cdot}cm^{-1}$) = 305 (13016), 353 (5789), 373 (6211), 389 (5809), 436 (4404), 483 (3145).

MB (solid, 80K): δ = 0.49 $mm{\cdot}s^{-1}$, ΔE_Q = 4.26.

SQUID (solid): S = 1, g_1 = 2.242, TIP = 865.6 emu, $\chi_m T$ = 1.245 $cm^3{\cdot}K{\cdot}mol^{-1}$ at 205 K.

Elemental Analysis: Calc. for $C_{40}H_{37}F_5FeN_6O_3S$ (**12b** + DFB): % C 57.7, % H 4.48, % N 10.09. Found: % C 57.18, % H 4.45, % N 10.04.

Synthesis of complex [(11)Fe(PrCN)$_2$][OTf]$_2$ (13a)

Complex [(**11**)Fe(CH$_3$CN)$_2$][OTf] (**12a**) (15.0 mg, 1.87·10^{-5} mol, 1 eq) was dissolved in dry and degassed CH$_3$CN in a nitrogen-filled glovebox. [Ag][OTf] (4.8 mg, 1.87·10^{-5} mol, 1 eq) was added and the orange color immediately turned blue, while a precipitate of Ag appeared. The suspension was stirred at RT for 30 minutes, then Ag was removed by filtration. The solvent was removed under vacuum and the residue dissolved in PrCN and filtered. Precipitation with diethyl ether afforded a blue powder that was dried under vacuum. X-ray diffraction quality single crystals were obtained by slow diffusion of Et$_2$O in a concentrated PrCN solution at RT inside a glovebox.

Yield 18.4 mg, 1.8·10^{-5} mol, 98%.

IR (ATR): $\tilde{\nu}$ / cm^{-1} = 3149 (w), 3084 (w), 2951 (w), 2907 (w), 2868 (w), 2360 (w), 2331 (w), 2298 (w), 1618 (w), 1612 (w), 1595 (w), 1579 (w), 1551 (w), 1523 (w), 1472 (w), 1463 (w), 1437 (w), 1426.8 (w), 1405 (w), 1364 (w), 1327 (w), 1265 (s), 1252 (s), 1222 (s), 1556 (s), 1027 (s), 993 (m), 867 (m), 783 (w), 755 (m), 719 (w), 706 (w), 692 (w), 637 (s), 575 (m), 516 (s).

UV/Vis (CH$_3$CN): λ_{max} / nm (ε / L·mol^{-1}·cm^{-1}) = 262 (~32569), 338 (8815), 419 (3224), 446 (2453), 602 (3122), 1005 (6504).

MB (solid, 80K): δ = 0.18 mm·s^{-1}, ΔE_Q = 3.84 mm·s^{-1}.

EPR (simulated g-values) g_1 = 2.132, g_2 = 2.054, g_3 = 1.957.

SQUID (solid): S = 0.5, g_1 = 2.23, PI = 2.0 % (S = 2.5), TIP = 623.5·10^{-6} emu, $\chi_m T$ = 0.537 cm^3·K·mol^{-1} at 295 K.

Elemental Analisis: Calc. for C$_{47}$H$_{54}$F$_6$FeN$_9$O$_6$S$_2$ (**13a** + PrCN): % C 52.52, % H 5.06, % N 11.73. Found: % C 52.24, % H 5.17, % N 11.80.

Synthesis of complex [(11)Fe(OTf)$_2$] (13b)

Complex [(**11**)Fe(OTf)] (**12b**) (15.0 mg, 2.09·10^{-5} mol, 1 eq) was dissolved in dry and degassed THF or acetone in a nitrogen-filled glovebox. [Ag][OTf] (5.4 mg, 2.1·10^{-5} mol, 1 eq) was added and the orange color immediately turned green, while a green-grey precipitate appeared. The suspension was stirred at RT for 30 minutes, then the product was fully precipitated with Et$_2$O. The residue was dissolved in acetone and filtered from solid Ag. Precipitation with Et$_2$O afforded a green powder that was dried under vacuum. X-ray diffraction quality single crystals were obtained by layering of diethyl ether on top of a concentrated acetone solution at RT inside a glovebox.

Yield 15.1 mg, 1.74·10^{-5} mol, 83%.

IR (ATR): $\tilde{\nu}$ / cm^{-1} = 3128 (w), 2963 (w), 2871 (w), 1705 (w), 1610 (w), 1595 (w), 1493 (w), 1455 (w), 1440 (w), 1423 (w), 1408 (w), 1363 (w), 1298 (m), 1232 (m), 1211 (s), 1171 (m), 1115 (w), 1054 (w), 1014 (s), 894 (w), 876 (w), 868 (w), 855 (w), 844 (w), 774 (w), 760 (w), 747 (w), 666 (w), 632 (s), 579 (w), 513 (m).

UV/Vis (acetone): λ_{max} / nm (ε / $L{\cdot}mol^{-1}{\cdot}cm^{-1}$) = 351 (8493), 405 (3321), 428 (4145), 703 (3143) nm. **MB** (solid, 80K): δ = 0.29 $mm{\cdot}s^{-1}$, ΔE_Q = 4.43 $mm{\cdot}s^{-1}$.

SQUID (solid): S = 1.5, g_{avg} = 2.131, TIP = $563.9{\cdot}10^{-6}$ emu, $\chi_m T$ = 2.122 $cm^3{\cdot}K{\cdot}mol^{-1}$ at 205 K.

Elemental Analisis: Calc. for $C_{35}H_{33}F_6FeN_6O_6S_2$: % C 48.45, % H 3.83, % N 9.69. Found: % C 48.15, % H 3.84, % N 9.58.

Synthesis of complex [(11)Fe(CH_3CN)$_2$][OTf]$_2$[PF_6] (14a)

Complex [(**11**)Fe(PrCN)$_2$][OTf]$_2$ (**13a**) (10.0 mg, $9.94{\cdot}10^{-6}$ mol, 1 eq) was dissolved in dry and degassed CH_3CN in a nitrogen-filled Glovebox and cooled down to −35°C. Thianthrene radical cation hexafluorophosphate (3.6 mg, $9.96{\cdot}10^{-6}$ mol, 1 eq.) was added to the blue solution and the resulting purple solution was kept at −35°C for 1 hour. During the reaction, a colorless precipitate of thianthrene appeared. The mixture was filtered, and the purple product precipitated with Et_2O. The resulting purple-grey solid was washed from unreacted **14a** with THF, dissolved in CH_3CN and precipitated again with Et_2O to obtain a purple-grey powder. Slow diffusion of diethyl ether at −35 °C into an CH_3CN solution of complex **14a** and 0.5 eq of thianthrene radical cation hexafluorophosphate (to prevent slow decomposition of **14a** to **13a**) allowed the formation of single crystals suitable for XRD analysis.

Yield 9.8 mg, $8.5{\cdot}10^{-6}$ mol, 86%.

IR (ATR): $\tilde{\nu}$ / cm^{-1} = 2962 (w), 2937 (w), 2870 (w), 2328 (w), 2301 (w), 1616 (w), 1597 (w), 1579 (w), 1564 (w), 1539 (w), 1471 (w), 1461 (w), 1427 (w), 1398 (w), 1366 (w), 1360 (w), 1345 (w), 1255 (s), 1225 (m), 1198 (w), 1148 (s), 1109 (w), 1088 (m), 1075 (m), 1056 (m), 1029 (s), 1021 (m), 987 (m), 898 (w), 874 (w), 835 (s), 765 (w), 755 (w), 742 (m), 716 (w), 690 (w), 648 (m), 637 (s), 572 (m), 557 (s), 516 (m).

^{1}H-NMR (400 MHz, CD_3CN) δ(ppm) = 8.64 (t, H1, 2H), 8.48 (1H), 8.36 (d, H2), 8.18 (2H), 8.01 (2H), 7.35 (2H), 5.14 (H4, 4H), 1.42 (H15, 18H).

UV/Vis (CH_3CN): λ_{max} / nm (ε / $L{\cdot}mol^{-1}{\cdot}cm^{-1}$) = 331 (11443), 377 (6504), 424 (4413), 511 (7672), 728 (11713), 804 (26672).

MB (solid, 80K): δ = 0.09 $mm{\cdot}s^{-1}$, ΔEQ = 4.36 $mm{\cdot}s^{-1}$.

SQUID (solid): S = 0, g_{avg} = 2.00 (fixed), PI = 2.7 % (S = 2.5), TIP = 595.6·10^{-6} emu, $\chi_m T$ = 0.079 cm^3·K·mol^{-1} at 220 K.

Synthesis of complex [(11)Fe(OTf)$_2$][PF$_6$] (14b)

Complex [(11)Fe(OTf)$_2$] (**13b**) (15.0 mg, 1.73·10^{-5} mol, 1 eq) was partially dissolved in dry and degassed THF in a nitrogen-filled Glovebox and cooled down to –35°C. Thianthrene radical cation hexafluorophosphate (6.9 mg, 1.90·10^{-5} mol, 1.1 eq.) was added to the blue solution and the resulting purple solution was kept at –35°C for 1 hour. During the reaction, a colorless precipitate of thianthrene appeared. The mixture was filtered, and the purple product precipitated with pentane. The resulting purple-grey solid was redissolved in acetone and precipitated again with pentane to obtain a purple-grey powder (8.5 mg, 49%).

Yield 8.5 mg, 8.4·10^{-6} mol, 49%.

IR (ATR): $\tilde{\nu}$ / cm^{-1} = 2962 (w), 2870 (w), 1596 (w), 1566 (w), 1541 (w), 1459 (w), 1439 (w), 1431 (w), 1362 (w), 1292 (w), 1230 (m), 1205 (m), 1153 (m), 1091 (w), 1077 (w), 1059 (w), 1021 (m), 835 (s), 760 (s), 752 (s), 716 (w), 635 (s), 557 (s).

UV/Vis (CH$_3$CN): λ_{max} / nm (ε / L·mol^{-1}·cm^{-1}) = 350 (17684), 409 (9229), 420 (9133), 512 (5905), 667 (5967), 739 (5812), 834 (9521).

MB (solid, 80K): δ = 0.16 mm·s^{-1}, ΔE_Q = 5.23 mm·s^{-1}.

SQUID (solid): S = 1, $g_{1,2}$ = 2.423, g_3 = 2.000 (fixed), J = –61.669 cm^{-1}, TIP = 122.4·10^{-6} emu, $\chi_m T$ = 2.202 cm^3·K·mol^{-1} at 220 K.

Synthesis of complex [(11)Fe(NO)][OTf] (15)

Complex [(11)Fe(CH$_3$CN)$_2$][OTf] (**12a**) (50.0 mg, 5.3·10^{-5} mol, 1 eq) was dissolved in 3 mL of CH$_3$CN at RT and treated with solid trityl S-nitrosothiol (16.1 mg, 5.3·10^{-5} mol, 1 eq). The solution immediately changed its color from orange to dark green/brown. The mixture was left stirring at RT overnight. Then the mixture was filtered, the product was fully precipitated with diethyl ether, washed with Et$_2$O, and dried. Final dissolution in 1 mL of CH$_3$CN and slow diffusion of Et$_2$O into the obtained solution allowed the formation of single crystals suitable for XRD analysis.

Yield 32.4 mg, 3.6·10^{-5} mol, 68%.

IR (ATR): $\tilde{\nu}$ / cm^{-1} = 2956 (w), 2902 (w), 2867 (w), 1661 (s), 1595 (m), 1438 (m), 1418 (m), 1408 (m), 1362 (w), 1329 (m), 1255 (s), 1222 (s), 1151 (s), 1027 (s), 891 (w), 872 (w), 844 (m), 821 (w), 780 (m), 750 (m), 716 (m), 679 (w), 667 (w), 636 (s), 571 (m), 540 (m), 517 (s).

MB (solid, 80K): δ = 0.14 mm·s^{-1}, ΔE_Q = 2.61 mm·s^{-1}.

MS (ESI(+), CH_3CN): *m/z* = 599 $[M–OTf]^+$.

Synthesis of complex [(11)Fe(NO)][OTf]$_2$ (16)

Complex [(11)Fe(NO)][OTf] (**15**) (20.0 mg, 2.7·10^{-5} mol, 1 eq) was dissolved in 2 mL of THF at RT and treated with solid [Ag][OTf] (7.6 mg, 2.9·10^{-5} mol, 1.1 eq). The dark green solution immediately changed to blue, and a blue/grey precipitate appeared. The mixture was left stirring at RT overnight. The blue product was fully precipitated with diethyl ether and the solid residue was washed, decanted, dried and dissolved in 3 mL of CH_3CN. The obtained mixture was filtered to remove solid Ag and the clear blue solution of product was dried under vacuum. Final dissolution of the blue residue in 1 mL of CH_3CN and slow diffusion of diethyl ether at RT allowed for the formation of single crystals suitable for XRD analysis.

Yield 14.2 mg, 1.6·10^{-5} mol, 59%.

IR (ATR): $\tilde{\nu}$ / cm^{-1} = 3128 (w), 3104 (w), 2963 (w), 2902 (w), 2871 (w), 1804 (s), 1625 (w), 1606 (m), 1579 (m), 1476 (m), 1458 (m), 1425 (m), 1401 (m), 1364 (w), 1342 (w), 1256 (s), 1222 (s), 1156 (s), 1109 (m), 1023 (s), 948 (w), 869 (m), 819 (w), 781 (m), 756(m), 718 (w), 695 (w), 685 (w), 637 (s), 573 (s), 514 (s).

UV/Vis (CH_3CN): λ_{max} / nm (ε / L·mol^{-1}·cm^{-1}) = 327 (3781), 376 (2496), 388 (2454), 560 (1026), 604 (1262), 990 (1786).

MB (solid, 80K): δ = 0.05 mm·s^{-1}, ΔE_Q = 2.94 mm·s^{-1}.

Synthesis of complex [(11)Fe(NO)][OTf]$_2$[PF$_6$] (17)

Complex [(11)Fe(NO)][OTf]$_2$ (**16**) (13.1 mg, 1.5·10^{-5} mol, 1 eq) was dissolved in 2 mL CH_3CN and the blue solution was cooled down to –35 °C in the glovebox freezer. Then solid thianthrene radical cation hexafluorophosphate (5.4 mg, 1.5·10^{-5} mol, 1.0 eq.) was added and the mixture left reacting at –35 °C overnight while the color changed from blue to purple. The mixture was then filtered from solid thianthrene, and the product was precipitated with cold diethyl ether and dried to obtain a purple powder.

Yield 9.6 mg, 9.3·10^{-6} mol, 62%.

IR (ATR): $\tilde{\nu}$ / cm^{-1} = 3126 (w), 2962 (w), 2912 (w), 2873 (w), 1862 (m), 1804 (m, from **16**), 1607 (m), 1581 (m), 1536 (m), 1478 (m), 1459 (m), 1427 (m), 1412 (m), 1365 (w), 1344 (w), 1256 (s), 1223 (s), 1556 (s), 1110 (m), 1061 (m), 1024 (s), 828 (s), 781 (m), 756 (m), 738 (m), 714 (m), 694 (m), 636 (s), 574 (m), 556 (s), 516 (s).

MB (solid, 80K): δ = –0.08 mm·s^{-1}, ΔE_Q = 3.42 mm·s^{-1}.

Synthesis of complex [(11)Fe(NO)] (18)

Complex [(11)Fe(NO)][OTf] (**15**) (20.0 mg, 2.7·10^{-5} mol, 1 eq) was dissolved in 2 mL of CH_3CN at RT and treated with excess dry magnesium powder. The mixture was left stirring overnight and the orange solution turned reddish. Remaining magnesium was then filtered away and the obtained solution was dried under vacuum to obtain a red/magenta powder. The solid was then dissolved in cold DCM, the solution filtered and dried under vacuum.

IR (ATR): $\tilde{\nu}$ / cm^{-1} = 2951 (m), 2904 (w), 2866 (w), 1687 (w), 1644 (w), 1577 (m), 1478 (m), 1437 (m), 1408 (m), 1383 (m), 1362 (m), 1299 (s), 1238 (s), 1222 (s), 1157 (s), 1029 (s), 846 (m), 777 (m), 751 (m), 705 (w), 668 (w), 637 (s), 573 (s), 515 (s).

MB (solid, 80K): δ = 0.19 mm·s^{-1}, ΔE_Q = 1.98 mm·s^{-1}.

10. DFT Calculations

Density functional theory (DFT) calculations were performed with the program ORCA 4.2.1, using the BP86 and B3LYP functionals and def2-tzvp def2/J basis sets.[265,266,319–321] The structural geometry of **12a**, **12b**, **13a** and **13b** were optimized starting from the corresponding crystal structures atomic coordinates. The broken symmetry (BS) geometry optimization of complex **14a** was run starting from the crystal structure coordinates of **13a**, while optimizations of the singlet and triplet state were run starting from the experimental coordinates of **14a**. The optimization of the structure of complex **14b** was run starting from the coordinates of the crystal structure of complex **13b**. UV/Vis spectra of the complexes were calculated by time dependent DFT (TD-DFT) computations at the B3LYP / D3BJ def2-tzvp def2/J level of theory employing 80 states and the CPCM continuum solvation model for solvent contributions.[322,323]

DFT Table 1. Coordinates of the optimized structure of **12a**.

Fe	-0.07600585849426	0.01977827648773	-0.01459357673962
N	1.85905173625469	0.03314230947609	-0.09847160042038
N	-2.12483063098800	0.00396163172063	0.07469505930187
N	0.10057552631246	0.06194233626237	1.85232913960291
N	-0.06115897857899	-0.01720235378797	-1.88893773806005
C	0.00656671399114	-1.91756791555565	-0.03360094713676
C	-0.02039867325795	1.95755096879917	0.00089096632202
C	2.68360692745055	1.09773789863331	0.16619437711058
C	2.67297504824907	-1.01582251730286	-0.44699236964548
C	-2.81746731727107	-1.05924901634589	0.58180273999678
C	-2.87617614464831	1.05390454874979	-0.37165069116916
C	0.38002935127226	0.16497793173946	2.97582863545068
C	0.11612948494254	-0.10856287874884	-3.03399760325676
N	0.99045186189069	-2.77096486676117	-0.46690624989490
N	-0.98769698507724	-2.74068490815193	0.39372114752804
N	-1.06367246230430	2.76572804475906	-0.32691426868673
N	0.98502882584093	2.82453676115657	0.34840365261108
C	2.34457376595271	2.41851918045452	0.48908071895530
C	4.06281912170404	0.74035374779730	0.01251082382897
C	4.05159729496457	-0.63716655314395	-0.43373889775167
C	2.32369253849989	-2.34437404924934	-0.73794873143609
C	-2.08185550370984	-2.22288915296419	1.19470553045110
C	-4.21109270212784	-1.10497794275404	0.63029974000091
C	-4.27027796182327	1.07044004125639	-0.31089555688309
C	-2.21644591103270	2.23696950345873	-1.03245074125754
C	0.76311713954557	0.30601914192147	4.36625557368090
C	0.37704888020706	-0.23323279050947	-4.45402697167984
C	0.58573699996292	-4.10157392247823	-0.32107805266780
C	-0.65801360195414	-4.08168641040399	0.22757796246193
C	-0.74260145317610	4.11104992605399	-0.17999619901094
C	0.54591120218395	4.14879533109448	0.25237404009529
C	3.36483658689782	3.32612890328118	0.78421039725644

C	5.06183539620369	1.67636887202456	0.28409932228187
C	5.03945160351355	-1.55575833940660	-0.80853427889093
C	3.32279420714117	-3.23032488913826	-1.13327347003680
H	-1.68130324278128	-1.91535646874770	2.17497575901630
H	-2.79272220422230	-3.03806649702263	1.36957328081196
H	-4.69603563356494	-1.99516177492606	1.03077239390793
C	-4.96462521767463	-0.02503404267964	0.18705910490463
H	-4.80326855943036	1.95123778925239	-0.66879400824866
H	-1.90246217800330	1.94863346574396	-2.04968456610361
H	-2.95351288926719	3.04192071586265	-1.13153034961845
H	-0.09921474260494	0.60722645348530	4.97757556218923
H	1.54538529788334	1.07351933985982	4.45927064862898
H	1.15729565002111	-0.64380058646885	4.75431430689578
H	0.31309770726821	-1.28632451956378	-4.76182801490834
H	1.38725368345322	0.13691113333983	-4.67971137993745
H	-0.34905796479762	0.34945812322573	-5.03775779005784
H	1.21495266515960	-4.93765817059975	-0.59151687260716
H	-1.32186703043831	-4.89038854604811	0.50818433706381
H	-1.44267613878611	4.91002962087983	-0.39219292024127
H	1.18241824648816	4.99423626051369	0.47179825779301
H	3.10264664313403	4.34455383245367	1.06117667276764
C	4.72713743588715	2.97248553847868	0.70597669659434
H	6.10955991949312	1.39341120253869	0.16906994240030
H	6.08547034169836	-1.25154569463127	-0.80150567024238
C	4.68449891979277	-2.85345713231603	-1.19427241530551
H	3.05426231477906	-4.25599340231800	-1.38325283140697
H	-6.05341484802113	-0.03623019991072	0.22969843341333
C	5.84320328610205	3.97517148575138	1.03529133061606
C	5.71690600676412	-3.89467110840362	-1.64890967589548
C	6.71354779207729	4.19941786814796	-0.21976691663622
C	5.29364357503351	5.33643727861596	1.48938318888598
C	6.71992097378466	3.40651875367963	2.17171786193079
C	7.14363934997926	-3.32521638295311	-1.66491325712144
C	5.69021862538976	-5.10148866001514	-0.68569027069509
C	5.37024685216732	-4.37023279586120	-3.07603051133448
H	7.52786024830240	4.90512675969596	0.00057505355012
H	6.11233701689685	4.61219943532723	-1.04287475205842
H	7.16700645758880	3.26251658989096	-0.57109636362228
H	6.12753450280282	6.00824045844638	1.73620714416433
H	4.66737964189496	5.24073050431078	2.38907666666450
H	4.70181272364277	5.82320669181689	0.69959020786564
H	7.54197203143113	4.09972142240659	2.40245199398757
H	7.16163310879053	2.43943484089839	1.89599962634711
H	6.12723719485087	3.25924686212557	3.08597263058963
H	7.84407916210533	-4.09803439202769	-2.01152168458282
H	7.46814955279210	-3.01054936745856	-0.66315901255392
H	7.23091372343072	-2.46531888369198	-2.34453360116428
H	6.42503267729458	-5.85723149253511	-0.99987321004077
H	4.70283563147394	-5.58368111804756	-0.66385789522640
H	5.93493764871137	-4.78749581694504	0.33909125198038
H	6.09440892494407	-5.12604462418896	-3.41387424636603
H	5.39373486850780	-3.52914977892886	-3.78381962272395
H	4.36943061423743	-4.82283914388300	-3.12156949658227

DFT Table 2. Coordinates of the optimized structure of **13a**.

Fe	-0.19648000446925	-0.07340633685816	-0.00175954996829
N	1.68408187570869	-0.11942476883623	-0.07745235622104
N	-2.28486632034169	-0.02755454414296	0.07931757119397
N	-0.12665260434993	0.07438172265607	1.87872482624127
C	-0.20339132300157	-2.01194544012733	0.08492973868039
C	-0.11063185482169	1.86309659733254	-0.09206459442848
N	-0.23449895470404	-0.26665347762647	-1.88714452139705
C	2.54992964515121	0.93364613096061	0.14673664324577
C	2.46079717472189	-1.20831521764561	-0.42565270084398
C	-2.99999094235595	-1.03872654656529	0.64765951982955
C	-2.99324569939184	1.02132410046721	-0.42553187534731
C	0.01085645647807	0.17185227177508	3.02737138676140
N	0.73261953064876	-2.91031648869976	-0.36253928596618
N	-1.20939467249262	-2.77949874283391	0.56072623777713
N	-1.12283496188592	2.67398235501972	-0.47220929948359
N	0.90329807636558	2.71783746657730	0.26161357238893
C	-0.07191856614219	-0.49809765334130	-3.01324273948871
C	2.24468769116986	2.27851672467026	0.41377925990796
C	3.90513176883365	0.53205257529495	-0.02834231438338
C	3.84498503351722	-0.86405972929762	-0.45381188205063
C	2.05969883496600	-2.52577555985663	-0.68066624193459
C	-2.31064314064760	-2.20415643865148	1.31489029005422
C	-4.39493255493152	-1.02946058318881	0.71006701723122
C	-4.38656218516226	1.08692226886643	-0.36582332056977
C	-2.29758449502536	2.14773706386331	-1.14897536811642
C	0.16442163183924	0.18213032752900	4.47185669167041
C	0.28391901890903	-4.22345266931211	-0.17407237065405
C	-0.93922835179021	-4.13865558351889	0.41025440417343
C	-0.78141081222445	4.01957223901024	-0.34831147528442
C	0.49372807434771	4.04958151135838	0.11727654413916
C	0.24052046167014	-0.85820459757946	-4.38497300613100
C	3.29740536104149	3.15824847698749	0.65874680432871
C	4.94094758642893	1.43279264265922	0.19085534064363
C	4.78700265881960	-1.79730658476212	-0.85589338789649
C	3.02167785142022	-3.44509425132579	-1.11412386289692
H	-1.93014693801161	-1.88503424135283	2.29879650840747
H	-3.04801350095950	-2.99362613575728	1.49330447072973
H	-4.91178568265259	-1.87477334763256	1.16393398724766
C	-5.11006460811534	0.04786873418558	0.20404414530996
H	-4.89483339141574	1.95951189724321	-0.77516247545566
H	-1.99725555492750	1.80218260269101	-2.15141128558973
H	-3.00703550357175	2.97062315974001	-1.28599607283638
H	-0.37565209502062	1.05106905271030	4.87905977811460
H	1.23371537248182	0.33623806282995	4.69201395374554
C	-0.33531544110762	-1.13787561138354	5.10905124532421
H	0.86908540950922	-5.09148746543931	-0.44406904518574
H	-1.62682356058656	-4.91321193502057	0.72815318679579
H	-1.46171812197266	4.82456602376503	-0.59947396444077
H	1.13490248668578	4.89221087858405	0.33512449311920
H	0.25830856039648	0.05810930373334	-4.99684373173399
H	-0.57319068237743	-1.49203450351471	-4.77180056329344

C	1.60493291865055	-1.59281675144388	-4.46123340222310
H	3.07969060422322	4.19878791896271	0.89228271813886
C	4.64840037651309	2.75593802588154	0.57920338459772
H	5.97501015522096	1.11741107578247	0.06328245263215
H	5.84296580156001	-1.52877704010647	-0.89010775563157
C	4.37847834711374	-3.09950424911985	-1.23407593102099
H	2.71762116525351	-4.46236647675376	-1.34654376548260
H	-6.19863790352878	0.07660309031743	0.25237732465688
H	-0.19145123469521	-1.04257175734483	6.19498600443438
H	-1.42085948033493	-1.22261416692432	4.94539001975440
C	0.39217696870224	-2.37244516641474	4.58038241560243
H	1.55537678690788	-2.49360140322364	-3.83274749611821
H	1.72311430712801	-1.93311484935304	-5.49967839177889
C	2.78069379089196	-0.71358898983481	-4.04524382403121
C	5.74393361983563	3.78155324872755	0.87783102881593
C	5.42233885796716	-4.09689262800596	-1.73890278074400
H	0.01353004750673	-3.28188883972524	5.06361939258059
H	1.47248686250888	-2.31598319921717	4.77739753816426
H	0.25832180252055	-2.48949957652230	3.49235503611731
H	3.71900460169594	-1.28234877027382	-4.07910436115746
H	2.66185065934336	-0.34073716443433	-3.01814257765890
H	2.88934046640136	0.15253752176286	-4.71266434504070
C	5.55647316985356	4.30707096019726	2.31921899753018
C	7.15184626002458	3.17884214436259	0.75767629472674
C	5.62522588222238	4.95498220019615	-0.12153434427845
C	6.50938757322210	-4.28430041011318	-0.65558337581231
C	6.06823381976064	-3.52415644868315	-3.02192556487119
C	4.81667936764474	-5.46948500219110	-2.06686007599971
H	6.33198367958640	5.05105838396201	2.54677728159876
H	5.63964470393184	3.49077337159287	3.05057502343231
H	4.57987790890737	4.79234371228323	2.45726386819248
H	7.89812234359018	3.94504374123436	1.00621230004243
H	7.36604061081766	2.83396152941097	-0.26377328515036
H	7.29731620492271	2.33935377938871	1.45241874202793
H	6.41350400023367	5.69352893335723	0.07948787606777
H	4.65920217714650	5.47255488095711	-0.04005873077101
H	5.73994959831374	4.60467112096106	-1.15716546867705
H	6.07318052829119	-4.65647072956424	0.28160716503335
H	7.04051805171512	-3.34814387770674	-0.43741883520897
H	7.25348286617105	-5.01532659709687	-1.00085225786396
H	6.84357410331849	-4.21113955654557	-3.38950891122592
H	6.54552186118423	-2.55088591183051	-2.84091178510941
H	5.32018367979171	-3.39774083171078	-3.81790691607266
H	5.60741951261088	-6.13775314640570	-2.43220812859849
H	4.05232325879120	-5.40499517569803	-2.85589585469097
H	4.37225089890806	-5.94657048233350	-1.18116803539203

DFT Table 3. Coordinates of the optimized structure of **14a**.

Fe	-0.05417122098318	-0.04316860692406	0.02841273587664
N	-1.91485616413111	-0.05057660724558	0.11706121800318
N	2.06006108432406	-0.03430606719479	-0.07099552581438
N	-0.07418551460989	0.12797469951834	-1.86494092725593
N	0.10444914243070	-0.20593322748419	1.91620065965030
N	-1.01719691640506	-2.86470223775083	0.44660392244655
N	0.92341123793796	-2.77776853130806	-0.48220724946326
N	0.94620124304777	2.70095451135742	0.44094634576924
N	-1.07386842323079	2.77058745238427	-0.29963231906638
C	-0.06830102242915	-1.98693570378200	-0.04054813834127
C	-0.07923788013474	1.90279402598112	0.09783557906886
C	-2.75125081307414	1.01500822547213	-0.14495287234576
C	-2.71241340388579	-1.12434838426961	0.46047168303532
C	2.75309521347724	-1.07761978465376	-0.61006083661074
C	2.79236805276011	1.01561654116854	0.39942496180345
C	-0.11680677217743	0.28487394820240	-3.01388371434029
C	0.17381631779395	-0.35368167805450	3.06508862272485
C	-2.40960486003970	2.35351959187011	-0.44444856316270
C	-4.12022668217126	0.64053050764611	0.00375732059717
C	-4.09354816084723	-0.76043997763157	0.44423732264660
C	-2.33332975428475	-2.45806985928219	0.71614678489066
C	2.04789492883395	-2.25154829532675	-1.24367200009197
C	4.14781798338077	-1.09866618566477	-0.67761567716889
C	4.18685717589802	1.04896169426606	0.33275487728210
C	2.13987850411338	2.18443405984359	1.09576148351092
C	-0.16770608203288	0.47669464497778	-4.44708540647438
C	-0.57300707297495	-4.19066379574156	0.31732504128885
C	0.64716998938884	-4.13192333824853	-0.26893866886847
C	0.64196147442351	4.05169834997719	0.25124721919464
C	-0.62934855418563	4.09943583393843	-0.21630564186779
C	0.26051377568634	-0.52563002382419	4.49916261097555
C	-3.44225295367417	3.24155239815167	-0.73903536645596
C	-5.12955973335123	1.54045205940333	-0.25980551023174
C	-5.06110973943497	-1.66993151484951	0.79495441035990
C	-3.32864482416685	-3.36548743275178	1.10468942058261
C	4.88709150224270	-0.02156394634649	-0.20725318530568
C	-4.80065065511421	2.86446742864298	-0.67995308482909
C	-4.68117948407816	-3.00141659018595	1.17638610653907
C	-5.87224685748922	3.88574408771098	-1.01424959738745
C	-5.75553348801887	-3.97493152396474	1.61200360375149
C	-5.60781014273839	4.44521731439630	-2.43654427329829
C	-7.29041851106112	3.29817569545375	-0.96448494204119
C	-5.77342623389839	5.04632656526619	0.01615107895427
C	-6.78841129801882	-4.12093468786703	0.45991427416052
C	-6.46870283671095	-3.37600180058875	2.85684024814382
C	-5.20155123781465	-5.35989406777863	1.96873856859641
H	1.68560481898542	-1.97019375078280	-2.24509750897063
H	2.76954092068464	-3.06329784986112	-1.38107763597995
H	4.64706800908243	-1.96660799220381	-1.10807074975652
H	4.71704519146804	1.92199333972585	0.71285720317865
H	1.87400175720568	1.90050894616868	2.12625890249221
H	2.86475071501136	3.00223481453300	1.16531516124130
H	0.27484156326553	1.44653403284372	-4.71655755863361

H	-1.21235961996951	0.45358379979002	-4.78931690866596
H	-1.15463895998242	-5.04772485184013	0.62821934905204
H	1.33179062576174	-4.92246566088326	-0.55508744174635
H	1.34470877561104	4.84810101419706	0.46901914150477
H	-1.24318918771567	4.95185462693242	-0.47330539380379
H	-0.29748972154121	0.27127429683612	5.01156949983606
H	1.31174625031065	-0.48673631332952	4.81969275199233
H	-3.20516438026645	4.27087405739057	-0.99810158803946
H	-6.17477757693816	1.25499181234767	-0.15473199253549
H	-6.11521974274376	-1.39518295789460	0.78702245318260
H	-3.05684387489146	-4.39178389234735	1.33601804491271
H	5.97613814932566	-0.01644710652139	-0.26037486748099
H	-6.37834526908086	5.19075189406502	-2.67187892531950
H	-5.65787335107099	3.64953047602812	-3.19239395107106
H	-4.63200037672700	4.94352918931073	-2.51642313467560
H	-8.01195212827780	4.07486935828053	-1.24778971190310
H	-7.56431590075056	2.96048321803579	0.04480724467053
H	-7.41672375506624	2.46402882959080	-1.66959113500010
H	-6.54890809253121	5.78806799662657	-0.21711123064040
H	-4.80119494526334	5.55562900744949	-0.02342168325521
H	-5.93937167593656	4.68517679529425	1.04021297785038
H	-6.31425588150412	-4.50013957601229	-0.45510398088674
H	-7.29599443108248	-3.17582838177380	0.22580674000740
H	-7.55787211695162	-4.83938937317275	0.77219814967499
H	-7.27508082493000	-4.05689849090724	3.16178672362305
H	-6.92428203272644	-2.39801239784496	2.64941430998914
H	-5.77131683288139	-3.26634192802033	3.69814077849827
H	-6.02418163643316	-6.00552161051712	2.30064348872637
H	-4.47436669872763	-5.31330986250022	2.79300302434556
H	-4.73439008525178	-5.85418937928136	1.10431386303797
H	-0.15825377306149	-1.49955694929491	4.79020244788230
H	0.38698419801967	-0.32210072136628	-4.96029777476556

DFT Table 4. Coordinates of the optimized structure of **12b**.

Fe	-0.01806366760169	0.11068241177898	0.00131676827048
N	1.86753211885492	0.08646927176326	-0.09727061320645
N	-2.07608550776126	0.12985794553643	0.29823040556338
C	0.04524224320649	2.02327146426774	-0.10888204775930
C	0.03701291567376	-1.79896940728314	0.25196516734993
O	-0.43343438274137	-0.06307406603697	-2.14606520218247
C	2.73113035532718	1.16569916405484	-0.02312071598891
C	2.65893125375420	-1.00755654318305	-0.40180468529946
C	-2.83614207858162	1.07099086589360	-0.32646677532799
C	-2.74090388280060	-0.90909349449794	0.88115554178211
N	1.06796042175202	2.92632580516305	0.09188367430918
N	-1.02481145037180	2.80333872192539	-0.43763843893362
N	0.96636919572291	-2.72281428517937	-0.17430888705343
N	-0.91118040290210	-2.55568515094167	0.86871864113893
S	-1.49461906948251	-0.91155304552467	-2.77788447079724
C	2.42694888112708	2.52291995341438	0.15486450864566
C	4.08313823811668	0.77292474052174	-0.24299556176606
C	2.27612701929620	-2.34780205948151	-0.55621520183331
C	4.02888822758176	-0.64576807008059	-0.53532507478592
C	-2.21391473361836	2.23677481870279	-1.05077726667759
C	-4.22617110768544	0.96571963198721	-0.42425766213395
C	-1.94983334607585	-1.92469312598466	1.65745141074364
C	-4.11993258099266	-1.06157270758846	0.80837628605661
C	0.61594850633850	4.23473726870130	-0.09486293647689
C	-0.69722314579613	4.15264492769463	-0.43884097076632
C	0.54765007075622	-4.02173393494897	0.12372740999397
C	-0.63516244768620	-3.91190590559230	0.78455625094056
O	-1.89574110257020	-2.07787799069214	-1.99546909374517
O	-2.56625350578659	-0.11129594745495	-3.36901523838279
C	-0.55935674105250	-1.63434398744694	-4.23412418750070
C	3.47453938927657	3.43892964257161	0.24287400294913
C	5.11719808105970	1.71233935046871	-0.17395677784143
C	3.23845532944467	-3.27532370125455	-0.94948779123991
C	4.98417954511389	-1.59950903953514	-0.90493768174651
H	-1.96699907483391	1.89494037340918	-2.07096087475136
H	-2.96168969122771	3.03473090423978	-1.13167865297471
H	-4.77403150603255	1.73912205472343	-0.96172689221262
C	-4.88697657840309	-0.11739482897557	0.13234152810825
H	-1.48074635132567	-1.43498125906286	2.52929178458549
H	-2.62468685468805	-2.70335239091955	2.03020826597400
H	-4.58149485313686	-1.93341163281132	1.27079158238941
H	1.25503313475906	5.09980927696338	0.01287157356125
H	-1.41205746825815	4.92908767290743	-0.68354427756066
H	1.12315409364951	-4.89897426152624	-0.13440836516762
H	-1.29604971973891	-4.67164110650579	1.18299830936582
F	0.49123236401271	-2.37163944780383	-3.80323948018526
F	-1.36619113433240	-2.43771934446267	-4.96333859167493
F	-0.08773938409946	-0.66205316716414	-5.04432610237313
C	4.82592915657942	3.05370161538965	0.09961764089996
H	3.24306555833443	4.49204759818000	0.40045892788045
H	6.14501980247596	1.39171399774541	-0.33833812551756
C	4.59233935264492	-2.92191956509854	-1.14310257231657
H	2.93791117656138	-4.31054066429639	-1.10462628050714

H	6.02606181319807	-1.30163322005693	-1.01547541147867
H	-5.96834503246694	-0.22378314976530	0.04631504815645
C	5.91580450693410	4.12870614910046	0.21115665436422
C	5.57710289383981	-4.00720217090904	-1.59999760340099
C	5.83556013358353	4.80144362774130	1.59803299831842
C	5.70504003767123	5.19304489917701	-0.88728979868308
C	7.32486149820068	3.54050407774250	0.04431880421853
C	5.13636291735330	-4.54409990092144	-2.97900660302253
C	5.58675844878496	-5.16369001762589	-0.57742845739369
C	7.01082442599869	-3.46994941192889	-1.72894628608573
H	6.60542799885892	5.58278465496062	1.69162884094229
H	5.99163424600573	4.06359015202664	2.39813965328792
H	4.85714401250298	5.27350537881835	1.76389954506028
H	6.48405214302116	5.96872637262873	-0.82524690957578
H	4.72967061547585	5.69042870024823	-0.79116206095326
H	5.75146065103329	4.73494700344315	-1.88578355283807
H	8.07358613621000	4.33918482880124	0.14991810225254
H	7.46041637578397	3.08616813340998	-0.94775033731793
H	7.53809474594244	2.77754504877617	0.80665435330602
H	5.82114495915802	-5.33567247349265	-3.32006002040274
H	5.13698201438016	-3.73792897932135	-3.72646934520382
H	4.12203538741239	-4.96602909632935	-2.94635696558535
H	6.29058957210961	-5.94838801627812	-0.89345652971802
H	4.59446153321055	-5.62418100767366	-0.47627715626848
H	5.89212395664326	-4.80366751211458	0.41553489121111
H	7.67806290819659	-4.27647752885066	-2.06606737485162
H	7.39429084463216	-3.09919039630142	-0.76768912804583
H	7.07390600748878	-2.65415557097519	-2.46377626511334

DFT Table 5. Coordinates of the optimized structure of **13b**.

Fe	-0.00348944381920	-0.00552014267548	-0.00641947725187
N	1.86819705486219	-0.00502374581444	-0.21001221970328
N	-2.12017614205994	-0.00715798976287	0.23132941252019
C	0.02507513210989	1.94014660691886	-0.20257221113786
C	0.06959164736586	-1.95124868204546	0.18011978895721
O	0.06771161969069	0.20947253405325	2.18095673937052
O	-0.42414901824723	-0.20391270920379	-2.15802281819738
C	2.71647789177842	1.08111744325164	-0.08717863813771
C	2.67229454279441	-1.09073219102662	-0.50650815793200
C	-2.87808677277695	1.01919354262358	-0.22966018465506
C	-2.75468635477620	-1.02915063223485	0.85830403245796
N	1.03449213141462	2.82731846002255	0.04940652343168
N	-1.04040354832129	2.70079076101114	-0.52547206762988
N	1.00069939165750	-2.83805798668274	-0.28471166606424
N	-0.89900117782045	-2.71257225389380	0.72939952738407
S	-0.84923006053561	1.02045156401348	3.05345933437792
S	-1.49554398770447	-1.04272966463307	-2.79799960336387
C	2.39472175236702	2.42623613354759	0.13943681383201
C	4.07462487122169	0.70270584388014	-0.27715281552412
C	2.31048415407697	-2.43596578467689	-0.66173914926588
C	4.04055722915048	-0.71273068054800	-0.60166585261176
C	-2.27086775169626	2.12862628226818	-1.04936901522686
C	-4.26188992780950	1.05437198366634	-0.06399529614979
C	-1.97849905407134	-2.13930271602523	1.51799876835865
C	-4.13901051779057	-1.05534703716960	1.02442598235132
C	0.56792237089051	4.13288462211713	-0.07010417781400
C	-0.74249476818344	4.04807098861656	-0.43834376890874
C	0.57132730436619	-4.14348762839777	-0.06776666736345
C	-0.62721396157417	-4.05952174626483	0.57779213310464
O	-1.32618768794108	2.25615567566593	2.44090339436671
O	-1.83281172309310	0.19724817508895	3.75201668519322
C	0.35530703254337	1.59017041923467	4.37437455402058
O	-1.73389253609886	-2.31973174518135	-2.13376230611932
O	-2.66648373980581	-0.26086511488702	-3.18660966840079
C	-0.64682459532718	-1.50183871397235	-4.40713236585844
C	3.43083297477307	3.34218947165081	0.30257549885697
C	5.09869422669216	1.64319368345128	-0.13369640720059
C	3.29028322668865	-3.35247804847390	-1.03553919948207
C	5.01315668198022	-1.65407155627354	-0.95178865230352
H	-2.07595495282613	1.72584874541581	-2.05724065444822
H	-3.00136052726497	2.93951810173624	-1.13840065596346
H	-4.81980221311541	1.90931255027375	-0.44339780322969
C	-4.91051580718145	0.00212290394848	0.56557355543800
H	-1.55863112325321	-1.73608503729624	2.45475031936808
H	-2.67063460442923	-2.94861624323584	1.77142344411126
H	-4.59688230439259	-1.90593487909391	1.52784361462214
H	1.19157725010005	4.99991364038886	0.09437364741209
H	-1.47137463614478	4.82307761039367	-0.64003027046812
H	1.14350467919631	-5.01019701304909	-0.36558480080775
H	-1.29536893810432	-4.83481643929422	0.93111003213409
F	1.33220487839179	2.34828786799688	3.82386890583162
F	-0.28461830008493	2.33228328999622	5.30239074525398
F	0.93308505190523	0.53870466322210	4.99257406656989

F	0.49041532039046	-2.19171985178813	-4.16014113573951
F	-1.45710384114580	-2.27538615536590	-5.16012698623697
F	-0.32794454207175	-0.39932335256064	-5.11839274270984
C	4.78814598852562	2.96989406813279	0.19094039158610
H	3.18705925262633	4.38363633936290	0.50763862133706
H	6.13474456422222	1.33561114518817	-0.26882618821600
C	4.64200686930164	-2.98115733626379	-1.20441628727638
H	3.00943141557560	-4.39391295453491	-1.18426823478026
H	6.05515628818118	-1.34730624224418	-1.03071969638362
H	-5.99266086615344	0.00668864304931	0.69688300377425
C	5.86461575533018	4.04216376143798	0.40330279700446
C	5.65012078967345	-4.05265355932588	-1.64068953028509
C	5.71152684894906	4.64533968141640	1.81605555713632
C	5.69472385180278	5.15530085455160	-0.65286284055158
C	7.28403544046837	3.46922540949384	0.27559202048981
C	5.24481151892948	-4.59043619997138	-3.03030884232469
C	5.65066145231088	-5.21091798692210	-0.62002977197946
C	7.07942841736389	-3.49708626181260	-1.73642974718404
H	6.47254906852045	5.42210672649973	1.98335412013389
H	5.83051012386788	3.87059806200392	2.58679277608410
H	4.72418784008366	5.10674104604358	1.95652710207290
H	6.46369784716612	5.93118189098688	-0.51843359743622
H	4.71265802031096	5.64308585103567	-0.57734334594627
H	5.79002289230102	4.74635955108607	-1.66917205361741
H	8.01979406178536	4.26511874846057	0.46052101479797
H	7.47357869985032	3.06919708838528	-0.73088309719899
H	7.46509736482621	2.66956070155025	1.00799289041832
H	5.94925015957062	-5.36942096387467	-3.35879920956151
H	5.24819491164928	-3.78248707491279	-3.77580349561818
H	4.23738878136035	-5.02979210989496	-3.01927100644454
H	6.37117015177612	-5.98498442011771	-0.92333150952766
H	4.66307007114594	-5.68576354671232	-0.54170538095934
H	5.93030818052060	-4.85048493043691	0.38022749292159
H	7.76286895510988	-4.29488135477739	-2.06078601681957
H	7.43789727198257	-3.12608090270301	-0.76575383712897
H	7.14997031312466	-2.67891236710684	-2.46792052693573

DFT Table 6. Coordinates of the optimized structure of **14b**.

Fe	0.01190408291341	-0.01887770585215	-0.17171348565275
N	1.86000887628847	-0.00881189354560	-0.25554115204038
N	-2.26354624188306	-0.00672005599654	0.18561871510299
C	-0.01180952265402	1.93602364288079	-0.24654970615860
C	0.03327289089698	-1.94741038778439	0.14637521244530
O	0.19534692580105	0.15242261088333	2.07839159252292
O	-0.20717558307346	-0.24021416554043	-2.05224801967124
C	2.69471986946645	1.08965905984534	-0.14438109481059
C	2.66016425064432	-1.10104747890695	-0.55146318280450
C	-2.99365197237553	1.06530354181535	-0.19216506642033
C	-2.86812349896022	-1.03106763722449	0.82270339600228
N	0.99409237368920	2.81885947353384	0.05710864002496
N	-1.09867846090183	2.70285244662172	-0.47998608186970
N	0.97920934414612	-2.84343240963069	-0.28328769567839
N	-0.95595262404698	-2.69730864264389	0.67728114097598
S	-0.73808516212654	0.95403876290103	2.97251553468674
S	-1.31608511723894	-0.99909402082909	-2.84050970988024
C	2.35467076875389	2.42867898641447	0.10426885926871
C	4.05106873335269	0.71284004610171	-0.34156213464603
C	2.28806266417632	-2.44887728713000	-0.66726036414138
C	4.02320921708820	-0.71550370688029	-0.65431311961002
C	-2.35848391077350	2.17338483460511	-0.99749381915987
C	-4.36273162644296	1.13953625858379	0.05817041997577
C	-2.07202624890685	-2.15178433966536	1.44354035088751
C	-4.24304569516399	-1.02212110002990	1.06764939001150
C	0.50286151119518	4.11961788664144	0.06412067151905
C	-0.81527891893576	4.04094737082711	-0.27708804823107
C	0.54445979079156	-4.14478842210633	-0.05118225274563
C	-0.67181894503583	-4.04716366703041	0.55652544244373
O	-1.22540564338167	2.18868348963480	2.37181455062605
O	-1.70213029929463	0.10131166106028	3.65503898765339
C	0.50106971551392	1.50004653484110	4.27774909672496
O	-1.73847275711266	-2.22431543811101	-2.19078372971378
O	-2.30709535832721	-0.06889219790369	-3.34567134907920
C	-0.24339834760231	-1.51326743072248	-4.30168566000311
C	3.38986135824467	3.34864043763330	0.26759832607394
C	5.06518474139382	1.65096346163506	-0.19207263779031
C	3.27036835777621	-3.37090091245977	-1.02453917244255
C	4.99286815040352	-1.65731360309292	-0.98031164246588
H	-2.18337686101043	1.79525626160477	-2.01786827632493
H	-3.06116149437947	3.01020034374244	-1.06414560129861
H	-4.91756834687325	2.02565786255011	-0.24719540512282
C	-5.00189782804073	0.07688044379267	0.68734390081299
H	-1.68000062103592	-1.76676593037509	2.40124601459952
H	-2.74976575576714	-2.98252356777648	1.66449548377635
H	-4.70266632307464	-1.87032459034644	1.57374781528534
H	1.11083326209358	4.98337980214469	0.29328375420929
H	-1.55961969192563	4.81962540064192	-0.39042079597383
H	1.12378373588856	-5.01893082342514	-0.31217121538106
H	-1.34396962885488	-4.81802637857796	0.91268830242553
F	1.46118973445143	2.25846313297928	3.70080988063662
F	-0.12547845756095	2.23103030052520	5.21213033742110
F	1.08093781922119	0.43794054403163	4.86058684059448

F	0.75319460809325	-2.31078419407782	-3.86843896117164
F	-1.00403727059886	-2.18943580012360	-5.17141228886864
F	0.28176064896188	-0.43720720156497	-4.90238799716378
C	4.74463782260673	2.98298574952386	0.14513978208107
H	3.14779547135046	4.38738408578513	0.48322017300800
H	6.10465990578706	1.35620352086146	-0.32485388452009
C	4.61858749654988	-2.99767068525072	-1.20571358441718
H	2.99811309502905	-4.41716757182057	-1.14836078540177
H	6.03661086752921	-1.35965275730685	-1.06220235174116
H	-6.07324061478929	0.10878100978354	0.88479592338229
C	5.81891111746556	4.05291565886726	0.35546363307327
C	5.63070479975230	-4.06973669575770	-1.61880124127984
C	5.65066695749606	4.66747993017868	1.76306844669588
C	5.64522893292720	5.15475925890560	-0.71431955732441
C	7.23935014619161	3.47987943097161	0.24034825898417
C	5.21844212719323	-4.63459326057133	-2.99735908584869
C	5.63114498685644	-5.20532203807641	-0.57111261323564
C	7.05730889114139	-3.50976421726969	-1.72858256599623
H	6.41856535249405	5.43617060802430	1.92756061296742
H	5.75574137459271	3.90160230888544	2.54421836183805
H	4.66956570510697	5.14609598065683	1.88841153558997
H	6.41398736998090	5.92930392982700	-0.58122107948488
H	4.66427927088944	5.64515765187756	-0.64393096047508
H	5.74676144405204	4.74017346949280	-1.72739495465312
H	7.96995828486626	4.27867969465958	0.42640102749893
H	7.44098065000476	3.07907885312107	-0.76337345205194
H	7.42113337594808	2.68706229935554	0.98008015897235
H	5.92751155025388	-5.41509247560206	-3.30733791586221
H	5.22004364912473	-3.84447520700155	-3.76149111264487
H	4.21499146804736	-5.08254749716562	-2.97648844796497
H	6.35957044514160	-5.97615609782674	-0.85854671277992
H	4.64937878519486	-5.69116567653727	-0.48869543455756
H	5.90667193919244	-4.82530351436652	0.42263783765452
H	7.74017420648707	-4.31176159060648	-2.03976339603122
H	7.42144268202562	-3.12293298701399	-0.76629791415953
H	7.12688138462387	-2.70828559772220	-2.47850803670171

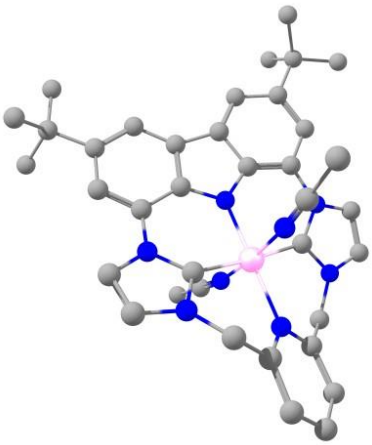

Figure 83. Visualization of the optimized geometry of the cation of complex **12a** based on DFT calculation at the BP86 level (grey: C, blue: N, pink: Fe; hydrogen atoms omitted for clarity).

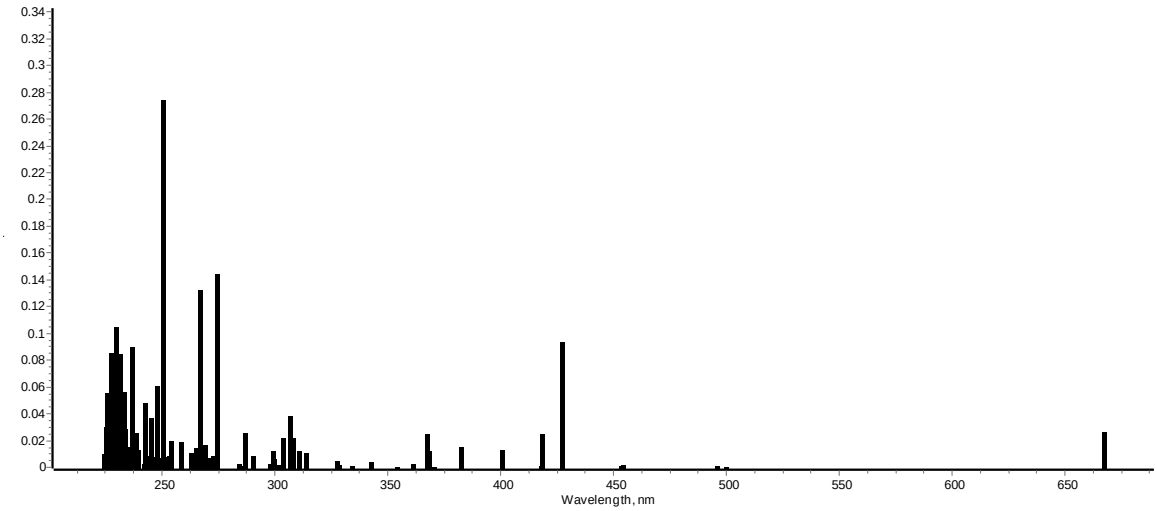

Figure 84. Calculated absorption spectrum of the cation of complex **12a** in CH_3CN at the B3LYP level.

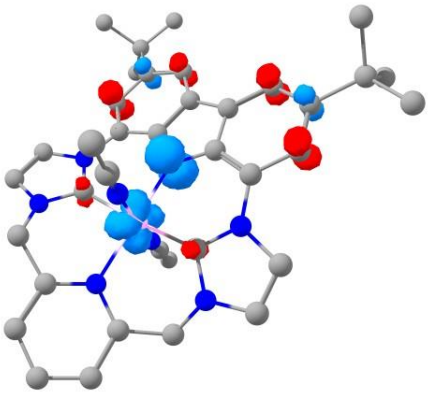

Figure 85. Calculated TD-DFT difference density of the cation of complex **12a** (red/blue indicates gain/loss of electron density) for state 4 (426 nm). Grey: C, blue: N, pink: Fe.

DFT Table 7. Selected TD-DFT (B3LYP level) calculated energies, oscillator strengths and compositions of the main electronic transitions of complex **12a**.

States	Energy (cm^{-1})	Wavelength (nm)	Osc. Strength	Major Contributions
4	23424.5	426.9	0.094227237	HOMO → LUMO+1 (94%)

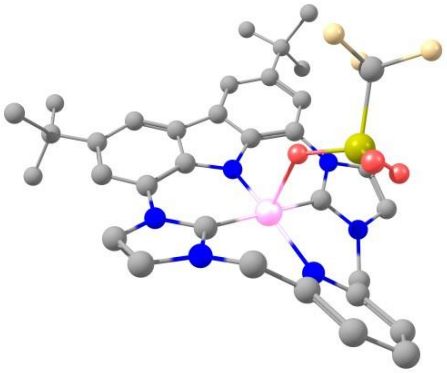

Figure 86. Visualization of the optimized geometry of complex **12b** based on DFT calculation at the BP86 level (grey: C, blue: N, red: O, yellow: S, white: F, pink: Fe; hydrogen atoms omitted for clarity).

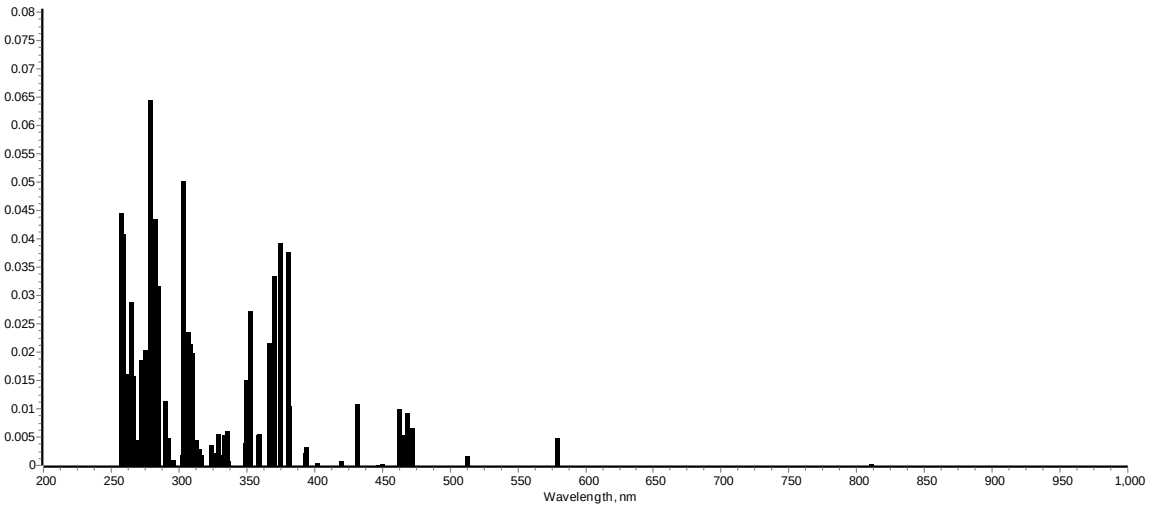

Figure 87. Calculated absorption spectrum of the cation of complex **12b** in acetone at the B3LYP level.

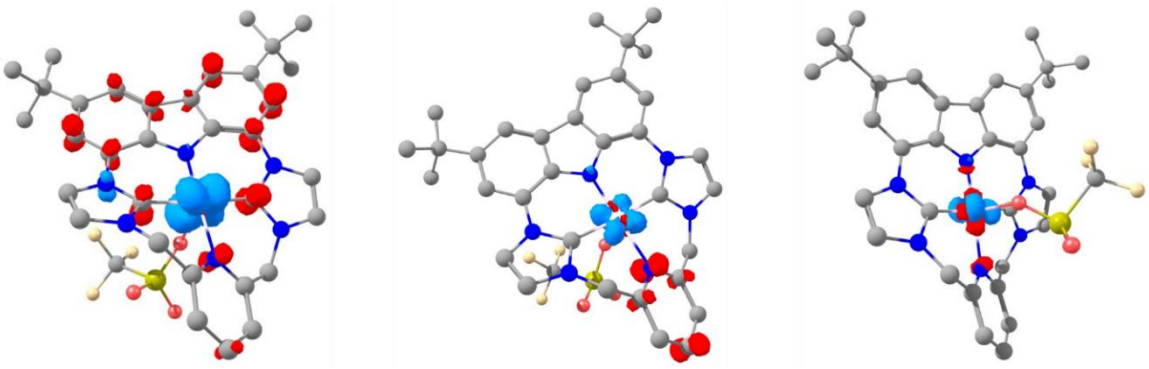

Figure 88. Calculated TD-DFT difference density of complex **12b** (red/blue indicates gain/loss of electron density) for, in order, state 12 (431.3 nm), 11 (468.0 nm) , and 8 (461.8 nm). Grey: C, blue: N, red: O, yellow: S, white: F, pink: Fe.

DFT Table 8. Selected TD-DFT (B3LYP level) calculated energies, oscillator strengths and compositions of the main electronic transitions of complex **12b**.

States	Energy (cm^{-1})	Wavelength (nm)	Osc. Strength	Major Contributions	Character
8	21654.5	461.8	0.010027554	HOMO → LUMO (14%) HOMO → LUMO+15 (9%)	d-d
11	21365.4	468.0	0.009127092	HOMO-2 → LUMO (61%) HOMO-1 → LUMO+3 (11%)	d-d/MLCT
12	23186.6	431.3	0.010885201	HOMO → LUMO+1 (55%) HOMO → LUMO+4 (9%)	MLCT

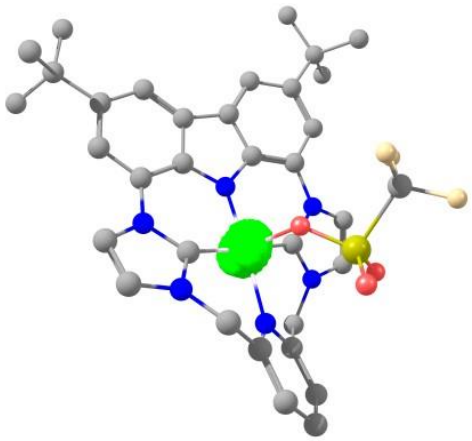

Figure 89. DFT calculated spin density plot for complex **12b** at the B3LYP level.

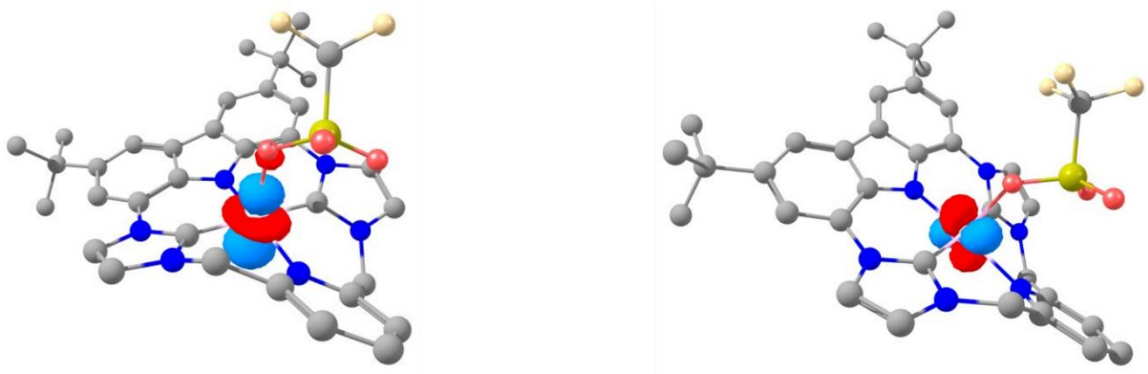

Figure 90. Spin-up magnetic orbitals of complex **12b**.

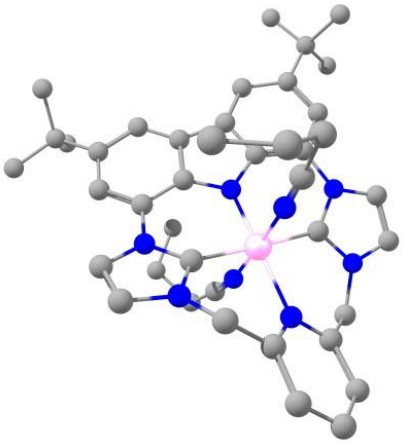

Figure 91. Visualization of the optimized geometry of the cation of complex **13a** based on DFT calculation at the BP86 level (grey: C, blue: N, pink: Fe; hydrogen atoms omitted for clarity).

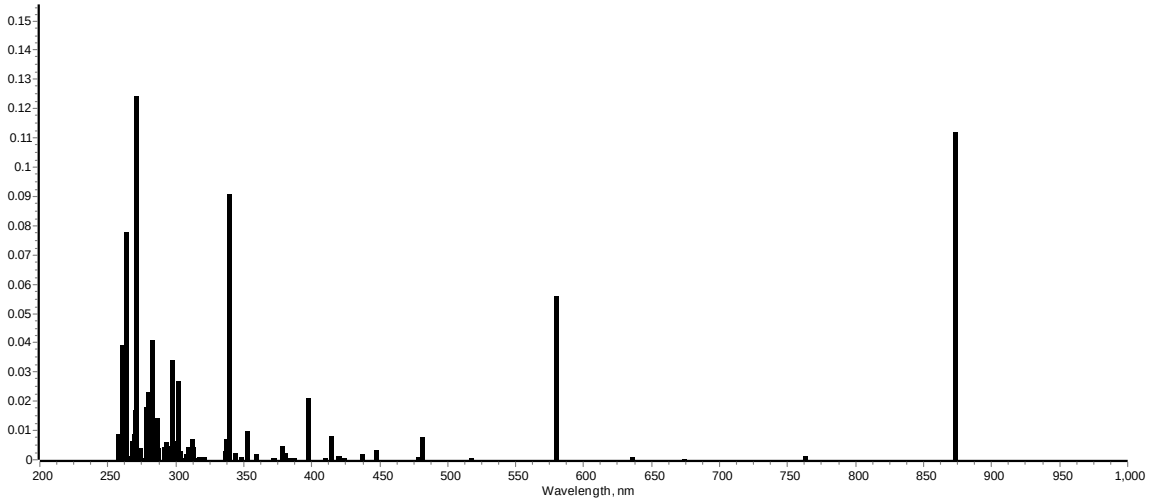

Figure 92. Calculated absorption spectrum of the cation of complex **13a** in CH_3CN at the B3LYP level.

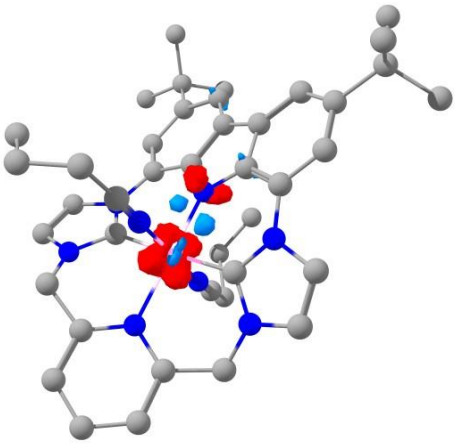

Figure 93. Calculated TD-DFT difference density of the cation of complex **13a** (red/blue indicates gain/loss of electron density) for state 3 (872.7 nm). Grey: C, blue: N, pink: Fe.

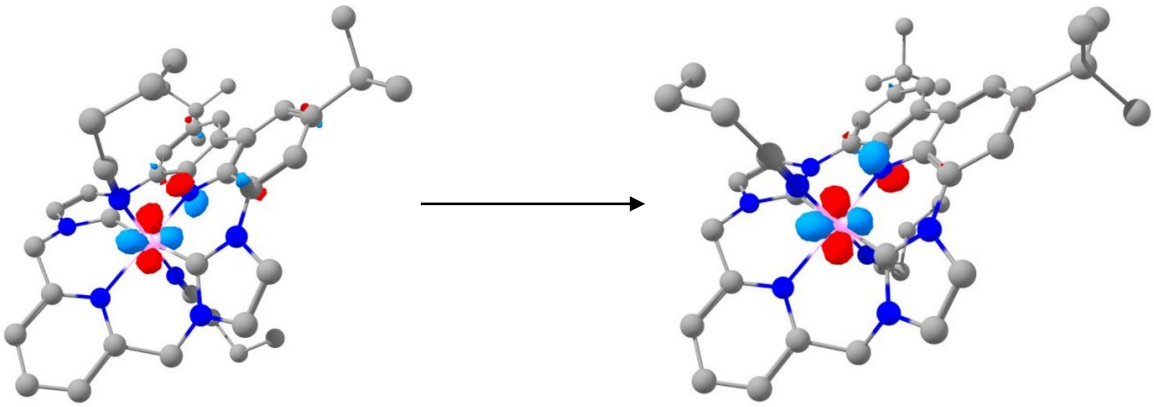

Figure 94. Natural transition orbitals that mainly contribute to state 3 for complex **13a**.

DFT Table 9. Selected TD-DFT (B3LYP level) calculated energies, oscillator strengths and compositions of the main electronic transitions of complex **13a**.

States	Energy (cm^{-1})	Wavelength (nm)	Osc. Strength	Major Contributions
3	11458.8	872.7	0.111879361	HOMO → LUMO (88%)

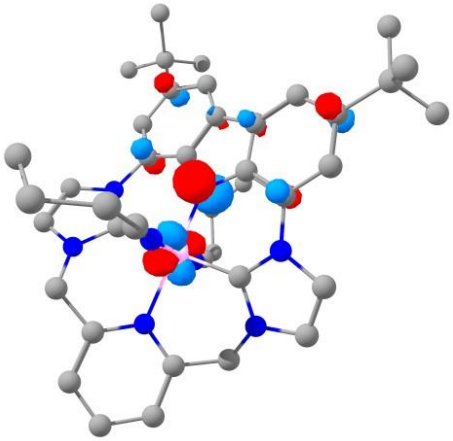

Figure 95. Plot of the magnetic orbital of complex **13a**.

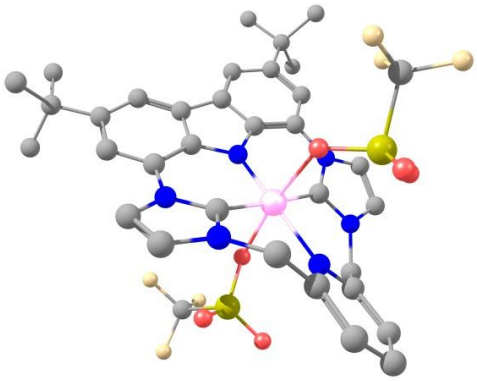

Figure 96. Visualization of the optimized geometry of complex **13b** based on DFT calculation at the BP86 level (grey: C, blue: N, red: O, yellow: S, white: F, pink: Fe; hydrogen atoms omitted for clarity).

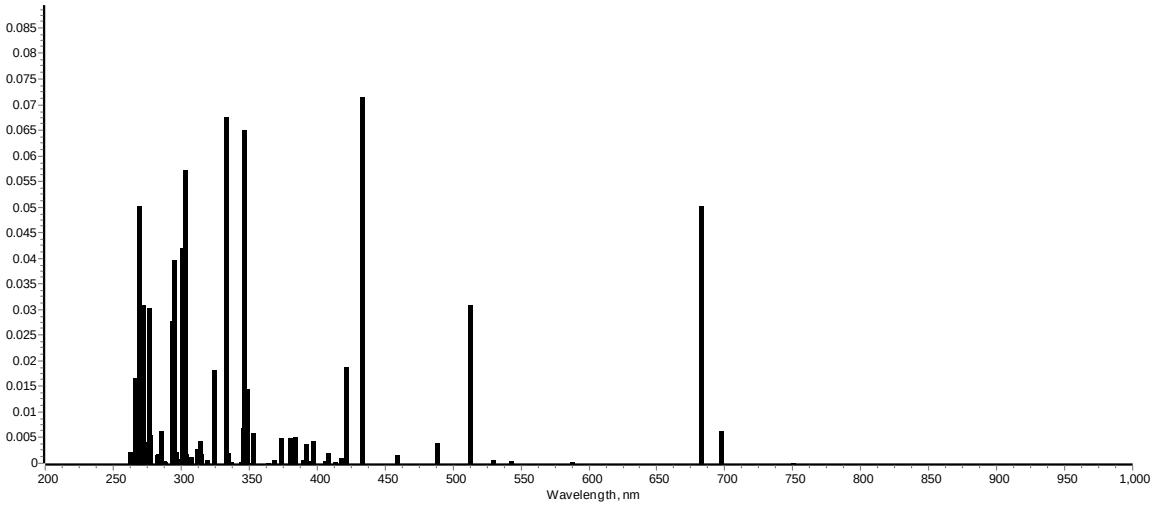

Figure 97. Calculated absorption spectrum of complex **13b** in acetone at the B3LYP level.

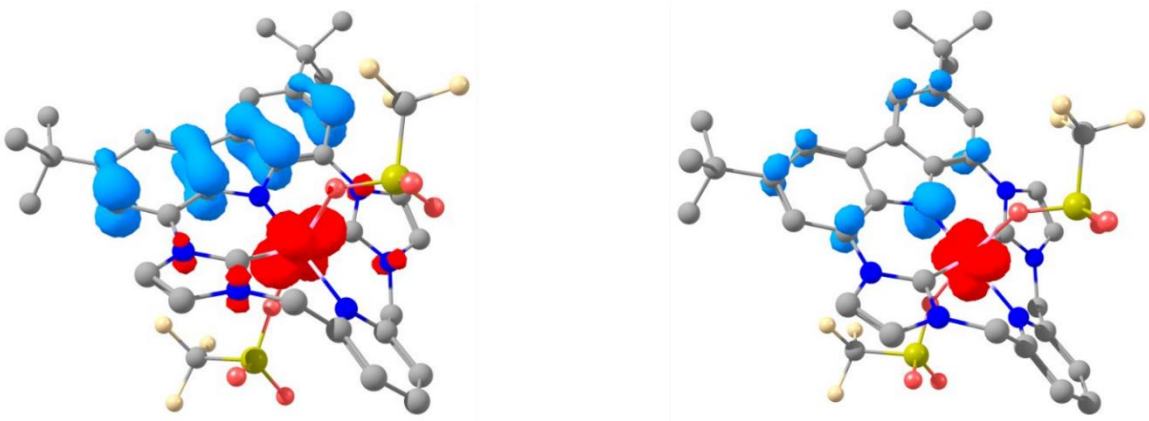

Figure 98. Calculated TD-DFT difference density of complex **13b** (red/blue indicates gain/loss of electron density) for state 6 (left, 696.0 nm) and 5 (right, 682.3 nm). Grey: C, blue: N, red: O, yellow: S, white: F, pink: Fe.

DFT Table 10. Selected TD-DFT (B3LYP level) calculated energies, oscillator strengths and compositions of the main electronic transitions of complex **13b**.

States	Energy (cm^{-1})	Wavelength (nm)	Osc. Strength	Major Contributions	Character
5	14657.0	682.3	0.050106261	HOMO → LUMO+1 (81%)	LMCT
6	14368.8	696.0	0.006282785	HOMO–1 → LUMO (97%)	LMCT

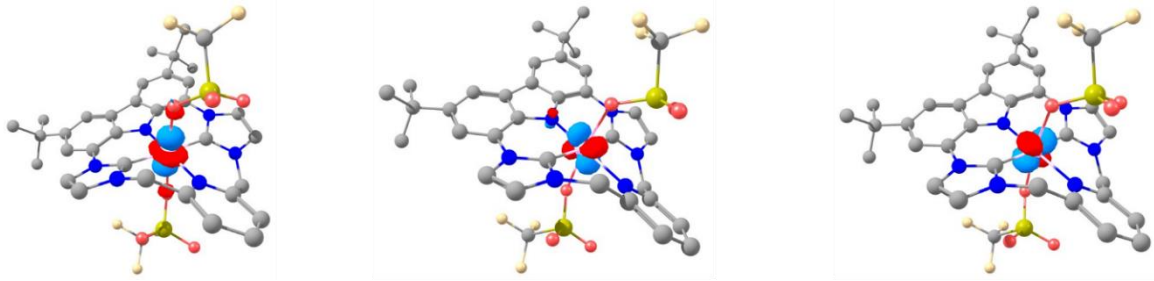

Figure 99. Magnetic orbitals of complex **13b**.

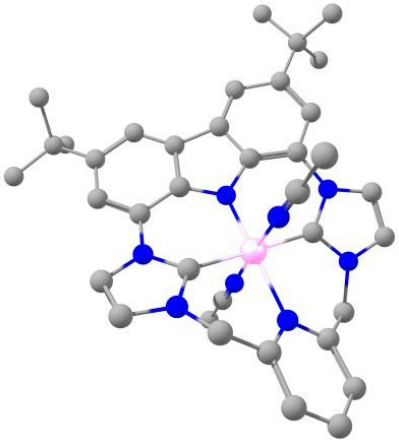

Figure 100. Visualization of the optimized geometry of the cation of complex **14a** based on DFT calculation at the BP86 level (grey: C, blue: N, pink: Fe; hydrogen atoms omitted for clarity).

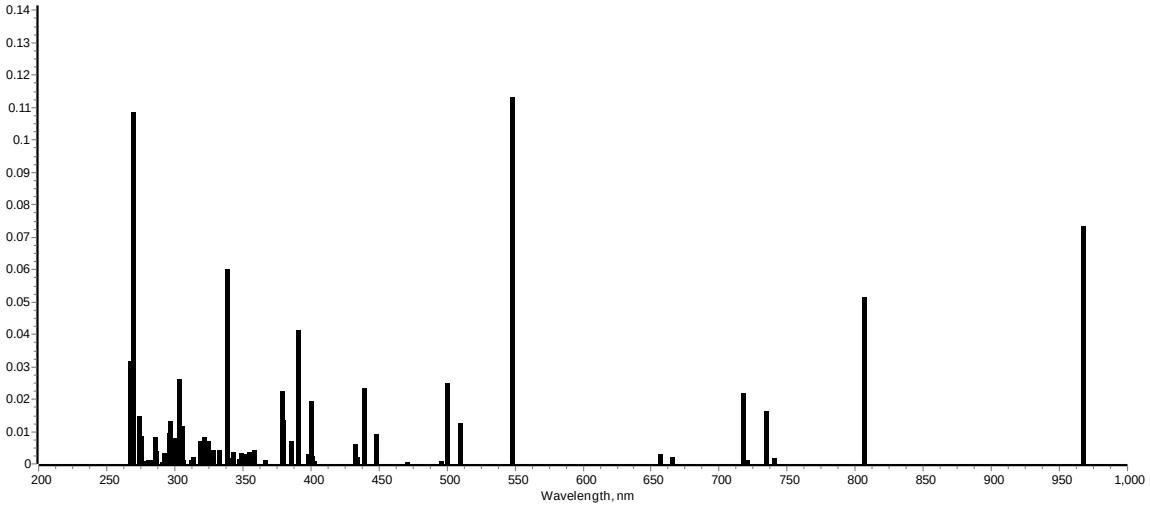

Figure 101. Calculated absorption spectrum of the cation of complex **14a** in CH_3CN at the B3LYP level.

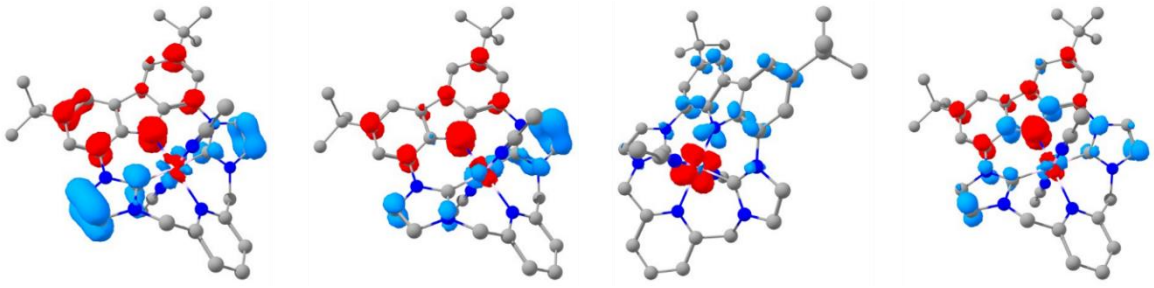

Figure 102. Calculated TD-DFT difference density of the cation of complex **14a** (red/blue indicates gain/loss of electron density) for, in order, state 7 (734 nm), 6 (717 nm), 5 (806 nm), and 4 (966 nm). Grey: C, blue: N, pink: Fe.

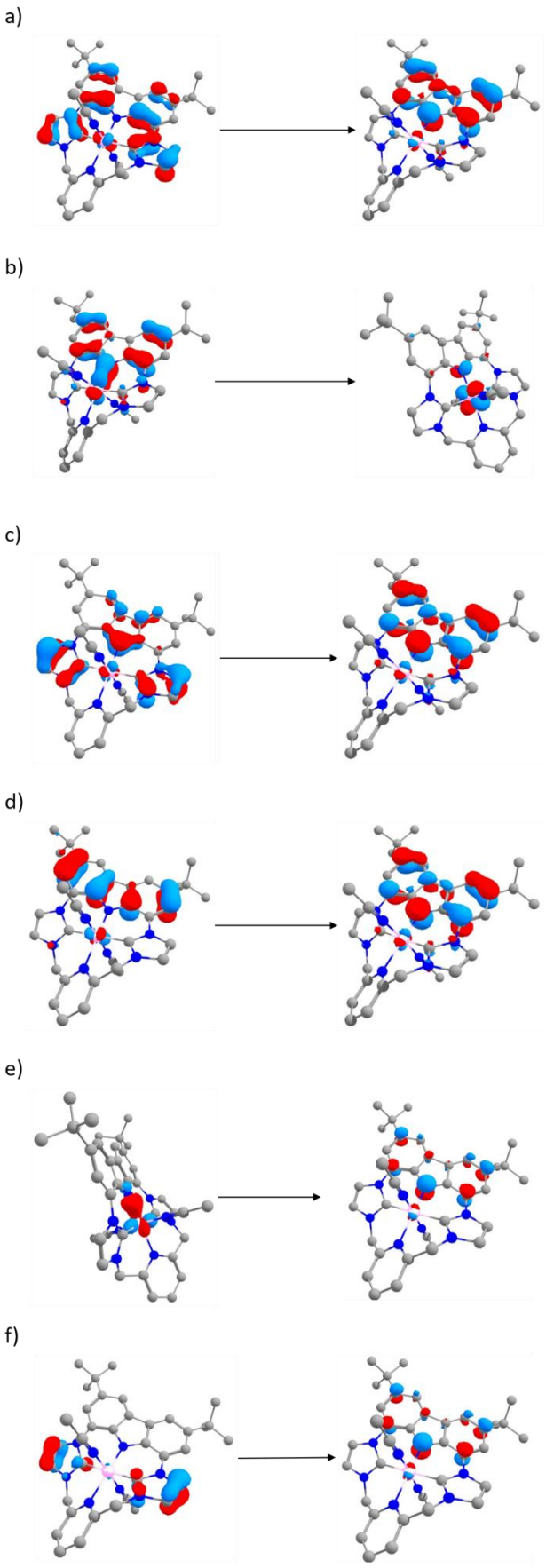

Figure 103. Natural transition orbitals that mainly contribute to state 4 (a), 5 (b), 6 (c, d) and 7 (e, f) for complex **14a**.

DFT Table 11. Selected TD-DFT (B3LYP level) calculated energies, oscillator strengths and compositions of the main electronic transitions of complex **14a**.

States	Energy (cm^{-1})	Wavelength (nm)	Osc. Strength	Major Contributions
4	10348.5	966.3	0.073554861	HOMO → LUMO (86%)
5	12406.8	806.0	0.051285636	HOMO → LUMO (83%)
7	13622.5	734.1	0.016162435	HOMO–3 → LUMO (52%) HOMO–2 → LUMO (31%)
6	13940.7	717.3	0.021924694	HOMO–3 → LUMO (56%) HOMO–2 → LUMO (31%)

DFT Table 12. Electronic energies and multiplicity of different ground states of **14a** as predicted at the B3LYP level.

Multiplicity	*E* [H]	Δ*E* [kcal mol^{-1}]
Singlet	–3134.01202	2.43
Triplet	–3134.0065	5.90
Singlet (BS)	–3134.01589	0

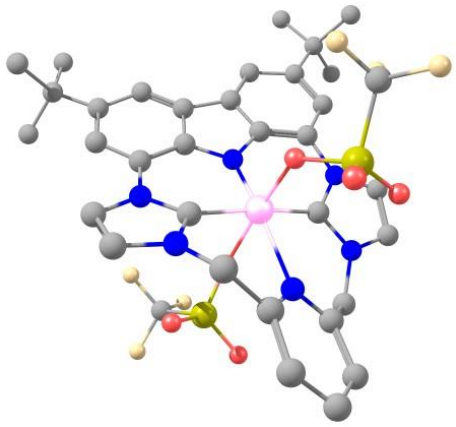

Figure 104. Visualization of the optimized geometry of the cation of complex **14b** based on DFT calculation at the BP86 level (grey: C, blue: N, red: O, yellow: S, white: F, pink: Fe; hydrogen atoms omitted for clarity).

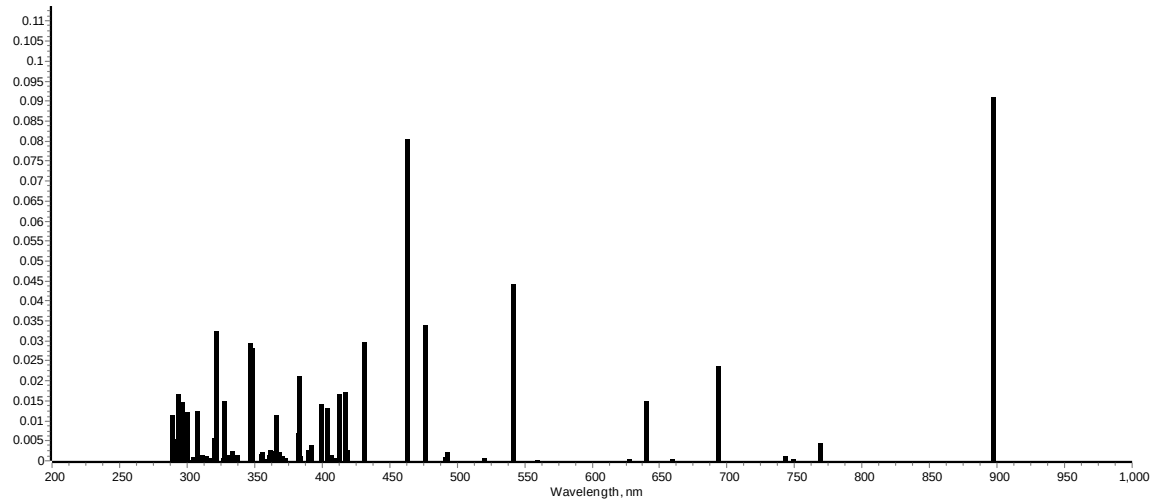

Figure 105. Calculated absorption spectrum of the cation of complex **14b** in acetone at the B3LYP level**.**

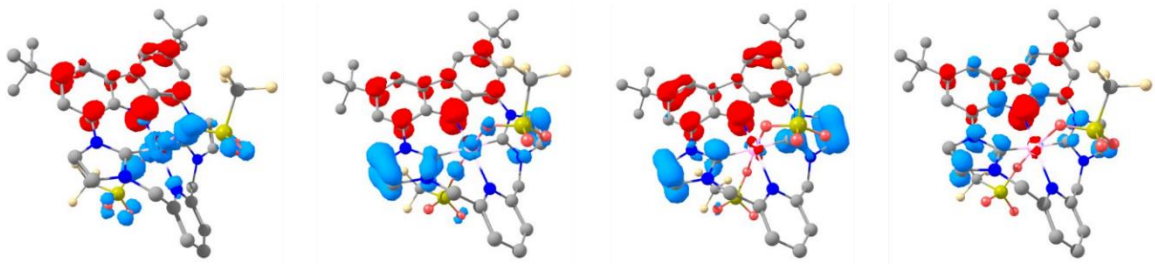

Figure 106. Calculated TD-DFT difference density of complex **14b** (red/blue indicates gain/loss of electron density) for, in order, state 9 (639.5 nm), 8 (693.0 nm), 6 (768.4 nm) and 4 (896.4 nm). Grey: C, blue: N, red: O, yellow: S, white: F, pink: Fe.

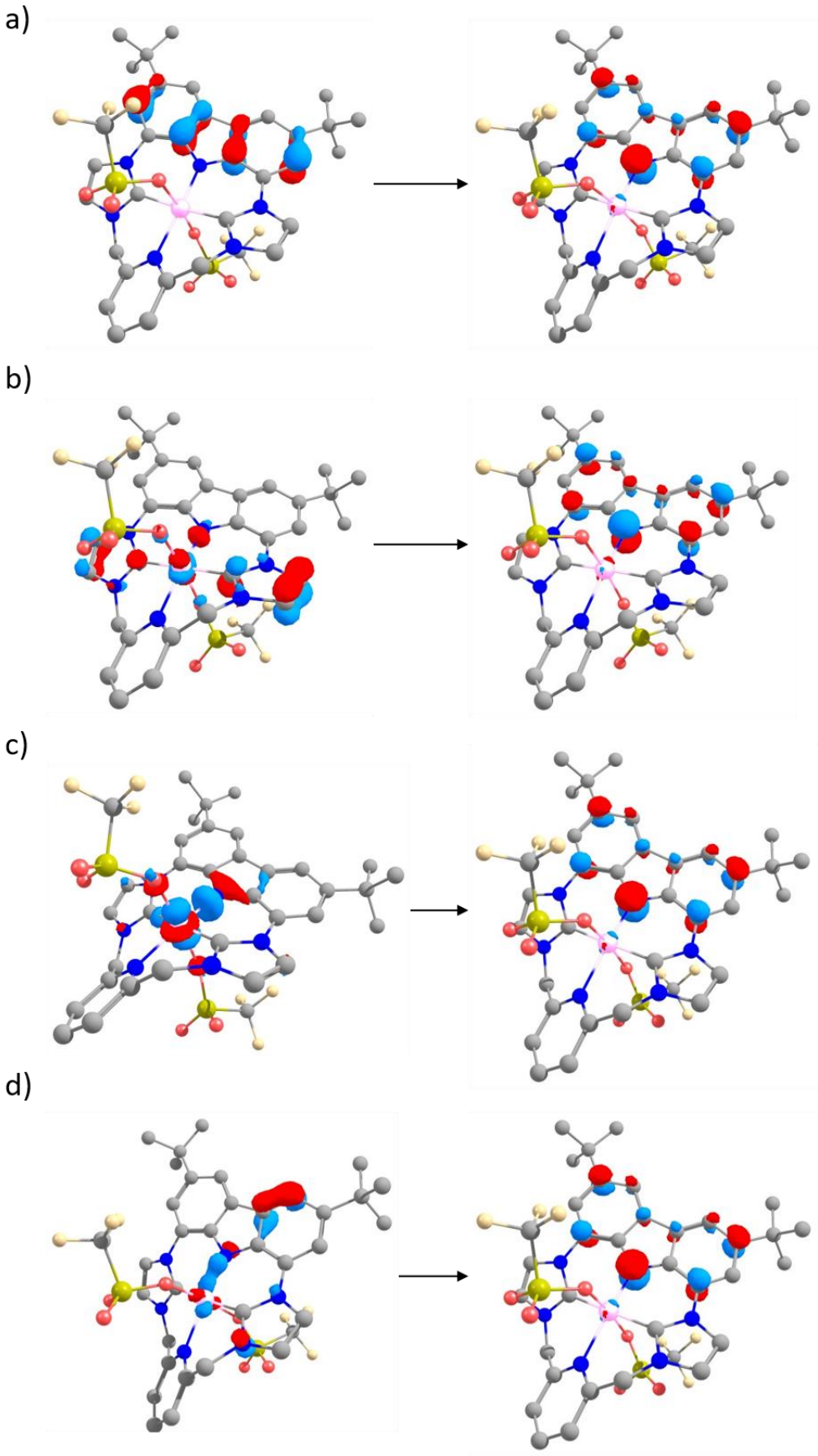

Figure 107. Natural transition orbitals that mainly contribute to state 4 (a), 6 (b), 8 (c) and 9 (d) for complex **14b**.

DFT Table 13. Selected TD-DFT (B3LYP level) calculated energies, oscillator strengths and compositions of the main electronic transitions of complex **14b**.

States	Energy (cm^{-1})	Wavelength (nm)	Osc. Strength	Major Contributions
4	11156.2	896.4	0.091032302	HOMO–1 → LUMO (87%)
6	13013.7	768.4	0.004368175	HOMO–2 → LUMO (95%)
8	14430.1	693.0	0.023851568	HOMO–3 → LUMO (92%)
9	15636.5	639.5	0.015037263	HOMO–4 → LUMO (88%)

DFT Table 14. Electronic energies and multiplicity of different ground states of **14b** as predicted at the B3LYP level.

Multiplicity	*E* [H]	ΔE [kcal mol^{-1}]
Triplet	–4792.21285	3.64
Triplet (BS)	–4792.21865	0

DFT Table 15. Experimental and DFT-calculated (italics) Mößbauer parameters of complexes **12a**/**b**, **13a**/**b**, **14a**/**b**.

Complex	δ	$\lvert\Delta E_Q\rvert$	Γ
12a	0.33 / *0.21*	2.33 / *2.23*	0.26
12b	0.48 / *0.31*	4.26 / *4.02*	0.28
13a	0.18 / *0.15*	3.84 / *3.05*	0.41
13b	0.29 / *0.18*	4.43 / *3.88*	0.32
14a	0.09 / *0.08*	4.36 / *3.99*	0.30
14b	0.16 / *0.17*	5.23 / *3.12*	0.31

11. Crystallographic Details

X-ray data were collected on a STOE IPDS II or a BRUKER D8-QUEST diffractometer (monochromated Mo-Kα radiation, λ = 0.71073 Å) by use of ω or ω and ϕ scans at low temperature. The structures were solved with SHELXT and refined on F^2 using all reflections with SHELXL.[324,325] Non-hydrogen atoms were refined anisotropically. Hydrogen atoms were placed in calculated positions and assigned to an isotropic displacement parameter of 1.5/1.2 U_{eq}(C/N). Face-indexed absorption corrections were performed numerically with the program X-RED or by the multi-scan method with SADABS.[326,327]

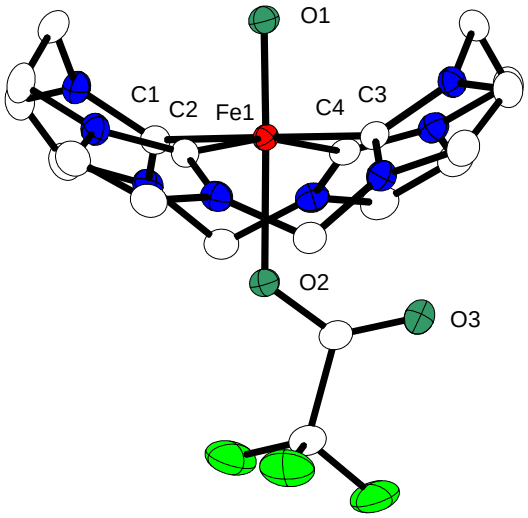

Figure 108. Plot (50% probability thermal ellipsoids) of the molecular structure of the cationic part of **4** (hydrogen atoms omitted for clarity). Selected bond lengths [Å] and angles [°]: Fe1–O1 1.671(1), Fe1–O2 2.069(1), Fe1–C1 2.025(2), Fe1–C2 1.970(2), Fe1–C3 2.038(2), Fe1–C4 1.980(2); O1–Fe1–O2 178.849(5), C1–Fe1–C3 179.40(7), C2–Fe1–C4 167.90(7).

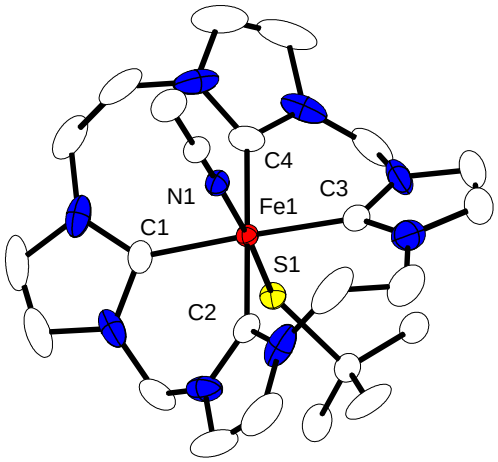

Figure 109. Plot (50% probability thermal ellipsoids) of the molecular structure of the cationic part of **6** (hydrogen atoms omitted for clarity). Fe1–S1 2.4032(9), Fe1–N1 1.913(3), Fe1–C1 2.021(4), Fe1–C2 1.963(4), Fe1–C3 2.005(4), Fe1–C4 1.968(4); N1–Fe1–S1 173.73(8), C1–Fe1–C3 174.0(1), C2–Fe1–C4 176.3(1).

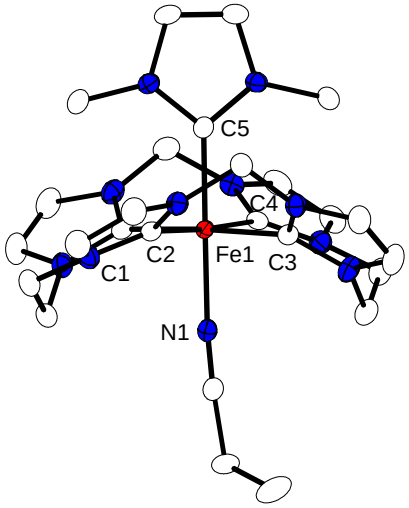

Figure 110. Plot (50% probability thermal ellipsoids) of the molecular structure of the cationic part of **8** (hydrogen atoms omitted for clarity). Fe1–C5 1.976(2), Fe1–N1 1.960(2), Fe1–C1 1.942 (2), Fe1–C2 2.010(2), Fe1–C3 1.963(2), Fe1–C4 1.988(2); N1–Fe1–C1 178.57(6), C1–Fe1–C3 176.86(6), C2–Fe1–C4 176.16(7).

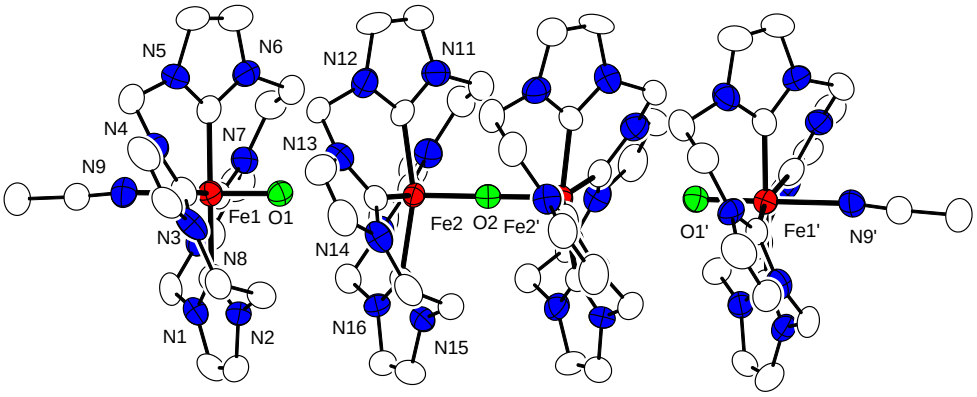

Figure 111. Plot (50% probability thermal ellipsoids) of the molecular structure of the cationic part of **9** (hydrogen atoms omitted for clarity). Fe1–N9 2.069(6), Fe1–O1 1.673(4), O1–Fe2 3.193(5), Fe2–O2 1.7685(9), O2–Fe2' 1.7685(9), Fe2'–O1' 3.193(5), Fe1'–N9' 2.069(6); N9–Fe1–O1 179.4(4), Fe1–O1···Fe2 178.2(3), Fe2–O2–Fe2' 179.7(8), Fe2'···O1'–Fe1' 178.2(3), O1'–Fe1'–N9' 179.4(4).

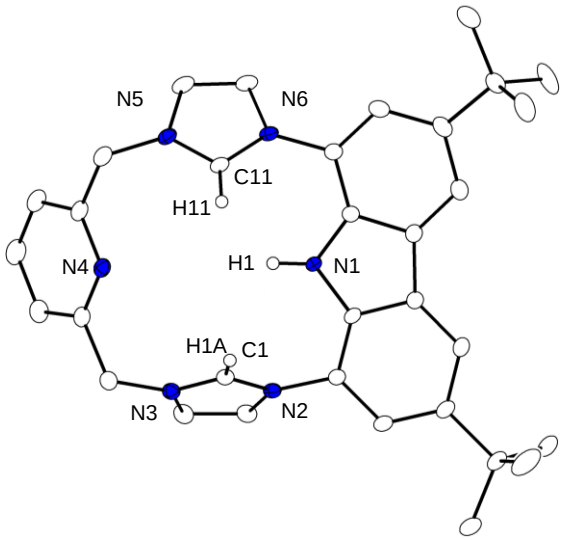

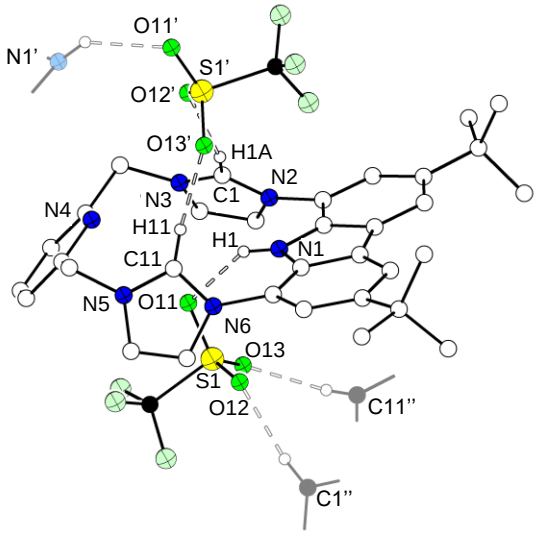

Figure 112. Top: Plot (30% probability thermal ellipsoids) of the cationic part of **[11H$_3$][OTf]$_2$** (most hydrogen atoms and disorder omitted for clarity); Bottom: Hydrogen bonds in **[11H$_3$][OTf]$_2$**. Selected bond lengths [Å] and angles [°]: N1···O11 2.8662(16), C1···O12' 2.9596(18), C11···O13' 2.9873(19); N1–H1···O11 142.0, C1–H1···O12' 151.2, C11–H11···O12' 153.9. Symmetry transformations used to generate equivalent atoms: (') 3/2–x, –1/2+y, 3/2–z; (") 3/2–x, 1/2+y, 3/2–z.

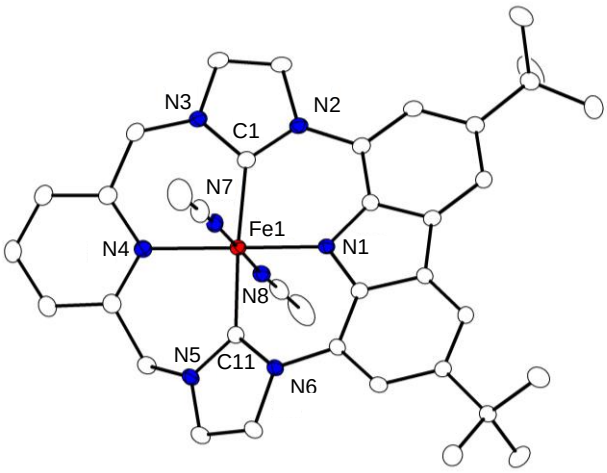

Figure 113. Plot (30% probability thermal ellipsoids) of the molecular structure of the cationic part of **12a** (hydrogen atoms omitted for clarity). Selected bond lengths [Å] and angles [°]: Fe1–N1 1.9380(16), Fe1–C1 1.942(2), Fe1–C11 1.941(2), Fe1–N4 2.0713(17), Fe1–N7 1.9338(18), Fe1–N8 1.9377(18); N7–Fe1–N8 178.83(7), N7–Fe1–N1 91.22(7), N8–Fe1–N1 88.49(7), N7–Fe1–C11 88.12(8), N8–Fe1–C11 90.73(8), N1–Fe1–C11 87.90(7), N7–Fe1–C1 91.37(8), N8–Fe1–C1 89.76(8), N1–Fe1–C1 88.01(8), C11–Fe1–C1 175.86(8), N7–Fe1–N4 88.68(7), N8–Fe1–N4 91.61(7), N1–Fe1–N4 179.88(7), C11–Fe1–N4 92.04(7), C1–Fe1–N4 92.06(8), C20–N1–Fe1 127.11(13), C19–N1–Fe1 127.59(13), C5–N4–Fe1 122.09(14), C9–N4–Fe1 121.82(14), C34–N7–Fe1 176.95(19), C36–N8–Fe1 175.78(17).

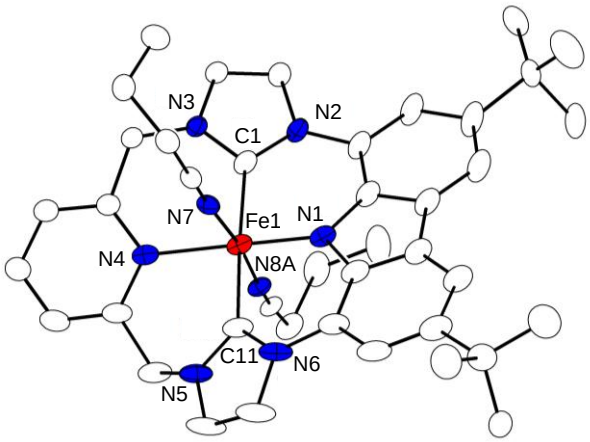

Figure 114. Plot (30% probability thermal ellipsoids) of the cationic part of **13a** (hydrogen atoms and disorder omitted for clarity). Selected bond lengths [Å] and angles [°]: Fe1–N1 1.859(3), Fe1–C1 1.956(3), Fe1–C11 1.958(3), Fe1–N4 2.104(3), Fe1–N7 1.937(2), Fe1–N8A 1.950(6); N1–Fe1–N7 92.48(11), N1–Fe1–N8A 95.0(4), N7–Fe1–N8A 172.5(4), N1–Fe1–C1 89.11(13), N7–Fe1–C1 90.45(11), N8A–Fe1–C1 90.2(3), N1–Fe1–C11 88.48(13), N7–Fe1–C11 90.66(11), N8A–Fe1–C11 89.0(3), C1–Fe1–C11 177.39(15), N1–Fe1–N4 179.19(10), N7–Fe1–N4 88.32(10), N8A–Fe1–N4 84.2(4), C1–Fe1–N4 90.89(12), C11–Fe1–N4 91.50(13), C34–N7–Fe1 175.7(2), C38A–N8A–Fe1 174.2(9).

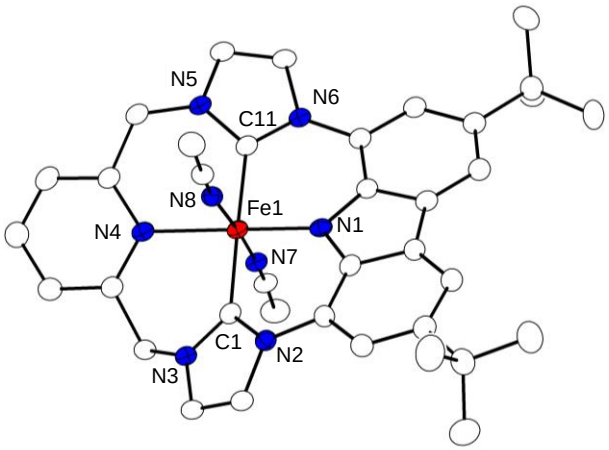

Figure 115. Plot (30% probability thermal ellipsoids) of the cationic part of **14a** (hydrogen atoms omitted for clarity). Selected bond lengths [Å] and angles [°]: Fe1–N1 1.837(3), Fe1–C1 1.942(3), Fe1–C11 1.944(3), Fe1–N4 2.087(3), Fe1–N7 1.917(3), Fe1–N8 1.921(3); N1–Fe1–N7 92.31(11), N1–Fe1–N8 91.91(11), N7–Fe1–N8 175.76(12), N1–Fe1–C1 89.60(12), N7–Fe1–C1 92.44(12), N8–Fe1–C1 87.98(12), N1–Fe1–C11 89.10(12), N7–Fe1–C11 87.50(12), N8–Fe1–C11 92.17(12), C1–Fe1–C11 178.70(14), N1–Fe1–N4 178.90(11), N7–Fe1–N4 86.65(11), N8–Fe1–N4 89.13(11), C1–Fe1–N4 90.77(12), C11–Fe1–N4 90.52(12), C34–N7–Fe1 177.2(3), C36–N8–Fe1 173.6(3).

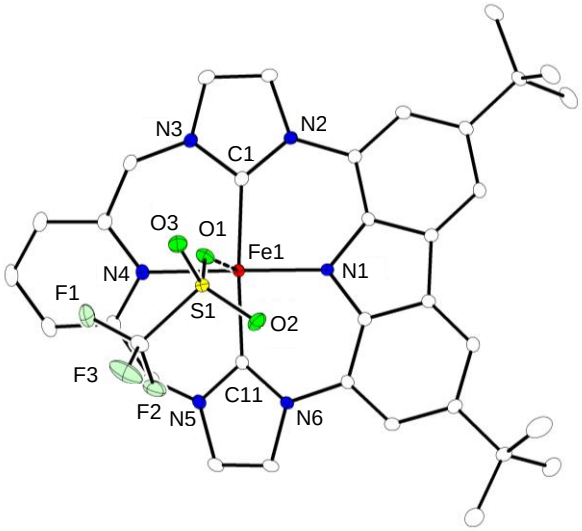

Figure 116. Plot (30% probability thermal ellipsoids) of the molecular structure of the **12b** (hydrogen atoms omitted for clarity). Selected bond lengths [Å] and angles [°]: Fe1–N1 1.8994(12), Fe1–C1 1.9431(15), Fe1–C11 1.9443(15), Fe1–N4 2.1003(13), Fe1–O1 2.3221(11); N1–Fe1–C1 88.25(6), N1–Fe1–C11 88.40(6), C1–Fe1–C11 173.82(6), N1–Fe1–N4 173.64(5), C1–Fe1–N4 91.62(6), C11–Fe1–N4 91.12(6), N1–Fe1–O1 100.24(5), C1–Fe1–O1 87.50(5), C11–Fe1–O1 98.22(5), N4–Fe1–O1 86.10(4).

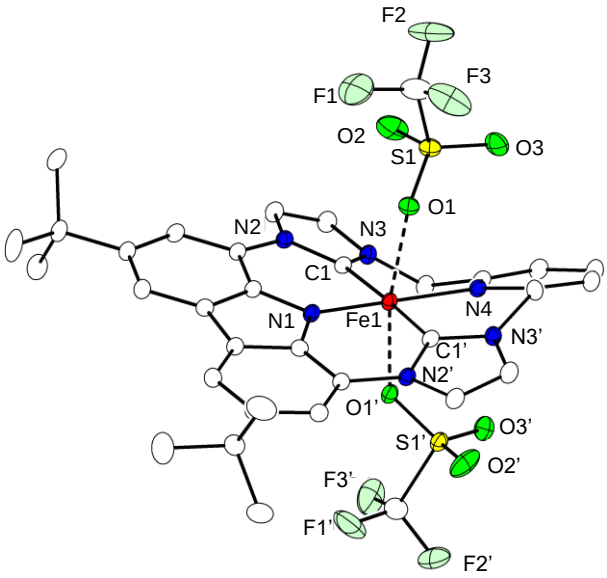

Figure 117. Plot (30% probability thermal ellipsoids) of the molecular structure of **13b** (hydrogen atoms omitted for clarity). Selected bond lengths [Å] and angles [°]: Fe1–N1 1.884(3), Fe1–C1 1.976(2), Fe1–N4 2.133(3), Fe1–O1 2.2261(17); N1–Fe1–C1 88.22(7), C1–Fe1–C1' 176.45(14), N1–Fe1–N4 180.0, C1–Fe1–N4 91.78(7), N1–Fe1–O1' 96.19(5), C1–Fe1–O1' 88.34(8), N1–Fe1–O1 96.19(5), C1–Fe1–O1 92.04(8), N4–Fe1–O1 83.81(5), O1'–Fe1–O1 167.62(9). Symmetry transformation used to generate equivalent atoms: (') 1–x, y, 3/2–z.

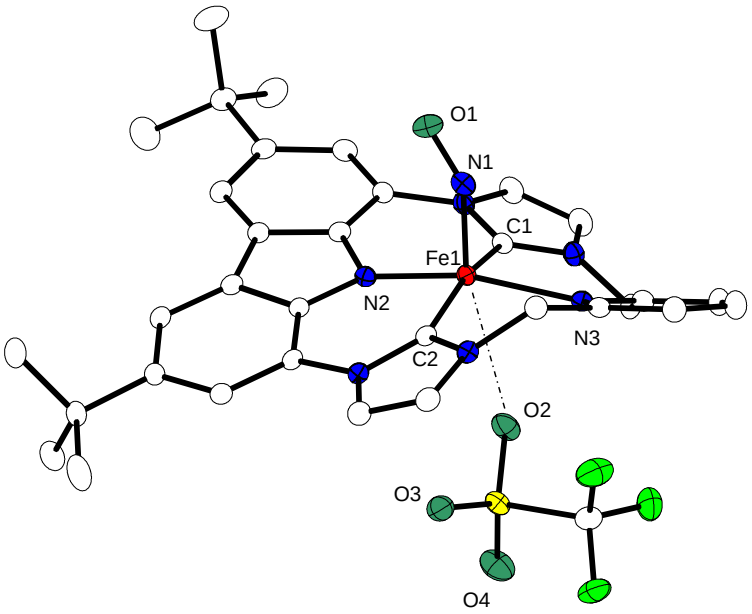

Figure 118. Plot (50% probability thermal ellipsoids) of the molecular structure of the **15** (hydrogen atoms omitted for clarity). Selected bond lengths [Å] and angles [°]: Fe1–N1 1.7142(12), N1–O1 1.1767(15), Fe1–C1 1.9673(13), Fe1–C2 1.9643(13), Fe1–N2 1.8952(11), Fe1–N3 2.1404(12), Fe1···O2 3.0067(12); Fe1–N1–O1 143.67(11), N2–Fe1–N3 166.11(4), C1–Fe1–C2 163.00(5), N1–Fe1–N2 97.30(5), C1–Fe1–N1 95.61(5), N3–Fe1–N1 96.59(5), N1–Fe1–C1 95.61.

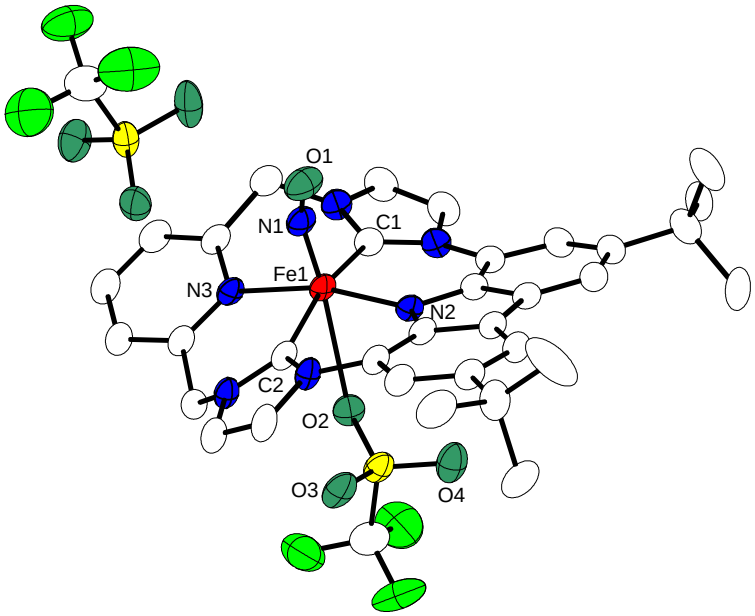

Figure 119. Plot (50% probability thermal ellipsoids) of the molecular structure of the **16** (hydrogen atoms omitted for clarity). Selected bond lengths [Å] and angles [°]: Fe1–N1 1.659(2), N1–O1 1.1520(39), Fe1–C1 1.9637(23), Fe1–C2 1.9519(22), Fe1–N2 1.8681(19), Fe1–N3 2.1424(19); Fe1–O2 2.8232(24), Fe1–N11–O1 158.10(19), N2–Fe1–N3 161.50(9), C1–Fe1–C2 163.87(11), N1–Fe1–O2 172.81(8), C1–Fe1–N3 88.30(9), C2–Fe1–N3 90.40(9), N2–Fe1–C2 88.04(9), C1–Fe1–N2 88.11(9),.

Table S1. Crystal data and refinement details for **4** and **6**.

compound	**4**	**6**
empirical formula	$C_{23}H_{23}F_6FeN_9O_6S$	$C_{27}H_{35}F_3FeN_{10}O_3S_2$
moiety formula	$C_{20}H_{20}F_3FeN_8O_3^+$, $CF_3O_3S^-$, C_2H_3N	$C_{24}H_{32}FeN_9S^+$, $CF_3O_3S^-$, C_2H_3N
formula weight	723.41	724.62
T [K]	133(2)	100(2)
crystal size [mm³]	0.500 x 0.490 x 0.340	0.453 x 0.264 x 0.204
crystal system	monoclinic	monoclinic
space group	*C*2/*c* (No. 15)	$P2_1/n$ (No. 14)
a [Å]	26.8979(8)	15.2410(4)
b [Å]	11.7811(4)	13.3093(4)
c [Å]	19.4343(5)	15.6102(4)
α [°]	90	90
β [°]	115.136(2)	102.2930(10)
γ [°]	90	90
V [Å³]	5575.3(3)	3093.88(15)
Z	8	4
ρ [g·cm^{-3}]	1.724	1.556
F(000)	2944	1504
μ [mm^{-1}]	0.715	0.690
T_{min} / T_{max}	0.6860 / 0.8077	0.82 / 0.87
θ-range [°]	1.673 - 26.793	2.052 - 27.902
hkl-range	±34, ±14, -24 to 21	-20 to 18, ±17, ±20
measured refl.	38833	81860
unique refl. [R_{int}]	5915 [0.0266]	7382 [0.0402]
observed refl. ($I > 2\sigma(I)$)	5240	6638
data / restr. / param.	5915 / 0 / 416	7382 / 146 / 476
goodness-of-fit (F^2)	1.039	1.035
$R1$, $wR2$ ($I > 2\sigma(I)$)	0.0276 / 0.0722	0.0693 / 0.1713
$R1$, $wR2$ (all data)	0.0327 / 0.0751	0.0751 / 0.1763
res. el. dens. [e·Å^{-3}]	-0.327 / 0.539	-1.030 / 1.622

Table S2. Crystal data and refinement details for **8** and **9**.

compound	**8**	**9**
empirical formula	$C_{31}H_{38}F_6FeN_{12}O_6S_2$	$C_{84}H_{86}F_{24}Fe_4N_{34}O_{27}S_8$
formula weight	908.70	2939.74
T [K]	133(2)	133(2)
crystal size [mm³]	0.500 x 0.490 x 0.440	0.400 x 0.370 x 0.250
crystal system	monoclinic	monoclinic
space group	$P2_1/c$ (No. 14)	$C2$ (No. 5)
a [Å]	16.6665(4)	33.8917(13)
b [Å]	15.1665(3)	17.2591(5)
c [Å]	14.8913(4)	14.2588(6)
α [°]	90	90
β [°]	96.707(2)	114.732(3)
γ [°]	90	90
V [Å³]	3738.35(15)	7575.5(5)
Z	4	2
ρ [g·cm⁻³]	1.615	1.289
F(000)	1872	2984
μ [mm⁻¹]	0.607	0.581
T_{min} / T_{max}	0.6792 / 0.7964	0.5900 / 0.7644
θ-range [°]	1.821 - 26.932	1.323 - 25.956
hkl-range	±21, ±19, ±18	±41, -21 to 20, ±17
measured refl.	51988	34343
unique refl. [R_{int}]	7935 [0.0182]	14247 [0.0281]
observed refl. ($I > 2\sigma(I)$)	7262	12781
data / restr. / param.	7935 / 171 / 588	14247 / 932 / 964
goodness-of-fit (F^2)	1.037	1.058
$R1$, $wR2$ ($I > 2\sigma(I)$)	0.0303 / 0.0784	0.0510 / 0.1363
$R1$, $wR2$ (all data)	0.0336 / 0.0805	0.0614 / 0.1497
res. el. dens. [e·Å⁻³]	-0.416 / 0.595	-0.369 / 0.505

Table S3. Crystal data and refinement details for **[11H$_3$][OTf]$_2$**, **12b**, and **12a**.

compound	**[11H$_3$][OTf]$_2$**	**12b**	**12a**
empirical formula	$C_{39}H_{42}F_6N_8O_6S_2$	$C_{40}H_{37}F_5FeN_6O_3S$	$C_{46}H_{59}F_3FeN_8O_5S$
moiety formula	$C_{33}H_{36}N_6^{2+}$, 2($CF_3O_3S^-$), 2(C_2H_3N)	$C_{34}H_{33}F_3FeN_6O_3S$, $C_6H_4F_2$	$C_{37}H_{39}FeN_8^+$, $CF_3O_3S^-$, 2($C_4H_{10}O$)
formula weight	896.92	832.66	948.92
T [K]	100(2)	120(2)	133(2)
crystal size [mm^3]	0.422 x 0.335 x 0.318	0.372 x 0.363 x 0.270	0.360 x 0.190 x 0.160
crystal system	monoclinic	monoclinic	monoclinic
space group	$P2_1/n$ (No. 14)	$P2_1/c$ (No. 14)	$P2_1/c$ (No. 14)
a [Å]	17.6175(4)	15.8121(5)	22.3544(7)
b [Å]	12.6128(3)	16.6628(5)	11.3554(2)
c [Å]	19.4018(6)	14.9904(5)	19.1330(6)
β [°]	96.791(1)	110.823(1)	100.480(2)
V [Å^3]	4280.95(19)	3691.6(2)	4775.8(2)
Z	4	4	4
ρ [g·cm^{-3}]	1.392	1.498	1.320
F(000)	1864	1720	2000
μ [mm^{-1}]	0.206	0.539	0.424
T_{min} / T_{max}	0.91 / 0.94$^{\$}$	0.81 / 0.87$^{\$}$	0.8077 / 0.9246*
θ–range [°]	2.318 – 27.895	1.899 – 27.909	1.853 – 26.905
hkl–range	–21 to 23, ±16, ±25	±20, ±21, ±19	±28, –14 to 12, ±24
measured refl.	113224	100758	66852
unique refl. [R_{int}]	10227 [0.0329]	8819 [0.0455]	10176 [0.0494]
observed refl. (I > 2σ(I))	8975	7702	7774
data / restr. / param.	10227 / 183 / 659	8819 / 0 / 511	10176 / 171 / 689
goodness–of–fit (F^2)	1.048	1.041	1.036
$R1$, $wR2$ (I > 2σ(I))	0.0417 / 0.1116	0.0318 / 0.0721	0.0405 / 0.0952
$R1$, $wR2$ (all data)	0.0486 / 0.1192	0.0396 / 0.0768	0.0617 / 0.1067
res. el. dens. [e·Å^{-3}]	–0.529 / 0.472	–0.394 / 0.523	–0.567 / 0.401

*) X-RED. $) SADABS.

Table S4. Crystal data and refinement details for **13b**, **14a**, and **13a**.

compound	**13b**	**14a**	**13a**
empirical formula	$C_{45}H_{55}F_6FeN_6O_9S_2$	$C_{52}H_{65}F_9FeN_{10}O_{11}S_3$	$C_{47}H_{54}F_6FeN_9O_6S_2$
moiety formula	$C_{35}H_{33}F_6FeN_6O_6S_2$, $C_4H_{10}O$, $2(C_3H_6O)$	$C_{37}H_{39}FeN_8^{3+}$, $3(CF_3O_3S^-)$, $2(C_4H_{10}O)$, $2(C_2H_3N)$	$C_{41}H_{47}FeN_8^{2+}$, $2(CF_3O_3S^-)$, C_4H_7N
formula weight	1057.92	1329.17	1074.96
T [K]	133(2)	133(2)	133(2)
crystal size [mm³]	0.500 x 0.240 x 0.200	0.480 x 0.340 x 0.180	0.500 x 0.140 x 0.080
crystal system	monoclinic	monoclinic	triclinic
space group	*C*2/*c* (No. 15)	$P2_1/c$ (No. 14)	*P*–1 (No. 2)
a [Å]	13.4731(4)	17.1718(4)	9.7933(4)
b [Å]	27.1045(10)	20.3275(4)	11.1501(5)
c [Å]	14.2582(4)	18.5181(5)	23.3424(12)
α [°]	90	90	87.425(4)
β [°]	102.227(2)	105.770(2)	80.913(4)
γ [°]	90	90	77.856(4)
V [Å³]	5088.7(3)	6220.6(3)	2460.4(2)
Z	4	4	2
ρ [g·cm^{-3}]	1.381	1.419	1.451
F(000)	2204	2760	1118
μ [mm^{-1}]	0.458	0.433	0.472
T_{min} / T_{max}	0.5707 / 0.8708*	0.7561 / 0.9344*	0.7746 / 0.9256*
θ–range [°]	1.503 – 26.928	1.232 – 25.820	1.767 – 25.712
hkl–range	±17, ±34, –18 to 17	–21 to 20, –22 to 24, ±22	±11, ±13, ±28
measured refl.	35310	76501	28152
unique refl. [R_{int}]	5412 [0.0728]	11802 [0.0582]	9229 [0.0408]
observed refl. ($I > 2\sigma(I)$)	4509	9571	6730
data / restr. / param.	5412 / 0 / 320	11802 / 226 / 910	9229 / 331 / 833
goodness–of–fit (F^2)	1.066	1.138	1.029
*R*1, *wR*2 ($I > 2\sigma(I)$)	0.0523 / 0.1349	0.0580 / 0.1418	0.0531 / 0.1268
*R*1, *wR*2 (all data)	0.0638 / 0.1440	0.0748 / 0.1540	0.0797 / 0.1413
res. el. dens. [e·Å^{-3}]	–0.369 / 0.775	–0.436 / 0.885	–0.417 / 0.773

*) X-RED. $) SADABS.

Table S5. Selected bond lengths [Å] and angles [deg] for complexes **12a/b** – **14a**.

	12b	**12a**	**13b**	**14a**	**13a**
$Fe–N^{carbazole}$	1.8994(12)	1.9380(16)	1.884(3)	1.837(3)	1.859(3)
$Fe–N^{py}$	2.1003(13)	2.0713(17)	2.133(3)	2.087(3)	2.104(3)
Fe–C	1.9431(15) / 1.9443(15)	1.941(2) / 1.942(2)	1.976(2)	1.942(3) / 1.944(3)	1.956(3) / 1.958(3)
$Fe–N^{nitrile}$	2.1003(13)	1.9338(18) / 1.9377(18)	-	1.917(3) / 1.921(3)	1.902(10) - 1.950(6)*
$Fe–O^{OTf}$	2.3221(11)	-	2.2261(17)	-	-
$N^{py}–Fe–N^{carbazole}$	173.64(5)	179.88(7)	180.0	178.90(11)	179.19(10)
C–Fe–C	173.82(6)	175.86(8)	176.45(14)	178.70(14)	177.39(15)
$N^{nitrile}$ –Fe– $N^{nitrile}$	-	178.83(7)	-	175.76(12)	171.0(6) / 172.5(4)
O^{OTf} –Fe–O^{OTf}	-	-	167.62(9)	-	-

*) one nitrile is disordered about two positions

Table S6. Crystal data and refinement details for **15**, and **16**.

compound	**15**	**16**
empirical formula	$C_{34}H_{33}F_3FeN_7O_4S$	$C_{35}H_{33}F_6FeN_7O_7S_2$
moiety formula	$C_{33}H_{33}FeN_7O^+$, $CF_3O_3S^-$	$C_{33}H_{33}FeN_7O^{2+}$, $2(CF_3O_3S^-)$
formula weight	748.58	897.65
T [K]	100(2)	100(2)
crystal size [mm³]	0.377 x 0.162 x 0.128	0.444 x 0.333 x 0.154
crystal system	orthorhombic	triclinic
space group	*Pbca* (No. 61)	*P*-1 (No. 2)
a [Å]	14.7713(4)	9.6055(14)
b [Å]	13.6945(4)	13.1572(19)
c [Å]	33.4493(9)	16.012(2)
α [°]	90	69.400(5)
β [°]	90	89.133(4)
γ [°]	90	77.722(4)
V [Å³]	6766.3(3)	1847.0(5)
Z	8	2
ρ [g·cm^{-3}]	1.470	1.614
F(000)	3096	920
μ [mm^{-1}]	0.574	0.612
T_{min} / T_{max}	0.86 / 0.93	0.80 / 0.91
θ-range [°]	2.117 - 27.893	2.444 - 27.194
hkl-range	-19 to 18, -18 to 16, -43 to 44	±12, ±16, ±20
measured refl.	75330	30030
unique refl. [R_{int}]	8062 [0.0299]	8156 [0.0404]
observed refl. ($I > 2\sigma(I)$)	7195	6560
data / restr. / param.	8062 / 0 / 457	8156 / 0 / 591
goodness-of-fit (F^2)	1.041	1.037
$R1$, $wR2$ ($I > 2\sigma(I)$)	0.0281 / 0.0697	0.0449 / 0.1106
$R1$, $wR2$ (all data)	0.0337 / 0.0742	0.0598 / 0.1219
res. el. dens. [e·Å^{-3}]	-0.429 / 0.358	-0.766 / 0.519

12. Appendix

Further Experimental Data

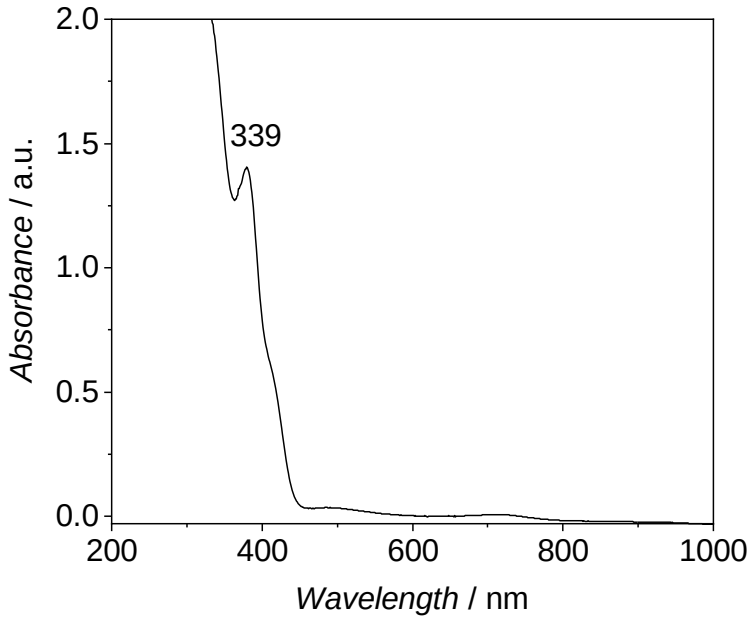

Figure 120. UV/Vis spectrum of a 0.25 mM solution of complex **6** in CH_3CN at RT.

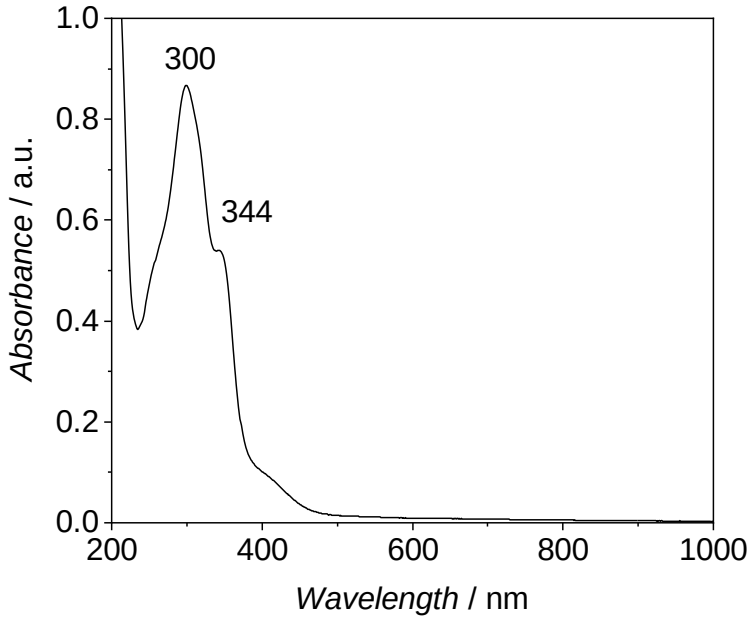

Figure 121. UV/Vis spectrum of a 0.05 mM solution of complex **8** in CH_3CN at RT.

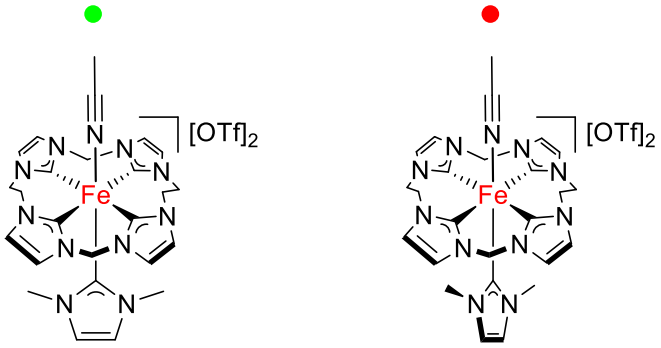

Figure 122. Color coding for NMR signal assignation of the two isomers of complex **8**.

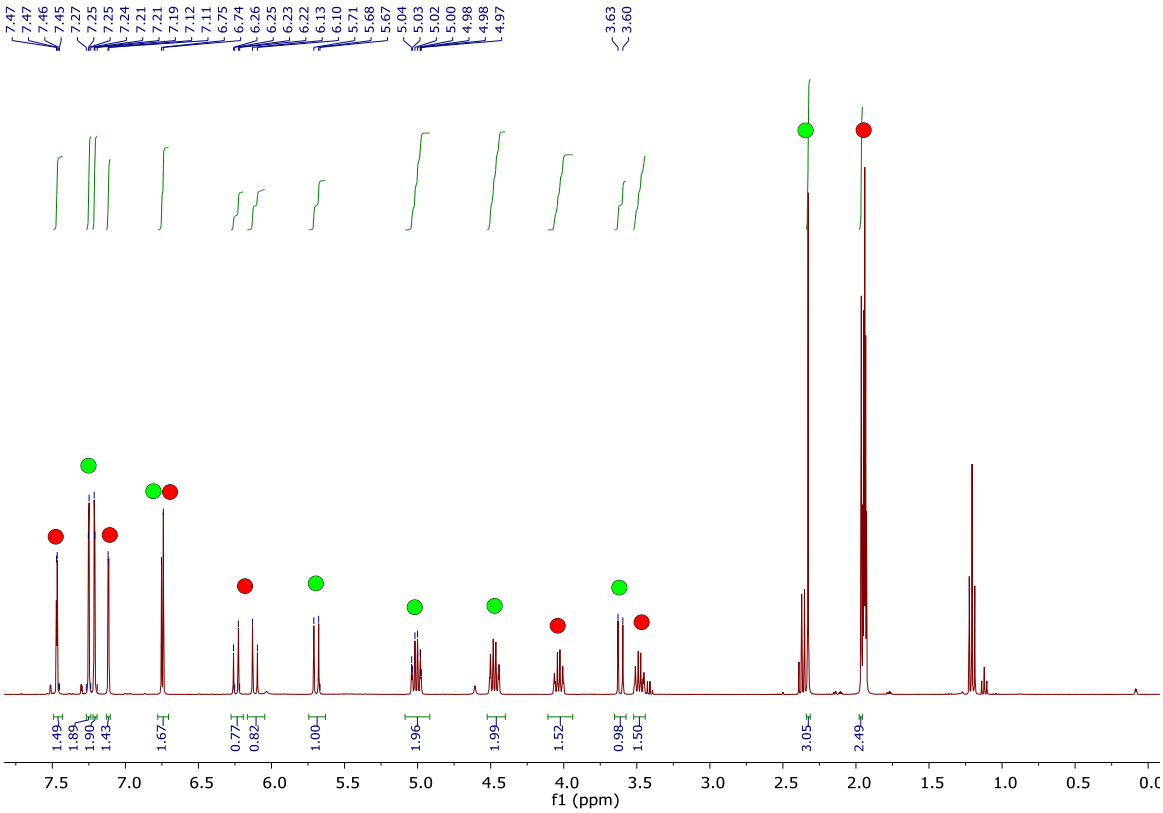

Figure 123. ^{1}H-NMR spectrum (400 MHz) of **8** in CD_3CN at RT.

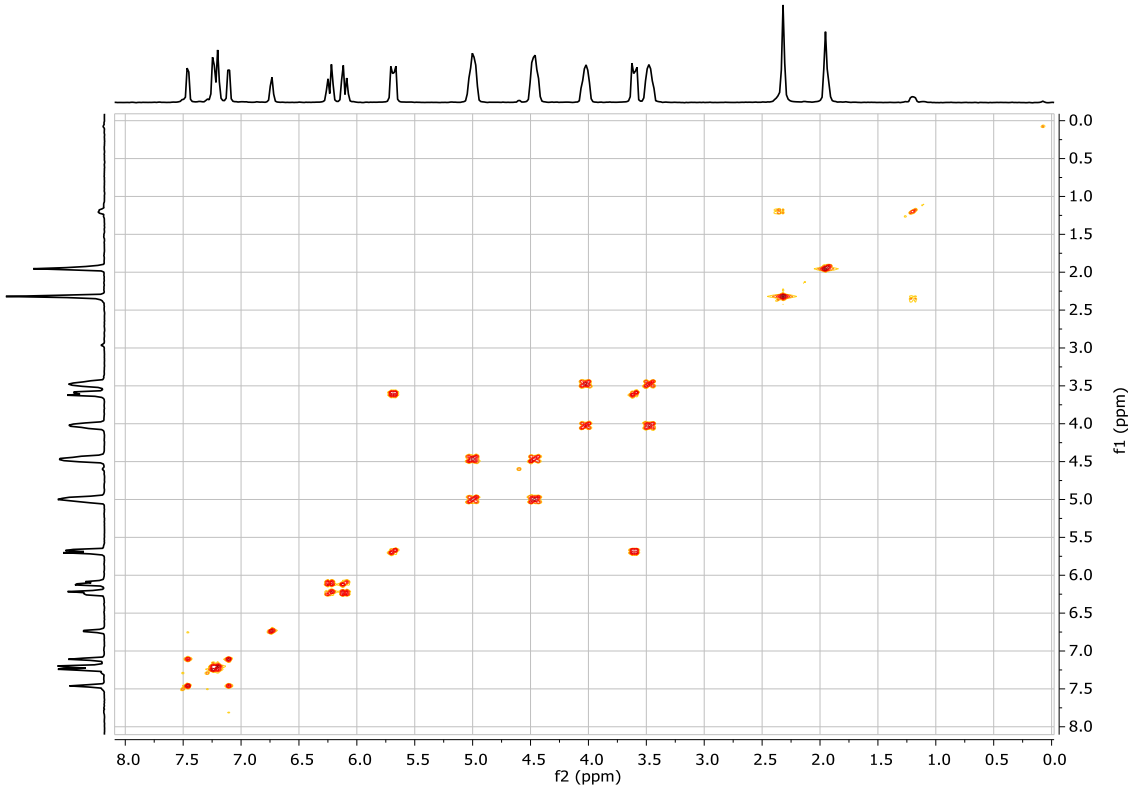

Figure 124. ^{1}H-^{1}H COSY NMR spectrum (400 MHz) of **8** in CD_3CN at RT.

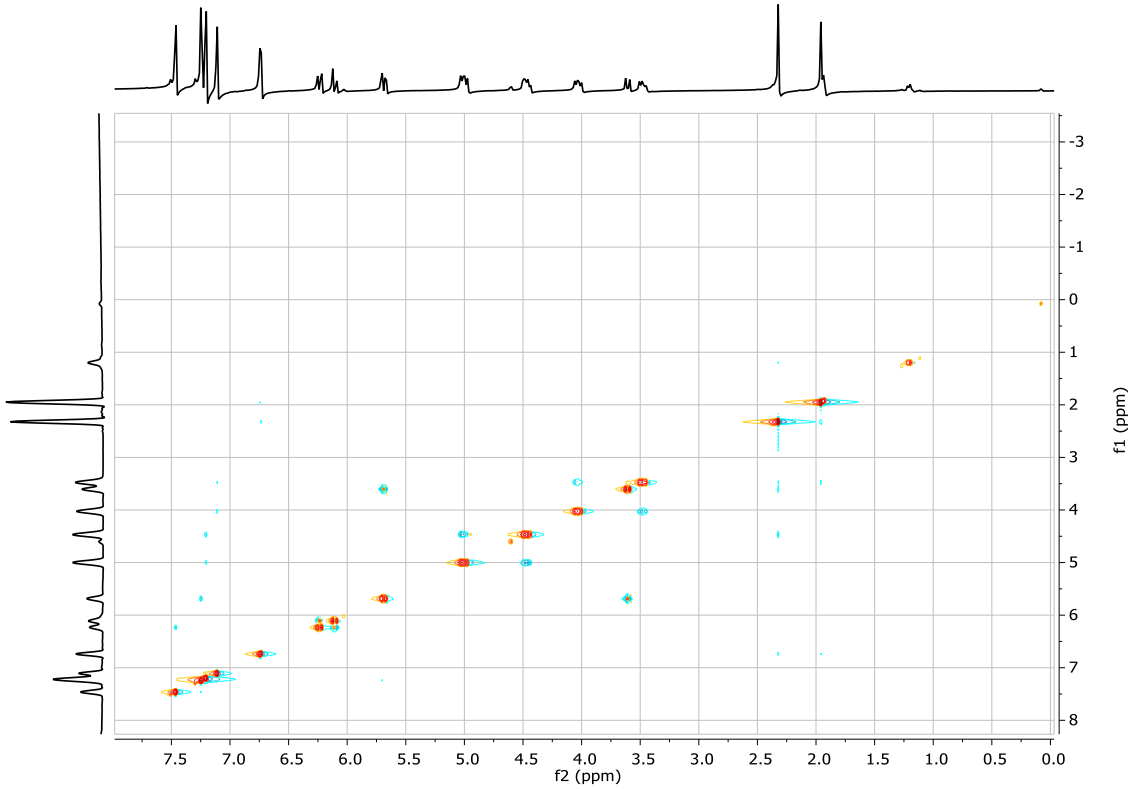

Figure 125. ^{1}H NOESY NMR spectrum (400 MHz) of **8** in CD_3CN at RT.

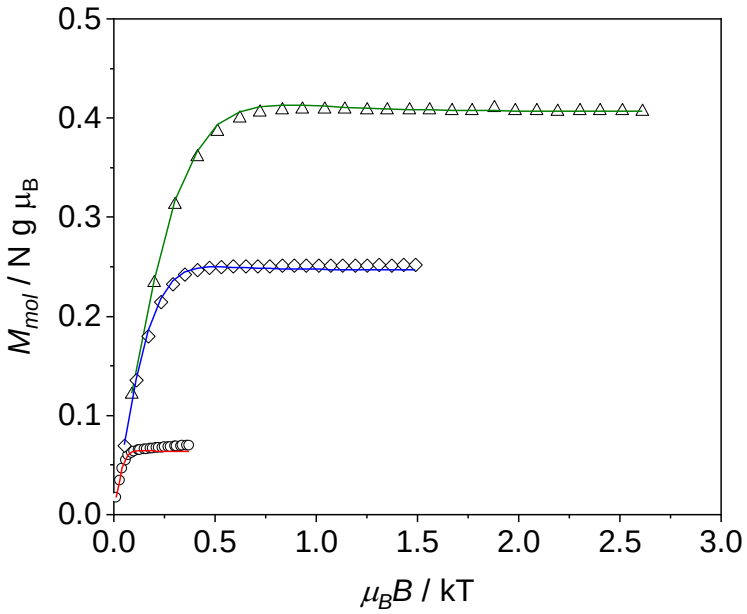

Figure 126. Variable temperature – variable field (VT-VH) magnetization measurements of a solid sample of **4** at applied fields of 1.0 (circles and red fit), 4.0 (diamonds and blue fit) and 7.0 T (triangles and green fit).

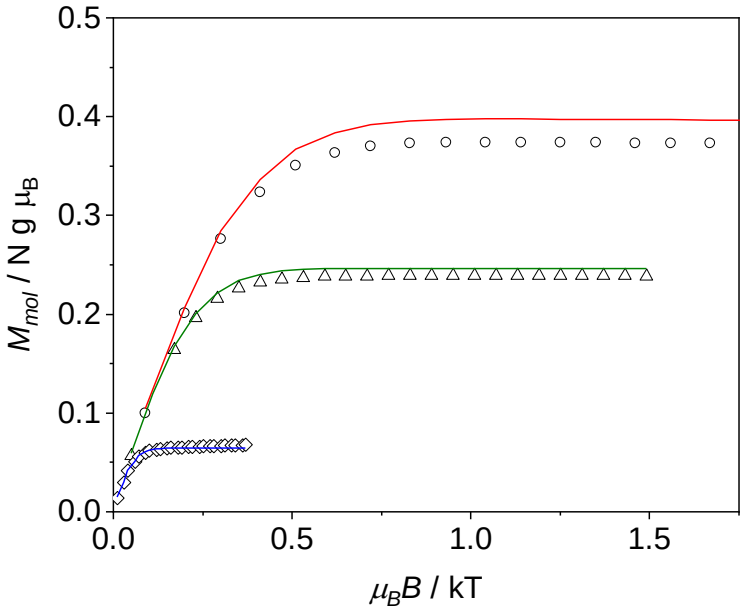

Figure 127. Variable temperature – variable field (VT-VH) magnetization measurements of a solid sample of **5** at applied fields of 1.0 (diamonds and blue fit), 4.0 (triangles and green fit) and 7.0 T (circles and red fit).

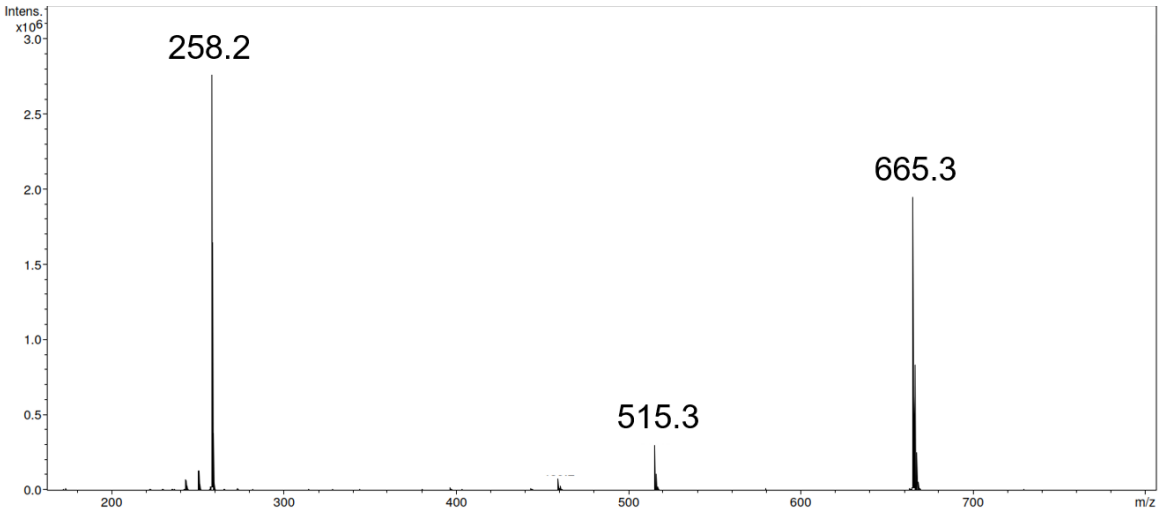

Figure 128. ESI(+)-MS of a CH_3CN solution of pro-ligand **[11H$_3$][OTf]$_2$**.

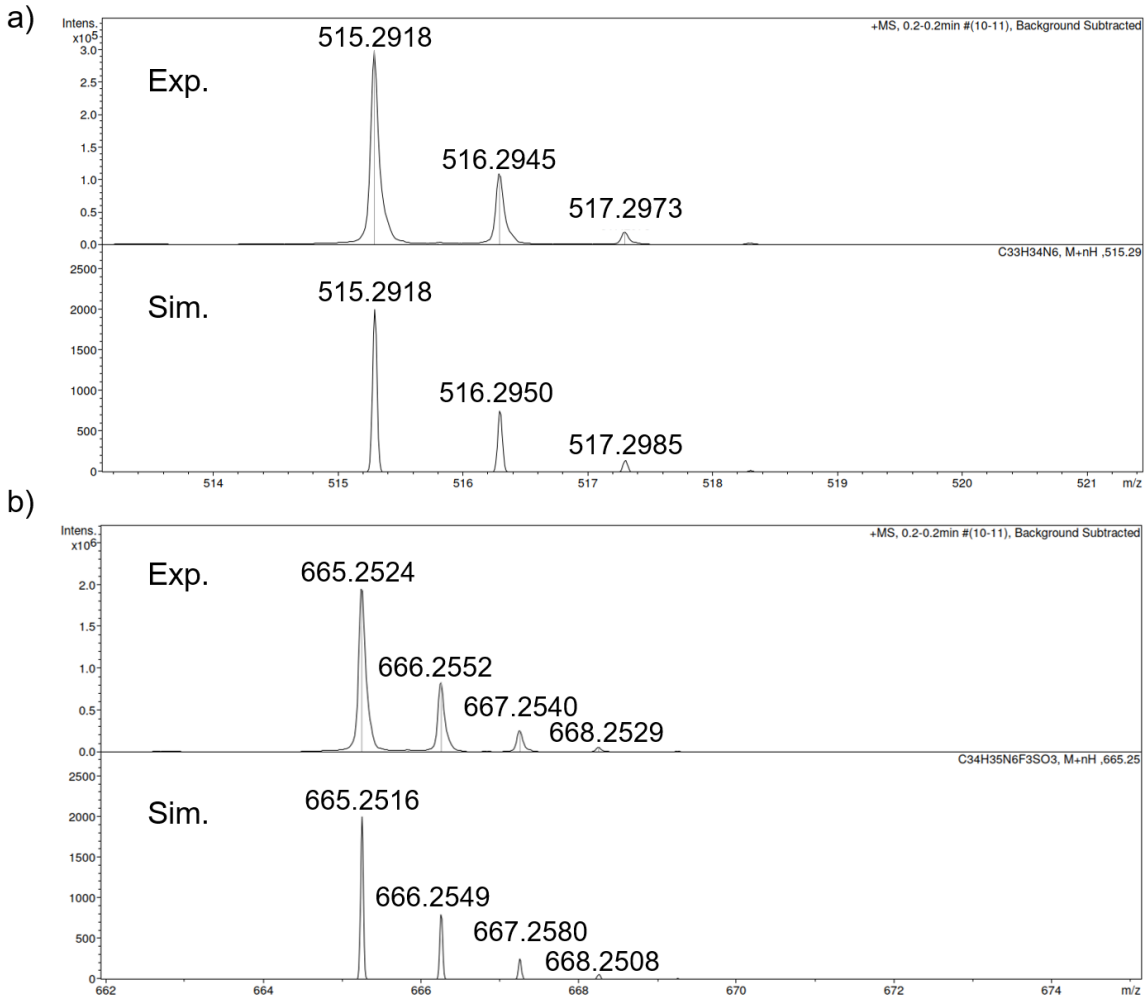

Figure 129. Experimental and simulated isotopic pattern of ESI signals at m/z 515 (top) and 665 (bottom) for a CH_3CN solution of **[11H$_3$][OTf]$_2$**.

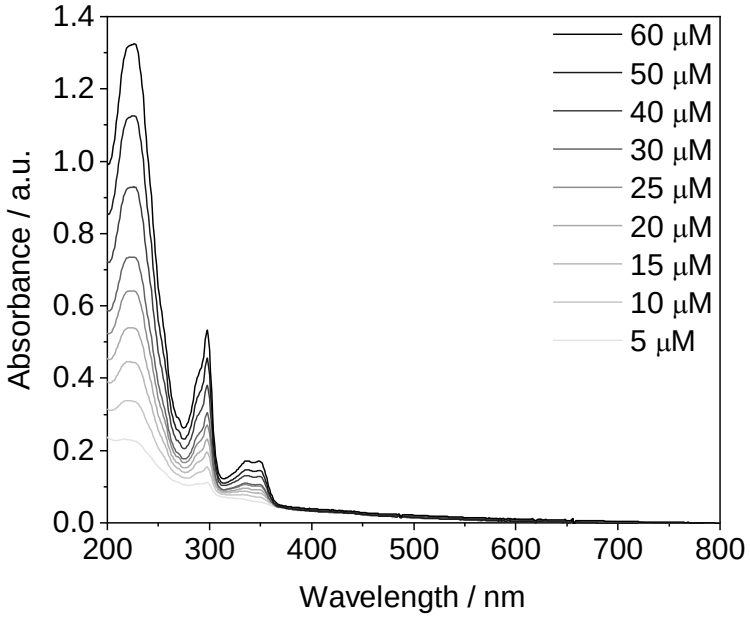

Figure 130. UV/Vis solution spectra of pro-ligand **[11H$_3$][OTf]$_2$** in CH_3CN at different concentrations at RT.

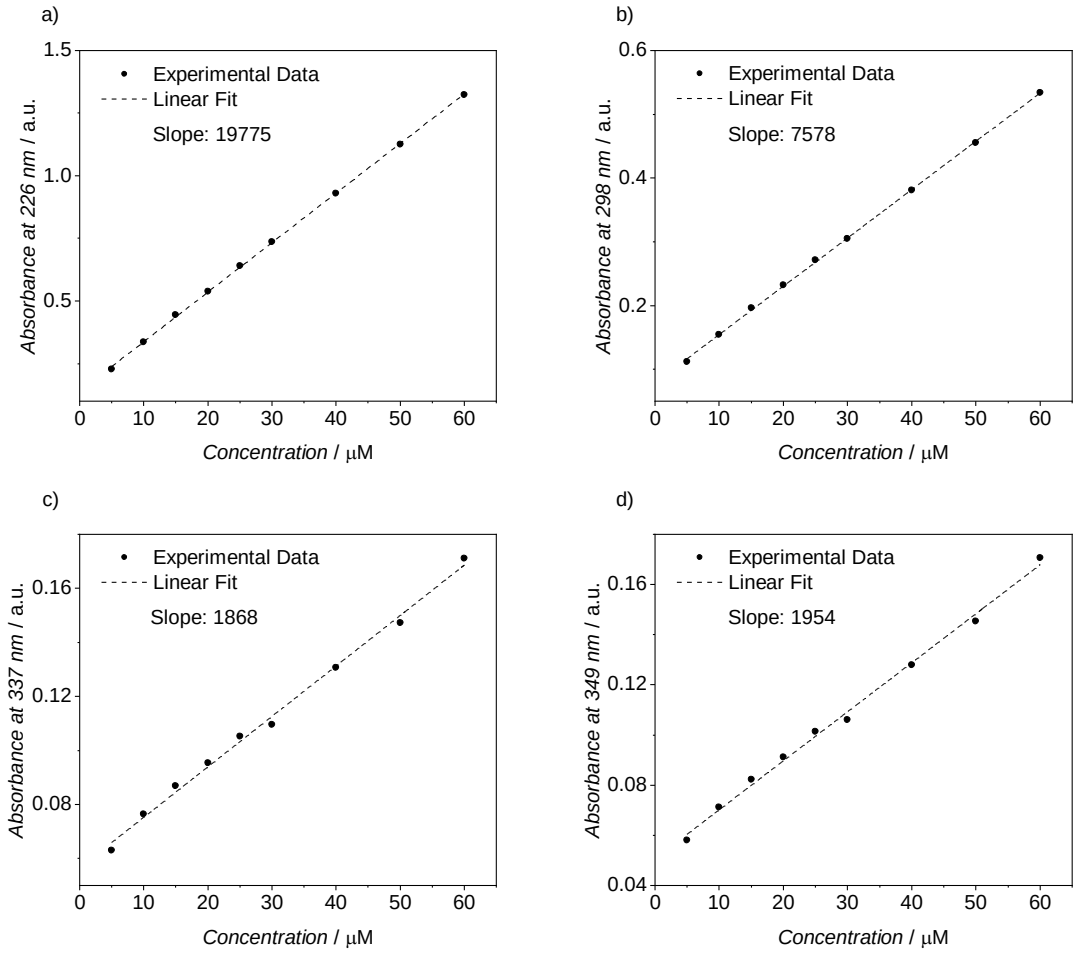

Figure 131. Plots and linear fits of absorbance at a) 226, b) 298, c) 337, d) 349 nm versus concentrations of **[11H$_3$][OTf]$_2$** in CH_3CN at room temperature. The slope of the linear fit has been used as an estimation of the molar extinction coefficients of the compound at the given wavelengths.

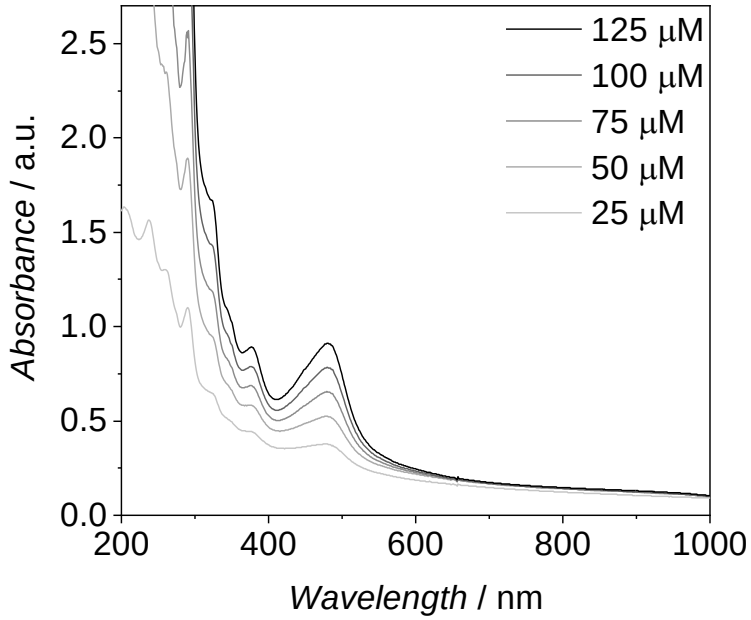

Figure 132. UV/Vis solution spectra of **12a** in CH_3CN at different concentrations at room temperature.

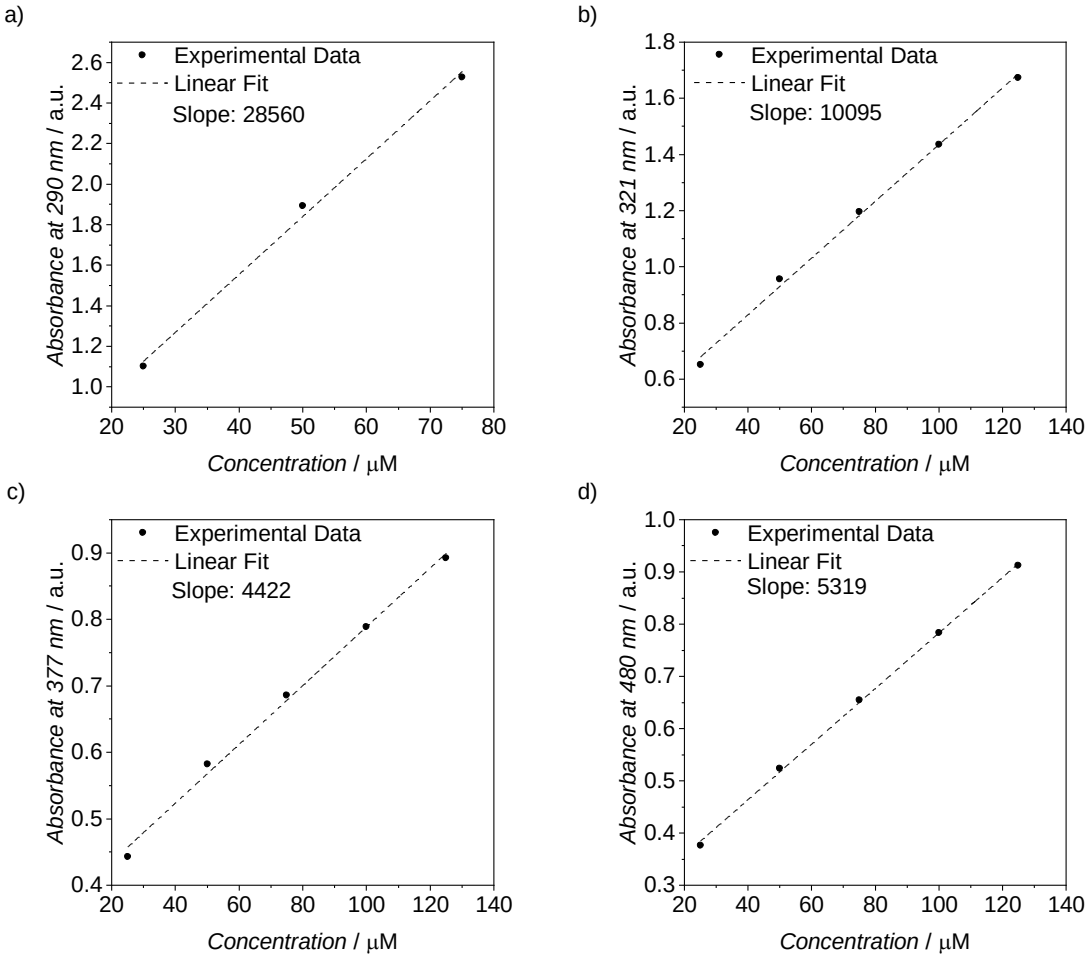

Figure 133. Plots and linear fits of absorbance at a) 290, b) 321, c) 377, d) 480 nm versus concentrations of **12a** in CH_3CN at room temperature. The slope of the linear fit has been used as an estimation of the molar extinction coefficients of the compound at the given wavelengths.

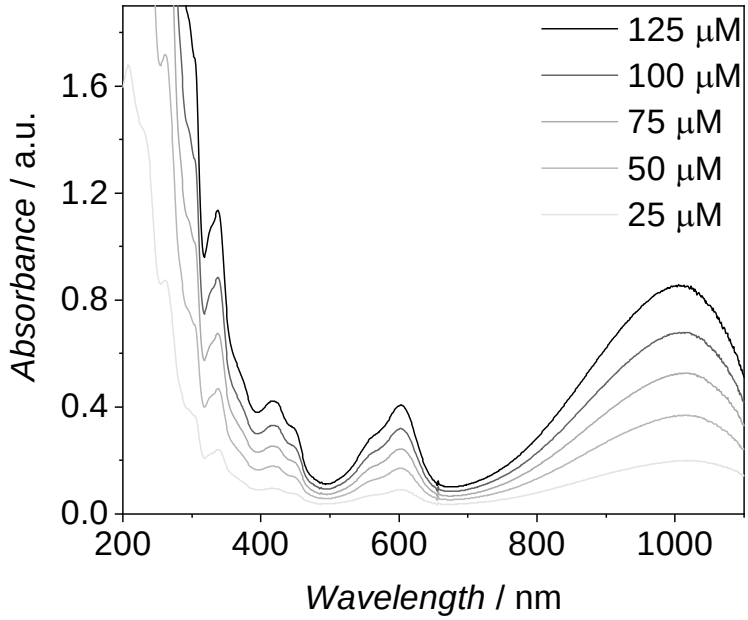

Figure 134. UV/Vis solution spectra of **13a** in CH_3CN at different concentrations at room temperature.

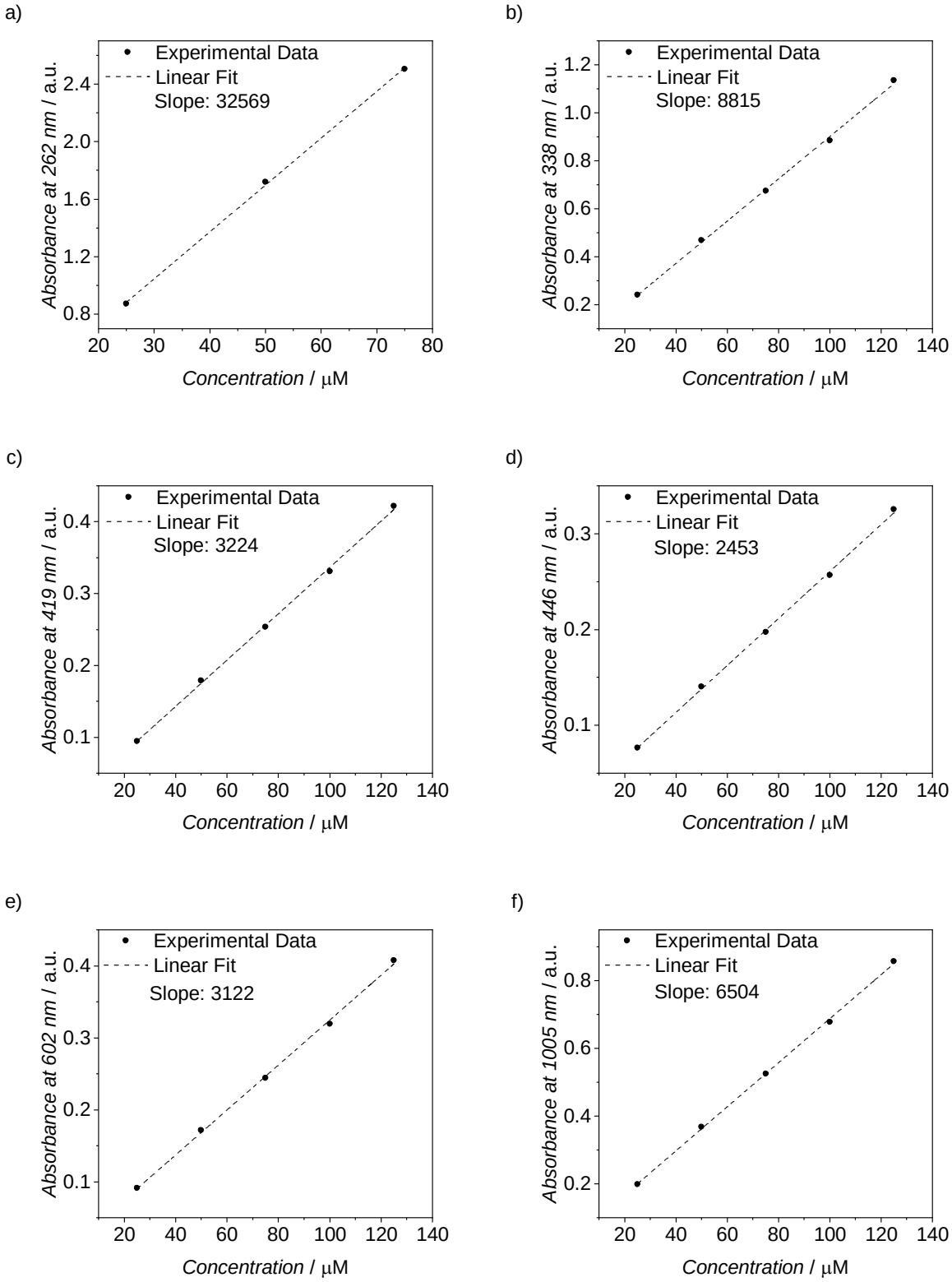

Figure 135. Plots and linear fits of absorbance at a) 262, b) 338, c) 419, d) 446, e) 602, f) 1005 nm versus concentrations of **13a** in CH_3CN at room temperature. The slope of the linear fit has been used as an estimation of the molar extinction coefficients of the compound at the given wavelengths.

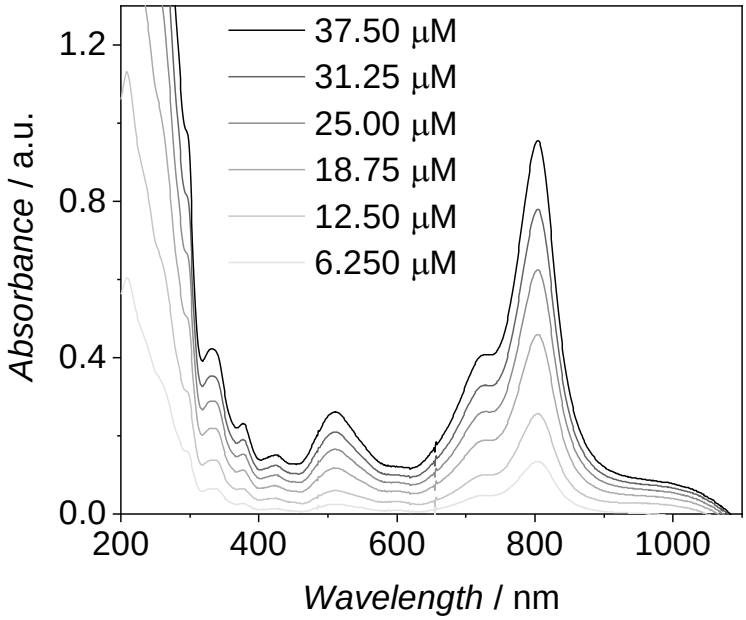

Figure 136. UV/Vis solution spectra of **14a** in CH_3CN at different concentrations at –35 °C.

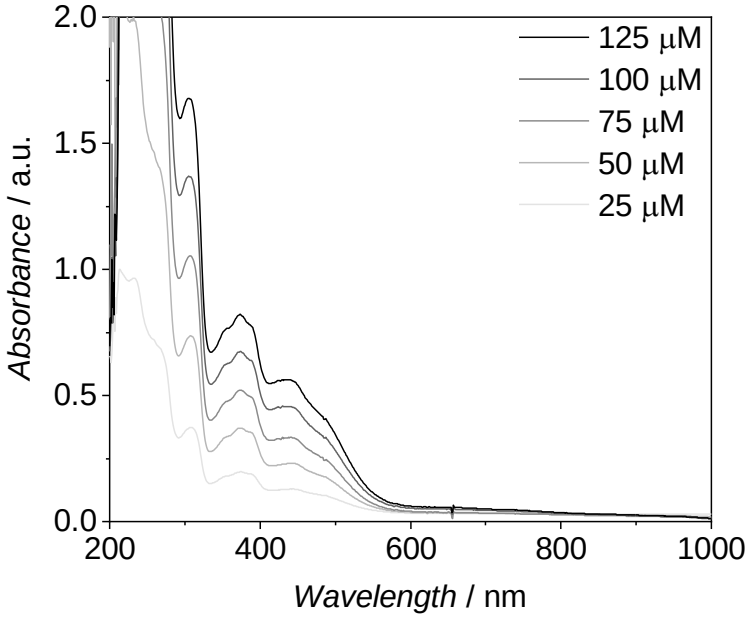

Figure 137. UV/Vis solution spectra of **12b** in THF at different concentrations at room temperature.

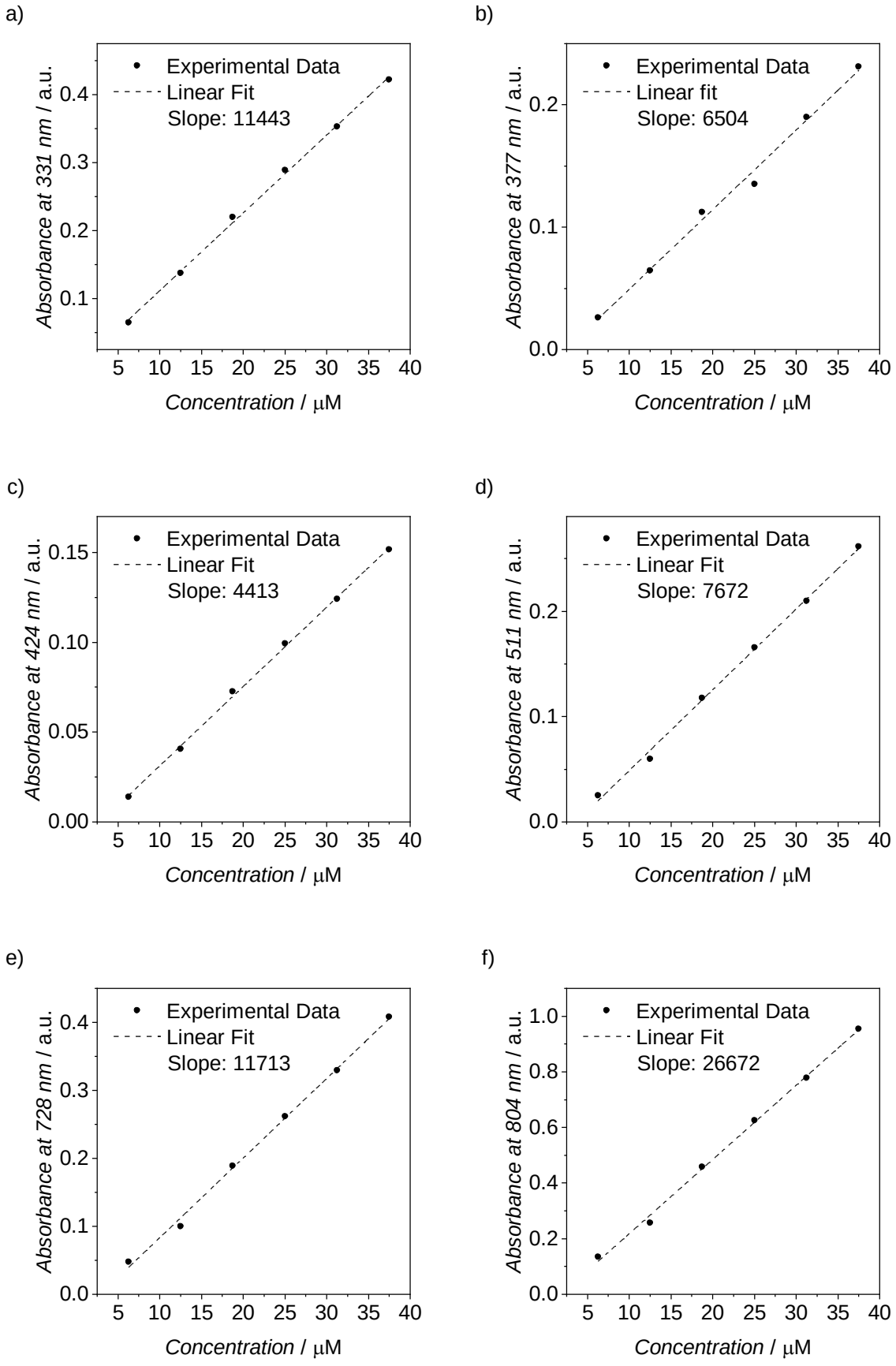

Figure 138. Plots and linear fits of absorbance at a) 331, b) 377, c) 424, d) 511, e) 728, f) 804 nm versus concentrations of **14a** in CH_3CN at −35 °C. The slope of the linear fit has been used as an estimation of the molar extinction coefficients of the compound at the given wavelengths.

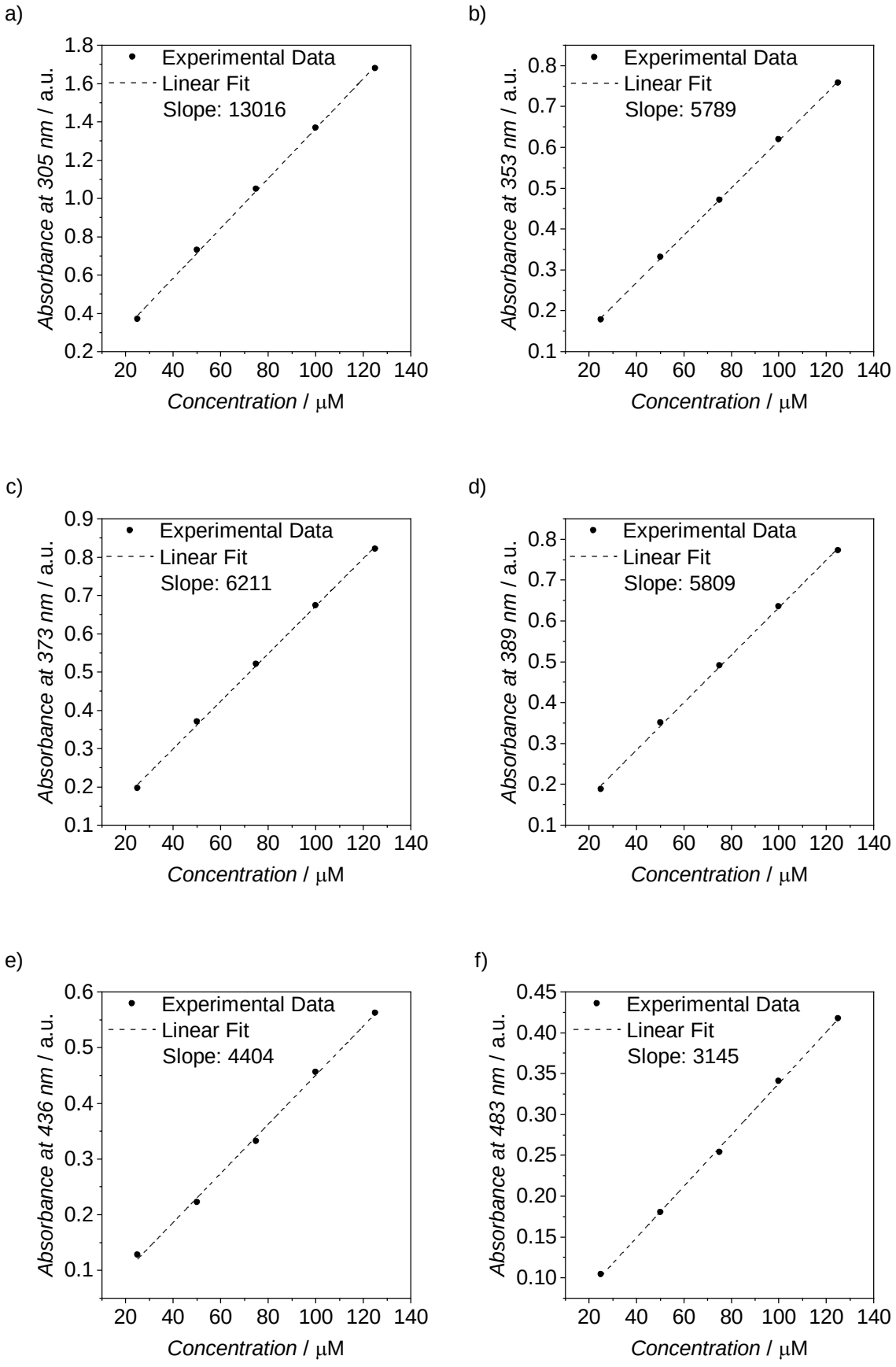

Figure 139. Plots and linear fits of absorbance at a) 305, b) 353, c) 373, d) 389, e) 436, f) 483 nm versus concentrations of **12b** in THF at room temperature. The slope of the linear fit has been used as an estimation of the molar extinction coefficients of the compound at the given wavelengths.

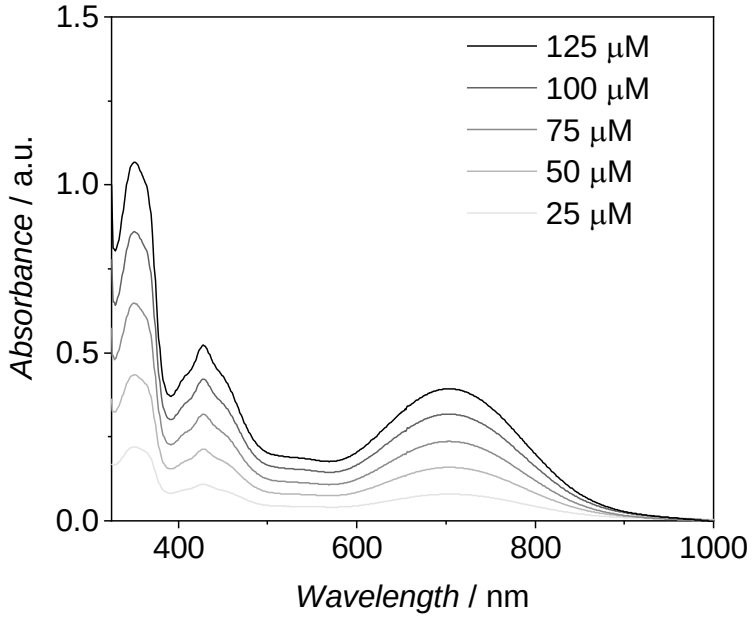

Figure 140. UV/Vis solution spectra of **13b** in acetone at different concentrations at room temperature.

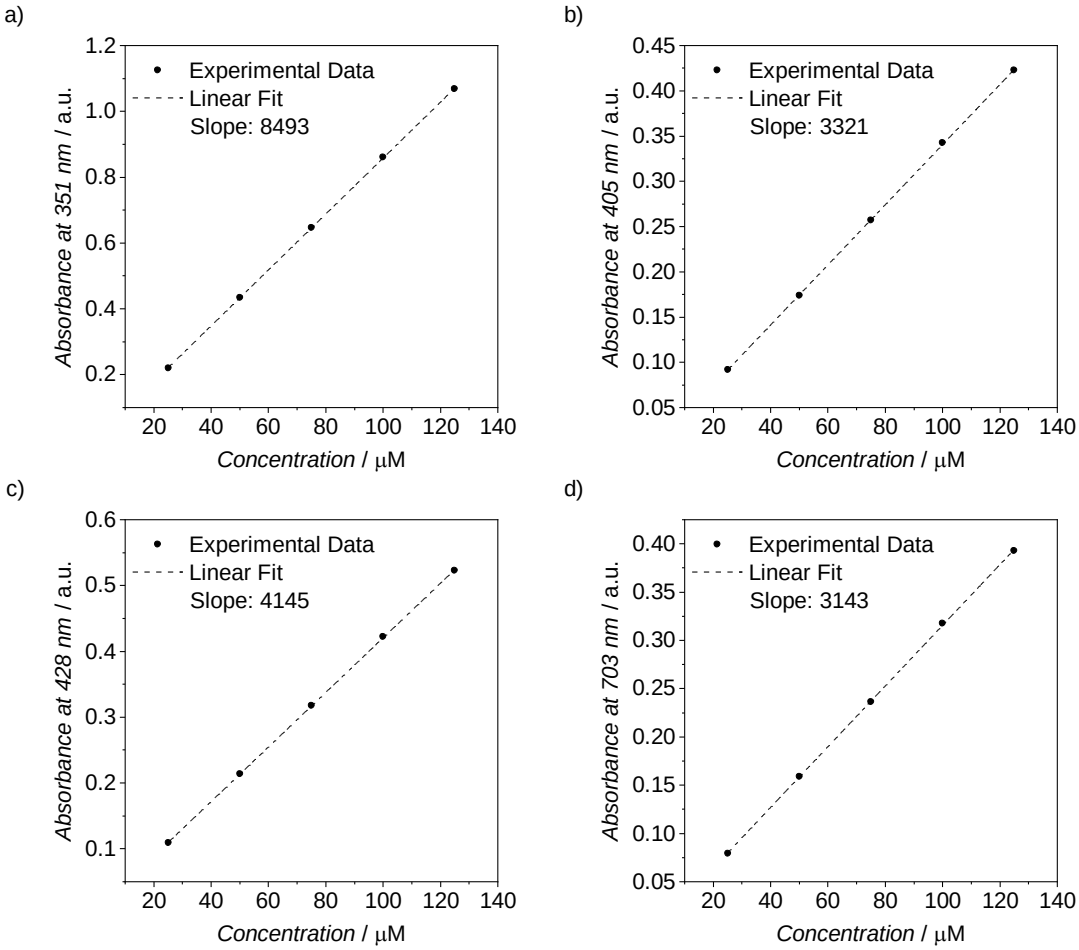

Figure 141. Plots and linear fits of absorbance at a) 351, b) 405, c) 428, d) 703 nm versus concentrations of **13b** in acetone at room temperature. The slope of the linear fit has been used as an estimation of the molar extinction coefficients of the compound at the given wavelengths.

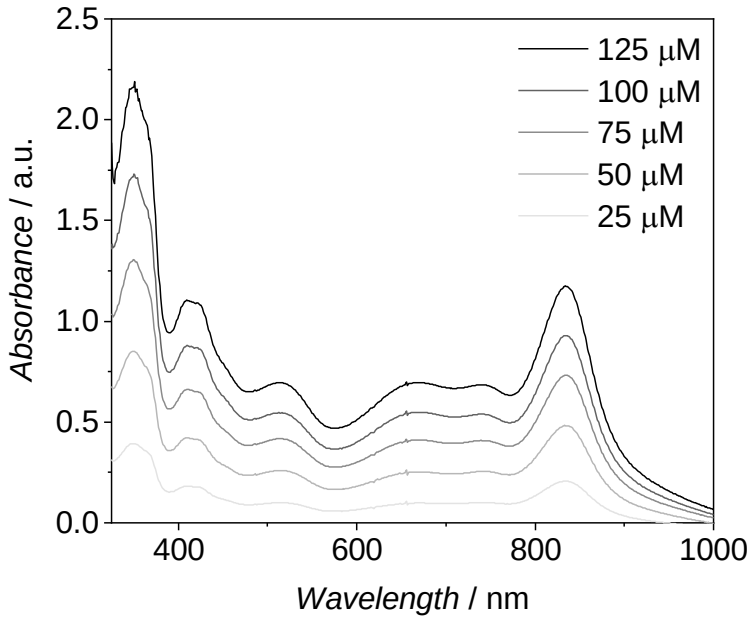

Figure 142. UV/Vis solution spectra of **14b** in acetone at different concentrations at –35 °C.

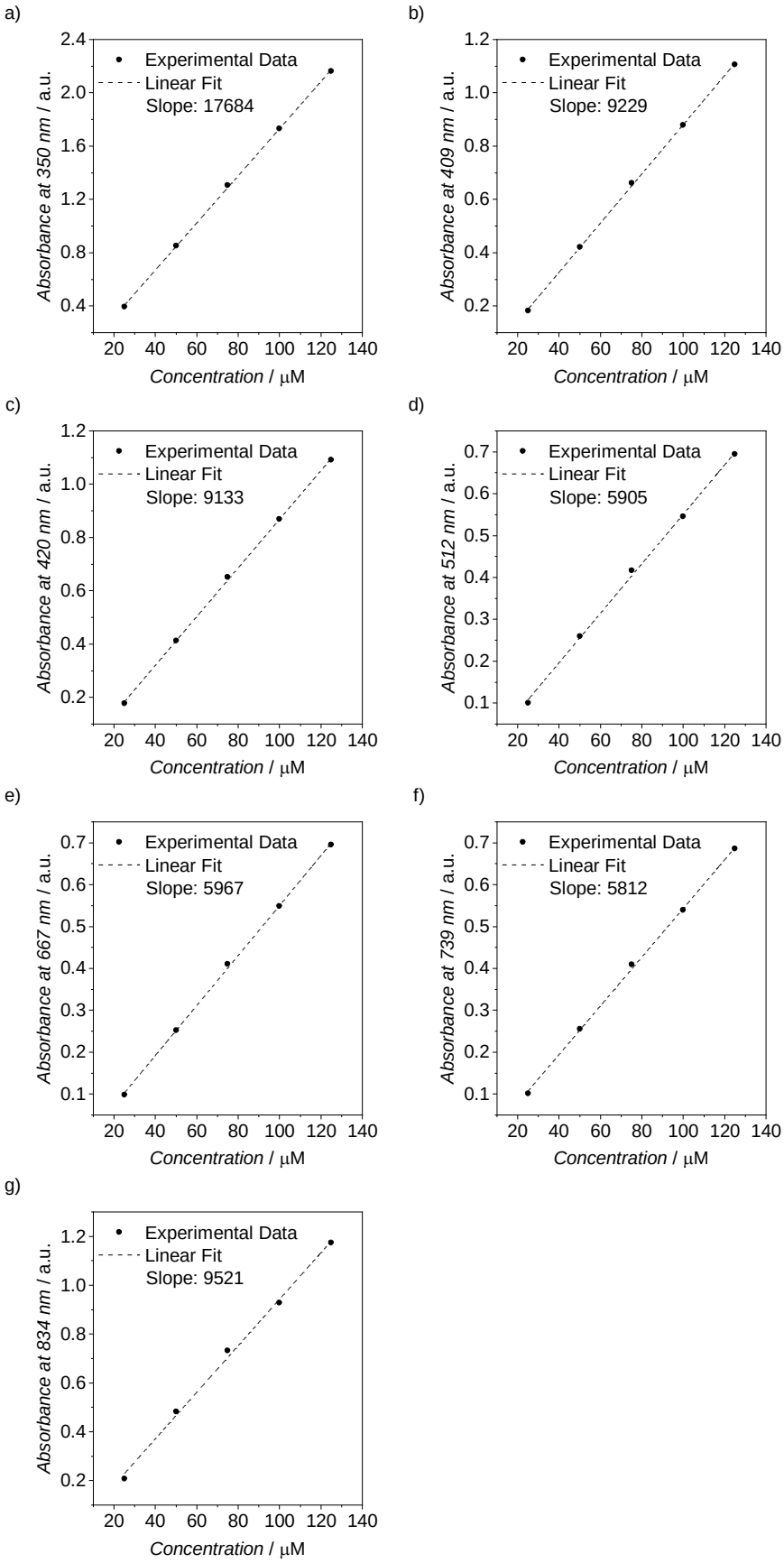

Figure 143. Plots and linear fits of absorbance at a) 350, b) 409, c) 420, d) 512, e) 667, f) 739, g) 834 nm versus concentrations of **14b** in acetone at −35 °C. The slope of the linear fit has been used as an estimation of the molar extinction coefficients of the compound at the given wavelengths.

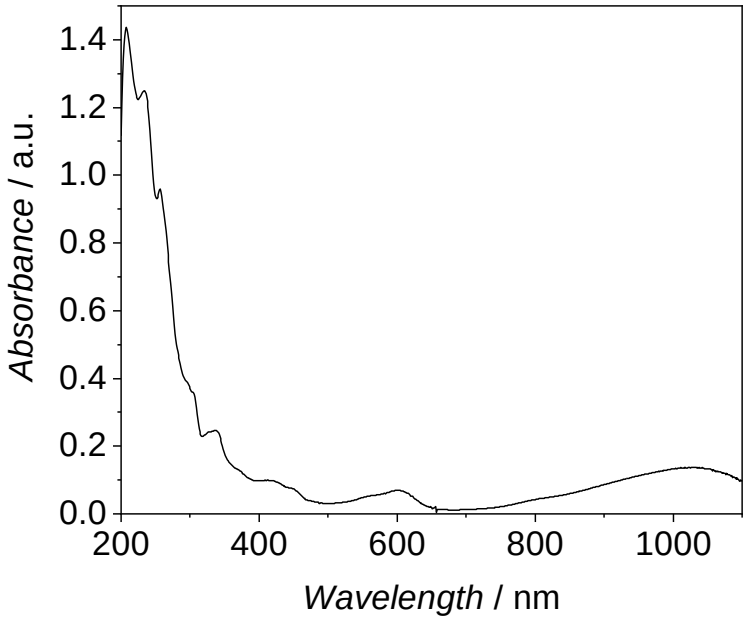

Figure 144. UV/Vis solution spectra of **14a** in CH_3CN after it was left decomposing at RT for 30 minutes.

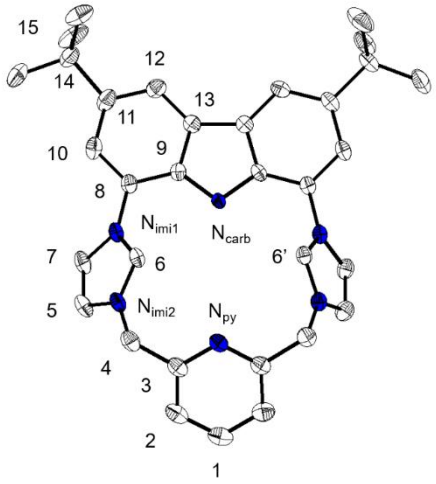

Figure 145. Numbering of positions used for **[11H$_3$][OTf]$_2$** and all the iron complexes **12a**/**b**–**14a** in the assignation of the NMR signals.

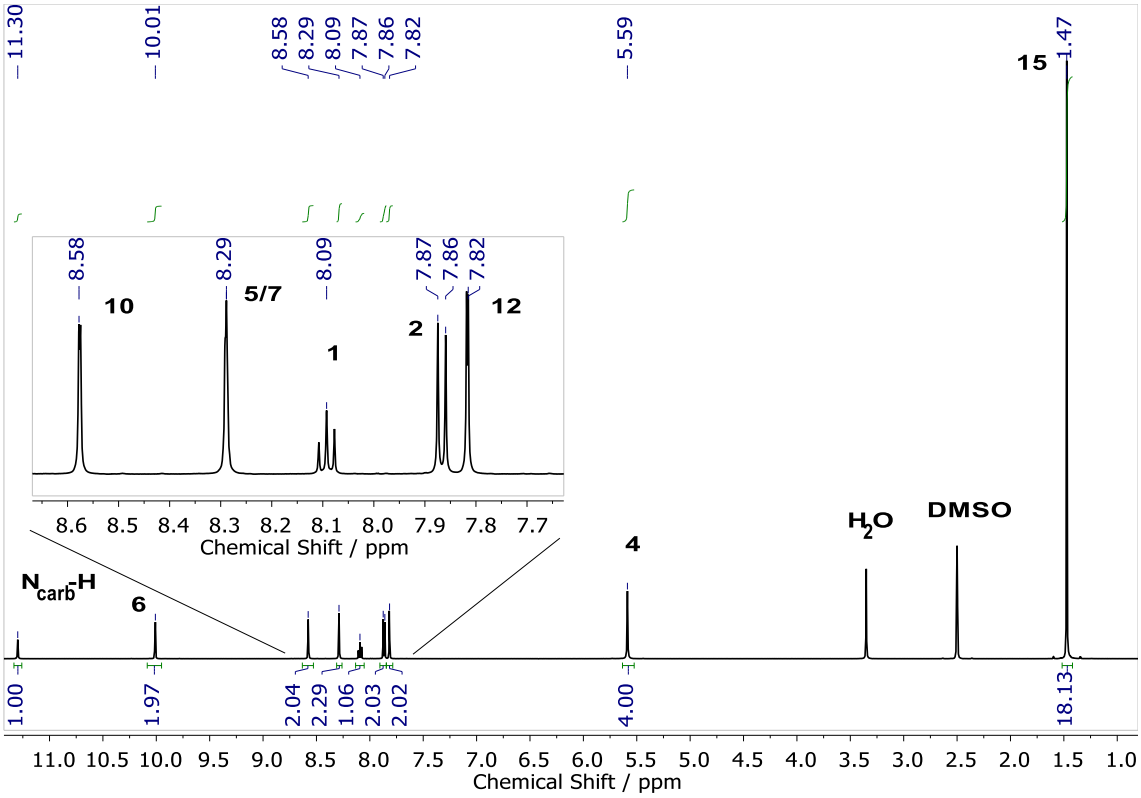

Figure 146. ^{1}H-NMR spectrum (500 MHz) of **[11H$_3$][OTf]$_2$** in DMSO-d6 at RT.

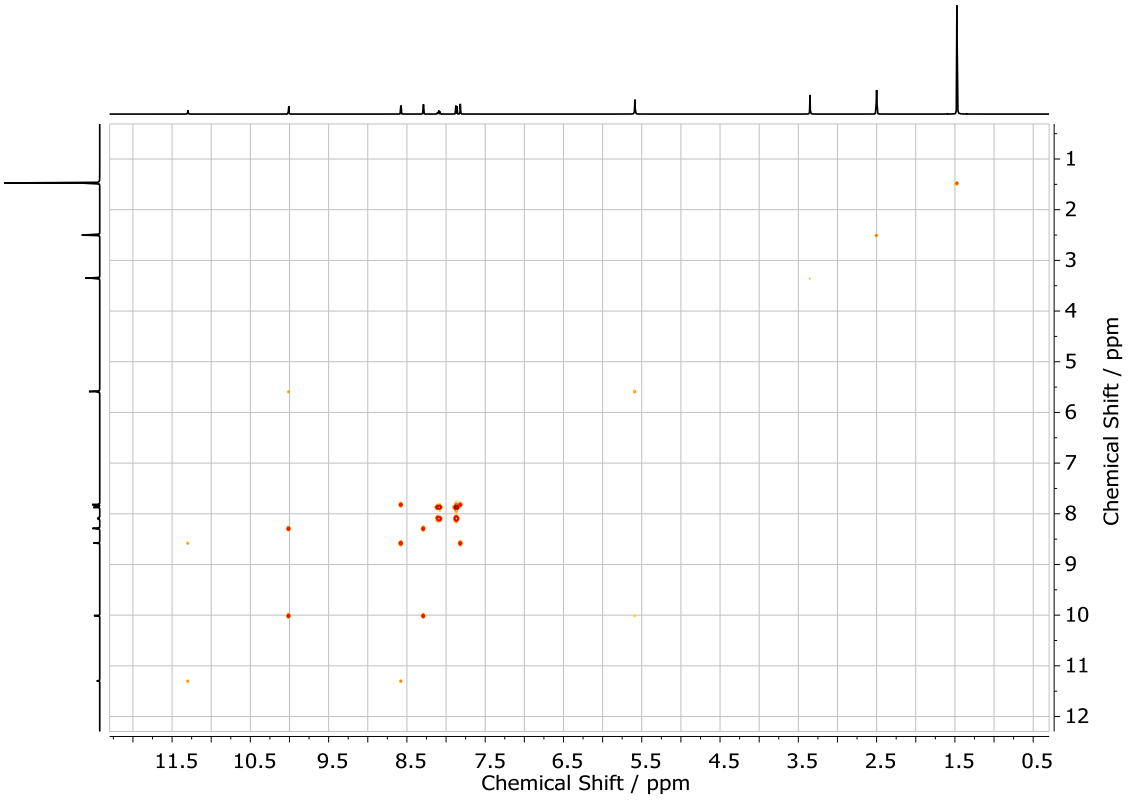

Figure 147. ^{1}H-^{1}H COSY NMR spectrum (500 MHz) of **[11H$_3$][OTf]$_2$** in DMSO-d6 at RT.

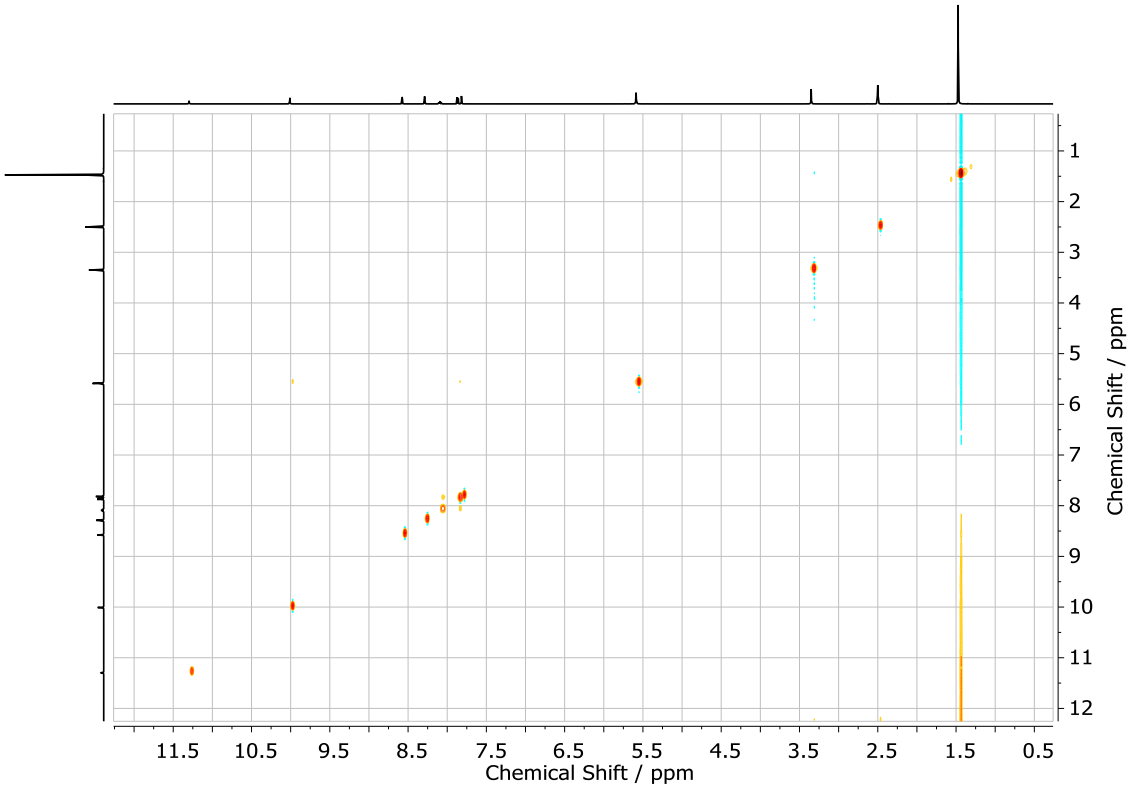

Figure 148. ^{1}H NOESY NMR spectrum (500 MHz) of **[11H$_3$][OTf]$_2$** in DMSO-d6 at RT.

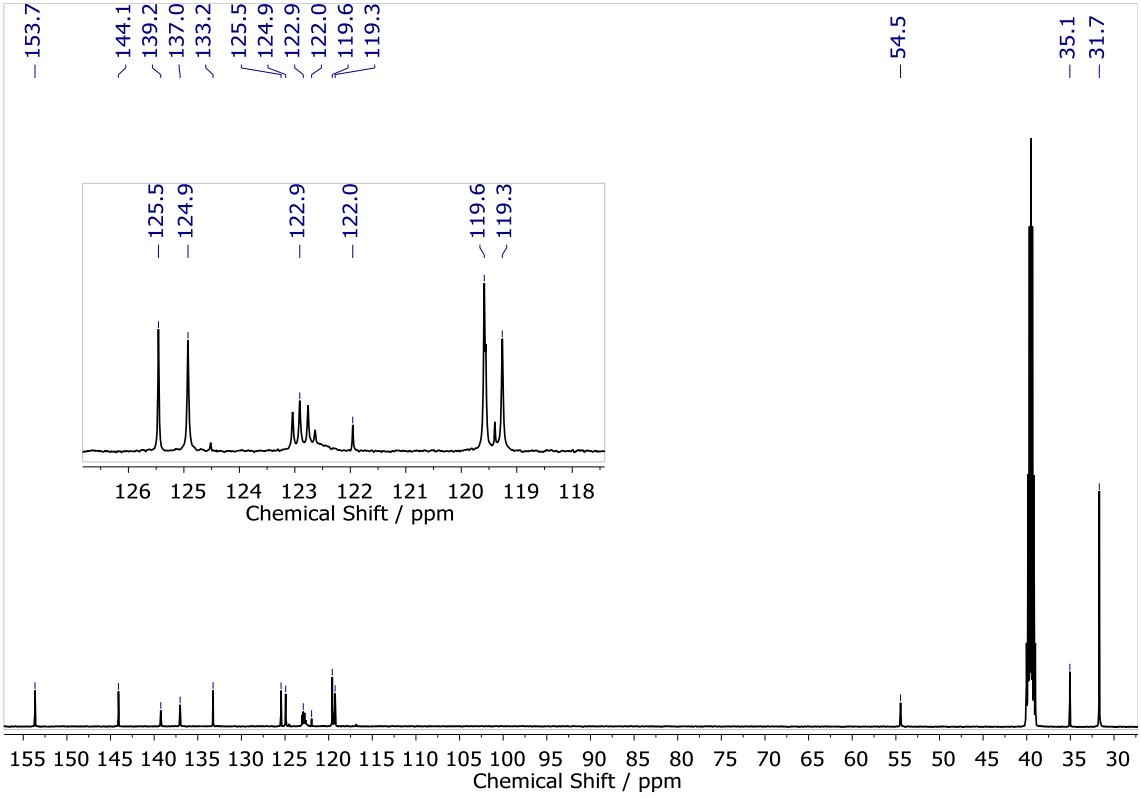

Figure 149. ^{13}C {^{1}H} NMR spectrum (500 MHz) of **[11H$_3$][OTf]$_2$** in DMSO-d6 at RT.

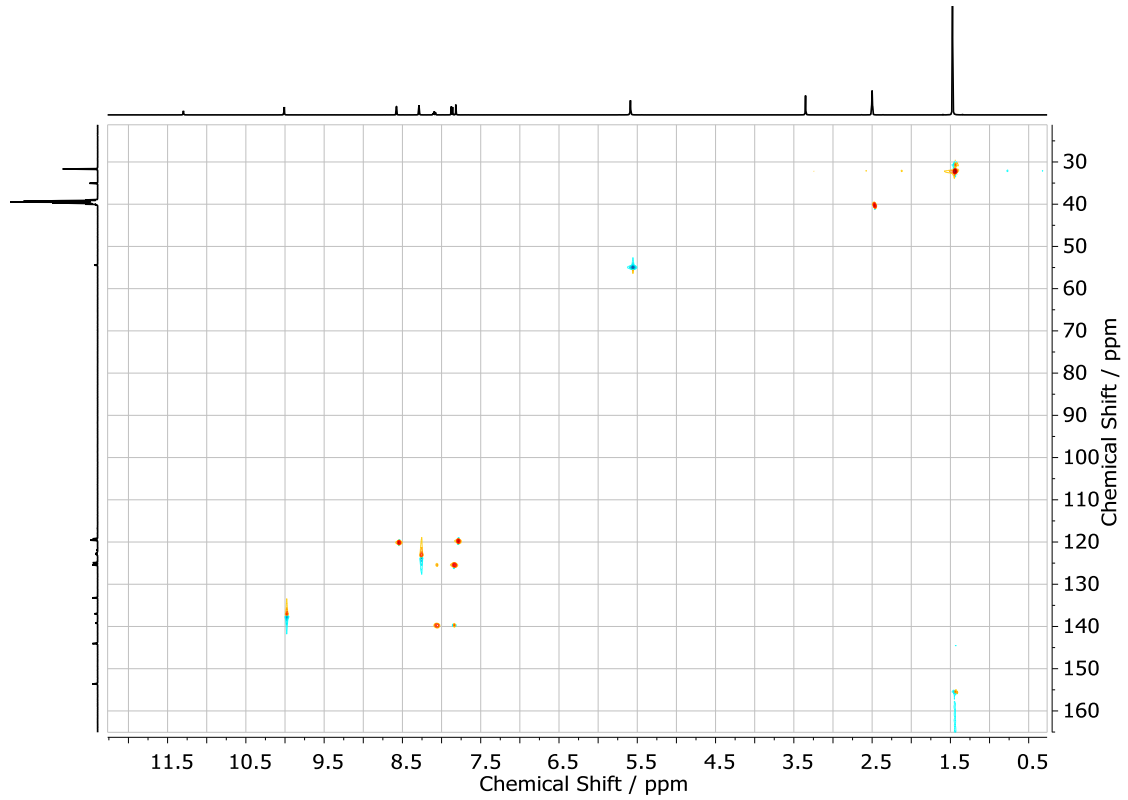

Figure 150. ^{1}H-^{13}C HSQC NMR spectrum (500 MHz) of **[11H$_3$][OTf]$_2$** in DMSO-d6 at RT.

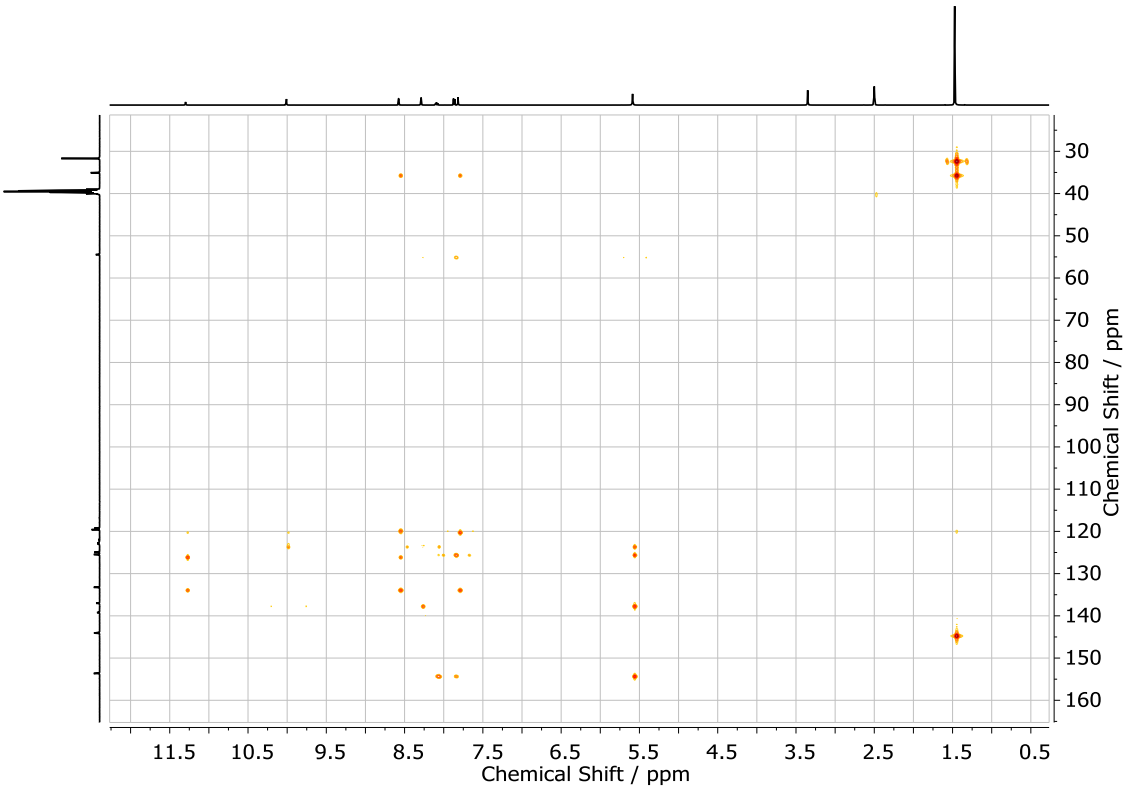

Figure 151. ^{1}H-^{13}C HMBC NMR spectrum (500 MHz) of **[11H$_3$][OTf]$_2$** in DMSO-d6 at RT.

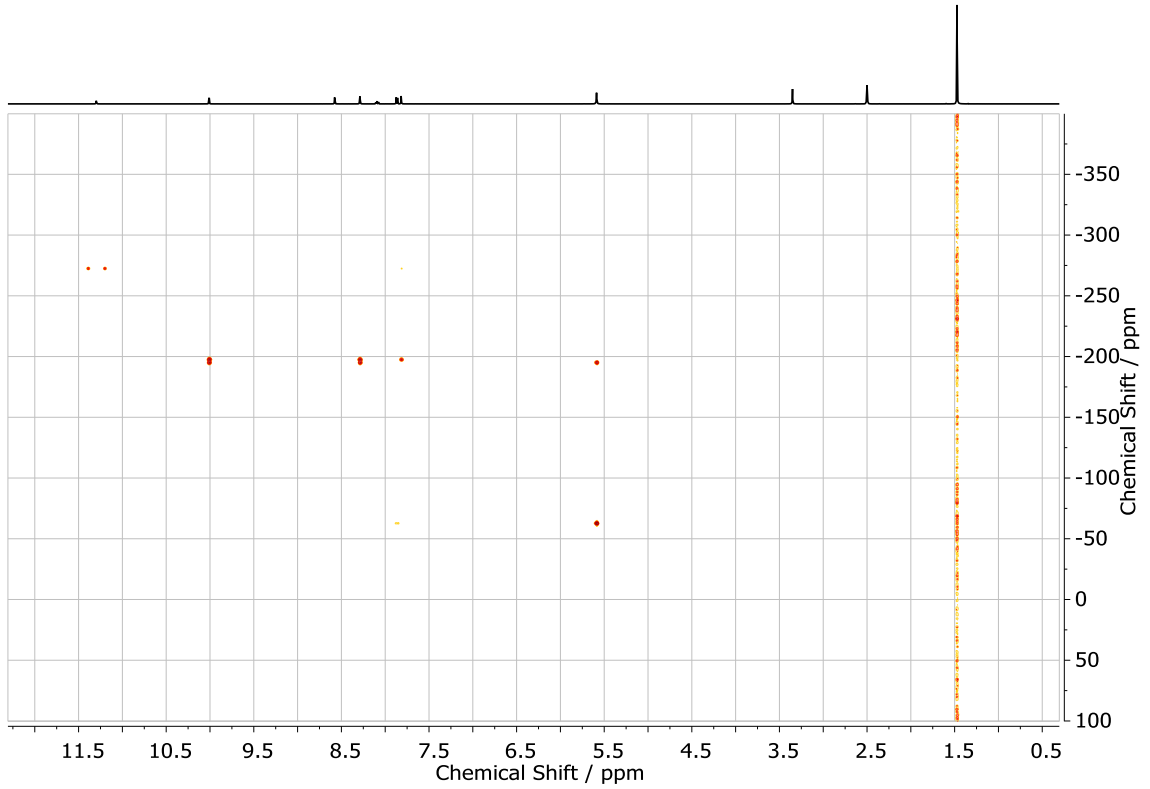

Figure 152. ^{1}H-^{15}N HMBC NMR spectrum (500 MHz) of **[11H$_3$][OTf]$_2$** in DMSO-d6 at RT.

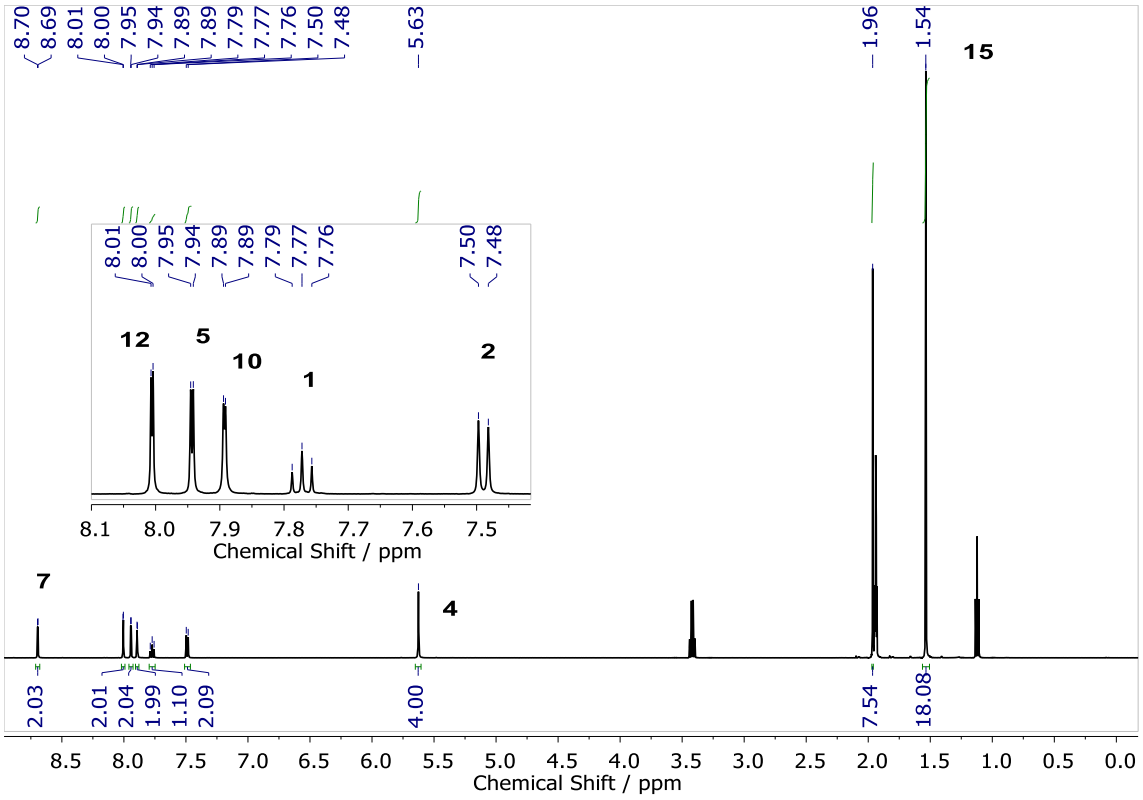

Figure 153. ^{1}H-NMR spectrum (500 MHz) of **12a** in CD_3CN at RT.

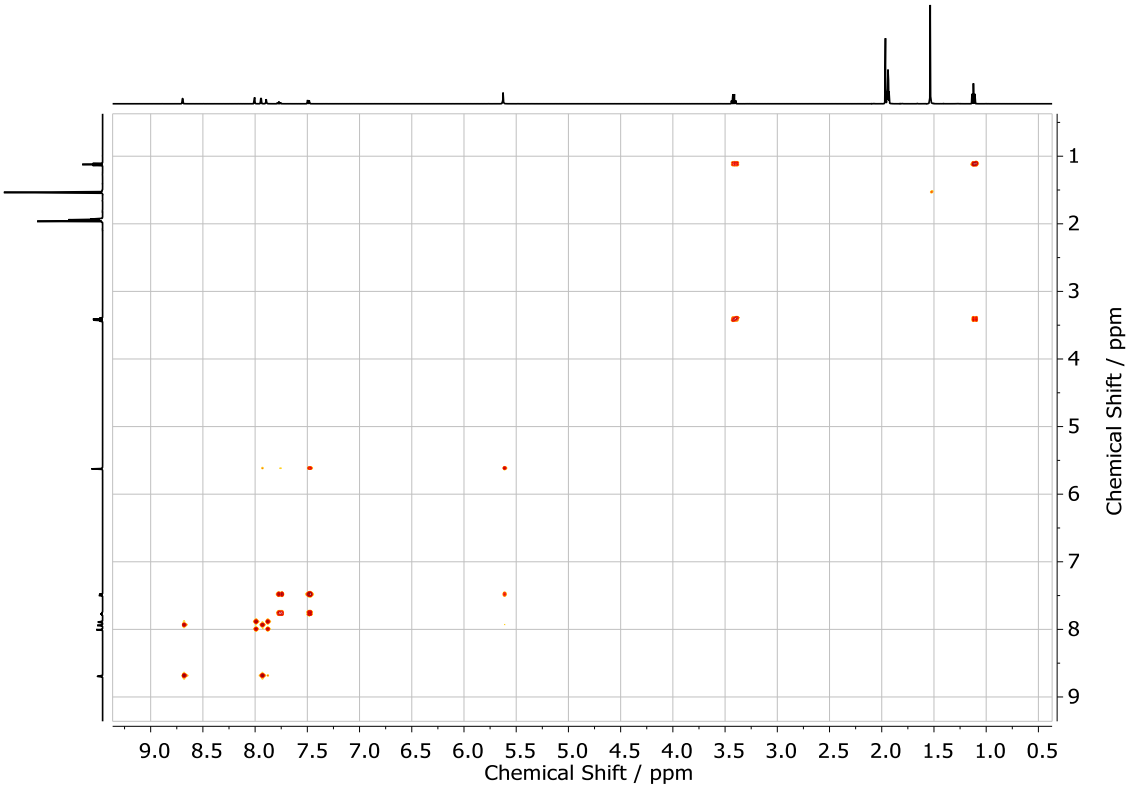

Figure 154. ^{1}H-^{1}H COSY NMR spectrum (500 MHz) of **12a** in CD_3CN at RT.

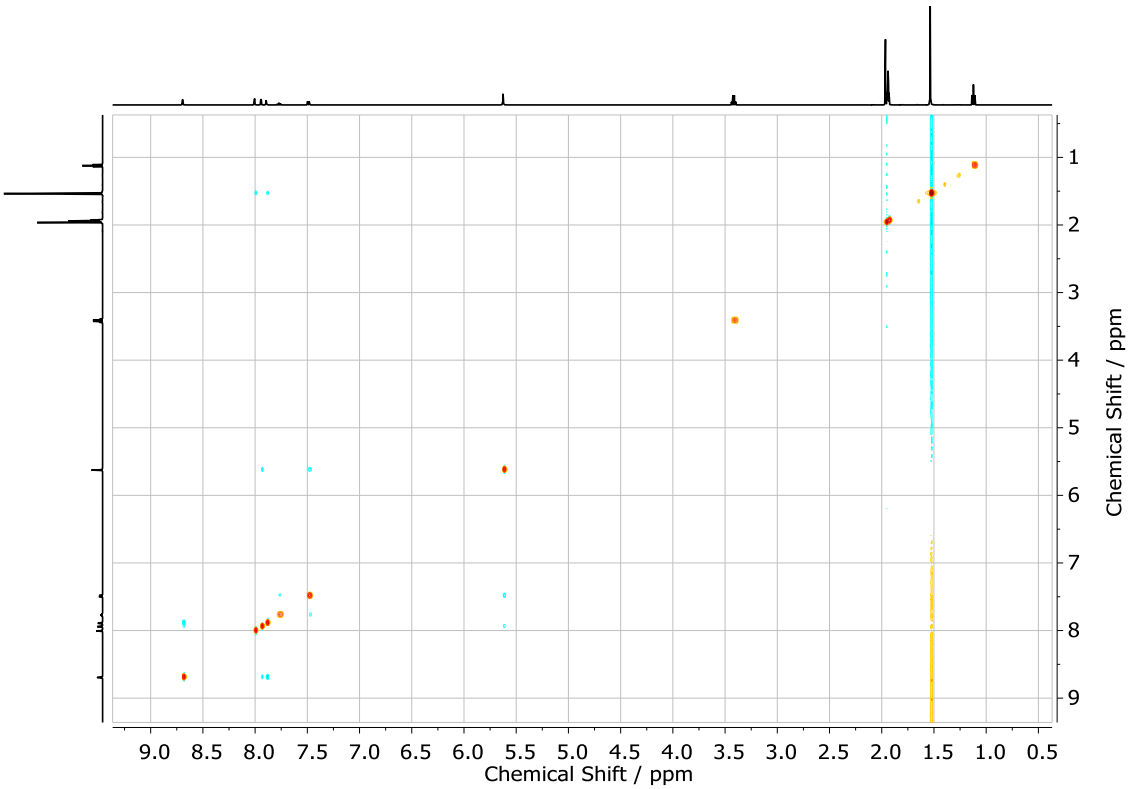

Figure 155. ^{1}H NOESY NMR spectrum (500 MHz) of **12a** in CD_3CN at RT.

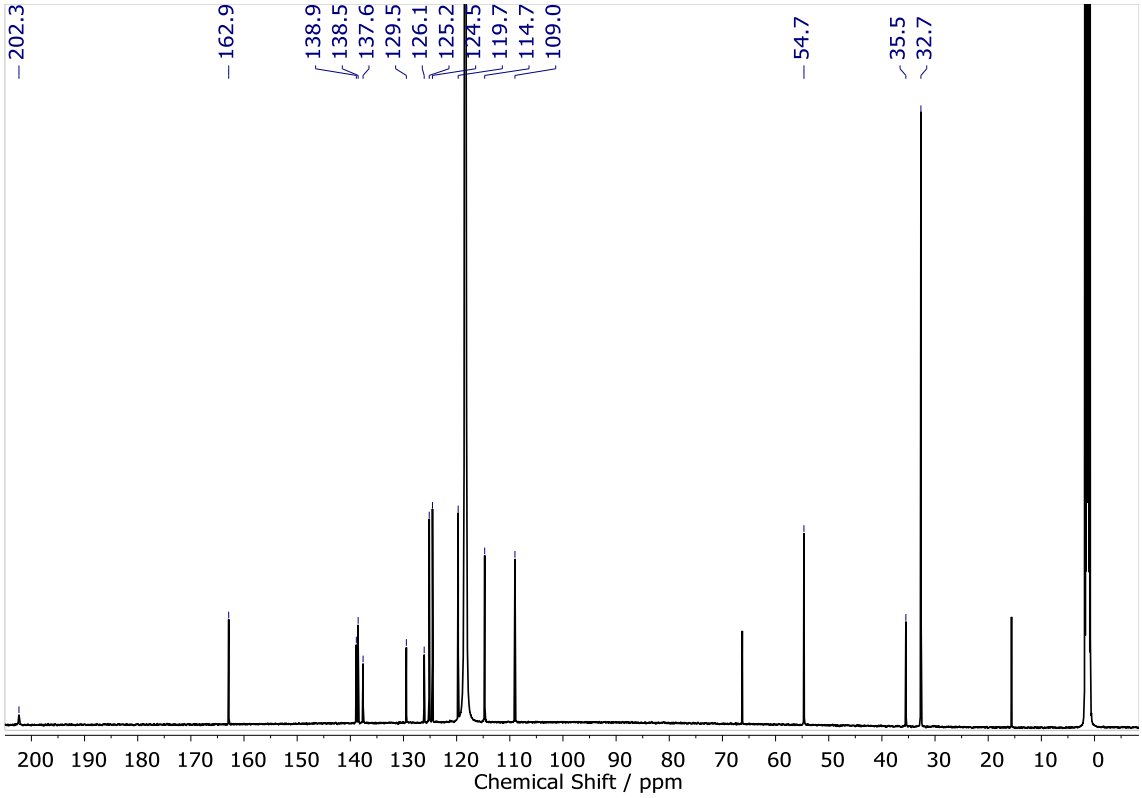

Figure 156. ^{13}C {^{1}H}-NMR spectrum (500 MHz) of **12a** in CD_3CN at RT.

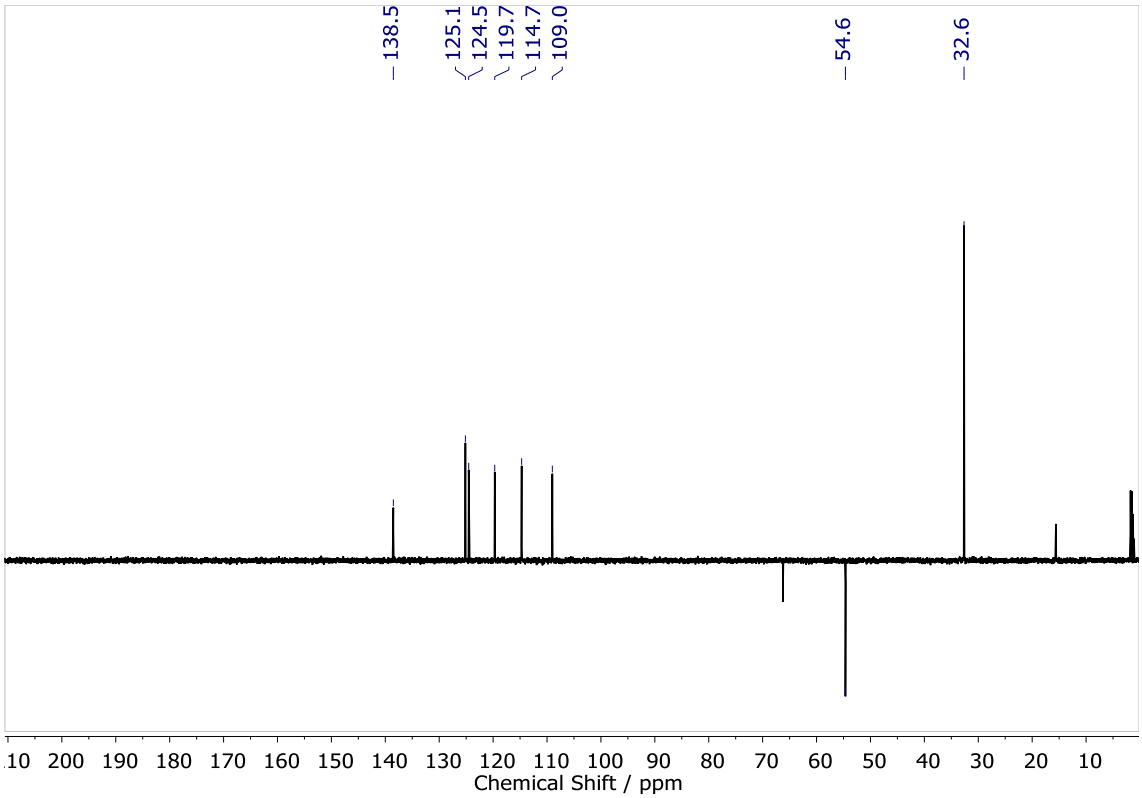

Figure 157. ^{13}C {^{1}H}-DEPT NMR spectrum (500 MHz) of **12a** in CD_3CN at RT.

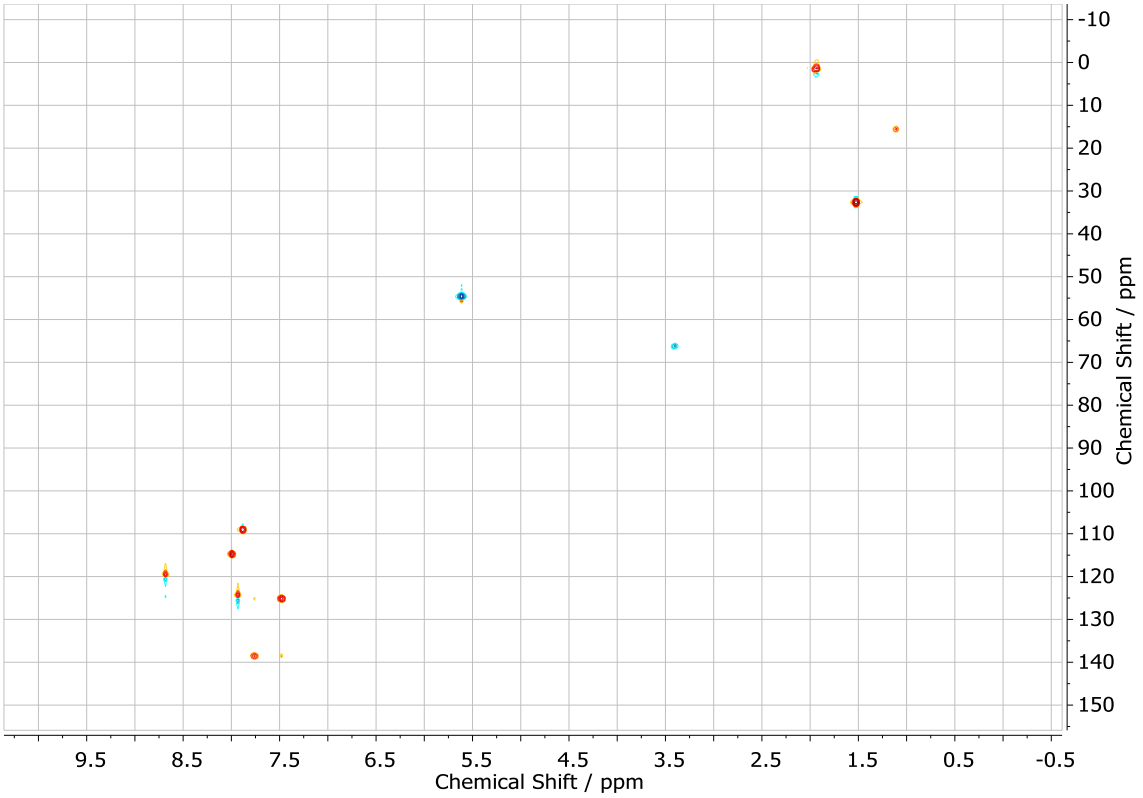

Figure 158. ^{1}H-^{13}C HSQC NMR spectrum (500 MHz) of **12a** in CD_3CN at RT.

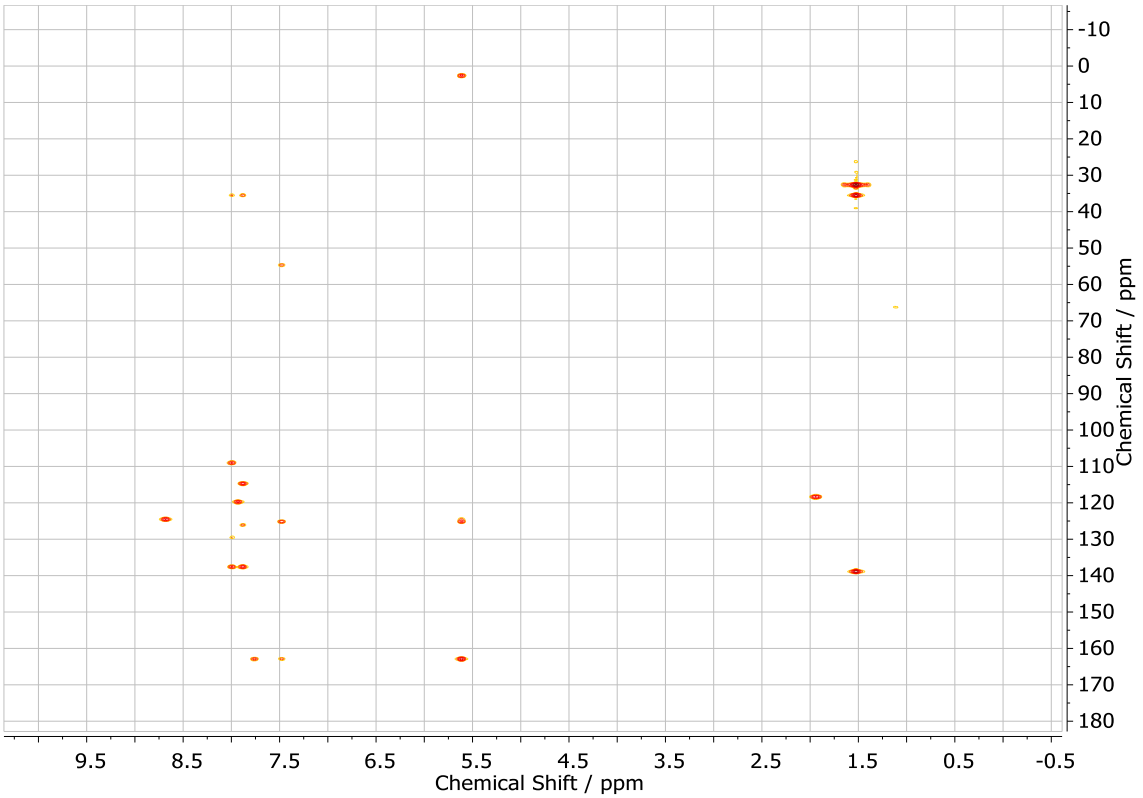

Figure 159. ^{1}H-^{13}C HMBC NMR spectrum (500 MHz) of **12a** in CD_3CN at RT.

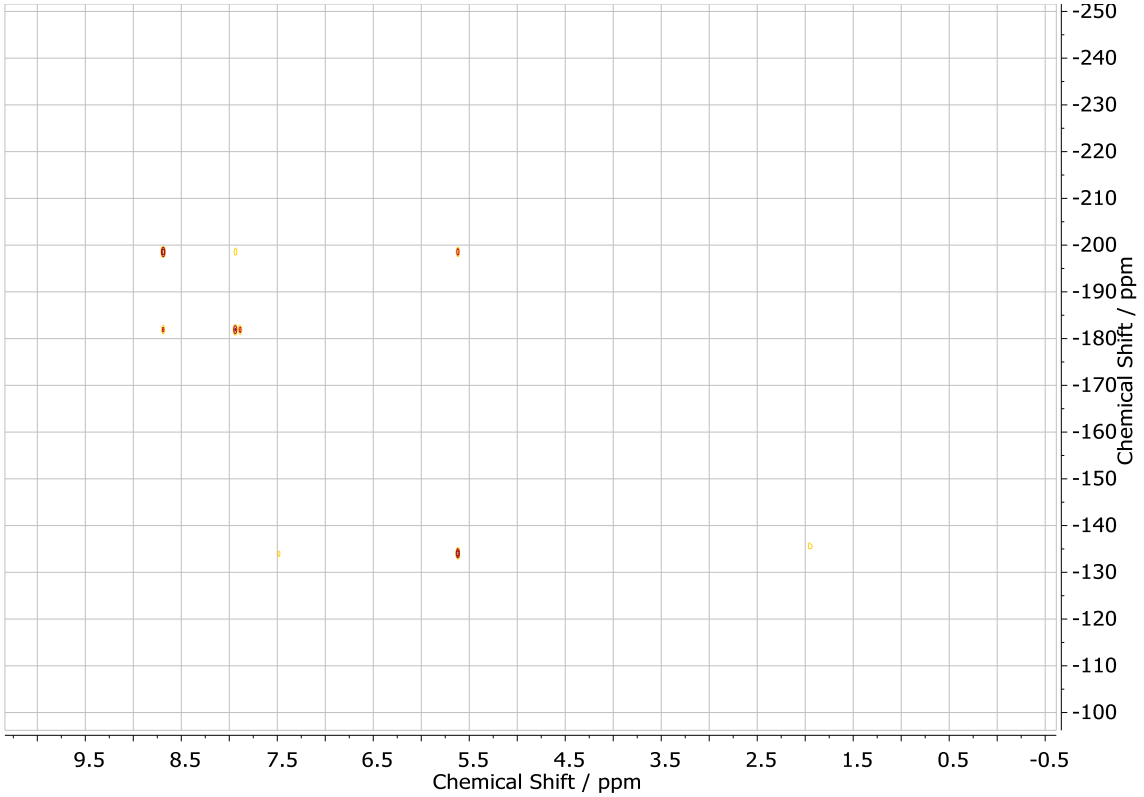

Figure 160. ^{1}H-^{15}N HMBC NMR spectrum (500 MHz) of **12a** in CD_3CN at RT.

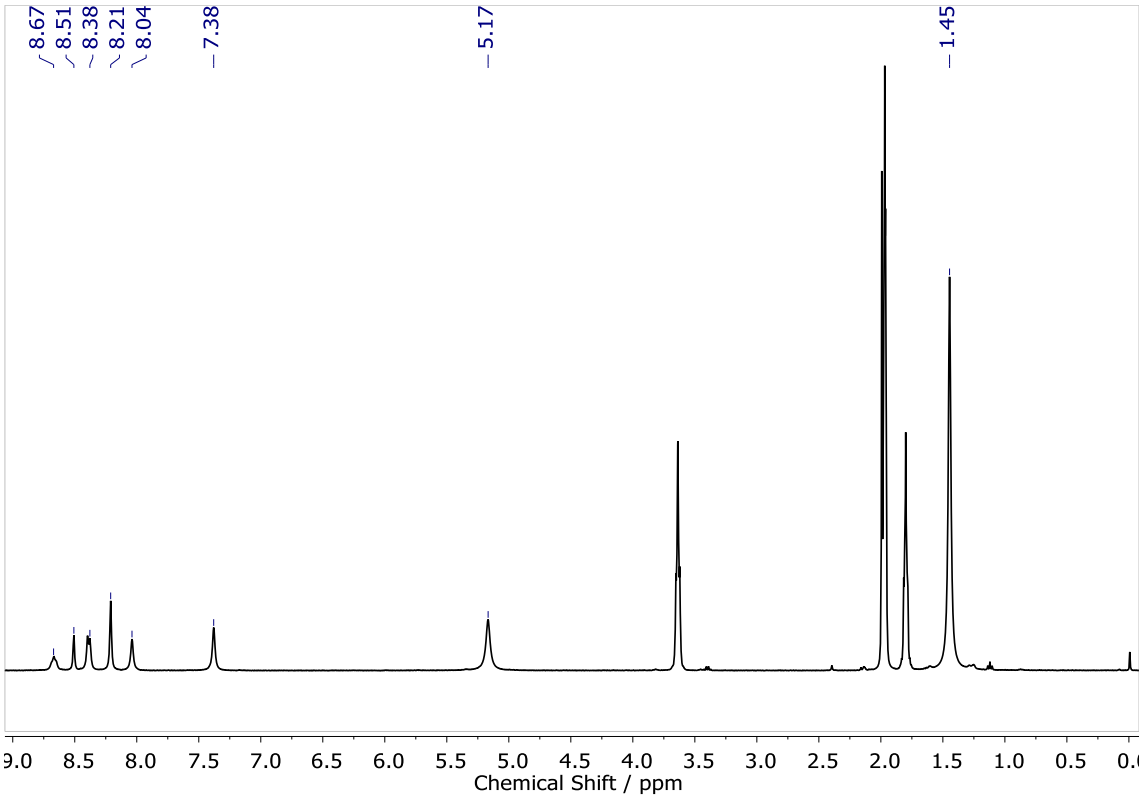

Figure 161. ^{1}H-NMR spectrum (400 MHz) of **14a** in CD_3CN at −35 °C.

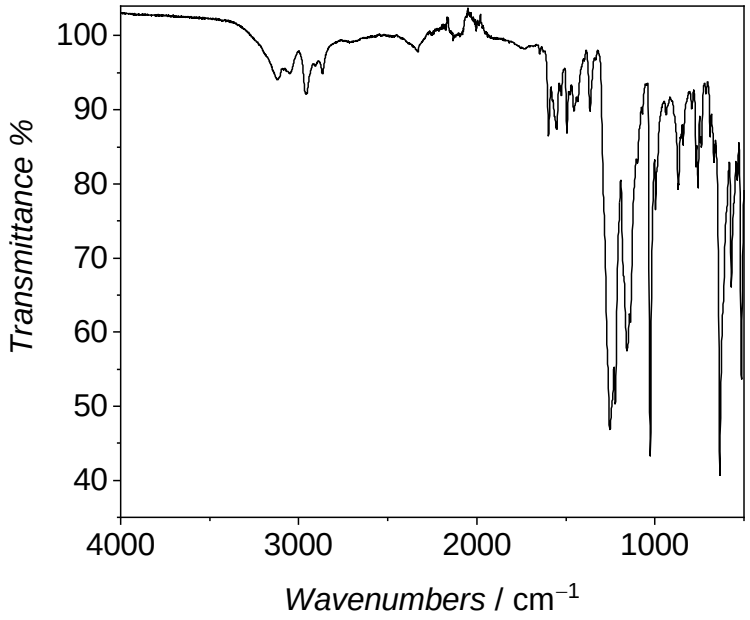

Figure 162. ATR-IR spectrum of solid **11**.

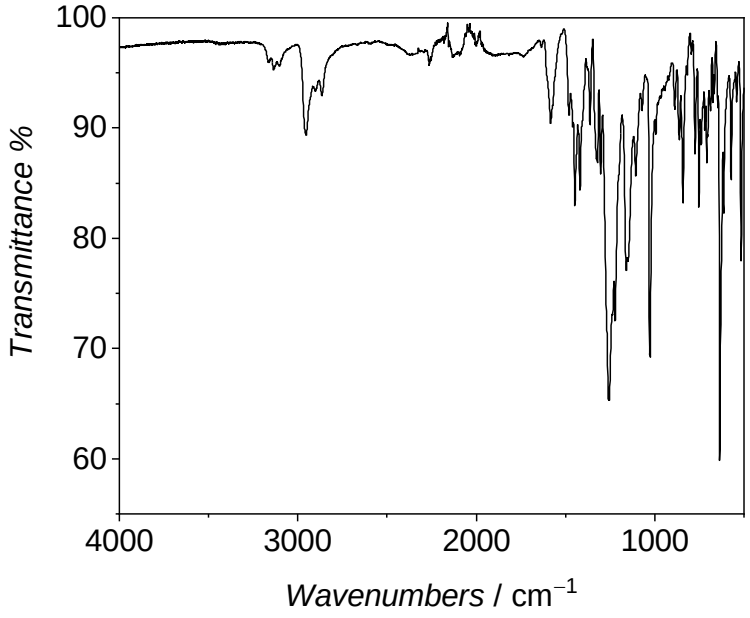

Figure 163. ATR-IR spectrum of solid **12a**.

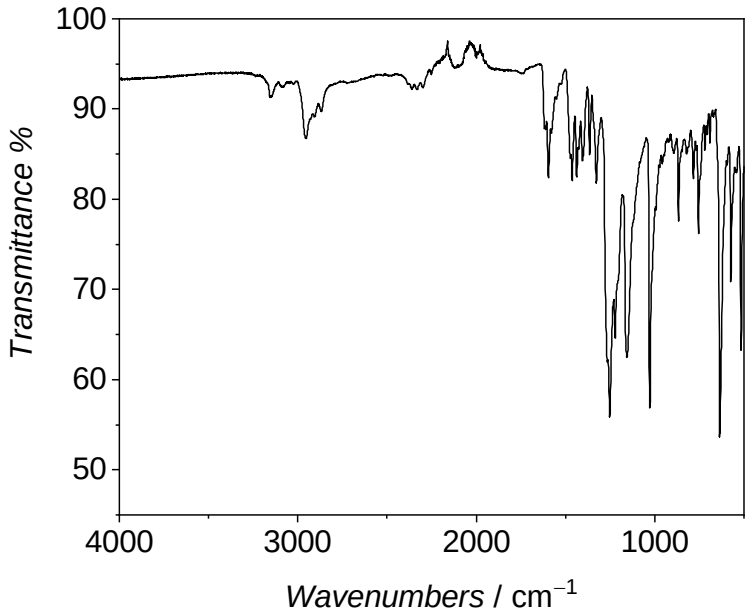

Figure 164. ATR-IR spectrum of solid **13a**.

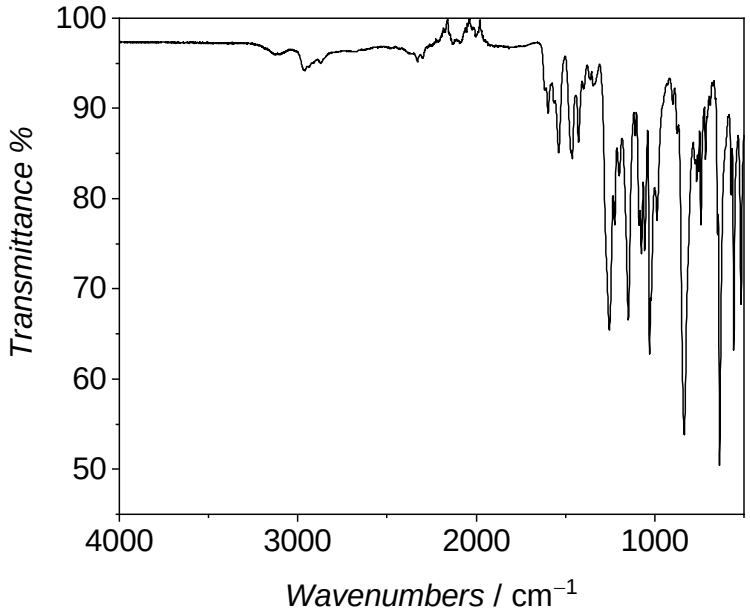

Figure 165. ATR-IR spectrum of solid **14a**.

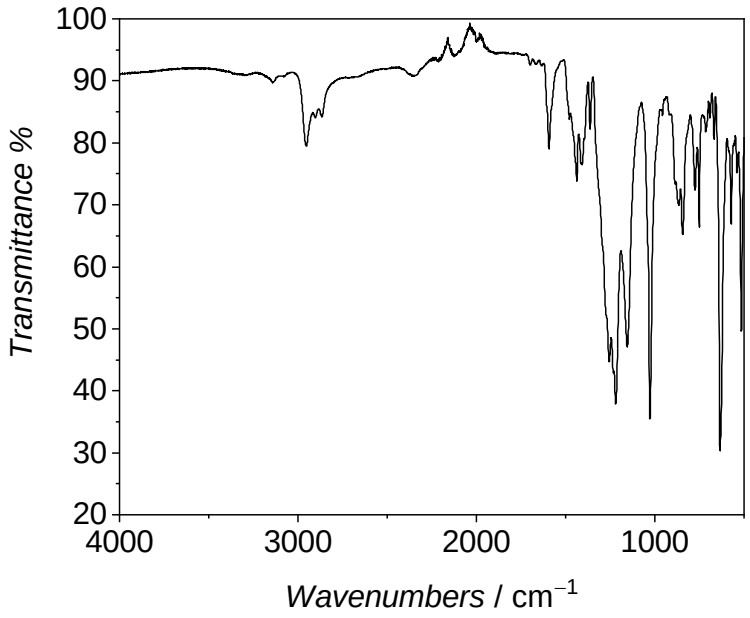

Figure 166. ATR-IR spectrum of solid **12b**.

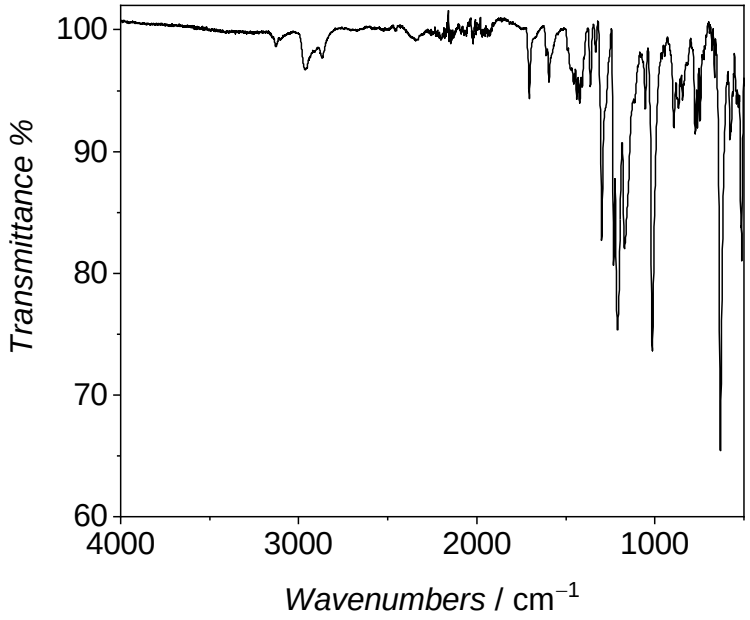

Figure 167. ATR-IR spectrum of solid **13b**.

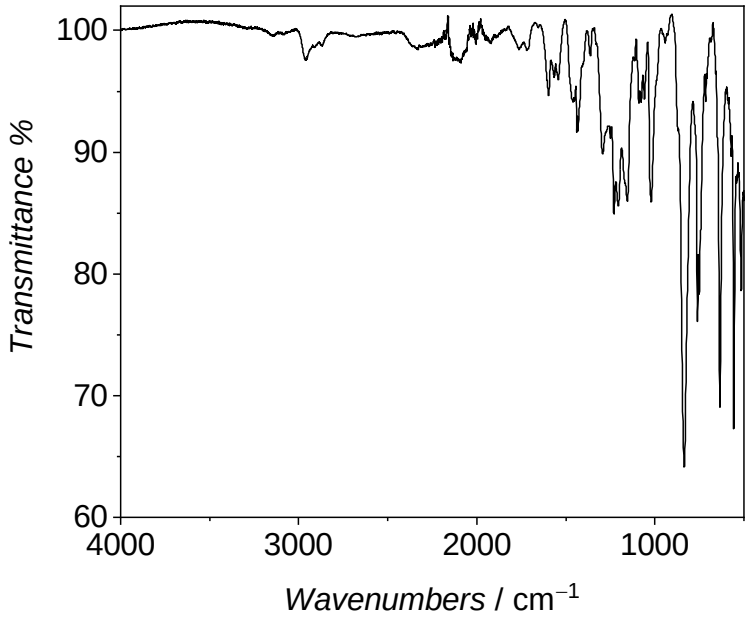

Figure 168. ATR-IR spectrum of solid **14b**.

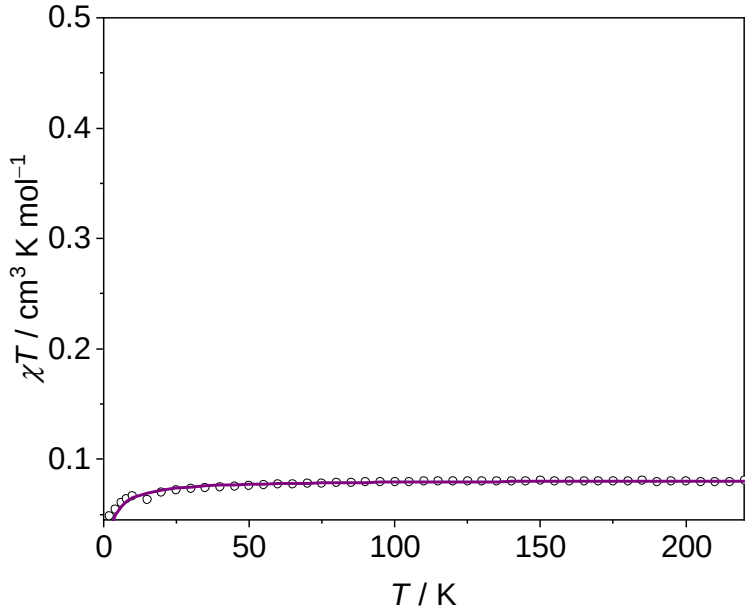

Figure 169. $\chi_m T$ *vs* T curves of a solid samples of **14a**. The empty circles represent experimental data, while the solid red line is a simulations taking in account the presence of 1.8 % of paramagnetic $S = 5/2$ impurity.

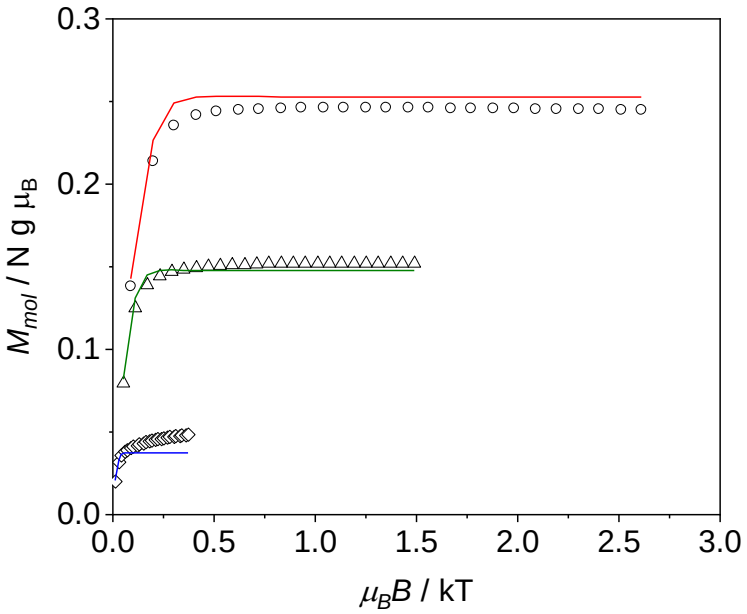

Figure 170. Variable temperature – variable field (VT-VH) magnetization measurements of a solid sample of **12b** at applied fields of 1.0 (diamonds and blue fit), 4.0 (triangles and green fit) and 7.0 T (circles and red fit).

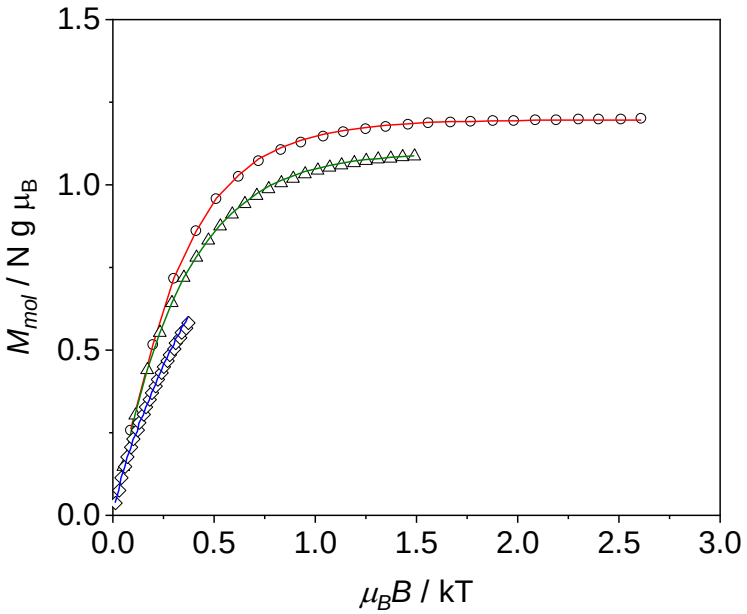

Figure 171. Variable temperature – variable field (VT-VH) magnetization measurements of a solid sample of **13b** at applied fields of 1.0 (diamonds and blue fit), 4.0 (triangles and green fit) and 7.0 T (circles and red fit).

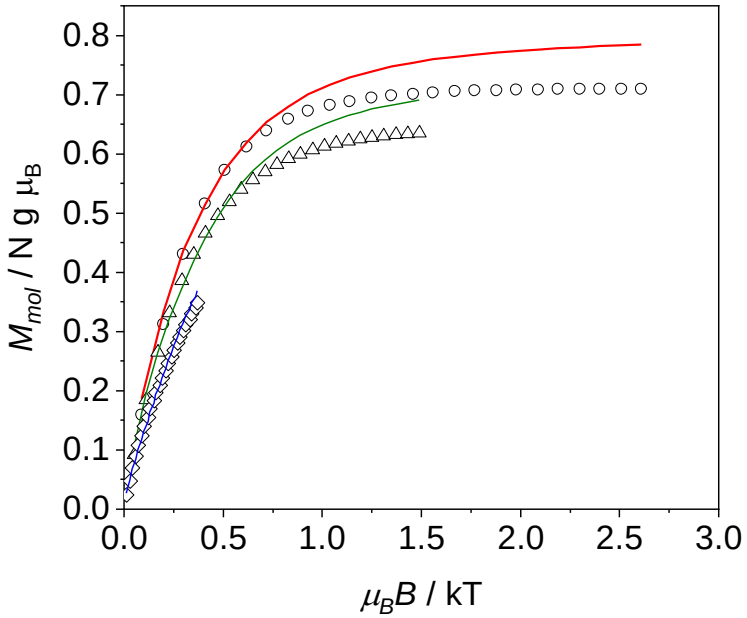

Figure 172. Variable temperature – variable field (VT-VH) magnetization measurements of a solid sample of **14b** at applied fields of 1.0 (diamonds and blue fit), 4.0 (triangles and green fit) and 7.0 T (circles and red fit).

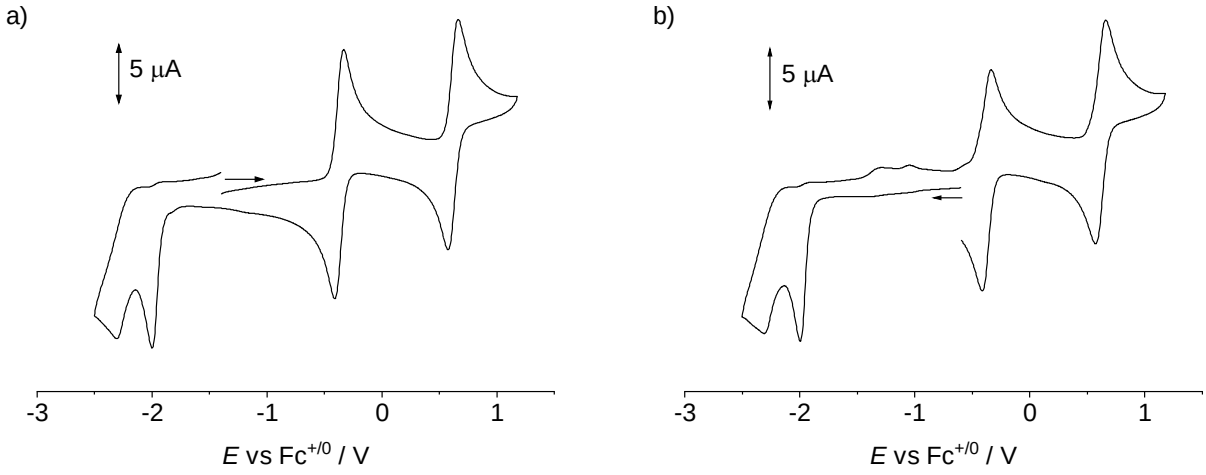

Figure 173. Cyclic voltammograms of a 1 mM CH_3CN solution of crystalline **12a**, in 0.1 M $^nBu_4NPF_6$ at RT. a) complete window scanned at 0.1 V/s starting from –1.4 V *vs* $Fc^{+/0}$ and scanning anodically first; b) complete window scanned at 0.1 V/s starting at the OCP and scanning cathodically first.

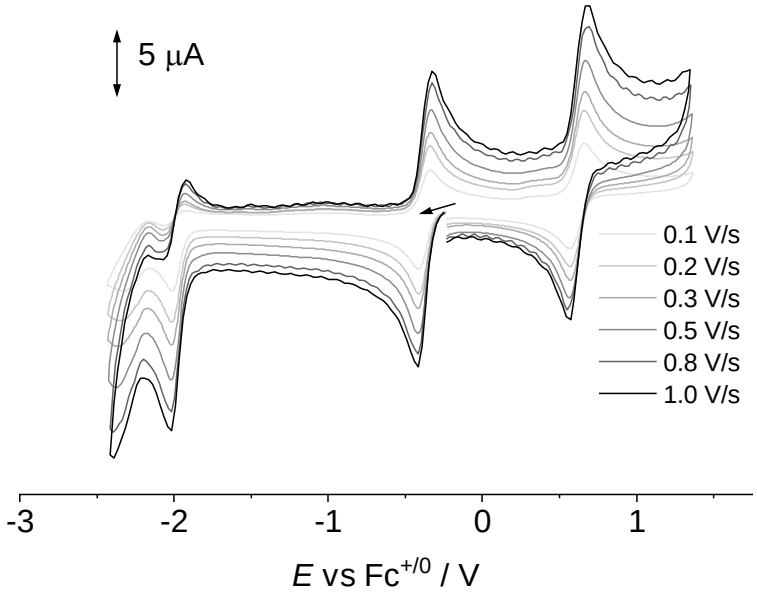

Figure 174. Cyclic voltammograms of a 1 mM CH_3CN solution of crystalline **13a** in 0.1 M $^nBu_4NPF_6$ at RT and their scan rate dependence. The measurements were started at the OCP and scanned cathodically first.

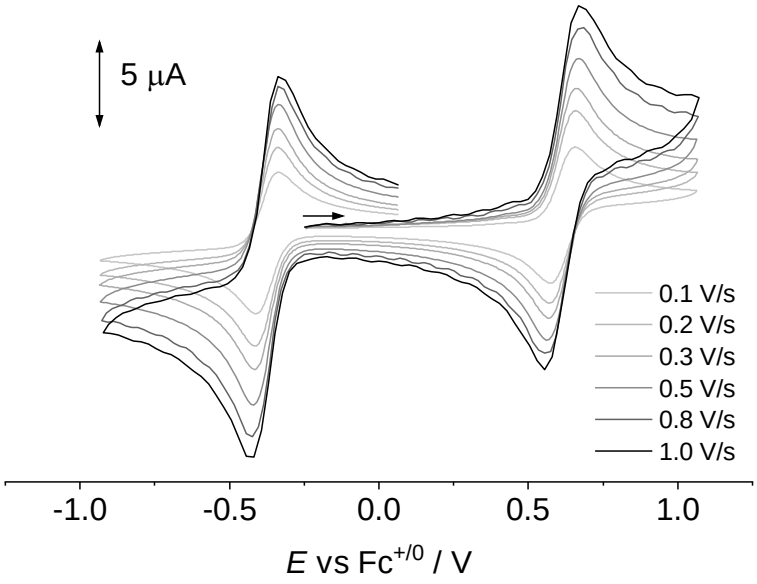

Figure 175. Cyclic voltammograms of a 1 mM CH_3CN solution of crystalline **13a**, in 0.1 M $^nBu_4NPF_6$ at RT and their scan rate dependence. The measurements were started at the OPC and scanned anodically first, extending the measurement beyond the first reduction.

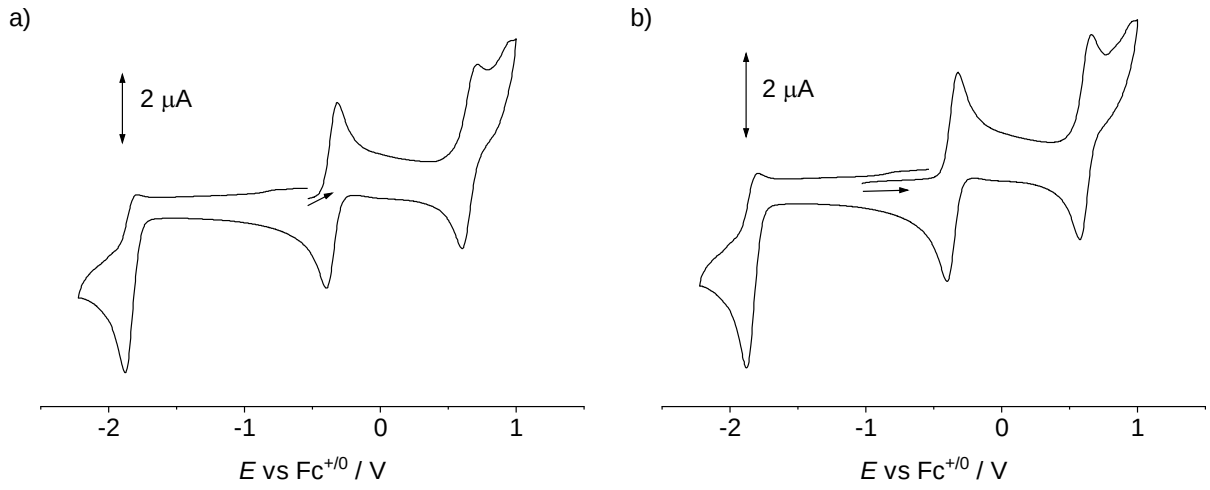

Figure 176. Cyclic voltammograms of a 1 mM THF solution of **12b**, in 0.2 M $^{n}Bu_4NPF_6$ at RT. a) complete window scanned at 0.1 V/s starting at OCP and scanning anodically first; b) complete window scanned at 0.1 V/s starting at −1.0 V and scanning anodically first.

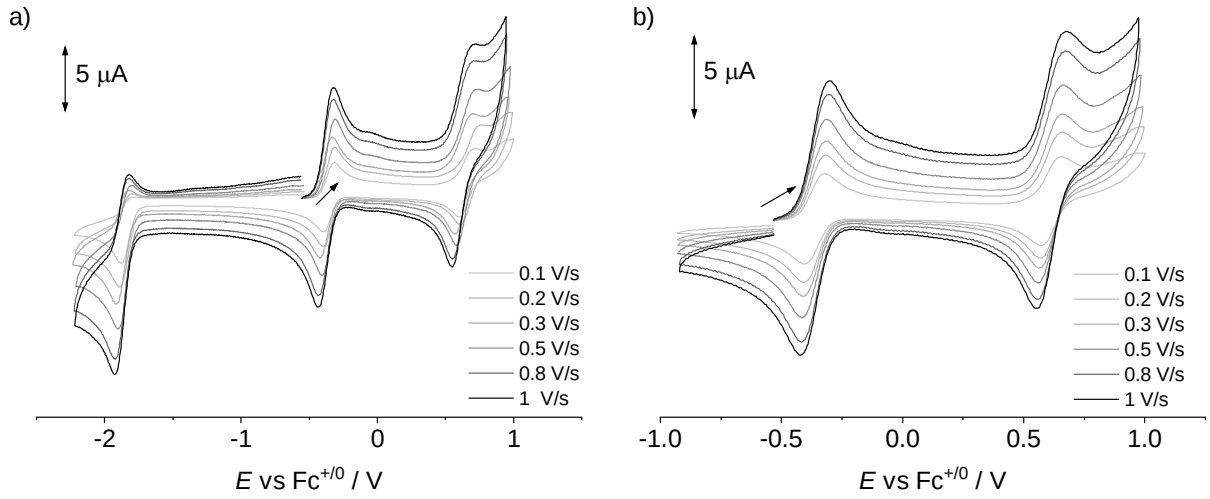

Figure 177. Cyclic voltammograms of a 1 mM THF solution of crystalline **12b** in 0.2 M $^{n}Bu_4NPF_6$ at RT and their scan rate dependence. a) complete window scanned starting from OCP; b) anodic portion only.

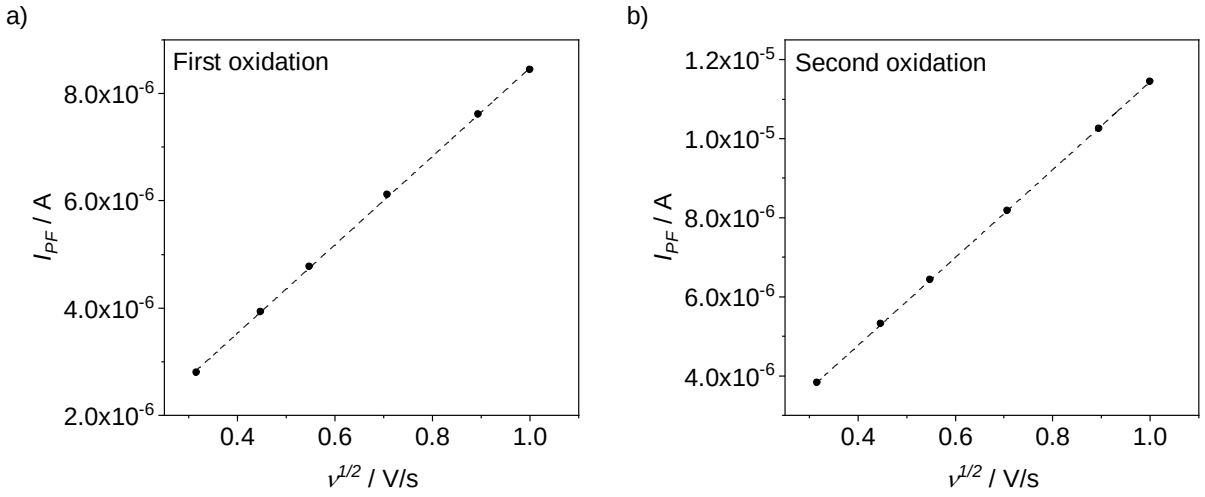

Figure 178. Plot and linear fit of the maximum of current intensity for the forward peak (I_{PF}) versus the square root of the scan rate ($\nu^{1/2}$) for the first (a) and second oxidation (b) of complex **12b**.

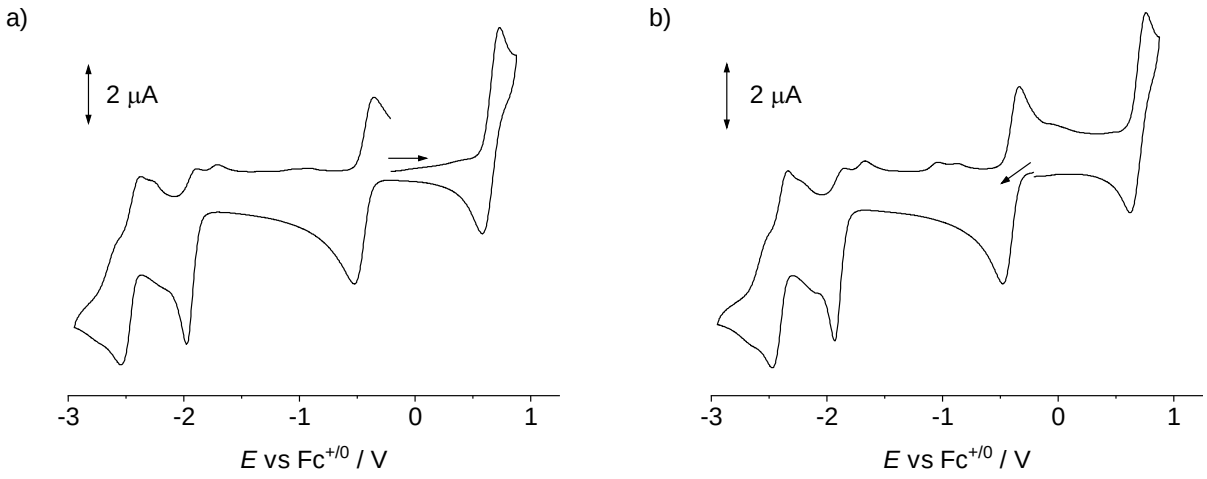

Figure 179. Cyclic voltammograms of a 1 mM acetone solution of crystalline **13b**, in 0.1 M $^{n}Bu_4NPF_6$ at RT. a) complete window scanned at 0.1 V/s starting from OCP and scanning anodically first; b) complete window scanned at 0.1 V/s starting at the OCP and scanning cathodically first.

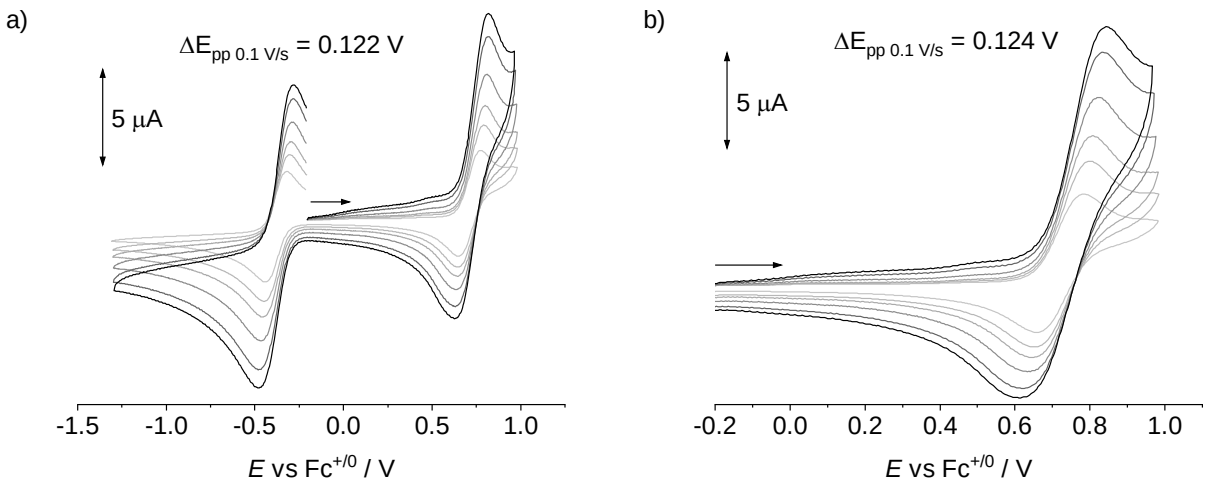

Figure 180. Cyclic voltammograms of a 1 mM acetone solution of crystalline **13b**, in 0.1 M $^{n}Bu_4NPF_6$ at room temperature and their scan rate dependence. a) the measurement was started at the OCP and scanned anodically first, extending the measurement beyond the first reduction.

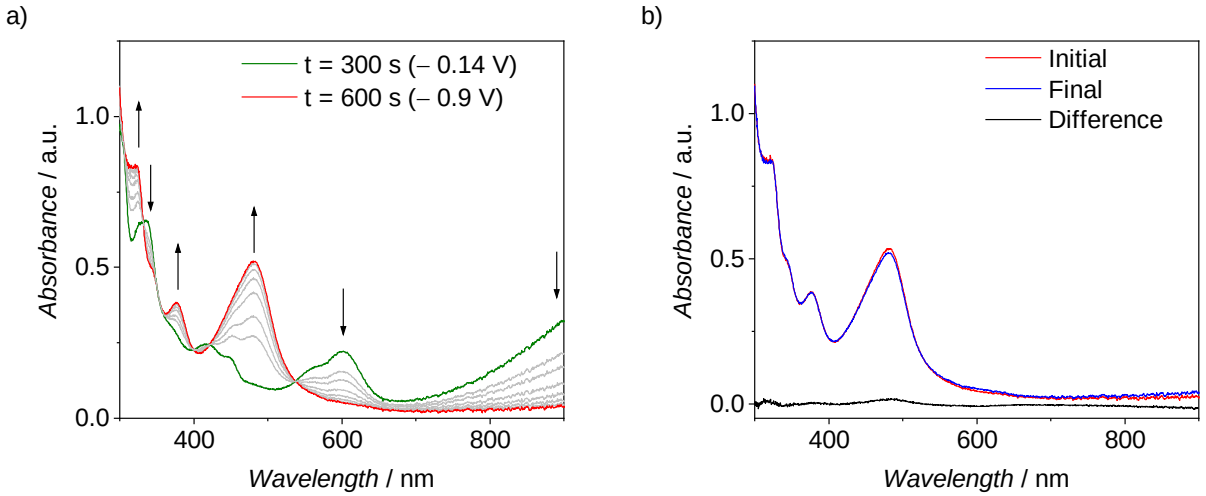

Figure 181. UV/Vis spectroelectrochemistry of a 1 mM solution of complex **12a** in CH_3CN with 0.1 M $^{n}Bu_4NPF_6$ as electrolyte at RT. a) re-reduction at an applied potential of –0.90 V *vs* $Fc^{+/0}$ (300 s), of the intermediate obtained oxidizing **12a** at –0.14 V for 300 s; b) overlap of the initial spectrum of **12a** with the final spectrum obtained at the end of the experiment (600 s).

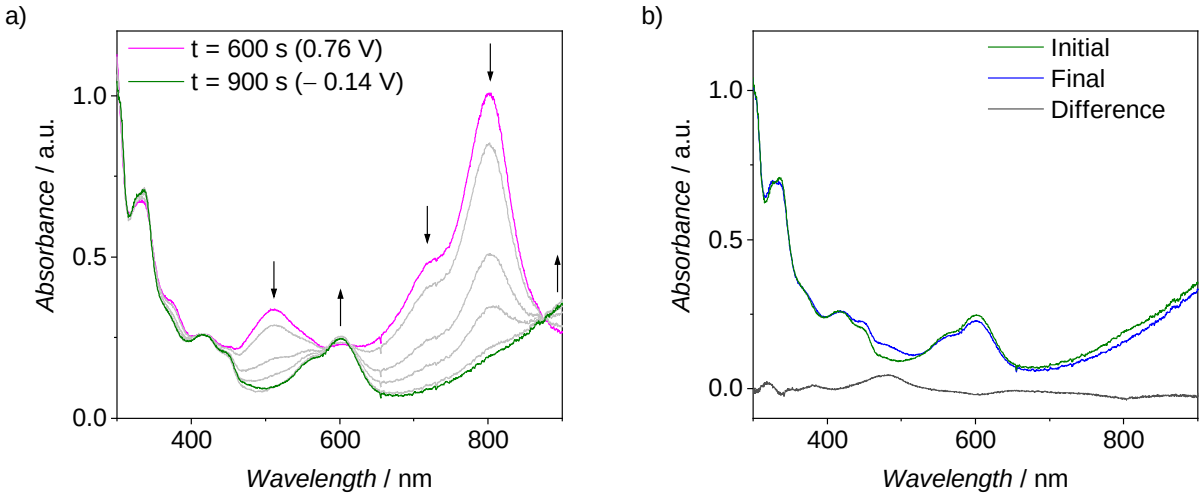

Figure 182. UV/Vis spectroelectrochemistry of a 1 mM solution of complex **12a** in CH_3CN with 0.1 M $^nBu_4NPF_6$ as electrolyte. a) re-reduction at an applied potential of –0.14 V *vs* $Fc^{+/0}$ (300 s), of the intermediate obtained oxidizing **12a** at –0.14 V for 300 seconds and applying a potential of 0.76 V for additional 300 s; b) overlap of the initial spectrum at 300 s with the final spectrum at 900 s obtained after re-reduction.

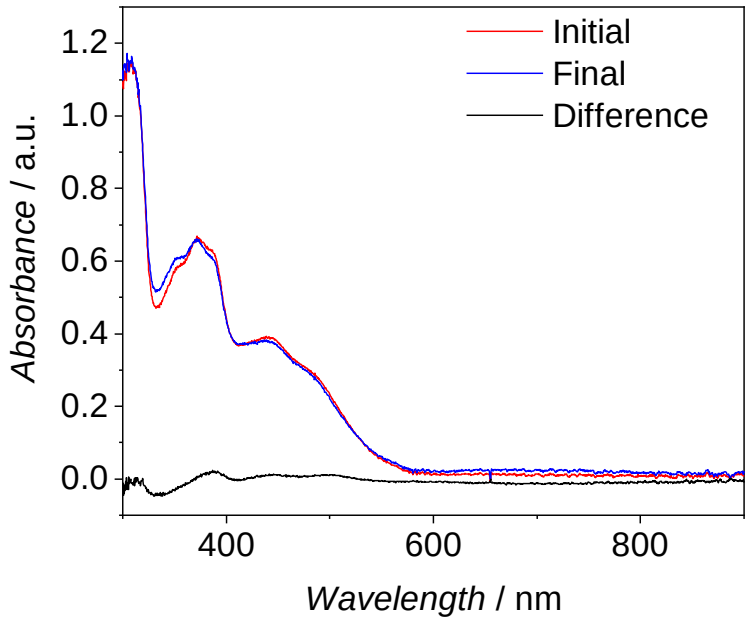

Figure 183. UV/Vis spectroelectrochemistry of a 1 mM solution of complex **12b** in THF with 0.2 M $^nBu_4NPF_6$ as electrolyte: overlap of the initial spectrum of **12b** with the final spectrum obtained after re-reduction of the product of the oxidation at –0.13 V vs $Fc^{+/0}$.

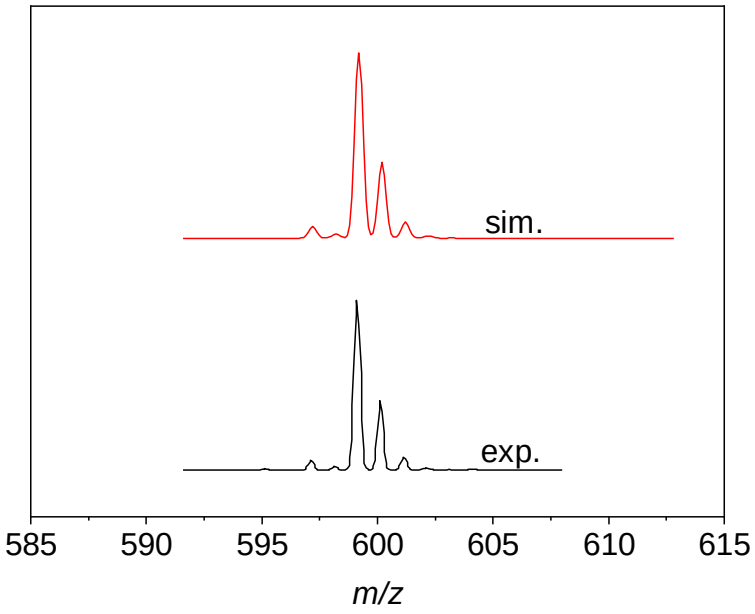

Figure 184. ESI(+)-MS of **15** in CH_3CN. Isotopic patterns of the experimental (top) and simulated (bottom) signal corresponding to [M-OTf] (*m/z* = 599).

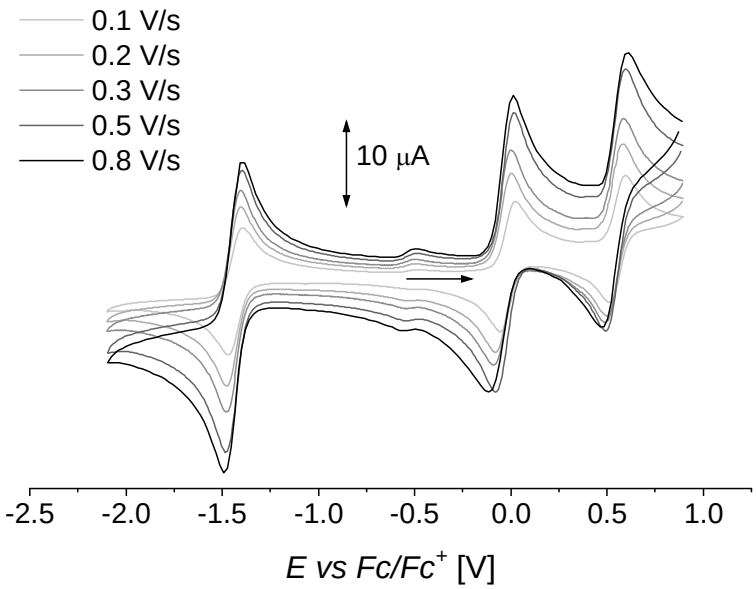

Figure 185. Cyclic voltammograms of a 1 mM CH_3CN solution of crystalline **15** in 0.1 M $^n Bu_4NPF_6$ at RT and their scan rate dependence. The measurements were started at the OCP and scanned anodically first.

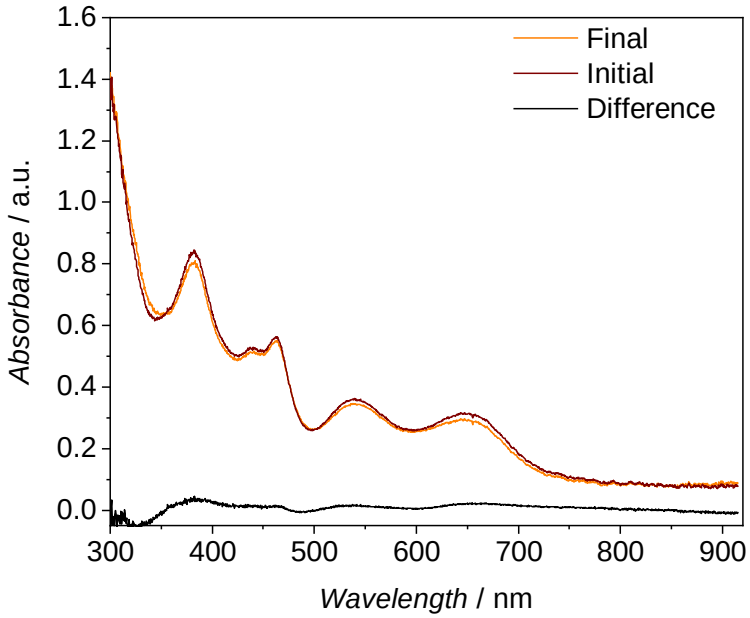

Figure 186. UV/Vis spectroelectrochemistry of a 1 mM solution of complex **15** in CH_3CN with 0.1 M $^nBu_4NPF_6$ as electrolyte: overlap of the initial spectrum of **15** with the final spectrum obtained after re-reduction of the product of the oxidation at 0.4 V vs $Fc^{+/0}$.

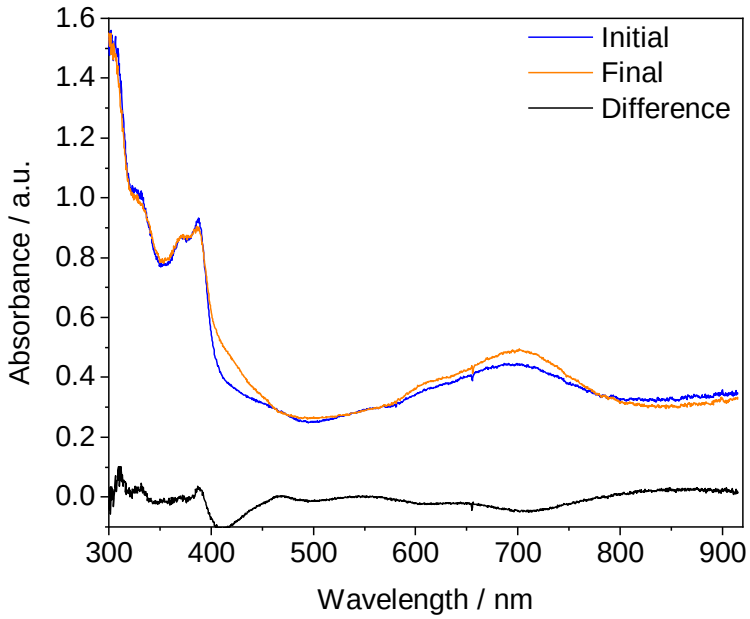

Figure 187. UV/Vis spectroelectrochemistry of a 1 mM solution of complex **15** in CH_3CN with 0.1 M $^nBu_4NPF_6$ as electrolyte: overlap of the initial spectrum obtained after oxidation at 1.1 V for 300 s (blue) with the final spectrum at obtained after re-reduction of the two-electron oxidized species.

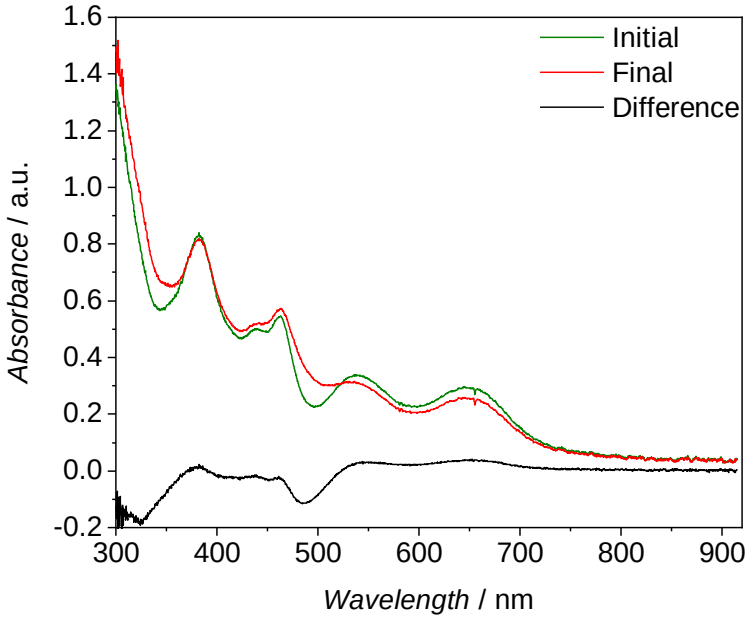

Figure 188. UV/Vis spectroelectrochemistry of a 1 mM solution of complex **15** in CH_3CN with 0.1 M $^nBu_4NPF_6$ as electrolyte: overlap of the initial spectrum of **15** with the final spectrum obtained after re-oxidation of the product of the reduction at −1.9 V vs $Fc^{+/0}$.

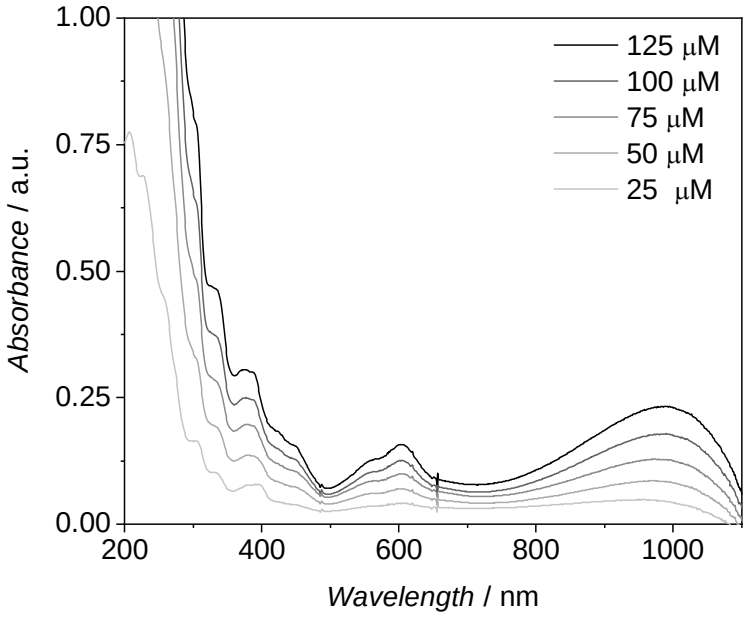

Figure 189. UV/Vis solution spectra of **16** in CH_3CN at different concentrations at room temperature.

Structures of Complexes

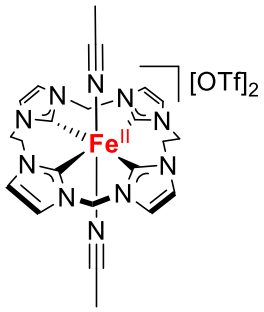

1

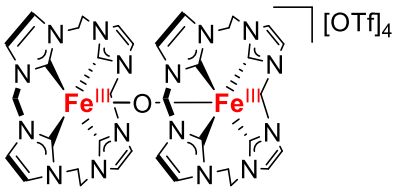

2

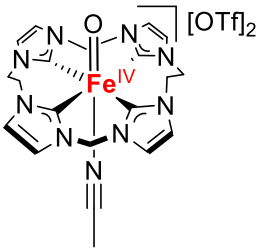

3

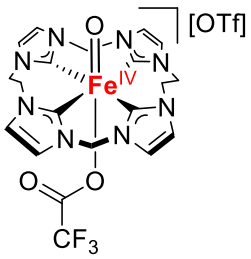

4

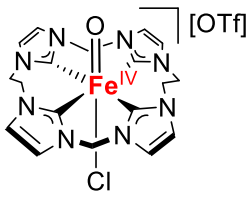

5

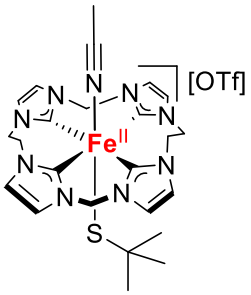

6

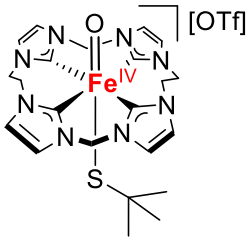

7

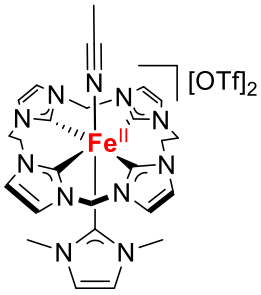

8

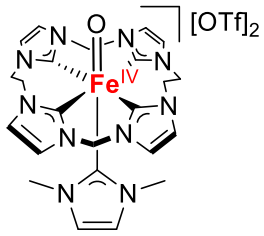

9

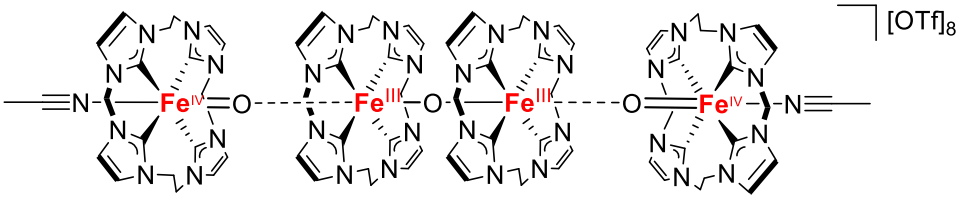

10

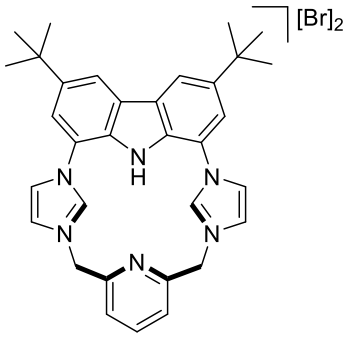

[11H$_3$][Br]$_2$

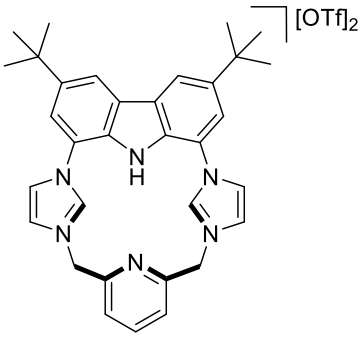

[11H$_3$][OTf]$_2$

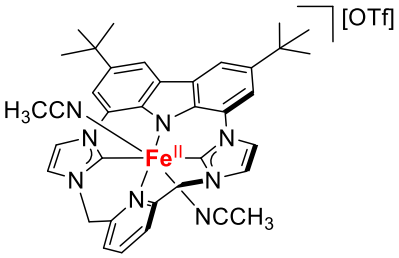

12a

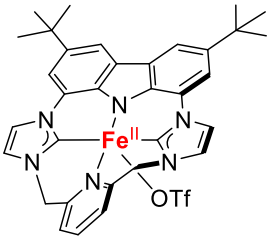

12b

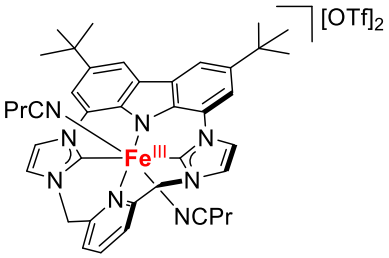

13a

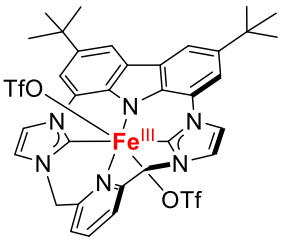

13b

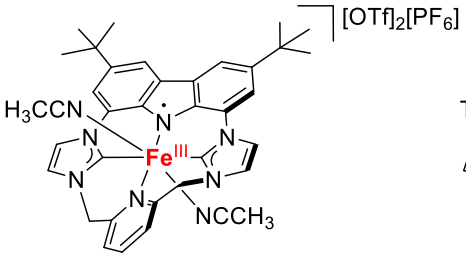

14a

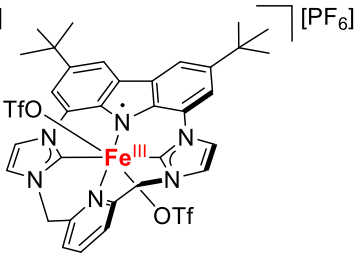

14b

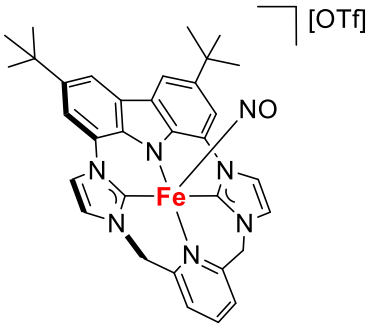
[OTf]
NO
N
N
Fe
N
N
N
N

15

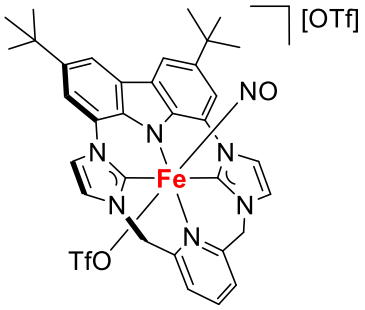
[OTf]
NO
N
N
Fe
N
N
N
TfO

16

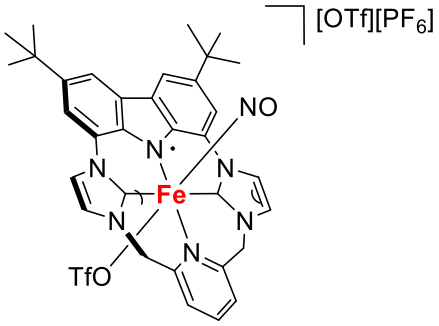
[OTf][PF6]
NO
N
N
Fe
N
N
N
TfO

17

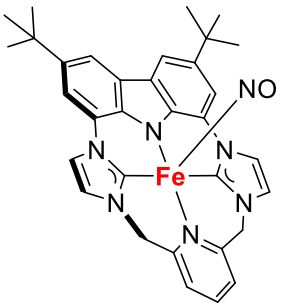
NO
N
N
Fe
N
N
N

18

List of Abbreviation

ATR	attenuated total reflection
BDE	bond dissociation energy
BS	broken symmetry
CHD	1,4-cyclohexadiene
CHN analysis	elemental analyses (carbon-hydrogen-nitrogen)
CID	collision-induced dissociation
COSY	correlation spectroscopy
CPCM	conductor-like polarizable continuum model
CT	charge transfer
CV	cyclic voltammetry
d	doublet (NMR)
DCM	dichloromethane CH_2Cl_2
DEPT-NMR	distortionless enhancement by polarization transfer NMR
DFB	1,2-difluorobenzene
DFT	density functional theory
DHA	9,10-dihydroanthracene
DMF	N,N-dimethylformamide
DMI	*N*,*N*-dimethylimidazol-e/-yl
DMSO	dimethylsulfoxide
DOSY	diffusion ordered spectroscopy
EA	elemental analysis
EPR	electron paramagnetic resonance
ESI	electron spray ionization
Et al.	*Et alia*
Et_2O	diethyl ether
$Fc^{+/0}$	ferrocenium/ferrocene
FT	Fourier transform
FT-ATR	Fourier transform attenuated total reflection
FT-ICR	Fourier-transform ion cyclotron resonance
GC	glassy carbon
HAA	hydrogen atom abstraction
HMBC	heteronuclear multiple bond correlation
HOMO	highest occupied molecular orbital
HSQC	heteronuclear single quantum coherence
IntS	intermediate-spin
^{i}Pr	isopropyl
IRPD	Infrared photodissociation
KIE	kinetic isotope effect
LMCT	ligand-to-metal charge transfer
LS	low-spin
LUMO	lowest unoccupied molecular orbital
m	multiplet (NMR), medium (IR)
m/z	mass per charge
MB	Mößbauer
MLCT	metal-to-ligand charge transfer
MS	mass spectrometry
NHC	*N*-heterocyclic carbene
NIR	near IR
NMR	nuclear magnetic resonance
NOESY	nuclear Overhauser enhancement spectroscopy
OAT	oxygen atom transfer
OCP	open circuit potential

OPO/POA	optic parameter oscillator/amplifier
OTf	trifluoromethanesulfonate
PI	paramagnetic impurity
ppm	parts per million
py	pyridine
RT	room temperature
S	spin
s	singlet (NMR), strong (IR)
SEC	spectroelectrochemistry
SOMO	singly occupied molecular orbital
sPhIO	2-(*tert*-butylsulfonyl)iodosobenzene
SQUID	superconducting quantum interference device
t	triplet (NMR)
^{t}Bu	*tert*-butyl
TDDFT	Temperature dependent DFT
THF	tetrahydrofuran
TIP	temperature-independent paramagnetism
TMC	tetramethylcyclam ligand
TMCS	tethered thiolate version of the TMC
UV/Vis/IR	ultraviolet/visible/infrared
VH	variable magnetic field
vs.	*versus*
VT	variable temperature
w	weak (IR)
XRD	X-ray diffraction
ZFS	zero-field splitting
ΔE_Q / QS	quadrupole splitting
δ / IS	isomer shift

References

[1] Sibly, R. M.; Hone, J.; Clutton–Brock, T. H.; Lutz, W.; Qiang, R. Determinants of human population growth. *Philosophical Transactions of the Royal Society of London. Series B: Biological Sciences* **2002**, *357* (1425), 1197–1210.

[2] Bongaarts, J. Human population growth and the demographic transition. *Philosophical Transactions of the Royal Society B: Biological Sciences* **2009**, *364* (1532), 2985–2990.

[3] Lee, J. Y.; Karlin, K. D. Elaboration of copper–oxygen mediated C–H activation chemistry in consideration of future fuel and feedstock generation. *Curr. Opin. Chem. Biol.* **2015**, *25*, 184–193.

[4] Kovaleva, E. G.; Lipscomb, J. D. Versatility of biological non-heme Fe(II) centers in oxygen activation reactions. *Nat. Chem. Biol.* **2008**, *4* (3), 186–193.

[5] Huang, X.; Groves, J. T. Oxygen Activation and Radical Transformations in Heme Proteins and Metalloporphyrins. *Chem. Rev.* **2018**, *118* (5), 2491–2553.

[6] Pau, M. Y. M.; Lipscomb, J. D.; Solomon, E. I. Substrate activation for O_2 reactions by oxidized metal centers in biology. *Proceedings of the National Academy of Sciences* **2007**, *104* (47), 18355.

[7] Groves, J. T. The bioinorganic chemistry of iron in oxygenases and supramolecular assemblies. *Proceedings of the National Academy of Sciences* **2003**, *100* (7), 3569.

[8] Groves, J. T. High-valent iron in chemical and biological oxidations. *J. Inorg. Biochem.* **2006**, *100* (4), 434–447.

[9] Sheng, Y.; Abreu, I. A.; Cabelli, D. E.; Maroney, M. J.; Miller, A.-F.; Teixeira, M.; Valentine, J. S. Superoxide Dismutases and Superoxide Reductases. *Chem. Rev.* **2014**, *114* (7), 3854–3918.

[10] Sahu, S.; Goldberg, D. P. Activation of Dioxygen by Iron and Manganese Complexes: A Heme and Nonheme Perspective. *J. Am. Chem. Soc.* **2016**, *138* (36), 11410–11428.

[11] Wood, P. M. The potential diagram for oxygen at pH 7. *Biochem J* **1988**, *253* (1), 287–289.

[12] Que, L. 60 years of dioxygen activation. *JBIC Journal of Biological Inorganic Chemistry* **2017**, *22* (2), 171–173.

[13] Nam, W. Dioxygen Activation by Metalloenzymes and Models. *Acc. Chem. Res.* **2007**, *40* (7), 465.

[14] Decker, A.; Solomon, E. I. Dioxygen activation by copper, heme and non-heme iron enzymes: comparison of electronic structures and reactivities. *Curr. Opin. Chem. Biol.* **2005**, *9* (2), 152–163.

[15] Fukuzumi, S.; Lee, Y.-M.; Nam, W. Mechanisms of Two-Electron versus Four-Electron Reduction of Dioxygen Catalyzed by Earth-Abundant Metal Complexes. *ChemCatChem* **2018**, *10* (1), 9–28.

[16] Zhang, W.; Lai, W.; Cao, R. Energy-Related Small Molecule Activation Reactions: Oxygen Reduction and Hydrogen and Oxygen Evolution Reactions Catalyzed by Porphyrin- and Corrole-Based Systems. *Chem. Rev.* **2017**, *117* (4), 3717–3797.

[17] Nastri, F.; Chino, M.; Maglio, O.; Bhagi-Damodaran, A.; Lu, Y.; Lombardi, A. Design and engineering of artificial oxygen-activating metalloenzymes. *Chem. Soc. Rev.* **2016**, *45* (18), 5020–5054.

[18] Hematian, S.; Garcia-Bosch, I.; Karlin, K. D. Synthetic Heme/Copper Assemblies: Toward an Understanding of Cytochrome c Oxidase Interactions with Dioxygen and Nitrogen Oxides. *Acc. Chem. Res.* **2015**, *48* (8), 2462–2474.

[19] Krebs, C.; Galonić Fujimori, D.; Walsh, C. T.; Bollinger, J. M. Non-Heme Fe(IV)–Oxo Intermediates. *Acc. Chem. Res.* **2007**, *40* (7), 484–492.

[20] Chakrabarty, S.; Austin, R. N.; Deng, D.; Groves, J. T.; Lipscomb, J. D. Radical Intermediates in Monooxygenase Reactions of Rieske Dioxygenases. *J. Am. Chem. Soc.* **2007**, *129* (12), 3514–3515.

[21] Fujii, H. Electronic structure and reactivity of high-valent oxo iron porphyrins. *Coord. Chem. Rev.* **2002**, *226* (1), 51–60.

[22] Groves, J. T.; Haushalter, R. C.; Nakamura, M.; Nemo, T. E.; Evans, B. J. High-valent iron-porphyrin complexes related to peroxidase and cytochrome P-450. *J. Am. Chem. Soc.* **1981**, *103* (10), 2884–2886.

[23] Tinberg, C. E.; Lippard, S. J. Dioxygen Activation in Soluble Methane Monooxygenase. *Acc. Chem. Res.* **2011**, *44* (4), 280–288.

[24] Ray, K.; Pfaff, F. F.; Wang, B.; Nam, W. Status of Reactive Non-Heme Metal–Oxygen Intermediates in Chemical and Enzymatic Reactions. *J. Am. Chem. Soc.* **2014**, *136* (40), 13942–13958.

[25] Larson, V. A.; Battistella, B.; Ray, K.; Lehnert, N.; Nam, W. Iron and manganese oxo complexes, oxo wall and beyond. *Nat. Rev. Chem.* **2020**, *4* (8), 404–419.

[26] Hohenberger, J.; Ray, K.; Meyer, K. The biology and chemistry of high-valent iron–oxo and iron–nitrido complexes. *Nat. Commun.* **2012**, *3* (1), 720.

[27] Guo, M.; Corona, T.; Ray, K.; Nam, W. Heme and Nonheme High-Valent Iron and Manganese Oxo Cores in Biological and Abiological Oxidation Reactions. *ACS Cent. Sci.* **2019**, *5* (1), 13–28.

[28] Frey, P. A.; Reed, G. H. The Ubiquity of Iron. *ACS Chem. Biol.* **2012**, *7* (9), 1477–1481.

[29] Costas, M.; Mehn, M. P.; Jensen, M. P.; Que, L. Dioxygen Activation at Mononuclear Nonheme Iron Active Sites: Enzymes, Models, and Intermediates. *Chem. Rev.* **2004**, *104* (2), 939–986.

[30] Abu-Omar, M. M.; Loaiza, A.; Hontzeas, N. Reaction Mechanisms of Mononuclear Non-Heme Iron Oxygenases. *Chem. Rev.* **2005**, *105* (6), 2227–2252.

[31] Solomon, E. I.; Brunold, T. C.; Davis, M. I.; Kemsley, J. N.; Lee, S.-K.; Lehnert, N.; Neese, F.; Skulan, A. J.; Yang, Y.-S.; Zhou, J. Geometric and Electronic Structure/Function Correlations in Non-Heme Iron Enzymes. *Chem. Rev.* **2000**, *100* (1), 235–350.

[32] Solomon, E. I.; Light, K. M.; Liu, L. V.; Srnec, M.; Wong, S. D. Geometric and Electronic Structure Contributions to Function in Non-heme Iron Enzymes. *Acc. Chem. Res.* **2013**, *46* (11), 2725–2739.

[33] Friedle, S.; Reisner, E.; Lippard, S. J. Current challenges of modeling diiron enzyme active sites for dioxygen activation by biomimetic synthetic complexes. *Chem. Soc. Rev.* **2010**, *39* (8), 2768–2779.

[34] Schulz, C. E.; Castillo, R. G.; Pantazis, D. A.; DeBeer, S.; Neese, F. Structure–Spectroscopy Correlations for Intermediate Q of Soluble Methane Monooxygenase: Insights from QM/MM Calculations. *J. Am. Chem. Soc.* **2021**, *143* (17), 6560–6577.

[35] Brazeau, B. J.; Austin, R. N.; Tarr, C.; Groves, J. T.; Lipscomb, J. D. Intermediate Q from Soluble Methane Monooxygenase Hydroxylates the Mechanistic Substrate Probe Norcarane: Evidence for a Stepwise Reaction. *J. Am. Chem. Soc.* **2001**, *123* (48), 11831–11837.

[36] Banerjee, R.; Jones, J. C.; Lipscomb, J. D. Soluble Methane Monooxygenase. *Annu. Rev. Biochem.* **2019**, *88* (1), 409–431.

[37] Ray, K.; Heims, F.; Pfaff, F. F. Terminal Oxo and Imido Transition-Metal Complexes of Groups 9–11. *Eur. J. Inorg. Chem.* **2013**, *2013* (22-23), 3784–3807.

[38] Smith, V. H.; Schaefer, H. F.; Morokuma, K., Eds. *Applied Quantum Chemistry*; Springer Netherlands, 1986.

[39] Jung, C. The mystery of cytochrome P450 Compound I: A mini-review dedicated to Klaus Ruckpaul. *Biochimica et Biophysica Acta (BBA) - Proteins and Proteomics* **2011**, *1814* (1), 46–57.

[40] Hersleth, H.-P.; Ryde, U.; Rydberg, P.; Görbitz, C. H.; Andersson, K. K. Structures of the high-valent metal-ion haem–oxygen intermediates in peroxidases, oxygenases and catalases. *J. Inorg. Biochem.* **2006**, *100* (4), 460–476.

[41] Roach, P. L.; Clifton, I. J.; Hensgens, C. M. H.; Shibata, N.; Schofield, C. J.; Hajdu, J.; Baldwin, J. E. Structure of isopenicillinN synthase complexed with substrate and the mechanism ofpenicillin formation. *Nature* **1997**, *387* (6635), 827–830.

[42] Price, J. C.; Barr, E. W.; Tirupati, B.; Bollinger,, J. Martin; Krebs, C. The First Direct Characterization of a High-Valent Iron Intermediate in the Reaction of an α-Ketoglutarate-Dependent Dioxygenase: A High-Spin Fe(IV) Complex in Taurine/α-Ketoglutarate Dioxygenase (TauD) from Escherichia coli. *Biochemistry* **2003**, *42* (24), 7497–7508.

[43] Wackett, L. P. Mechanism and applications of Rieske non-heme iron dioxygenases. *Enzyme Microb. Technol.* **2002**, *31* (5), 577–587.

[44] Bugg, T. D. H.; Ramaswamy, S. Non-heme iron-dependent dioxygenases: unravelling catalytic mechanisms for complex enzymatic oxidations. *Curr. Opin. Chem. Biol.* **2008**, *12* (2), 134–140.

[45] Barry, S. M.; Challis, G. L. Mechanism and Catalytic Diversity of Rieske Non-Heme Iron-Dependent Oxygenases. *ACS Catal.* **2013**, *3* (10), 2362–2370.

[46] Ferraro, D. J.; Gakhar, L.; Ramaswamy, S. Rieske business: Structure–function of Rieske non-heme oxygenases. *Biochem. Biophys. Res. Commun.* **2005**, *338* (1), 175–190.

[47] Huang, X.; Groves, J. T. Beyond ferryl-mediated hydroxylation: 40 years of the rebound mechanism and C–H activation. *JBIC Journal of Biological Inorganic Chemistry* **2017**, *22* (2), 185–207.

[48] Rittle, J.; Green, M. T. Cytochrome P450 Compound I: Capture, Characterization, and C–H Bond Activation Kinetics. *Science* **2010**, *330* (6006), 933.

[49] Krest, C. M.; Onderko, E. L.; Yosca, T. H.; Calixto, J. C.; Karp, R. F.; Livada, J.; Rittle, J.; Green, M. T. Reactive Intermediates in Cytochrome P450 Catalysis*. *J. Biol. Chem.* **2013**, *288* (24), 17074–17081.

[50] Krest, C. M.; Silakov, A.; Rittle, J.; Yosca, T. H.; Onderko, E. L.; Calixto, J. C.; Green, M. T. Significantly shorter Fe–S bond in cytochrome P450-I is consistent with greater reactivity relative to chloroperoxidase. *Nat. Chem.* **2015**, *7* (9), 696–702.

[51] Yosca, T. H.; Green, M. T. Preparation of Compound I in P450cam: The Prototypical P450. *Isr. J. Chem.* **2016**, *56* (9-10), 834–840.

[52] Groves, J. T.; van der Puy, M. Stereospecific aliphatic hydroxylation by iron-hydrogen peroxide. Evidence for a stepwise process. *J. Am. Chem. Soc.* **1976**, *98* (17), 5290–5297.

[53] Groves, J. T.; McClusky, G. A.; White, R. E.; Coon, M. J. Aliphatic hydroxylation by highly purified liver microsomal cytochrome P-450. Evidence for a carbon radical intermediate. *Biochem. Biophys. Res. Commun.* **1978**, *81* (1), 154–160.

[54] Groves, J. T.; McClusky, G. A. Aliphatic hydroxylation via oxygen rebound. Oxygen transfer catalyzed by iron. *J. Am. Chem. Soc.* **1976**, *98* (3), 859–861.

[55] Green, M. T.; Dawson, J. H.; Gray, H. B. Oxoiron(IV) in Chloroperoxidase Compound II Is Basic: Implications for P450 Chemistry. *Science* **2004**, *304* (5677), 1653.

[56] Behan, R. K.; Green, M. T. On the status of ferryl protonation. *J. Inorg. Biochem.* **2006**, *100* (4), 448–459.

[57] Yosca, T. H.; Rittle, J.; Krest, C. M.; Onderko, E. L.; Silakov, A.; Calixto, J. C.; Behan, R. K.; Green, M. T. Iron(IV)hydroxide pKa; and the Role of Thiolate Ligation in C–H Bond Activation by Cytochrome P450. *Science* **2013**, *342* (6160), 825.

[58] Bordwell, F. G. Equilibrium acidities in dimethyl sulfoxide solution. *Acc. Chem. Res.* **1988**, *21* (12), 456–463.

[59] Janousek, B. K.; Reed, K. J.; Brauman, J. I. Electron photodetachment from mercaptyl anions (RS^-). Electron affinities of mercaptyl radicals and the sulfur-hydrogen bond strength in mercaptans. *J. Am. Chem. Soc.* **1980**, *102* (9), 3125–3129.

[60] Green, M. T. C–H bond activation in heme proteins: the role of thiolate ligation in cytochrome P450. *Curr. Opin. Chem. Biol.* **2009**, *13* (1), 84–88.

[61] Stone, K. L.; Hoffart, L. M.; Behan, R. K.; Krebs, C.; Green, M. T. Evidence for Two Ferryl Species in Chloroperoxidase Compound II. *J. Am. Chem. Soc.* **2006**, *128* (18), 6147–6153.

[62] Stone, K. L.; Behan, R. K.; Green, M. T. Resonance Raman spectroscopy of chloroperoxidase compound II provides direct evidence for the existence of an iron(IV)–hydroxide. *Proceedings of the National Academy of Sciences* **2006**, *103* (33), 12307.

[63] Behan, R. K.; Hoffart, L. M.; Stone, K. L.; Krebs, C.; Green, M. T. Evidence for Basic Ferryls in Cytochromes P450. *J. Am. Chem. Soc.* **2006**, *128* (35), 11471–11474.

[64] Groves, J. T. Using push to get pull. *Nat. Chem.* **2014**, *6* (2), 89–91.

[65] Penner-Hahn, J. E.; McMurry, T. J.; Renner, M.; Latos-Grazynsky, L.; Eble, K. S.; Davis, I. M.; Balch, A. L.; Groves, J. T.; Dawson, J. H.; Hodgson, K. O. X-ray absorption spectroscopic studies of high valent iron porphyrins. Horseradish peroxidase compounds I and II and synthetic models. *J. Biol. Chem.* **1983**, *258* (21), 12761–12764.

[66] Costas, M. Selective C–H oxidation catalyzed by metalloporphyrins. *Coord. Chem. Rev.* **2011**, *255* (23), 2912–2932.

[67] Boso, B.; Lang, G.; McMurry, T. J.; Groves, J. T. Mössbauer effect study of tight spin coupling in oxidized chloro-5,10,15,20-tetra(mesityl)porphyrinatoiron(III). *The Journal of Chemical Physics* **1983**, *79* (3), 1122–1126.

[68] Schröder, D.; Shaik, S.; Schwarz, H. Two-State Reactivity as a New Concept in Organometallic Chemistry. *Acc. Chem. Res.* **2000**, *33* (3), 139–145.

[69] Shaik, S.; Visser, S. P. de; Ogliaro, F.; Schwarz, H.; Schröder, D. Two-state reactivity mechanisms of hydroxylation and epoxidation by cytochrome P-450 revealed by theory. *Curr. Opin. Chem. Biol.* **2002**, *6* (5), 556–567.

[70] Shaik, S.; Kumar, D.; Visser, S. P. de; Altun, A.; Thiel, W. Theoretical Perspective on the Structure and Mechanism of Cytochrome P450 Enzymes. *Chem. Rev.* **2005**, *105* (6), 2279–2328.

[71] Kang, Y.; Chen, H.; Jeong, Y. J.; Lai, W.; Bae, E. H.; Shaik, S.; Nam, W. Enhanced Reactivities of Iron(IV)-Oxo Porphyrin π-Cation Radicals in Oxygenation Reactions by Electron-Donating Axial Ligands. *Chemistry – A European Journal* **2009**, *15* (39), 10039–10046.

[72] Takahashi, A.; Kurahashi, T.; Fujii, H. Redox Potentials of Oxoiron(IV) Porphyrin π-Cation Radical Complexes: Participation of Electron Transfer Process in Oxygenation Reactions. *Inorg. Chem.* **2011**, *50* (15), 6922–6928.

[73] Takahashi, A.; Yamaki, D.; Ikemura, K.; Kurahashi, T.; Ogura, T.; Hada, M.; Fujii, H. Effect of the Axial Ligand on the Reactivity of the Oxoiron(IV) Porphyrin π-Cation Radical Complex: Higher Stabilization of the Product State Relative to the Reactant State. *Inorg. Chem.* **2012**, *51* (13), 7296–7305.

[74] Proshlyakov, D. A.; Henshaw, T. F.; Monterosso, G. R.; Ryle, M. J.; Hausinger, R. P. Direct Detection of Oxygen Intermediates in the Non-Heme Fe Enzyme Taurine/α-Ketoglutarate Dioxygenase. *J. Am. Chem. Soc.* **2004**, *126* (4), 1022–1023.

[75] Riggs-Gelasco, P. J.; Price, J. C.; Guyer, R. B.; Brehm, J. H.; Barr, E. W.; Bollinger, J. M.; Krebs, C. EXAFS Spectroscopic Evidence for an Fe═O Unit in the Fe(IV) Intermediate Observed during Oxygen Activation by Taurine:α-Ketoglutarate Dioxygenase. *J. Am. Chem. Soc.* **2004**, *126* (26), 8108–8109.

[76] Hoffart, L. M.; Barr, E. W.; Guyer, R. B.; Bollinger, J. M.; Krebs, C. Direct spectroscopic detection of a C–H-cleaving high-spin Fe(IV) complex in a prolyl-4-hydroxylase. *Proceedings of the National Academy of Sciences* **2006**, *103* (40), 14738.

[77] Wong, S. D.; Srnec, M.; Matthews, M. L.; Liu, L. V.; Kwak, Y.; Park, K.; Bell III, C. B.; Alp, E. E.; Zhao, J.; Yoda, Y.; Kitao, S.; Seto, M.; Krebs, C.; Bollinger, J. M.; Solomon, E. I. Elucidation of the Fe(IV)=O intermediate in the catalytic cycle of the halogenase SyrB2. *Nature* **2013**, *499* (7458), 320–323.

[78] Yan, W.; Song, H.; Song, F.; Guo, Y.; Wu, C.-H.; Sae Her, A.; Pu, Y.; Wang, S.; Naowarojna, N.; Weitz, A.; Hendrich, M. P.; Costello, C. E.; Zhang, L.; Liu, P.; Jessie Zhang, Y. Endoperoxide formation by an α-ketoglutarate-dependent mononuclear non-haem iron enzyme. *Nature* **2015**, *527* (7579), 539–543.

[79] Price, J. C.; Barr, E. W.; Glass, T. E.; Krebs, C.; Bollinger, J. M. Evidence for Hydrogen Abstraction from C1 of Taurine by the High-Spin Fe(IV) Intermediate Detected during Oxygen Activation by Taurine:α-Ketoglutarate Dioxygenase (TauD). *J. Am. Chem. Soc.* **2003**, *125* (43), 13008–13009.

[80] Mayer, J. M. Hydrogen Atom Abstraction by Metal−Oxo Complexes: Understanding the Analogy with Organic Radical Reactions. *Acc. Chem. Res.* **1998**, *31* (8), 441–450.

[81] Gardner, K. A.; Kuehnert, L. L.; Mayer, J. M. Hydrogen Atom Abstraction by Permanganate: Oxidations of Arylalkanes in Organic Solvents. *Inorg. Chem.* **1997**, *36* (10), 2069–2078.

[82] Engelmann, X.; Monte-Pérez, I.; Ray, K. Oxidation Reactions with Bioinspired Mononuclear Non-Heme Metal–Oxo Complexes. *Angew. Chem. Int. Ed.* **2016**, *55* (27), 7632–7649.

[83] Srnec, M.; Wong, S. D.; England, J.; Que, L.; Solomon, E. I. π-Frontier molecular orbitals in $S = 2$ ferryl species and elucidation of their contributions to reactivity. *Proceedings of the National Academy of Sciences* **2012**, *109* (36), 14326.

[84] Grapperhaus, C. A.; Mienert, B.; Bill, E.; Weyhermüller, T.; Wieghardt, K. Mononuclear (Nitrido)iron(V) and (Oxo)iron(IV) Complexes via Photolysis of [(cyclam-acetato)$Fe^{III}(N_3)$]+ and Ozonolysis of [(cyclam-acetato)$Fe^{III}(O_3SCF_3)$]+ in Water/Acetone Mixtures. *Inorg. Chem.* **2000**, *39* (23), 5306–5317.

[85] Rohde, J.-U.; In, J.-H.; Lim, M. H.; Brennessel, W. W.; Bukowski, M. R.; Stubna, A.; Münck, E.; Nam, W.; Que, L. Crystallographic and Spectroscopic Characterization of a Nonheme Fe(IV)=O Complex. *Science* **2003**, *299* (5609), 1037.

[86] Nam, W. Synthetic Mononuclear Nonheme Iron–Oxygen Intermediates. *Acc. Chem. Res.* **2015**, *48* (8), 2415–2423.

[87] Biswas, A. N.; Puri, M.; Meier, K. K.; Oloo, W. N.; Rohde, G. T.; Bominaar, E. L.; Münck, E.; Que, L. Modeling TauD-J: A High-Spin Nonheme Oxoiron(IV) Complex with High Reactivity toward C–H Bonds. *J. Am. Chem. Soc.* **2015**, *137* (7), 2428–2431.

[88] Puri, M.; Que, L. Toward the Synthesis of More Reactive *S* = 2 Non-Heme Oxoiron(IV) Complexes. *Acc. Chem. Res.* **2015**, *48* (8), 2443–2452.

[89] Bigi, J. P.; Harman, W. H.; Lassalle-Kaiser, B.; Robles, D. M.; Stich, T. A.; Yano, J.; Britt, R. D.; Chang, C. J. A High-Spin Iron(IV)–Oxo Complex Supported by a Trigonal Nonheme Pyrrolide Platform. *J. Am. Chem. Soc.* **2012**, *134* (3), 1536–1542.

[90] England, J.; Martinho, M.; Farquhar, E. R.; Frisch, J. R.; Bominaar, E. L.; Münck, E.; Que Jr., L. A Synthetic High-Spin Oxoiron(IV) Complex: Generation, Spectroscopic Characterization, and Reactivity. *Angew. Chem. Int. Ed.* **2009**, *48* (20), 3622–3626.

[91] Hirao, H.; Que Jr., L.; Nam, W.; Shaik, S. A Two-State Reactivity Rationale for Counterintuitive Axial Ligand Effects on the C–H Activation Reactivity of Nonheme Fe^{IV}–O Oxidants. *Chemistry – A European Journal* **2008**, *14* (6), 1740–1756.

[92] Srnec, M.; Wong, S. D.; Solomon, E. I. Excited state potential energy surfaces and their interactions in Fe^{IV}=O active sites. *Dalton Trans.* **2014**, *43* (47), 17567–17577.

[93] Decker, A.; Rohde, J.-U.; Klinker, E. J.; Wong, S. D.; Que,, Lawrence; Solomon, E. I. Spectroscopic and Quantum Chemical Studies on Low-Spin $Fe^{IV}O$ Complexes: Fe−O Bonding and Its Contributions to Reactivity. *J. Am. Chem. Soc.* **2007**, *129* (51), 15983–15996.

[94] Shaik, S.; Chen, H.; Janardanan, D. Exchange-enhanced reactivity in bond activation by metal–oxo enzymes and synthetic reagents. *Nat. Chem.* **2011**, *3* (1), 19–27.

[95] Hirao, H.; Kumar, D.; Que, L.; Shaik, S. Two-State Reactivity in Alkane Hydroxylation by Non-Heme Iron−Oxo Complexes. *J. Am. Chem. Soc.* **2006**, *128* (26), 8590–8606.

[96] Sastri, C. V.; Lee, J.; Oh, K.; Lee, Y. J.; Lee, J.; Jackson, T. A.; Ray, K.; Hirao, H.; Shin, W.; Halfen, J. A.; Kim, J.; Que, L.; Shaik, S.; Nam, W. Axial ligand tuning of a nonheme iron(IV)–oxo unit for hydrogen atom abstraction. *Proceedings of the National Academy of Sciences* **2007**, *104* (49), 19181.

[97] Jackson, T. A.; Rohde, J.-U.; Seo, M. S.; Sastri, C. V.; DeHont, R.; Stubna, A.; Ohta, T.; Kitagawa, T.; Münck, E.; Nam, W.; Que, L. Axial Ligand Effects on the Geometric and Electronic Structures of Nonheme Oxoiron(IV) Complexes. *J. Am. Chem. Soc.* **2008**, *130* (37), 12394–12407.

[98] England, J.; Bigelow, J. O.; van Heuvelen, K. M.; Farquhar, E. R.; Martinho, M.; Meier, K. K.; Frisch, J. R.; Münck, E.; Que, L. An ultra-stable oxoiron(IV) complex and its blue conjugate base. *Chem. Sci.* **2014**, *5* (3), 1204–1215.

[99] Kupper, C.; Mondal, B.; Serrano-Plana, J.; Klawitter, I.; Neese, F.; Costas, M.; Ye, S.; Meyer, F. Nonclassical Single-State Reactivity of an Oxo-Iron(IV) Complex Confined to Triplet Pathways. *J. Am. Chem. Soc.* **2017**, *139* (26), 8939–8949.

[100] Suzuki, N.; Higuchi, T.; Nagano, T. Multiple Active Intermediates in Oxidation Reaction Catalyzed by Synthetic Heme−Thiolate Complex Relevant to Cytochrome P450. *J. Am. Chem. Soc.* **2002**, *124* (32), 9622–9628.

[101] Bukowski, M. R.; Koehntop, K. D.; Stubna, A.; Bominaar, E. L.; Halfen, J. A.; Münck, E.; Nam, W.; Que, L. A Thiolate-Ligated Nonheme Oxoiron(IV) Complex Relevant to Cytochrome P450. *Science* **2005**, *310* (5750), 1000.

[102] Dedushko, M. A.; Pikul, J. H.; Kovacs, J. A. Superoxide Oxidation by a Thiolate-Ligated Iron Complex and Anion Inhibition. *Inorg. Chem.* **2021**.

[103] Gordon, J. B.; McGale, J. P.; Siegler, M. A.; Goldberg, D. P. Proton-Coupled Electron-Transfer Reactivity Controls Iron versus Sulfur Oxidation in Nonheme Iron–Thiolate Complexes. *Inorg. Chem.* **2021**, *60* (9), 6255–6265.

[104] McQuilken, A. C.; Jiang, Y.; Siegler, M. A.; Goldberg, D. P. Addition of Dioxygen to an N_4S(thiolate) Iron(II) Cysteine Dioxygenase Model Gives a Structurally Characterized Sulfinato–Iron(II) Complex. *J. Am. Chem. Soc.* **2012**, *134* (21), 8758–8761.

[105] Badiei, Y. M.; Siegler, M. A.; Goldberg, D. P. O2 Activation by Bis(imino)pyridine Iron(II)−Thiolate Complexes. *J. Am. Chem. Soc.* **2011**, *133* (5), 1274–1277.

[106] Jiang, Y.; Widger, L. R.; Kasper, G. D.; Siegler, M. A.; Goldberg, D. P. Iron(II)-Thiolate S-Oxygenation by O_2: Synthetic Models of Cysteine Dioxygenase. *J. Am. Chem. Soc.* **2010**, *132* (35), 12214–12215.

[107] McDonald, A. R.; Bukowski, M. R.; Farquhar, E. R.; Jackson, T. A.; Koehntop, K. D.; Seo, M. S.; Hont, R. F. de; Stubna, A.; Halfen, J. A.; Münck, E.; Nam, W.; Que, L. Sulfur versus Iron Oxidation in an Iron−Thiolate Model Complex. *J. Am. Chem. Soc.* **2010**, *132* (48), 17118–17129.

[108] Bass, H. M.; Cramer, S. A.; Price, J. L.; Jenkins, D. M. 18-Atom-Ringed Macrocyclic Tetra-imidazoliums for Preparation of Monomeric Tetra-carbene Complexes. *Organometallics* **2010**, *29* (15), 3235–3238.

[109] Meyer, S.; Klawitter, I.; Demeshko, S.; Bill, E.; Meyer, F. A Tetracarbene–Oxoiron(IV) Complex. *Angew. Chem. Int. Ed.* **2013**, *52* (3), 901–905.

[110] Ye, S.; Kupper, C.; Meyer, S.; Andris, E.; Navrátil, R.; Krahe, O.; Mondal, B.; Atanasov, M.; Bill, E.; Roithová, J.; Meyer, F.; Neese, F. Magnetic Circular Dichroism Evidence for an Unusual Electronic Structure of a Tetracarbene–Oxoiron(IV) Complex. *J. Am. Chem. Soc.* **2016**, *138* (43), 14312–14325.

[111] Orłowski, R.; Gryko, D.; Gryko, D. T. Synthesis of Corroles and Their Heteroanalogs. *Chem. Rev.* **2017**, *117* (4), 3102–3137.

[112] Anguera, G.; Sánchez-García, D. Porphycenes and Related Isomers: Synthetic Aspects. *Chem. Rev.* **2017**, *117* (4), 2481–2516.

[113] Chatterjee, T.; Shetti, V. S.; Sharma, R.; Ravikanth, M. Heteroatom-Containing Porphyrin Analogues. *Chem. Rev.* **2017**, *117* (4), 3254–3328.

[114] Lash, T. D. Carbaporphyrinoid Systems. *Chem. Rev.* **2017**, *117* (4), 2313–2446.

[115] Matano, Y. Synthesis of Aza-, Oxa-, and Thiaporphyrins and Related Compounds. *Chem. Rev.* **2017**, *117* (4), 3138–3191.

[116] Reddy, B. K.; Basavarajappa, A.; Ambhore, M. D.; Anand, V. G. Isophlorinoids: The Antiaromatic Congeners of Porphyrinoids. *Chem. Rev.* **2017**, *117* (4), 3420–3443.

[117] Shimizu, S. Recent Advances in Subporphyrins and Triphyrin Analogues: Contracted Porphyrins Comprising Three Pyrrole Rings. *Chem. Rev.* **2017**, *117* (4), 2730–2784.

[118] Furuta, H.; Asano, T.; Ogawa, T. "N-Confused Porphyrin": A New Isomer of Tetraphenylporphyrin. *J. Am. Chem. Soc.* **1994**, *116* (2), 767–768.

[119] Furuta, H.; Maeda, H.; Osuka, A. Doubly N-Confused Porphyrin: A New Complexing Agent Capable of Stabilizing Higher Oxidation States. *J. Am. Chem. Soc.* **2000**, *122* (5), 803–807.

[120] Furuta, H.; Ishizuka, T.; Osuka, A.; Ogawa, T. "N-Fused Porphyrin" from N-Confused Porphyrin. *J. Am. Chem. Soc.* **1999**, *121* (12), 2945–2946.

[121] Longevial, J.-F.; Rose, C.; Poyac, L.; Clément, S.; Richeter, S. Molecular Systems Combining Porphyrinoids and N-Heterocyclic Carbenes. *Eur. J. Inorg. Chem.* **2021**, *2021* (9), 776–791.

[122] Fei, F.; Lu, T.; Chen, X.-T.; Xue, Z.-L. Synthesis and structural characterization of metal complexes with macrocyclic tetracarbene ligands. *New J. Chem.* **2017**, *41* (22), 13442–13453.

[123] Hameury, S.; Frémont, P. de; Braunstein, P. Metal complexes with oxygen-functionalized NHC ligands: synthesis and applications. *Chem. Soc. Rev.* **2017**, *46* (3), 632–733.

[124] Benhamou, L.; Chardon, E.; Lavigne, G.; Bellemin-Laponnaz, S.; César, V. Synthetic routes to N-heterocyclic carbene precursors. *Chem. Rev.* **2011**, *111* (4), 2705–2733.

[125] Liu, B.; Zhang, Y.; Xu, D.; Chen, W. Facile synthesis of metal N-heterocyclic carbene complexes. *Chemical communications (Cambridge, England)* **2011**, *47* (10), 2883–2885.

[126] Liu, B.; Xia, Q.; Chen, W. Direct synthesis of iron, cobalt, nickel, and copper complexes of N-heterocyclic carbenes by using commercially available metal powders. *Angewandte Chemie (International ed. in English)* **2009**, *48* (30), 5513–5516.

[127] Kühl, O. The chemistry of functionalised N-heterocyclic carbenes. *Chem. Soc. Rev.* **2007**, *36* (4), 592–607.

[128] McGuinness, D. S.; Gibson, V. C.; Steed, J. W. Bis(carbene)pyridine Complexes of the Early to Middle Transition Metals: Survey of Ethylene Oligomerization and Polymerization Capability. *Organometallics* **2004**, *23* (26), 6288–6292.

[129] Simons, R. S.; Garrison, J. C.; Kofron, W. G.; Tessier, C. A.; Youngs, W. J. Synthesis and structural characterization of two bis-imidazolium-linked cyclophanes: precursors toward 'carbeneporphyrinoid' ligands. *Tetrahedron Lett.* **2002**, *43* (18), 3423–3425.

[130] Riener, K.; Haslinger, S.; Raba, A.; Högerl, M. P.; Cokoja, M.; Herrmann, W. A.; Kühn, F. E. Chemistry of iron N-heterocyclic carbene complexes: syntheses, structures, reactivities, and catalytic applications. *Chem. Rev.* **2014**, *114* (10), 5215–5272.

[131] Klawitter, I.; Anneser, M. R.; Dechert, S.; Meyer, S.; Demeshko, S.; Haslinger, S.; Pöthig, A.; Kühn, F. E.; Meyer, F. Iron Complexes of a Macrocyclic N-Heterocyclic Carbene/Pyridine Hybrid Ligand. *Organometallics* **2015**, *34* (12), 2819–2825.

[132] Liu, Y.; Resch, S. G.; Klawitter, I.; Cutsail III, G. E.; Demeshko, S.; Dechert, S.; Kühn, F. E.; DeBeer, S.; Meyer, F. An Adaptable N-Heterocyclic Carbene Macrocycle Hosting Copper in Three Oxidation States. *Angew. Chem. Int. Ed.* **2020**, *59* (14), 5696–5705.

[133] Maulbetsch, T.; Kunz, D. Carbenaporphyrins: No Longer Missing Ligands in N-Heterocyclic Carbene Chemistry. *Angew. Chem. Int. Ed.* **2021**, *60* (4), 2007–2012.

[134] Moser, M.; Wucher, B.; Kunz, D.; Rominger, F. 1,8-Bis(imidazolin-2-yliden-1-yl)carbazolide (bimca): A New CNC Pincer-Type Ligand with Strong Electron-Donating Properties. Facile Oxidative Addition of Methyl Iodide to Rh(bimca)(CO). *Organometallics* **2007**, *26* (4), 1024–1030.

[135] Jürgens, E.; Buys, K. N.; Schmidt, A.-T.; Furfari, S. K.; Cole, M. L.; Moser, M.; Rominger, F.; Kunz, D. Optimised synthesis of monoanionic bis(NHC)-pincer ligand precursors and their Li-complexes. *New J. Chem.* **2016**, *40* (11), 9160–9169.

[136] Maulbetsch, T.; Jürgens, E.; Kunz, D. Deoxygenation of Epoxides with Carbon Monoxide. *Chem. Eur. J.* **2020**, *26* (46), 10634–10640.

[137] Tian, Y.; Kunz, D. Nucleophilic Rh^{I} Catalyzed Selective Isomerization of Terminal Aziridines to Enamides. *ChemCatChem* **2020**, *12* (17), 4272–4275.

[138] Tian, Y.; Jürgens, E.; Mill, K.; Jordan, R.; Maulbetsch, T.; Kunz, D. Nucleophilic Isomerization of Epoxides by Pincer-Rhodium Catalysts: Activity Increase and Mechanistic Insights. *ChemCatChem* **2019**, *11* (16), 4028–4035.

[139] Tian, Y.; Jürgens, E.; Kunz, D. Regio- and chemoselective rearrangement of terminal epoxides into methyl alkyl and aryl ketones. *Chem. Commun.* **2018**, *54* (80), 11340–11343.

[140] Niwa, T.; Nakada, M. A non-heme iron(III) complex with porphyrin-like properties that catalyzes asymmetric epoxidation. *J. Am. Chem. Soc.* **2012**, *134* (33), 13538–13541.

[141] James F., A.; Lawrence L., C.; Robert F., I. Elecrochemical and Spectroscopic Properties of Cation Radicals III. Reaction Pathways of Carbazolium Radical Ions. *J. Electrochem. Soc.* **1975**, *122*, 876–893.

[142] Mössbauer, R. L. Kernresonanzfluoreszenz von Gammastrahlung in Ir191. *Z. Angew. Phys.* **1958**, *151* (2), 124–143.

[143] Gütlich, P.; Bill, E.; Trautwein, A. *Mössbauer spectroscopy and transition metal chemistry*:*Fundamentals and application*; Springer, 2011.

[144] Neese, F. Prediction and interpretation of the ^{57}Fe isomer shift in Mössbauer spectra by density functional theory. *Inorg. Chim. Acta* **2002**, *337*, 181–192.

[145] Ye, S.; Bill, E.; Neese, F. Electronic Structures of the $[Fe(N_2)(SiP^{i}Pr_3)]^{+1/0/-1}$ Electron Transfer Series: A Counterintuitive Correlation between Isomer Shifts and Oxidation States. *Inorg. Chem.* **2016**, *55* (7), 3468–3474.

[146] Claudia Kupper. Electronic Structure and Reactivity of Bioinspired Organometallic Iron Complexes Relevant to Small Molecule Activation, Georg-August Universität Göttingen, **2017**.

[147] Ehudin, M. A.; Gee, L. B.; Sabuncu, S.; Braun, A.; Moënne-Loccoz, P.; Hedman, B.; Hodgson, K. O.; Solomon, E. I.; Karlin, K. D. Tuning the Geometric and Electronic Structure of Synthetic High-Valent Heme Iron(IV)-Oxo Models in the Presence of a Lewis Acid and Various Axial Ligands. *J. Am. Chem. Soc.* **2019**, *141* (14), 5942–5960.

[148] Kumar, D.; Latifi, R.; Kumar, S.; Rybak-Akimova, E. V.; Sainna, M. A.; Visser, S. P. de. Rationalization of the Barrier Height for p-Z-styrene Epoxidation by Iron(IV)-Oxo Porphyrin Cation Radicals with Variable Axial Ligands. *Inorg. Chem.* **2013**, *52* (14), 7968–7979.

[149] Kumar, D.; Sastry, G. N.; Visser, S. P. de. Axial Ligand Effect On The Rate Constant of Aromatic Hydroxylation By Iron(IV)–Oxo Complexes Mimicking Cytochrome P450 Enzymes. *The Journal of Physical Chemistry B* **2012**, *116* (1), 718–730.

[150] Visser, S. P. de; Latifi, R.; Tahsini, L.; Nam, W. The Axial Ligand Effect on Aliphatic and Aromatic Hydroxylation by Non-heme Iron(IV)–oxo Biomimetic Complexes. *Chemistry – An Asian Journal* **2011**, *6* (2), 493–504.

[151] Visser, S. P. de; Tahsini, L.; Nam, W. How Does the Axial Ligand of Cytochrome P450 Biomimetics Influence the Regioselectivity of Aliphatic versus Aromatic Hydroxylation? *Chemistry – A European Journal* **2009**, *15* (22), 5577–5587.

[152] Rohde, J.-U.; Que Jr., L. Axial Coordination of Carboxylate Activates the Non-heme Fe^{IV}=O Unit. *Angew. Chem. Int. Ed.* **2005**, *44* (15), 2255–2258.

[153] Hsieh, C.-C.; Liu, Y.-C.; Tseng, M.-C.; Chiang, M.-H.; Horng, Y.-C. Dioxygen activation by a dinuclear thiolate-ligated Fe(II) complex. *Dalton Trans.* **2019**, *48* (2), 379–386.

[154] Fiedler, A. T.; Halfen, H. L.; Halfen, J. A.; Brunold, T. C. Synthesis, Structure Determination, and Spectroscopic/Computational Characterization of a Series of Fe(II)−Thiolate Model Complexes: Implications for Fe−S Bonding in Superoxide Reductases. *J. Am. Chem. Soc.* **2005**, *127* (6), 1675–1689.

[155] Zdilla, M. J.; Verma, A. K.; Lee, S. C. Reactivity of a Sterically Hindered Fe(II) Thiolate Dimer with Amines and Hydrazines. *Inorg. Chem.* **2008**, *47* (23), 11382–11390.

[156] Namuswe, F.; Kasper, G. D.; Sarjeant, A. A. N.; Hayashi, T.; Krest, C. M.; Green, M. T.; Moënne-Loccoz, P.; Goldberg, D. P. Rational Tuning of the Thiolate Donor in Model Complexes of Superoxide Reductase: Direct Evidence for a trans Influence in Fe^{III}−OOR Complexes. *J. Am. Chem. Soc.* **2008**, *130* (43), 14189–14200.

[157] Albrecht, M.; Maji, P.; Häusl, C.; Monney, A.; Müller-Bunz, H. N-Heterocyclic carbene bonding to cobalt porphyrin complexes. *Inorg. Chim. Acta* **2012**, *380*, 90–95.

[158] Anding, B. J.; Ellern, A.; Woo, L. K. Comparative Study of Rhodium and Iridium Porphyrin Diaminocarbene and N-Heterocyclic Carbene Complexes. *Organometallics* **2014**, *33* (9), 2219–2229.

[159] Yao, Z.; Li, H.; Liang, X.; Xu, X.; Li, J. The first isolated Manganese(II) porphyrin N-Heterocyclic carbenes: Synthesis and spectroscopic characterizations. *Dyes Pigm.* **2019**, *162*, 75–79.

[160] Yao, Z.; Li, H.; Fan, Y.; Liang, X.; Xu, X.; Li, J. Pentacoordinated Cobalt(II) and Manganese(II) porphyrin N-Heterocyclic carbenes: Isolation, characterization and spectroscopy. *Dyes Pigm.* **2020**, *173*, 107961.

[161] Voutchkova, A. M.; Appelhans, L. N.; Chianese, A. R.; Crabtree, R. H. Disubstituted Imidazolium-2-Carboxylates as Efficient Precursors to N-Heterocyclic Carbene Complexes of Rh, Ru, Ir, and Pd. *J. Am. Chem. Soc.* **2005**, *127* (50), 17624–17625.

[162] Voutchkova, A. M.; Feliz, M.; Clot, E.; Eisenstein, O.; Crabtree, R. H. Imidazolium Carboxylates as Versatile and Selective N-Heterocyclic Carbene Transfer Agents: Synthesis, Mechanism, and Applications. *J. Am. Chem. Soc.* **2007**, *129* (42), 12834–12846.

[163] Shing, K.-P.; Liu, Y.; Cao, B.; Chang, X.-Y.; You, T.; Che, C.-M. N-Heterocyclic Carbene Iron(III) Porphyrin-Catalyzed Intramolecular C(sp^3)–H Amination of Alkyl Azides. *Angew. Chem. Int. Ed.* **2018**, *57* (37), 11947–11951.

[164] Schremmer, C.; Cordes, C.; Klawitter, I.; Bergner, M.; Schiewer, C. E.; Dechert, S.; Demeshko, S.; John, M.; Meyer, F. Spin-State Variations of Iron(III) Complexes with Tetracarbene Macrocycles. *Chemistry – A European Journal* **2019**, *25* (15), 3918–3929.

[165] Fränkel, R.; Kernbach, U.; Bakola-Christianopoulou, M.; Plaia, U.; Suter, M.; Ponikwar, W.; Nöth, H.; Moinet, C.; Fehlhammer, W. P. Homoleptic carbene complexes: Part VIII. Hexacarbene complexes. *J. Organomet. Chem.* **2001**, *617-618*, 530–545.

[166] Ingleson, M. J.; Layfield, R. A. N-Heterocyclic carbene chemistry of iron: fundamentals and applications. *Chem. Commun.* **2012**, *48* (30), 3579–3589.

[167] Prakash, O.; Chábera, P.; Rosemann, N. W.; Huang, P.; Häggström, L.; Ericsson, T.; Strand, D.; Persson, P.; Bendix, J.; Lomoth, R.; Wärnmark, K. A Stable Homoleptic Organometallic Iron(IV) Complex. *Chemistry – A European Journal* **2020**, *26* (56), 12728–12732.

[168] Zhdankin, V. V. Organoiodine(V) Reagents in Organic Synthesis. *The Journal of Organic Chemistry* **2011**, *76* (5), 1185–1197.

[169] Steffen Meyer. Bioinspired Organometallic Analogues of Iron-Sites in Metalloproteins, Georg-August Universität Göttingen, **2013**.

[170] Sastri, C. V.; Park, M. J.; Ohta, T.; Jackson, T. A.; Stubna, A.; Seo, M. S.; Lee, J.; Kim, J.; Kitagawa, T.; Münck, E.; Que,, Lawrence; Nam, W. Axial Ligand Substituted Nonheme $Fe^{IV}O$ Complexes: Observation of Near-UV LMCT Bands and FeO Raman Vibrations. *J. Am. Chem. Soc.* **2005**, *127* (36), 12494–12495.

[171] Castillo, C. E.; Gamba, I.; Vicens, L.; Clémancey, M.; Latour, J.-M.; Costas, M.; Basallote, M. G. Spin State Tunes Oxygen Atom Transfer towards $Fe^{IV}O$ Formation in Fe^{II} Complexes. *Chemistry – A European Journal* **2021**, *27* (15), 4946–4954.

[172] Sahoo, D.; Guchhait, T.; Rath, S. P. Spin Modulation in Highly Distorted Fe^{III} Porphyrinates by Using Axial Coordination and Their π-Cation Radicals. *Eur. J. Inorg. Chem.* **2016**, *2016* (21), 3441–3453.

[173] Adams, D. M.; Long, G. J.; Williams, A. D. Spectroscopy at very high pressures. 36. An infrared study of spin-state equilibriums in some iron(II) complexes. *Inorg. Chem.* **1982** (21), 1049–1053.

[174] Guionneau, P.; Brigouleix, C.; Barrans, Y.; Goeta, A. E.; Létard, J.-F.; Howard, J. A.K.; Gaultier, J.; Chasseau, D. High Pressure and Very Low Temperature Effects on the Crystal Structures of Some Iron(II) Complexes. *C. R. Acad. Sci. Paris* **2001** (4), 161–171.

[175] Alonso, J. A.; Martínez-Lope, M. J.; Casais, M. T.; Fernández-Díaz, M. T. Evolution of the Jahn-Teller distortion of MnO_6 octahedra in $RMnO_3$ perovskites (R = Pr, Nd, Dy, Tb, Ho, Er, Y): a neutron diffraction study. *Inorg. Chem.* **2000**, *39* (5), 917–923.

[176] Deeney, F. A.; Harding, C. J.; Morgan, G. G.; McKee, V.; Nelson, J.; Teat, S. J.; Clegg, W. Response to steric constraint in azacryptate and related complexes of iron-(II) and -(III) *. *J. Chem. Soc., Dalton Trans.* **1998** (11), 1837–1844.

[177] Neese, F. Theoretical spectroscopy of model-nonheme $[Fe(IV)OL_5]^{2+}$ complexes in their lowest triplet and quintet states using multireference ab initio and density functional theory methods. *J. Inorg. Biochem.* **2006**, *100* (4), 716–726.

[178] Jašík, J.; Žabka, J.; Roithová, J.; Gerlich, D. Infrared spectroscopy of trapped molecular dications below 4K. *Int. J. Mass Spectrom.* **2013**, *354-355*, 204–210.

[179] Kumar, R.; Ansari, A.; Rajaraman, G. Axial vs. Equatorial Ligand Rivalry in Controlling the Reactivity of Iron(IV)-Oxo Species: Single-State vs. Two-State Reactivity. *Chemistry – A European Journal* **2018**, *24* (26), 6818–6827.

[180] Ghosh, M.; Singh, K. K.; Panda, C.; Weitz, A.; Hendrich, M. P.; Collins, T. J.; Dhar, B. B.; Sen Gupta, S. Formation of a Room Temperature Stable $Fe^{V}(O)$ Complex: Reactivity Toward Unactivated C–H Bonds. *J. Am. Chem. Soc.* **2014**, *136* (27), 9524–9527.

[181] Bigelow, J. O.; England, J.; Klein, Johannes E. M. N.; Farquhar, E. R.; Frisch, J. R.; Martinho, M.; Mandal, D.; Münck, E.; Shaik, S.; Que, L. Oxoiron(IV) Tetramethylcyclam Complexes with Axial Carboxylate Ligands: Effect of Tethering the Carboxylate on Reactivity. *Inorg. Chem.* **2017**, *56* (6), 3287–3301.

[182] Janardanan, D.; Wang, Y.; Schyman, P.; Que Jr., L.; Shaik, S. The Fundamental Role of Exchange-Enhanced Reactivity in C–H Activation by *S*=2 Oxo Iron(IV) Complexes. *Angew. Chem. Int. Ed.* **2010**, *49* (19), 3342–3345.

[183] Boaz, N. C.; Bell, S. R.; Groves, J. T. Ferryl Protonation in Oxoiron(IV) Porphyrins and Its Role in Oxygen Transfer. *J. Am. Chem. Soc.* **2015**, *137* (8), 2875–2885.

[184] Wang, X.; Ullrich, R.; Hofrichter, M.; Groves, J. T. Heme-thiolate ferryl of aromatic peroxygenase is basic and reactive. *Proceedings of the National Academy of Sciences* **2015**, *112* (12), 3686.

[185] Comba, P.; Fukuzumi, S.; Kotani, H.; Wunderlich, S. Electron-Transfer Properties of an Efficient Nonheme Iron Oxidation Catalyst with a Tetradentate Bispidine Ligand. *Angew. Chem. Int. Ed.* **2010**, *49* (14), 2622–2625.

[186] Kaizer, J.; Klinker, E. J.; Oh, N. Y.; Rohde, J.-U.; Song, W. J.; Stubna, A.; Kim, J.; Münck, E.; Nam, W.; Que, L. Nonheme $Fe^{IV}O$ Complexes That Can Oxidize the C−H Bonds of Cyclohexane at Room Temperature. *J. Am. Chem. Soc.* **2004**, *126* (2), 472–473.

[187] Bryant, J. R.; Mayer, J. M. Oxidation of C−H Bonds by $[(bpy)_2(py)Ru^{IV}O]^{2+}$ Occurs by Hydrogen Atom Abstraction. *J. Am. Chem. Soc.* **2003**, *125* (34), 10351–10361.

[188] Tedder, J. M. Which Factors Determine the Reactivity and Regioselectivity of Free Radical Substitution and Addition Reactions? *Angew. Chem. Int. Ed. Engl.* **1982**, *21* (6), 401–410.

[189] Goetz, M. K.; Anderson, J. S. Experimental Evidence for pKa-Driven Asynchronicity in C–H Activation by a Terminal Co(III)–Oxo Complex. *J. Am. Chem. Soc.* **2019**, *141* (9), 4051–4062.

[190] Wang, X.; Peter, S.; Kinne, M.; Hofrichter, M.; Groves, J. T. Detection and Kinetic Characterization of a Highly Reactive Heme–Thiolate Peroxygenase Compound I. *J. Am. Chem. Soc.* **2012**, *134* (31), 12897–12900.

[191] Compton, R. G.; Banks, C. E. *Understanding Voltammetry*; IMPERIAL COLLEGE PRESS, 2010. DOI: 10.1142/p726.

[192] Weinberg, D. R.; Gagliardi, C. J.; Hull, J. F.; Murphy, C. F.; Kent, C. A.; Westlake, B. C.; Paul, A.; Ess, D. H.; McCafferty, D. G.; Meyer, T. J. Proton-Coupled Electron Transfer. *Chem. Rev.* **2012**, *112* (7), 4016–4093.

[193] Andris, E.; Navrátil, R.; Jasic, J.; Puri, M.; Costas, M.; Que, L.; Roithová, J. Trapping Iron(III)-Oxo Species at the Boundary of the "Oxo Wall": Insights into the Nature of the Fe(III)-O Bond. *J. Am. Chem. Soc.* **2018**, *140* (43), 14391–14400.

[194] Murray, K. S. Binuclear oxo-bridged iron(III) complexes. *Coord. Chem. Rev.* **1974**, *12* (1), 1–35.

[195] Chin, D.-H.; La Mar, G. N.; Balch, A. L. Mechanism of autoxidation of iron(II) porphyrins. Detection of a peroxo-bridged iron(III) porphyrin dimer and the mechanism of its thermal decomposition to the oxo-bridged iron(III) porphyrin dimer. *J. Am. Chem. Soc.* **1980**, *102* (13), 4344–4350.

[196] Vernik, I.; Stynes, D. V. (μ-Oxo)diiron Complexes of Borylated Dimethylglyoximes. Stepwise Ligation to Allosterically Linked Binding Sites and ^{1}H NMR Spectra of Paramagnetic Nitrile, Amine, Imidazole, and Pyridine Derivatives. *Inorg. Chem.* **1996**, *35* (7), 2011–2018.

[197] Weihe, H.; Güdel, H. U. Angular and Distance Dependence of the Magnetic Properties of Oxo-Bridged Iron(III) Dimers. *J. Am. Chem. Soc.* **1997**, *119* (28), 6539–6543.

[198] Carrasco, M. C.; Hematian, S. (Hydr)oxo-bridged heme complexes: From structure to reactivity. *J. Porphyrins Phthalocyanines* **2019**, *23* (11n12), 1286–1307.

[199] Kurtz, D. M. Oxo- and hydroxo-bridged diiron complexes: a chemical perspective on a biological unit. *Chem. Rev.* **1990**, *90* (4), 585–606.

[200] Horikawa, R.; Fujimoto, C.; Yazaki, R.; Ohshima, T. μ-Oxo-Dinuclear-Iron(III)-Catalyzed O-Selective Acylation of Aliphatic and Aromatic Amino Alcohols and Transesterification of Tertiary Alcohols. *Chem. Eur. J.* **2016**, *22* (35), 12278–12281.

[201] Payra, P.; Hung, S.-C.; Kwok, W. H.; Johnston, D.; Gallucci, J.; Chan, M. K. Structural, Magnetic and Catalytic Properties of a Self-Recognized μ-Oxo-Bridged Diiron(III) Bis(benzimidazole) Complex. *Inorg. Chem.* **2001**, *40* (16), 4036–4039.

[202] Collins, T. J. TAML Oxidant Activators: A New Approach to the Activation of Hydrogen Peroxide for Environmentally Significant Problems. *Acc. Chem. Res.* **2002**, *35* (9), 782–790.

[203] Balogh-Hergovich, É.; Speier, G.; Réglier, M.; Giorgi, M.; Kuzmann, E.; Vértes, A. Synthesis, Structure, and Catalytic Activity of New μ-Oxo-Bridged Diiron(III) Complexes. *Eur. J. Inorg. Chem.* **2003**, *2003* (9), 1735–1740.

[204] Wasser, I. M.; Fry, H. C.; Hoertz, P. G.; Meyer, G. J.; Karlin, K. D. Photochemical Organic Oxidations and Dechlorinations with a μ-Oxo Bridged Heme/Non-Heme Diiron Complex. *Inorg. Chem.* **2004**, *43* (26), 8272–8281.

[205] Kodera, M.; Itoh, M.; Kano, K.; Funabiki, T.; Reglier, M. A Diiron Center Stabilized by a Bis-TPA Ligand as a Model of Soluble Methane Monooxygenase: Predominant Alkene Epoxidation with H_2O_2. *Angew. Chem. Int. Ed.* **2005**, *44* (43), 7104–7106.

[206] Ghosh, A.; Tiago de Oliveira, F.; Yano, T.; Nishioka, T.; Beach, E. S.; Kinoshita, I.; Münck, E.; Ryabov, A. D.; Horwitz, C. P.; Collins, T. J. Catalytically Active μ-Oxodiiron(IV) Oxidants from Iron(III) and Dioxygen. *J. Am. Chem. Soc.* **2005**, *127* (8), 2505–2513.

[207] Taktak, S.; Kryatov, S. V.; Haas, T. E.; Rybak-Akimova, E. V. Diiron(III) oxo-bridged complexes with BPMEN and additional monodentate or bidentate ligands: Synthesis and reactivity in olefin epoxidation with H_2O_2. *J. Mol. Catal. A: Chem.* **2006**, *259* (1), 24–34.

[208] Singh, K. K.; Tiwari, M. k.; Dhar, B. B.; Vanka, K.; Sen Gupta, S. Mechanism of Oxygen Atom Transfer from $Fe^{V}(O)$ to Olefins at Room Temperature. *Inorg. Chem.* **2015**, *54* (13), 6112–6121.

[209] Kejriwal, A.; Bandyopadhyay, P.; Biswas, A. N. Aromatic hydroxylation using an oxo-bridged diiron(III) complex: a bio-inspired functional model of toluene monooxygenases. *Dalton Trans.* **2015**, *44* (39), 17261–17267.

[210] Ghosh, M.; Nikhil, Y. L. K.; Dhar, B. B.; Sen Gupta, S. Mechanism of Alcohol Oxidation by $Fe^{V}(O)$ at Room Temperature. *Inorg. Chem.* **2015**, *54* (24), 11792–11798.

[211] Dyckhoff, F.; Schlagintweit, J. F.; Reich, R. M.; Kühn, F. E. Pushing the limits of activity and stability: the effects of Lewis acids on non-heme iron–NHC epoxidation catalysts. *Catalysis Science & Technology* **2020**, *10* (11), 3532–3536.

[212] Bernd, M. A.; Dyckhoff, F.; Hofmann, B. J.; Böth, A. D.; Schlagintweit, J. F.; Oberkofler, J.; Reich, R. M.; Kühn, F. E. Tuning the electronic properties of tetradentate iron-NHC complexes: Towards stable and selective epoxidation catalysts. *J. Catal.* **2020**, *391*, 548–561.

[213] Zhou, W.-J.; Wu, X.-D.; Miao, M.; Wang, Z.-H.; Chen, L.; Shan, S.-Y.; Cao, G.-M.; Yu, D.-G. Light Runs Across Iron Catalysts in Organic Transformations. *Chem. Eur. J.* **2020**, *26* (66), 15052–15064.

[214] Chen, J.; Stepanovic, S.; Draksharapu, A.; Gruden, M.; Browne, W. R. A Non-Heme Iron Photocatalyst for Light-Driven Aerobic Oxidation of Methanol. *Angew. Chem. Int. Ed.* **2018**, *57* (12), 3207–3211.

[215] Cordes, C.; Morganti, M.; Klawitter, I.; Schremmer, C.; Dechert, S.; Meyer, F. Disproportionation Equilibrium of a μ-Oxodiiron(III) Complex Giving Rise to C−H Activation Reactivity: Structural Snapshot of a Unique Oxoiron(IV) Adduct. *Angew. Chem. Int. Ed.* **2019**, *58* (32), 10855–10858.

[216] Venturinelli Jannuzzi, S. A.; Phung, Q. M.; Domingo, A.; Formiga, A. L. B.; Pierloot, K. Spin State Energetics and Oxyl Character of Mn-Oxo Porphyrins by Multiconfigurational ab Initio Calculations: Implications on Reactivity. *Inorg. Chem.* **2016**, *55* (11), 5168–5179.

[217] Balcells, D.; Raynaud, C.; Crabtree, R. H.; Eisenstein, O. A Rational Basis for the Axial Ligand Effect in C−H Oxidation by $[MnO(porphyrin)(X)]^+$ ($X = H_2O, OH^-, O^{2-}$) from a DFT Study. *Inorg. Chem.* **2008**, *47* (21), 10090–10099.

[218] Meyer, S.; Krahe, O.; Kupper, C.; Klawitter, I.; Demeshko, S.; Bill, E.; Neese, F.; Meyer, F. A trans-1,2 End-On Disulfide-Bridged Iron–Tetracarbene Dimer and Its Electronic Structure. *Inorg. Chem.* **2015**, *54* (20), 9770–9776.

[219] Fukuzumi, S.; Ohkubo, K.; Lee, Y.-M.; Nam, W. Lewis Acid Coupled Electron Transfer of Metal–Oxygen Intermediates. *Chem. Eur. J.* **2015**, *21* (49), 17548–17559.

[220] Marshall, A. G.; Hendrickson, C. L.; Jackson, G. S. Fourier transform ion cyclotron resonance mass spectrometry: A primer. *Mass Spectrom. Rev.* **1998**, *17* (1), 1–35.

[221] Crestoni, M. E.; Fornarini, S. Compound I of Naked Heme (Iron Protoporphyrin IX). *Inorg. Chem.* **2007**, *46* (22), 9018–9020.

[222] Crestoni, M. E.; Fornarini, S. Probing the Cytochrome P450-like Reactivity of High-Valent Oxo Iron Intermediates in the Gas Phase. *Inorg. Chem.* **2005**, *44* (15), 5379–5387.

[223] Cantú Reinhard, F. G.; Sainna, M. A.; Upadhyay, P.; Balan, G. A.; Kumar, D.; Fornarini, S.; Crestoni, M. E.; Visser, S. P. de. A Systematic Account on Aromatic Hydroxylation by a Cytochrome P450 Model Compound I: A Low-Pressure Mass Spectrometry and Computational Study. *Chem. Eur. J.* **2016**, *22* (51), 18608–18619.

[224] Sainna, M. A.; Kumar, S.; Kumar, D.; Fornarini, S.; Crestoni, M. E.; Visser, S. P. de. A comprehensive test set of epoxidation rate constants for iron(IV)–oxo porphyrin cation radical complexes. *Chem. Sci.* **2015**, *6* (2), 1516–1529.

[225] Chiavarino, B.; Crestoni, M. E.; Fornarini, S.; Lanucara, F. Probing Bare High-Valent Transition Oxo–Metal Complexes: An Electrospray Ionization Fourier Transform Ion Cyclotron Resonance Study of Reactive Intermediates. *Eur. J. Mass Spectrom.* **2010**, *16* (3), 407–414.

[226] Crestoni, M. E.; Fornarini, S.; Lanucara, F. Oxygen-Atom Transfer by a Naked Manganese(V)–Oxo–Porphyrin Complex Reveals Axial Ligand Effect. *Chem. Eur. J.* **2009**, *15* (32), 7863–7866.

[227] Grützmacher, H. Cooperating ligands in catalysis. *Angew. Chem. Int. Ed.* **2008**, *47* (10), 1814–1818.

[228] Dzik, W. I.; Zhang, X. P.; Bruin, B. de. Redox noninnocence of carbene ligands: carbene radicals in (catalytic) C–C bond formation. *Inorg. Chem.* **2011**, *50* (20), 9896–9903.

[229] Plundrich, G. T.; Wadepohl, H.; Clot, E.; Gade, L. H. η6-Arene-Zirconium-PNP-Pincer Complexes: Mechanism of Their Hydrogenolytic Formation and Their Reactivity as Zirconium(II) Synthons. *Chem. Eur. J.* **2016**, *22* (27), 9283–9292.

[230] Richeter, S.; Jeandon, C.; Kyritsakas, N.; Ruppert, R.; Callot, H. J. Preparation of Six Isomeric Bis-acylporphyrins with Chromophores Reaching the Near-Infrared via Intramolecular Friedel−Crafts Reaction. *J. Org. Chem.* **2003**, *68* (24), 9200–9208.

[231] Arnold, L.; Norouzi-Arasi, H.; Wagner, M.; Enkelmann, V.; Müllen, K. A porphyrin-related macrocycle from carbazole and pyridine building blocks: synthesis and metal coordination. *Chem. Commun.* **2011**, *47* (3), 970–972.

[232] Gee, H.-C.; Lee, C.-H.; Jeong, Y.-H.; Jang, W.-D. Highly sensitive and selective cyanide detection via Cu^{2+} complex ligand exchange. *Chemical communications (Cambridge, England)* **2011**, *47* (43), 11963–11965.

[233] Broere, D. L. J.; Čorić, I.; Brosnahan, A.; Holland, P. L. Quantitation of the THF Content in $Fe[N(SiMe_3)_2]_2 \cdot xTHF$. *Inorg. Chem.* **2017**, *56* (6), 3140–3143.

[234] Drew, M. G. B.; Harding, C. J.; McKee, V.; Morgan, G. G.; Nelson, J. Geometric control of manganese redox state. *J. Chem. Soc., Chem. Commun.* **1995** (10), 1035.

[235] Raba, A.; Cokoja, M.; Ewald, S.; Riener, K.; Herdtweck, E.; Pöthig, A.; Herrmann, W. A.; Kühn, F. E. Synthesis and Characterization of Novel Iron(II) Complexes with Tetradentate Bis(N-heterocyclic carbene)–Bis(pyridine) (NCCN) Ligands. *Organometallics* **2012**, *31* (7), 2793–2800.

[236] Yu, R. P.; Darmon, J. M.; Hoyt, J. M.; Margulieux, G. W.; Turner, Z. R.; Chirik, P. J. High-Activity Iron Catalysts for the Hydrogenation of Hindered, Unfunctionalized Alkenes. *ACS Catal.* **2012**, *2* (8), 1760–1764.

[237] Danopoulos, A. A.; Pugh, D.; Smith, H.; Sassmannshausen, J. Structural and reactivity studies of "pincer" pyridine dicarbene complexes of Fe^0: experimental and computational comparison of the phosphine and NHC donors. *Chemistry (Weinheim an der Bergstrasse, Germany)* **2009**, *15* (22), 5491–5502.

[238] Duan, L.; Wang, M.; Li, P.; Na, Y.; Wang, N.; Sun, L. Carbene-pyridine chelating 2Fe2S hydrogenase model complexes as highly active catalysts for the electrochemical reduction of protons from weak acid (HOAc). *Dalton transactions (Cambridge, England : 2003)* **2007** (13), 1277–1283.

[239] Britovsek, G. J. P.; England, J.; White, A. J. P. Non-heme iron(II) complexes containing tripodal tetradentate nitrogen ligands and their application in alkane oxidation catalysis. *Inorg. Chem.* **2005**, *44* (22), 8125–8134.

[240] Danopoulos, A. A.; Wright, J. A.; Motherwell, W. B. Molecular N_2 complexes of iron stabilised by N-heterocyclic 'pincer' dicarbene ligands. *Chemical communications (Cambridge, England)* **2005** (6), 784–786.

[241] Amort, C.; Malaun, M.; Krajete, A.; Kopacka, H.; Wurst, K.; Christ, M.; Lilge, D.; Kristen, M. O.; Bildstein, B. N-Pyrrolyl-[N,N,N]-bis(imino)pyridyl iron(II) and cobalt(II) olefin polymerization catalysts. *Appl. Organomet. Chem.* **2002**, *16* (9), 506–516.

[242] Higuchi, J.; Kuriyama, S.; Eizawa, A.; Arashiba, K.; Nakajima, K.; Nishibayashi, Y. Preparation and reactivity of iron complexes bearing anionic carbazole-based PNP-type pincer ligands toward catalytic nitrogen fixation. *Dalton transactions (Cambridge, England : 2003)* **2018**, *47* (4), 1117–1121.

[243] Lin, H.-J.; Lutz, S.; O'Kane, C.; Zeller, M.; Chen, C.-H.; Al Assil, T.; Lee, W.-T. Synthesis and characterization of an iron complex bearing a hemilabile NNN-pincer for catalytic hydrosilylation of organic carbonyl compounds. *Dalton Trans.* **2018**, *47* (10), 3243–3247.

[244] Ott, J. C.; Blasius, C. K.; Wadepohl, H.; Gade, L. H. Synthesis, Characterization, and Reactivity of a High-Spin Iron(II) Hydrido Complex Supported by a PNP Pincer Ligand and Its Application as a Homogenous Catalyst for the Hydrogenation of Alkenes. *Inorg. Chem.* **2018**, *57* (6), 3183–3191.

[245] Ashley, A. E.; Cowley, A. R.; Green, J. C.; Johnston, D. R.; Watkin, D. J.; Kays, D. L. Synthesis and Characterisation of Low-Coordinate Transition-Metal Complexes Stabilised by Sterically Demanding Carbazolido Ligands. *Eur. J. Inorg. Chem.* **2009**, *2009* (17), 2547–2552.

[246] Gibson, V. C.; Spitzmesser, S. K.; White, A. J. P.; Williams, D. J. Synthesis and reactivity of 1,8-bis(imino)carbazolide complexes of iron, cobalt and manganese. *Dalton Trans.* **2003** (13), 2718.

[247] Thompson, C. V.; Arman, H. D.; Tonzetich, Z. J. A Pyrrole-Based Pincer Ligand Permits Access to Three Oxidation States of Iron in Organometallic Complexes. *Organometallics* **2017**, *36* (9), 1795–1802.

[248] Britovsek, G. J. P.; Gibson, V. C.; Hoarau, O. D.; Spitzmesser, S. K.; White, A. J. P.; Williams, D. J. Iron and cobalt ethylene polymerization catalysts: variations on the central donor. *Inorg. Chem.* **2003**, *42* (11), 3454–3465.

[249] Anneser, M. R.; Elpitiya, G. R.; Powers, X. B.; Jenkins, D. M. Toward a Porphyrin-Style NHC: A 16-Atom Ringed Dianionic Tetra-NHC Macrocycle and Its Fe(II) and Fe(III) Complexes. *Organometallics* **2019**, *38* (4), 981–987.

[250] Kück, J. W.; Anneser, M. R.; Hofmann, B.; Pöthig, A.; Cokoja, M.; Kühn, F. E. Fighting Fenton Chemistry: A Highly Active Iron(III) Tetracarbene Complex in Epoxidation Catalysis. *ChemSusChem* **2015**, *8* (23), 4056–4063.

[251] Meyer, S.; Orben, C. M.; Demeshko, S.; Dechert, S.; Meyer, F. Synthesis and Characterization of Di- and Tetracarbene Iron(II) Complexes with Chelating N-Heterocyclic Carbene Ligands and Their Application in Aryl Grignard–Alkyl Halide Cross-Coupling. *Organometallics* **2011**, *30* (24), 6692–6702.

[252] Chandrachud, P. P.; Bass, H. M.; Jenkins, D. M. Synthesis of Fully Aliphatic Aziridines with a Macrocyclic Tetracarbene Iron Catalyst. *Organometallics* **2016**, *35* (11), 1652–1657.

[253] Berry, J. F.; Bill, E.; Bothe, E.; Neese, F.; Wieghardt, K. Octahedral non-heme oxo and non-oxo Fe(IV) complexes: an experimental/theoretical comparison. *J. Am. Chem. Soc.* **2006**, *128* (41), 13515–13528.

[254] Berry, J. F.; Bill, E.; Bothe, E.; Weyhermüller, T.; Wieghardt, K. Octahedral non-heme non-oxo Fe(IV) species stabilized by a redox-innocent N-methylated cyclam-acetate ligand. *J. Am. Chem. Soc.* **2005**, *127* (33), 11550–11551.

[255] Karon, K.; Lapkowski, M. Carbazole electrochemistry: a short review. *J. Solid State Electrochem.* **2015**, *19* (9), 2601–2610.

[256] Masahide, Y.; Yoshinobu, T.; Akira, T. Near-Infrared Charge Resonance Band of Intramolecular Carbazole Dimer Radical Cations Studied by Nanosecond Laser Photolysis. *Chemical Phisics Letters* **1989**, *154* (6), 559-562.

[257] Yoshinobu, T.; Akira, T.; Yoshihiko, O.; Masahide, Y. Stabilization of carbazole radical cation formed in poly(N-vinylcarbazole) by charge delocalization. *Macromolecules* **1990**, *23*, 4019–4023.

[258] Ikezaki, A.; Takahashi, M.; Nakamura, M. Equilibrium between Fe(IV) porphyrin and Fe(III) porphyrin radical cation: new insight into the electronic structure of high-valent iron porphyrin complexes. *Chemical communications (Cambridge, England)* **2013**, *49* (30), 3098–3100.

[259] Banerjee, P.; Company, A.; Weyhermüller, T.; Bill, E.; Hess, C. R. Zn and Fe complexes containing a redox active macrocyclic biquinazoline ligand. *Inorg. Chem.* **2009**, *48* (7), 2944–2955.

[260] Shen, J.; Shao, J.; Ou, Z.; E, W.; Koszarna, B.; Gryko, D. T.; Kadish, K. M. Electrochemistry and spectroelectrochemistry of meso-substituted free-base corroles in nonaqueous media: reactions of (Cor)H_3, (Cor)H_4^+, and (Cor)H_2^-. *Inorg. Chem.* **2006**, *45* (5), 2251–2265.

[261] Connelly, N. G.; Geiger, W. E. Chemical Redox Agents for Organometallic Chemistry. *Chem. Rev.* **1996**, *96* (2), 877–910.

[262] Strautmann, J. B. H.; George, S. D.; Bothe, E.; Bill, E.; Weyhermüller, T.; Stammler, A.; Bögge, H.; Glaser, T. Molecular and electronic structures of mononuclear iron complexes using strongly electron-donating ligands and their oxidized forms. *Inorg. Chem.* **2008**, *47* (15), 6804–6824.

[263] Katz, B. A.; Strouse, C. E. Molecular transformations in the solid state. Crystallographic resolution of the spin isomers of tris(2-picolylamine)iron(II) dichloride and the structural relationship between the methanol and ethanol solvates. *J. Am. Chem. Soc.* **1979**, *101* (21), 6214–6221.

[264] Sinn, E.; Sim, G.; Dose, E. V.; Tweedle, M. F.; Wilson, L. J. Iron(III) chelates with hexadentate ligands from triethylenetetramine and .beta.-diketones or salicylaldehyde. Spin state dependent crystal and molecular structures of [Fe(acac)2trien]PF_6 (S = 5/2), [Fe(acacCl)2trien]PF_6 (S = 5/2), [Fe(sal)2trien]Cl·2H_2O (S = 1/2), and [Fe(sal)2trien]NO_3·H_2O(S = 1/2). *J. Am. Chem. Soc.* **1978**, *100* (11), 3375–3390.

[265] Neese, F. The ORCA program system. *WIREs Comput. Mol. Sci.* **2012**, *2* (1), 73–78.

[266] Neese, F. Software update: the ORCA program system, version 4.0. *WIREs Comput. Mol. Sci.* **2018**, *8* (1), e1327.

[267] Muresan, N.; Lu, C. C.; Ghosh, M.; Peters, J. C.; Abe, M.; Henling, L. M.; Weyhermöller, T.; Bill, E.; Wieghardt, K. Bis(alpha-diimine)iron complexes: electronic structure determination by spectroscopy and broken symmetry density functional theoretical calculations. *Inorg. Chem.* **2008**, *47* (11), 4579–4590.

[268] Gütlich, P.; Bill, E.; Trautwein, A. X. *Mössbauer Spectroscopy and Transition-metal Chemistry: Fundamentals and Applications*, 2010.

[269] Keutel, H.; Käpplinger, I.; Jäger, E.-G.; Grodzicki, M.; Schünemann, V.; Trautwein, A. X. Structural, Magnetic, and Electronic Properties of a Pentacoordinated Intermediate-Spin (S = 3/2) Iron(III) Complex with a Macrocyclic $[N_4]^{2-}$ Ligand. *Inorg. Chem.* **1999**, *38* (10), 2320–2327.

[270] Masuda, H.; Taga, T.; Osaki, K.; Sugimoto, H.; Yoshida, Z.-i.; Ogoshi, H. The Crystal and Molecular Structure of Six-coordinate Intermediate-spin Porphinatoiron(III) Complex. (Octaethylporphinato)bis(tetrahydrofuran)iron(III) Perchlorate. *Bull. Chem. Soc. Jpn.* **1982**, *55* (12), 3891–3895.

[271] Ikeue, T.; Ohgo, Y.; Yamaguchi, T.; Takahashi, M.; Takeda, M.; Nakamura, M. Saddle-Shaped Six-Coordinate Iron(III) Porphyrin Complexes Showing a Novel Spin Crossover between S=1/2 and S=3/2 Spin States. *Angew. Chem. Int. Ed.* **2001**, *40* (14), 2617–2620.

[272] Koch, W. O.; Schünemann, V.; Gerdan, M.; Trautwein, A. X.; Krüger, H.-J. Evidence for an Unusual Thermally Induced Low-Spin (S=1/2) ⇄ Intermediate-Spin (S=3/2) Transition in a Six-Coordinate Iron(III) Complex: Structure and Electronic Properties of a (1,2-Benzenedithiolato)iron(III) Complex Containing N,N′-Dimethyl-2,11-diaza[3.3](2,6)pyridinophane as Ligand. *Chem. Eur. J.* **1998**, *4* (4), 686–691.

[273] Neese, F. Prediction and interpretation of the ^{57}Fe isomer shift in Mössbauer spectra by density functional theory. *Inorg. Chim. Acta* **2002**, *337*, 181–192.

[274] Ghosh, M.; Cramer, H. H.; Dechert, S.; Demeshko, S.; John, M.; Hansmann, M. M.; Ye, S.; Meyer, F. A μ-Phosphido Diiron Dumbbell in Multiple Oxidation States. *Angew. Chem. Int. Ed.* **2019**, *58* (40), 14349–14356.

[275] Culotta, E.; Koshland, Daniel E., Jr. NO news is good news. *Science* **1992**, *258*, 1862+.

[276] Lowenstein, C. J.; Dinerman, J. L.; Snyder, S. H. Nitric Oxide: A Physiologic Messenger. *Annals of Internal Medicine* **1994**, *120* (3), 227–237.

[277] Bogdan, C. Nitric oxide and the immune response. *Nat. Immunol.* **2001**, *2* (10), 907–916.

[278] Averill, B. A. Dissimilatory Nitrite and Nitric Oxide Reductases. *Chem. Rev.* **1996**, *96* (7), 2951–2964.

[279] Maia, L. B.; Moura, J. J. G. How Biology Handles Nitrite. *Chem. Rev.* **2014**, *114* (10), 5273–5357.

[280] Sudhamsu, J.; Crane, B. R. Bacterial nitric oxide synthases: what are they good for? *Trends Microbiol.* **2009**, *17* (5), 212–218.

[281] Gardner, P. R. Nitric oxide dioxygenase function and mechanism of flavohemoglobin, hemoglobin, myoglobin and their associated reductases. *J. Inorg. Biochem.* **2005**, *99* (1), 247–266.

[282] Wasser, I. M.; Vries, S. de; Moënne-Loccoz, P.; Schröder, I.; Karlin, K. D. Nitric Oxide in Biological Denitrification: Fe/Cu Metalloenzyme and Metal Complex NO_x Redox Chemistry. *Chem. Rev.* **2002**, *102* (4), 1201–1234.

[283] Shiro, Y. Structure and function of bacterial nitric oxide reductases: Nitric oxide reductase, anaerobic enzymes. *Biochimica et Biophysica Acta (BBA) - Bioenergetics* **2012**, *1817* (10), 1907–1913.

[284] Lehnert, N.; Dong, H. T.; Harland, J. B.; Hunt, A. P.; White, C. J. Reversing nitrogen fixation. *Nat. Rev. Chem.* **2018**, *2* (10), 278–289.

[285] Enemark, J. H.; Feltham, R. D. Principles of structure, bonding, and reactivity for metal nitrosyl complexes. *Coord. Chem. Rev.* **1974**, *13* (4), 339–406.

[286] Goodrich, L. E.; Paulat, F.; Praneeth, V. K. K.; Lehnert, N. Electronic Structure of Heme-Nitrosyls and Its Significance for Nitric Oxide Reactivity, Sensing, Transport, and Toxicity in Biological Systems. *Inorg. Chem.* **2010**, *49* (14), 6293–6316.

[287] Brown, C. A.; Pavlosky, M. A.; Westre, T. E.; Zhang, Y.; Hedman, B.; Hodgson, K. O.; Solomon, E. I. Spectroscopic and Theoretical Description of the Electronic Structure of S = 3/2 Iron-Nitrosyl Complexes and Their Relation to O_2 Activation by Non-Heme Iron Enzyme Active Sites. *J. Am. Chem. Soc.* **1995**, *117* (2), 715–732.

[288] Zhang, Y.; Pavlosky, M. A.; Brown, C. A.; Westre, T. E.; Hedman, B.; Hodgson, K. O.; Solomon, E. I. Spectroscopic and theoretical description of the electronic structure of the S = 3/2 nitrosyl complex of non-heme iron enzymes. *J. Am. Chem. Soc.* **1992**, *114* (23), 9189–9191.

[289] Hauser, C.; Glaser, T.; Bill, E.; Weyhermüller, T.; Wieghardt, K. The Electronic Structures of an Isostructural Series of Octahedral Nitrosyliron Complexes $\{Fe{-}NO\}^{6,7,8}$ Elucidated by Mössbauer Spectroscopy. *J. Am. Chem. Soc.* **2000**, *122* (18), 4352–4365.

[290] Serres, R. G.; Grapperhaus, C. A.; Bothe, E.; Bill, E.; Weyhermüller, T.; Neese, F.; Wieghardt, K. Structural, Spectroscopic, and Computational Study of an Octahedral, Non-Heme $\{Fe{-}NO\}^{6-8}$ Series: $[Fe(NO)(cyclam\text{-}ac)]^{2+/+/0}$. *J. Am. Chem. Soc.* **2004**, *126* (16), 5138–5153.

[291] Kupper, C.; Rees, J. A.; Dechert, S.; DeBeer, S.; Meyer, F. Complete Series of {FeNO}^{8}, {FeNO}^{7}, and {FeNO}^{6} Complexes Stabilized by a Tetracarbene Macrocycle. *J. Am. Chem. Soc.* **2016**, *138* (25), 7888–7898.

[292] Kupper, C.; Schober, A.; Demeshko, S.; Bergner, M.; Meyer, F. An Exclusively Organometallic {FeNO}^{7} Complex with Tetracarbene Ligation and a Linear FeNO Unit. *Inorg. Chem.* **2015**, *54* (7), 3096–3098.

[293] Keilwerth, M.; Hohenberger, J.; Heinemann, F. W.; Sutter, J.; Scheurer, A.; Fang, H.; Bill, E.; Neese, F.; Ye, S.; Meyer, K. A Series of Iron Nitrosyl Complexes {Fe–NO}$^{6–9}$ and a Fleeting {Fe–NO}^{10} Intermediate en Route to a Metalacyclic Iron Nitrosoalkane. *J. Am. Chem. Soc.* **2019**, *141* (43), 17217–17235.

[294] Arulsamy, N.; Bohle, D. S.; Butt, J. A.; Irvine, G. J.; Jordan, P. A.; Sagan, E. Interrelationships between Conformational Dynamics and the Redox Chemistry of S-Nitrosothiols. *J. Am. Chem. Soc.* **1999**, *121* (30), 7115–7123.

[295] Harrop, T. C.; Tonzetich, Z. J.; Reisner, E.; Lippard, S. J. Reactions of Synthetic [2Fe-2S] and [4Fe-4S] Clusters with Nitric Oxide and Nitrosothiols. *J. Am. Chem. Soc.* **2008**, *130* (46), 15602–15610.

[296] Singh, R. J.; Hogg, N.; Joseph, J.; Kalyanaraman, B. Mechanism of Nitric Oxide Release from S-Nitrosothiols*. *J. Biol. Chem.* **1996**, *271* (31), 18596–18603.

[297] Addison, A. W.; Rao, T. N.; Reedijk, J.; van Rijn, J.; Verschoor, G. C. Synthesis, structure, and spectroscopic properties of copper(II) compounds containing nitrogen–sulphur donor ligands; the crystal and molecular structure of aqua[1,7-bis(N-methylbenzimidazol-2′-yl)-2,6-dithiaheptane]copper(II) perchlorate. *J. Chem. Soc., Dalton Trans.* **1984** (7), 1349–1356.

[298] Berto, T. C.; Speelman, A. L.; Zheng, S.; Lehnert, N. Mono- and dinuclear non-heme iron–nitrosyl complexes: Models for key intermediates in bacterial nitric oxide reductases. *Coord. Chem. Rev.* **2013**, *257* (1), 244–259.

[299] Speelman, A. L.; White, C. J.; Zhang, B.; Alp, E. E.; Zhao, J.; Hu, M.; Krebs, C.; Penner-Hahn, J.; Lehnert, N. Non-heme High-Spin {FeNO}$^{6–8}$ Complexes: One Ligand Platform Can Do It All. *J. Am. Chem. Soc.* **2018**, *140* (36), 11341–11359.

[300] Wolf, M.; Klüfers, P. Structure and Bonding of High-Spin Nitrosyl–Iron(II) Compounds with Mixed N,O-Chelators and Aqua Ligands. *Eur. J. Inorg. Chem.* **2017**, *2017* (17), 2303–2312.

[301] Wyllie, G. R. A.; Scheidt, W. R. Solid-State Structures of Metalloporphyrin NOx Compounds. *Chem. Rev.* **2002**, *102* (4), 1067–1090.

[302] Dai, P.; Dussault, P. H.; Trullinger, T. K. Magnesium/Methanol: An Effective Reducing Agent for Peroxides. *The Journal of Organic Chemistry* **2004**, *69* (8), 2851–2852.

[303] Praneeth, V. K. K.; Paulat, F.; Berto, T. C.; George, S. D.; Näther, C.; Sulok, C. D.; Lehnert, N. Electronic Structure of Six-Coordinate Iron(III)−Porphyrin NO Adducts: The Elusive Iron(III)−NO(radical) State and Its Influence on the Properties of These Complexes. *J. Am. Chem. Soc.* **2008**, *130* (46), 15288–15303.

[304] McQuarters, A. B.; Kampf, J. W.; Alp, E. E.; Hu, M.; Zhao, J.; Lehnert, N. Ferric Heme-Nitrosyl Complexes: Kinetically Robust or Unstable Intermediates? *Inorg. Chem.* **2017**, *56* (17), 10513–10528.

[305] Ellison, M. K.; Scheidt, W. R. Synthesis, Molecular Structures, and Properties of Six-Coordinate [Fe(OEP)(L)(NO)]$^{+}$ Derivatives: Elusive Nitrosyl Ferric Porphyrins. *J. Am. Chem. Soc.* **1999**, *121* (22), 5210–5219.

[306] Patra, A. K.; Rose, M. J.; Olmstead, M. M.; Mascharak, P. K. Reactions of Nitric Oxide with a Low-Spin Fe(III) Center Ligated to a Tetradentate Dicarboxamide N_4 Ligand: Parallels between Heme and Non-heme Systems. *J. Am. Chem. Soc.* **2004**, *126* (15), 4780–4781.

[307] Patra, A. K.; Dube, K. S.; Sanders, B. C.; Papaefthymiou, G. C.; Conradie, J.; Ghosh, A.; Harrop, T. C. A thermally stable $\{FeNO\}^8$ complex: properties and biological reactivity of reduced MNO systems. *Chem. Sci.* **2012**, *3* (2), 364–369.

[308] Lehnert, N.; Galinato, M. G. I.; Paulat, F.; Richter-Addo, G. B.; Sturhahn, W.; Xu, N.; Zhao, J. Nuclear Resonance Vibrational Spectroscopy Applied to [Fe(OEP)(NO)]: The Vibrational Assignments of Five-Coordinate Ferrous Heme−Nitrosyls and Implications for Electronic Structure. *Inorg. Chem.* **2010**, *49* (9), 4133–4148.

[309] Mu, X. H.; Kadish, K. M. In situ FTIR and UV-visible spectroelectrochemical studies of iron nitrosyl porphyrins in nonaqueous media. *Inorg. Chem.* **1988**, *27* (26), 4720–4725.

[310] Nasri, H.; Ellison, M. K.; Chen, S.; Huynh, B. H.; Scheidt, W. R. Sharing the π-Bonding. An Iron Porphyrin Derivative with Trans, π-Accepting Axial Ligands. Synthesis, EPR and Mössbauer Spectra, and Molecular Structure of Two Forms of the Complex Nitronitrosyl(α,α,α,α-tetrakis(o-pivalamidophenyl)- porphinato)ferrate(II). *J. Am. Chem. Soc.* **1997**, *119* (27), 6274–6283.

[311] Pellegrino, J.; Bari, S. E.; Bikiel, D. E.; Doctorovich, F. Successful Stabilization of the Elusive Species $\{FeNO\}^8$ in a Heme Model. *J. Am. Chem. Soc.* **2010**, *132* (3), 989–995.

[312] Speelman, A. L.; Lehnert, N. Characterization of a High-Spin Non-Heme $\{FeNO\}^8$ Complex: Implications for the Reactivity of Iron Nitroxyl Species in Biology. *Angew. Chem. Int. Ed.* **2013**, *52* (47), 12283–12287.

[313] Hu, B.; Li, J. One Electron Makes Differences: From Heme $\{FeNO\}^7$ to $\{FeNO\}^8$. *Angew. Chem. Int. Ed.* **2015**, *54* (36), 10579–10582.

[314] Boduszek, B.; Shine, H. J. Preparation of solid thianthrene cation radical tetrafluoroborate. *The Journal of Organic Chemistry* **1988**, *53* (21), 5142–5143.

[315] Gottlieb, H. E.; Kotlyar, V.; Nudelman, A. NMR Chemical Shifts of Common Laboratory Solvents as Trace Impurities. *J. Org. Chem.* **1997**, *62* (21), 7512–7515.

[316] Elgrishi, N.; Rountree, K. J.; McCarthy, B. D.; Rountree, E. S.; Eisenhart, T. T.; Dempsey, J. L. A Practical Beginner's Guide to Cyclic Voltammetry. *J. Chem. Educ.* **2018**, *95* (2), 197–206.

[317] Stoll, S.; Schweiger, A. EasySpin, a comprehensive software package for spectral simulation and analysis in EPR. *Journal of magnetic resonance (San Diego, Calif. : 1997)* **2006**, *178* (1), 42–55.

[318] E. Bill. julX:Max-Planck Institute For Chemical Energy Conversion, Mülheim/Ruhr, Germany, **n.d.**

[319] Petersson, G. A.; Al-Laham, M. A. A complete basis set model chemistry. II. Open-shell systems and the total energies of the first-row atoms. *The Journal of Chemical Physics* **1991**, *94* (9), 6081–6090.

[320] Petersson, G. A.; Bennett, A.; Tensfeldt, T. G.; Al-Laham, M. A.; Shirley, W. A.; Mantzaris, J. A complete basis set model chemistry. I. The total energies of closed-shell atoms and hydrides of the first-row elements. *The Journal of Chemical Physics* **1988**, *89* (4), 2193–2218.

[321] Weigend, F.; Ahlrichs, R. Balanced basis sets of split valence, triple zeta valence and quadruple zeta valence quality for H to Rn: Design and assessment of accuracy. *PCCP* **2005**, *7* (18), 3297–3305.

[322] Runge, E.; Gross, E. K. U. Density-Functional Theory for Time-Dependent Systems. *Phys. Rev. Lett.* **1984**, *52* (12), 997–1000.

[323] Casida, M. E.; Jamorski, C.; Casida, K. C.; Salahub, D. R. Molecular excitation energies to high-lying bound states from time-dependent density-functional response theory: Characterization and correction of the time-dependent local density approximation ionization threshold. *The Journal of Chemical Physics* **1998**, *108* (11), 4439–4449.

[324] Sheldrick, G. M. SHELXT - integrated space-group and crystal-structure determination. *Acta crystallographica. Section A, Foundations and advances* **2015**, *71* (Pt 1), 3–8. Published Online: Jan. 1, 2015.

[325] Sheldrick, G. M. Crystal structure refinement with SHELXL. *Acta crystallographica. Section C, Structural chemistry* **2015**, *71* (Pt 1), 3–8. Published Online: Jan. 1, 2015.

[326] STOE & CIE GmbH. X-RED:Darmstadt, Germany **2002**.

[327] BRUKER AXS GmbH. SADABS:Karlsruhe, Germany **2016**.

Affidavit

I, Massimiliano Morganti, hereby declare that the present work constitutes my doctoral dissertation in its final version. The official disputation of this doctoral work has taken place on September 2nd 2021.

14.03.2022, Sierre, Switzerland

Massimiliano Morganti